Constraints on the Magmatic History of Paleo- and Mesoarchean Meta-Igneous Rocks of the Eastern Kaapvaal Craton, Southern Africa

Kathrin Schneider

Dissertation

zur Erlangung des Grades eines

Doktors der Naturwissenschaften

(doctor rerum naturalium)

am Fachbereich Geowissenschaften

der Freien Universität Berlin

November 2018 – Berlin, Germany

Erstgutachter:	Prof. Harry Becker, Freie Universität Berlin
Zweitgutachter:	Prof. Carsten Münker, Universität zu Köln

Tag der Disputation: 18.12.2018

Eidesstattliche Erklärung

Hiermit versichere ich, die vorliegende Dissertation selbstständig und ohne unerlaubte Hilfe angefertigt zu haben. Bei der Verfassung der Dissertation wurden keine anderen als die im Text aufgeführten Hilfsmittel verwendet. Alle Aussagen innerhalb der vorliegenden Arbeit, welche dem Wortlaut oder dem Sinne nach aus anderen Quellen entnommen wurden, sind im Text kenntlich gemacht und befinden sich in einem vollständigen Verzeichnis. Beiträge von Koautoren zu publizierten und zur Publikation vorbereiteten Manuskripten sind im Chapter 1.6 „Main chapters of the thesis“ dieser Arbeit dargelegt.

Ein Promotionsverfahren zu einem früheren Zeitpunkt an einer anderen Hochschule oder bei einem anderen Fachbereich wurde nicht beantragt.

_____

Berlin, den 12.11.2018

Summary

Understanding the formation and stabilization of Archean crust is important for our knowledge about geological processes that operated on the early Earth. The eastern Kaapvaal Craton in southern Africa represents a unique and well-preserved fragment of Paleo- to Mesoarchean continental crust that is ideal to shed some light on this conundrum. Hence, this dissertation aims to answer the following questions: I) Was the early Earth´s crust solely formed in the Archean or did Hadean crustal or mantle-derived material contribute to Archean crust formation?; if so, what was the nature of these Hadean reservoirs? II) How did the mantle sources that contributed material to crustal thickening evolve throughout the Paleo- to Mesoarchean, and in what kind of geological setting did this crust formation occur, early plate subduction or mantle plume-controlled magmatism?

The methods applied to answer these two questions are major and trace element analysis in combination with analysis of the whole-rock ^{176}Lu-^{177}Hf, ^{147}Sm-^{143}Nd, and ^{146}Sm-^{142}Nd isotope systems. The long-lived ^{176}Lu-^{177}Hf and ^{147}Sm-^{143}Nd isotope systems were applied to trace mantle differentiation in the Archean, whereas the short-lived ^{146}Sm-^{142}Nd isotope system was applied to trace crust-mantle differentiation in the Hadean.

To answer the first research question whether or not Hadean crust or mantle-derived material contributed to Archean crust formation, granitoids and amphibolites of the eastern Kaapvaal Craton, namely the Ancient Gneiss Complex (AGC) of Swaziland and the Barberton Greenstone Belt (BGB) in the Mpumalanga Province of South Africa were investigated for abundance variations of ^{142}Nd. The well-preserved crustal and mantle-derived samples cover an age range from 3.66 to 3.22 Ga and are representative of major geological units of the AGC and the lower Onverwacht Group of the BGB. The investigated samples yielded μ^{142}Nd values ranging from -8 ppm to +3 ppm with typical uncertainties smaller than ± 4.4 ppm, relative to the JNdi-1 terrestrial standard. The μ^{142}Nd values of these 17 measured samples show a bimodal distribution with ten samples showing a tendency towards slightly negative μ^{142}Nd anomalies and seven samples having μ^{142}Nd values similar to the terrestrial reference. The only clearly resolvable μ^{142}Nd anomalies were found in a 3.44 Ga Ngwane Gneiss sample of the AGC and in amphibolites of the ca. 3.45 Ga Dwalile Greenstone Remnant, infolded in the AGC, revealing μ^{142}Nd values that range from -7.9 ± 4.4 to -6.1 ± 4.3 ppm. The μ^{142}Nd

deficits do not correlate with age, lithological unit, or sample locality. Instead, the mantle-derived rocks of the BGB and AGC were likely formed by derivation from two distinct mantle reservoirs that can be distinguished by their μ^{142}Nd signatures. One mantle reservoir preserved the enriched ^{142}Nd signature at least until 3.46 Ga, and one modern-like mantle reservoir that did not preserve a ^{142}Nd signature. Furthermore, the granitoids showing negative μ^{142}Nd anomalies likely formed by re-melting and incorporation of Hadean protocrustal material and preserved their negative μ^{142}Nd signature at least until 3.22 Ga. However, it cannot be resolved whether the negative μ^{142}Nd signature in this Hadean protocrustal material was ultimately derived from crust-mantle differentiation of a modern-like or from an already enriched mantle source. In contrast, the oldest gneisses showing no μ^{142}Nd anomaly are up to 3.64 Ga in age, indicating that a modern terrestrial ^{142}Nd reservoir was already present by early Archean times and coexisted with the enriched ^{142}Nd mantle reservoir.

To constrain the evolution of the mantle sources providing material to crustal thickening in the Paleo- to Mesoarchean, metabasalts and metakomatiites of the lower Onverwacht Group of the BGB, and ca. 2.9 to 2.8 Ga metabasalts collected in the vicinity of the Kubuta Ranch in central Swaziland (AGC) were investigated.

The metabasalts of the 3.55 to 3.48 Ga Sandspruit and Theespruit Formations of the lower Onverwacht Group can be subdivided into three groups, based on their incompatible trace element characteristics: a light rare earth element (LREE) depleted group, a LREE-undepleted group, and a LREE-enriched group. Positive $\varepsilon Hf_{(t)}$ and $\varepsilon Nd_{(t)}$ values of ca. +3 to +4 and 0 to +2, respectively, together with depletions in Th and La_{CN}/Yb_{CN} below one for the LREE-depleted metabasalts indicate derivation from an incompatible element-depleted mantle source, possibly the ancient upper mantle. However, chondritic $\varepsilon Hf_{(t)}$ and $\varepsilon Nd_{(t)}$ values combined with positive Th and La_{CN}/Yb_{CN} of the LREE-enriched samples indicate a contribution from older AGC crust in the petrogenesis of these samples.

Trace element patterns of metakomatiites and metabasalts of the 3.48 to 3.45 Ga Komati Formation of the lower Onverwacht Group are generally flat relative to primitive mantle, with slight depletions in heavy rare earth elements and Th and overall positive $\varepsilon Hf_{(t)}$ of +2.5 ± 3.5 (2s.d.) and $\varepsilon Nd_{(t)}$ of +0.5 ± 2.2 (2s.d.) for both metalava types. The similarity in trace element and Hf-Nd isotope characteristics suggests a common magmatic origin for the basalts and komatiites by high degrees of melting of an incompatible element-depleted mantle source containing residual garnet. Hence, the

komatiites are interpreted as being plume generated, whereas the basalts are interpreted to be the products of fractional crystallization from the komatiitic parental magma.

Based on the current data set, and in combination with previously published data, I propose a geodynamic evolution model for volcanic rocks of the lower Onverwacht Group that involves the evolution from a continent-type setting (for the Sandspruit and Theespruit Formations) to an oceanic setting (for the Komati Formation) as a consequence of continental rifting.

The ca. 2.9 to 2.8 Ga Kubuta metavolcanic rocks are most likely genetically related to the ca. 3.0 Ga Usushwana Igneous Complex in west-central Swaziland and the ca. 2.9 Ga Hlagothi Complex located in KwaZulu-Natal Province of South Africa. The coeval ca. 3.0 Ga Nsuze and ca. 2.9 Ga Mozaan Groups of the Pongola Supergroup of south-central Swaziland and northern KwaZulu-Natal Province have similar elemental anomalies, albeit slightly elevated concentrations, compared to the Kubuta metavolcanic rocks.

This study shows that the Nsuze and Mozaan Groups were sourced from komatiitic parental magmas derived from a weakly depleted mantle source, whereas the Usushwana, Hlagothi, and Kubuta units were sourced from a more depleted mantle reservoir comparable to modern depleted upper mantle. Prior to eruption, all mafic rocks underwent assimilation-fractional crystallization processes involving ca. 3.5 Ga crustal rocks of the AGC.

Combining these geochemical observations with literature age data leads to a refined petrogenetic model for continental flood volcanism in a Mesoarchean large igneous province (LIP) on the eastern Kaapvaal Craton. This refined model includes the presence of two distinct mantle sources in the formation of this continental LIP – a deep mantle plume producing komatiite melts as well as ambient upper mantle producing more incompatible element-depleted melts such as the Kubuta rocks.

Collectively, the Paleo- to Mesoarchean mantle-derived rocks investigated in this study record the transitional development from a submerged continental setting to an oceanic setting and back to a continental setting within a time period of about 600 Ma.

Zusammenfassung

Das Verständnis der Bildung und Stabilisierung von Archaischer Kruste ist fundamental für unser Wissen über die geologischen Prozesse, die auf der frühen Erde stattgefunden haben. Der östliche Kaapvaal-Kraton im südlichen Afrika repräsentiert ein einmaliges und gut erhaltenes Fragment von paläo- bis mesoarchaischer, kontinentaler Kruste, das ideal ist um neue Erkenntnisse zur Lösung dieses Rätsel zu liefern. Daher beabsichtige ich in dieser Dissertation die folgenden Fragen zu beantworten: I) Wurde die Kruste der frühen Erde nur im Archaikum gebildet oder hat auch Hadaisches Krusten- oder Mantelmaterial zur Bildung von archaischer Kruste beigetragen? Und wenn dies zutrifft, was waren die Eigenschaften dieses Hadaischen Reservoirs? II) Wie haben sich die Mantelquellen, die Material zur Krustenverdickung geliefert haben, während dem Paläo- zum Mesoarchaikum entwickelt, und in welcher Art geologischem Regime hat Krustenbildung damals stattgefunden? Zwei mögliche geologische Regime, die zur Kurstenverdickung im Archaikum beigetragen haben könnten sind zum einen frühe Subduktion oder zum anderen durch einen Mantelplume kontollierten Magmatismus.

Zur Beantwortung dieser beiden Fragestellungen wurden Gesteinsproben auf ihre Haupt- und Spurenelementkonzentrationen in Kombination mit den Gesamtgesteins-isotopien der ^{176}Lu-^{177}Hf, ^{147}Sm-^{143}Nd und ^{146}Sm-^{142}Nd Isotopensysteme analysiert. Die langlebigen ^{176}Lu-^{177}Hf und ^{147}Sm-^{143}Nd Isotopensysteme wurden angewendet um Manteldifferentiation im Archaikum festzustellen, wohingegen das kurzlebige ^{146}Sm-^{142}Nd Isotopensystem verwendet wurde um die Differentiation von Kruste und Mantel im Hadaikum zu identifizieren.

Um die Frage zu beantworten, ob hadaisches Krusten- oder Mantelmaterial in der Bildung der archaischen Kruste involviert war, wurden Granitoide und Amphibolite des östlichen Kaapvaal-Kratons, genauer des Antiken Gneis Komplexes und des Barberton Grünsteingürtels in der südafrikanischen Mpumalanga-Provinz, untersucht. Die gut erhaltenen Krusten- und Mantelproben decken eine Alterspanne von 3.66 bis 3.22 Ga ab und sind repräsentativ für die großen geologischen Einheiten des Antiken Gneis Komplexes und der unteren Onverwacht Gruppe des Barberton Grünsteingürtels. Die untersuchten Proben ergaben μ^{142}Nd-Werte zwischen -8 ppm und +3 ppm mit typischen Unsicherheiten kleiner als ± 4.4 ppm, relativ zum terrestrischen Standard JNdi-1. Die μ^{142}Nd-Werte der 17 gemessenen Proben zeigen eine bimodale Verteilung mit zehn Proben, die eine Tendenz zu leicht negativen μ^{142}Nd-Werten aufweisen, und sieben

Proben, deren μ^{142}Nd-Werte ähnlich zu dem terrestrischen Referenzmaterial sind. Die einzigen auflösbaren μ^{142}Nd-Anomalien wurden in einer 3.44 Ga alten Probe des Ngwane Gneises des Antiken Gneis Komplexes und in Amphiboliten des ca. 3.45 Ga alten Dwalile Grünsteingürtels, der in den Antiken Gneis Komplexe eingefaltet ist, gefunden. Diese Gesteine weisen μ^{142}Nd-Werte von -7.9 ± 4.4 bis -6.1 ± 4.3 ppm auf. Die μ^{142}Nd-Defizite korrelieren weder mit dem Alter, noch der lithologischen Einheit oder der Proben-lokation. Unsere Ergebnisse zeigen vielmehr, dass zwei verschiedene Mantelquellen in die Bildung der mafischen Gesteine des Barberton Grünsteingürtels und des Antiken Gneis Komplexes involviert waren, welche anhand ihrer ^{142}Nd-Signaturen unterschieden werden können. Das eine Mantelreservoir konservierte die angereicherte ^{142}Nd-Signatur mindestens bis 3.46 Ga, und das andere Mantelreservoir hat keine ^{142}Nd-Signatur enthalten und entspricht in seiner Geochemie einem modernen Mantelreservoir. Des Weiteren wurden die Granitoide, die negative μ^{142}Nd-Anomalien enthalten, durch Aufschmelzung und Einarbeitung von Hadaischer Protokruste gebildet und konservierten ihre negative ^{142}Nd-Signatur bis mindestens 3.22 Ga. Jedoch kann nicht aufgelöst werden, ob die negative ^{142}Nd-Signatur dieser Hadaischen Protokruste letzendlich aus der Differentiation von einer Mantelquelle stammt, die bereits an ^{142}Nd angereichert war oder die im ^{142}Nd ähnlich einer modernen Mantelquelle war. Im Gegensatz dazu, sind die ältesten Gneise, die keine μ^{142}Nd-Anomalien enthalten, bis zu 3.64 Ga alt. Dies deutet darauf hin, dass ein terrestrisches ^{142}Nd-Reservoir mit modernem geochemischem Charakter schon zu früharchaischen Zeiten existiert hat und mit dem angereicherten ^{142}Nd-Mantelreservoir koexistierte.

Um die Entwicklung der Mantelquellen zu untersuchen, die Material zur Krustenverdickung im Paläo- bis Mesoarchaikum beigetragen haben, wurden Metabasalte und Metakomatiite der unteren Onverwacht Gruppe des Barberton Grünsteingürtels sowie ca. 2.9 bis 2.8 Ga alte Metabasalte, die in der Nähe der Kubuta Ranch in Zentralswasiland (Antiker Gneis Komplex) genommen wurden, ausgewählt.

Die Metabasalte der 3.55 bis 3.48 Ga alten Sandspruit und Theespruit Formationen der unteren Onverwacht Gruppe können in drei Gruppen unterteilt werden, basierend auf ihren inkompatiblen Elementcharakteristika: Eine an leichten Seltenen Erden verarmte Gruppe, eine nicht an leichten Seltenen Erden verarmte Gruppe und eine an leichten Seltenen Erden angereicherte Gruppe. Positive $\varepsilon Hf_{(t)}$- und $\varepsilon Nd_{(t)}$-Werte von ca. +3 bis +4 beziehungsweise 0 bis +2, zusammen mit Verarmungen in Th und La_{CN}/Yb_{CN} für die an leichten Seltenen Erden verarmten Metabasalte deuten auf die Abstammung von einer

Mantelquelle hin, die an inkompatiblen Elementen verarmt ist, möglicherweise der ehemalige obere Mantel. Allerdings deuten chondritische $\varepsilon Hf_{(t)}$- und $\varepsilon Nd_{(t)}$-Werte zusammen mit positiven Th-Anomalien und La_{CN}/Yb_{CN}-Verhältnissen der an leichten Seltenen Erden angereicherten Proben auf einen Beitrag des älteren Antiken Gneis Komplexes in der Petrogenese dieser Proben hin.

Spurenelementmuster der Metakomatiite und Metabasalte der 3.48 bis 3.45 Ga alten Komati Formation der unteren Onverwacht Gruppe sind im Allgemeinen flach, relativ zum primitiven Mantel, mit leichten Verarmungen in den schweren Seltenen Erden und Th, sowie generell positiven $\varepsilon Hf_{(t)}$ von $+2.5 \pm 3.5$ (2s.d.) und $\varepsilon Nd_{(t)}$ von $+0.5 \pm 2.2$ (2s.d.) für beide Typen von Metalaven. Die Ähnlichkeit der Spurenelement- und Hf-Nd-Isotopencharakteristika deutet auf eine gemeinsame magmatische Herkunft dieser Basalte und Komatiite hin, die durch hohe Aufschmelzgrade einer an inkompatiblen Elementen verarmten Mantelquelle mit zurückbleibendem Granat in der Mantelquelle entstanden sind. Hierbei werden die Komatiite als Mantelplumerzeugnisse interpretiert, wohingegen die Basalte als Produkte von fraktionierter Kristallisation der komatiitischen parentalen Schmelze interpretiert werden.

Basierend auf dem vorliegenden Datensatz, in Kombination mit vorherigen publizierten Daten, schlage ich ein geodynamisches Entwicklungsmodell für die vulkanischen Gesteine er unteren Onverwacht Gruppe vor, das die Entwicklung von einem kontinentalen (für die Sandspruit und Theespruit Formationen) zu einem ozeanischen (für die Komati Formation) Regime als Konsequenz von kontinentaler Spreizung beinhaltet.

Die 2.9 bis 2.8 Ga alten metavulkanischen Kubuta-Gesteine sind vermutlich genetisch verwandt mit dem ca. 3.0 Ga Usushwana magmatischen Komplex in Westzentralswasiland und dem ca. 2.9 Ga Hlagothi Komplex in der KwaZulu-Natal-Provinz von Südafrika. Die zeitgleichen ca. 3.0 Ga Nsuze und ca. 2.9 Ga Mozaan Gruppen der Pongola Supergruppe von Südzentralswasiland und der nördlichen KwaZulu-Natal-Provinz haben ähnliche elementare Anomalien, wenn auch leicht erhöhte Konzentrationen verglichen mit den metavulkanischen Kubuta-Gesteinen.

Diese Studie zeigt, dass die Nsuze und Mozaan Gruppen von einer komatiitischen parentalen Schmelze abstammen, die von einer schwach verarmten Mantelquelle gespeist wurden. Im Gegensatz dazu stammen die Usushwana-, Hlagothi- und Kubuta-Einheiten von einer verarmteren Mantelquelle, die vergleichbar ist mit dem modernen verarmten oberen Mantel. Vor der Eruption haben alle mafischen Gesteine Assimilations- und

Kristallisationsprozesse erfahren. Hierbei waren die ca. 3.5 Ga alten, krustalen Gesteine des Antiken Gneis Komplexes mögliche Kontaminanten.

Die Kombination von geochemischen Beobachtungen mit Altersdatierungen aus der Literatur führt zu einem verfeinerten petrogenetischen Modell für kontinentalen Flutbasaltvulkanismus in einer mesoarchaischen, magmatischen Großprovinz auf dem östlichen Kaapvaal-Kraton. Dieses verfeinerte Modell schließt die Präsenz von zwei verschiedenen Mantelquellen in die Bildung dieser kontinentalen magmatischen Großprovinz ein. Einerseits einen tiefen Mantelplume, der komatiitische Schmelzen produziert, andererseits den oberen Mantel, der an inkompatiblen Elementen verarmte Schmelzen, wie zum Beispiel die Kubuta-Gesteine, produziert.

Zusammenfassend kann man sagen, dass die untersuchten paläo- bis mesoarchaischen, mafischen Gesteine dieser Studie den Übergang von einem kontinentalen zu einem ozeanischen und wieder zurück zu einem kontinentalen Regime innerhalb einer Zeitperiode von etwa 600 Ma dokumentieren.

Acknowledgements

First of all, I am deeply grateful to my supervisor Elis Hoffmann for the possibility to work with him and for his patient and considerate guidance and support during my dissertation. His door was always open for my questions and for discussion, and I learned a lot about data acquisition, data analysis, and interpretation from him. Especially, I appreciate his open and friendly character that created a warm and confiding atmosphere.

I am very thankful to Harry Becker for welcoming me in his geochemistry workgroup and for his patience and advice. I thank him for being the first referee of my dissertation.

I particularly want to thank Carsten Münker for his guidance in the lab and his constructive feedback that added to an improvement of data interpretation. I am glad that he is the second referee of my dissertation.

I would like to thank Monika Feth for support in the labs at FU Berlin and Almut Katzemich for XRF analysis at the University of Cologne.

Furthermore, special thanks to Maud Boyet for hosting and advising me in the LMV in Clermont-Ferrand. I had a great time there. Also, I am indebted to Peter Sprung for his patience and help with MC-ICP-MS analysis. In addition, I want to thank Philip Gleißner, Chunhui Li, Yogita Kadlag, and Zaicong Wang for their help with ICP-MS measurements.

I wish to thank Alfred Kröner for his guidance in the field in South Africa and Swaziland. He always gave constructive feedback that improved the quality of this dissertation.

I am very thankful to the DFG (Deutsche Forschungsgemeinschaft) for financial support of my project with the grants HO4697/1-1 and HO4697/1-2. I also want to thank the TRR 170 “Late accretion onto terrestrial planets” for financial support during the end of my dissertation.

I would like to express my particular gratitude to my current and former colleagues and friends, amongst some of them are Lea, Franziska, Dennis, Philip, Julian, Kerstin, Gerrit, Lina, and Thomas for their personal and professional support in easy and not so easy times during this dissertation. And also many thanks to Thomas for his feedback on my German abstract. Furthermore, I am grateful to the workgroups of FU Berlin and the Schloss-people of the University of Cologne and the University of Bonn, especially Raúl

Fonseca and Maria Kirchenbaur who introduced me into the geochemistry world and supported me beyond my Master thesis with their advice and friendship.

Finally, I want to express my deepest appreciation to my parents and Moritz who were always there for me.

Table of Contents

Chapter 1

Introduction

1.1 Distribution of Archean crust on Earth

Cratons are stable segments of continental crust and thick lithospheric roots (~250 km; Drummond, 1988; Vinnik et al. 1996; Carlson et al., 2000) that formed in Archean times and remained largely unaffected by geological recycling processes since then. Cratons are preserved on almost all continents on Earth (e.g., Tang et al. 2013; Anhaeusser 2014; Fig.1.1), and provide a unique record of Archean geology. However, the small quantity of preserved Archean crust is one of the main reasons for our limited knowledge about the composition and evolution of the early Earth.

The oldest rocks on Earth are exposed in the Acasta Gneiss Complex in the Slave Craton of northwestern Canada (Fig. 1.1). These gneisses range in age from 4.03 to 3.96 Ga (Iizuka et al. 2007) and are composed of strongly deformed tonalite-trondhjemite-granodiorite (TTG) suites (Bowring et al. 1989). However, the oldest minerals found on Earth are detrital zircons from the ca. 3.0 Ga Jack Hills and Mt. Narryer quartzites of the Yilgarn Craton in Western Australia that date even further back into the Hadean. These zircons range in age from 4.4 to 3.5 Ga (Froude et al., 1983; Amelin et al., 1999; Wilde et al., 2001; Harrison et al., 2005), and it is argued in the literature whether these minerals have crystallized from an evolved granitic melt (Mojzsis et al., 2001) or from an intermediate to mafic igneous rock (Kemp et al. 2010). More xenocystic zircons of Hadean age (i.e. ≥4.0 Ga) were found in late Archean granitic gneisses of the Narryer and Murchison terranes of the Yilgarn Craton (Nelson et al. 2000), in an Ordovician felsic volcanic rock of the North Qinling Orogenic Belt, China (Diwu et al. 2013), and in an Archean mica-schist of the São Francisco Craton in northeast Brazil (Paquette et al. 2015).

Other prominent examples of exposed early Archean continental crust are the 3.95 to 3.8 Ga high-grade Napier Complex of Antarctica (Black et al., 1986; Harley and Kelly, 2007), the 3.9 to 2.8 Ga Itsaq Gneiss Complex of the North Atlantic Craton in southwestern Greenland (Nutman et al.,1996, 2002; Friend and Nutman, 2005), the 3.8 to 3.7 Ga Porpoise Cove supracrustal sequence of the Superior Craton in northeastern Canada (O'Neil et al., 2007), the ca. 3.8 Ga Anshan area of the North China Craton (Song

et al., 1996; Wan et al., 2015), the 3.52 to 3.17 Ga East Pilbara Terrane of Western Australia (Van Kranendonk et al., 2002, 2007a,b), and the 3.66 to 3.2 Ga Kaapvaal Craton of southern Africa (Compston and Kröner 1988; Poujol et al., 2003, 2007; Kröner, 2007; Hoffmann and Kröner in press; Fig. 1.1).

In order to understand how the continental crust formed, that is now exposed in Archean cratons, and in which prevalent tectonic setting its formation occurred it is crucial to characterize the mantle sources from which the early magmas were derived. Furthermore, the lack of pre-Archean crust (pre-3.85 Ga) in most Archean terrains raises the question whether or not the existence of Hadean mafic protocrust was abundant and how it may have contributed to continental crust formation and evolution.

Figure 1.1: Current worldwide exposure of Archean cratons. Modified after Tang et al. (2013) and Anhaeusser (2014).

1.2 Evidence for the existence of Hadean protocrust

Direct evidence for the existence of Hadean protocrust is mainly based on zircon mineral dating. As summarized in the previous chapter, the oldest detrital zircons were found in the ca. 3.0 Ga Jack Hill and Mt. Narryer quartzites of the Yilgarn Craton in Western Australia, and yielded ages up to 4.4 Ga. In addition, the oldest preserved magmatic zircons occur in TTGs of the Acasta Gneiss Complex of the Slave Craton in northwestern Canada, and yielded ages up to 4.03 Ga.

In all other Archean terrains, direct evidence of Hadean protocrustal material is lacking. However, differentiation of Earth´s mantle can be traced by the coupled application of the short-lived ^{146}Sm-^{142}Nd decay system ($t_{1/2}$ = 103 ± 5 Ma, Meissner et al., 1987) in combination with the long-lived ^{147}Sm-^{143}Nd and ^{167}Lu-^{176}Hf isotope systems. All four elements are refractory and lithophile and therefore should not be affected by planetary accretion and core segregation. However, during partial melting of the mantle, Lu-Hf and Sm-Nd will fractionate due to the more incompatible behavior of Hf and Nd compared to Lu and Sm. As a result, crustal reservoirs will have lower Sm/Nd and Lu/Hf evolving with time to negative ε^{176}Hf and ε^{143}Nd values compared to a chondritic bulk earth composition [$\varepsilon^{143}Nd = (^{143}Nd/^{144}Nd_{sample} - {}^{143}Nd/^{144}Nd_{CHUR})/(^{143}Nd/^{144}Nd_{CHUR}) \times 10^4$]. In contrast, the mantle will evolve to positive ε^{176}Hf and ε^{143}Nd values. Therefore, the long-lived ^{176}Lu-^{176}Hf and ^{147}Sm-^{143}Nd isotope systems represent powerful tools for tracing mantle differentiation events in the Archean (e.g., DePaolo and Wasserburg 1976, 1979; Jacobsen and Wasserburg 1979; Patchett et al. 1981; White and Patchett 1984). In contrast, due to its short half-life, the ^{146}Sm-^{142}Nd decay system was only active during the first ca. 500 million years of Earth's history. Consequently, differentiation of crustal material from a mantle or crustal source before extinction of ^{146}Sm would have lead to heterogeneities in the ^{142}Nd/^{144}Nd isotope composition of early differentiated terrestrial reservoirs (e.g., Harper and Jacobsen, 1992; Boyet et al., 2005; Caro et al., 2006; Rizo et al., 2012). During early crust-mantle differentiation the continental crust developed towards low Sm/Nd ratios, expressed as negative μ^{142}Nd [$\mu^{142}Nd = (^{142}Nd/^{144}Nd_{sample}/^{142}Nd/^{144}Nd_{standard} - 1) \times 10^6$ in ppm], and the depleted mantle developed with a high Sm/Nd ratio, resulting in positive μ^{142}Nd values, compared to a modern terrestrial standard. Consequently, the short-lived ^{146}Sm-^{142}Nd decay system is an important tool to shed light on the possible involvement of Hadean crustal and/or mantle sources in the formation of Archean cratonic crust.

Applying the coupled ^{146,147}Sm-^{142,143}Nd isotope systems, the existence of amphibolites of Hadean age in the Nuvvuagittuq greenstone belt of the Superior Craton in northeastern Canada has been proposed by O´Neil et al. (2008). According to these authors, the amphibolites of the Ujaraaluk unit plot on a regression line in a ^{142}Nd/^{144}Nd vs. ^{147}Sm/^{144}Nd isotope diagram that corresponds to an age of 4.28 Ga, suggesting that these mantle-derived rocks could be relicts of Hadean protocrust. However, this hypothesis is strongly debated in the literature, because the regression line obtained from a ^{143}Nd/^{144}Nd vs. ^{147}Sm/^{144}Nd isotope diagram for these amphibolites and zircon dating of interlayered felsic units give only an age of ca. 3.8 Ga (e.g., O`Neil et al. 2008; Caro 2011; Caro et al. 2017).

By means of ^{142}Nd isotopes, crustal and mantle material that differentiated in the Hadean can be traced in Eo- to Mesoarchean cratonic crust. Its involvement in the formation of early continental crust could be constrained in several sequences of the Superior (O'Neil et al., 2008, 2012; Debaille et al. 2013; Roth et al., 2013; Caro et al., 2017; O'Neil and Carlson 2017) and Slave Cratons in Canada (Roth et al., 2014), and of the North Atlantic Craton in Greenland (Boyet and Carlson, 2006; Caro et al., 2006; Bennett et al., 2007; Rizo et al., 2011, 2012, 2013; O'Neil et al., 2016). Additionally, the involvement of Hadean protocrustal material on the Kaapvaal Craton is preserved in komatiites of the Schapenburg Greenstone Remnant (Puchtel et al. 2016b). In contrast, the Barberton komatiites do not record the involvement of Hadean material in their formation (Caro et al. 2006; Puchtel et al. 2013), indicating that at least more than one mantle source must have existed that gave rise to the rocks from the Kaapvaal Craton.

Another isotope system that has proven to be useful in tracing the involvement of Hadean mantle material in Archean rocks is the short-lived ^{182}Hf-^{182}W chronometer ($t_{1/2}$ = 8.9 Ma; Vockenhuber et al. 2004). Due to its short half-life, variations in the ^{182}W/^{184}W isotope composition in terrestrial rocks can only be produced during differentiation events in the first ca. 50 Ma years of solar system history. The μ^{182}W isotope composition [$\mu^{182}W = (^{182}W/^{184}W_{sample}/^{182}W/^{184}W_{standard} - 1) \times 10^6$ in ppm] of the Earth´s mantle can be affected in three ways leading to enrichments and/or depletions in μ^{182}W relative to the modern terrestrial reference, i.e. by (1) late accretion of meteorites after core formation, (2) metal-silicate fractionation due to the siderophile behavior of W compared Hf which is lithophile (Goldschmidt 1930), and (3) during silicate-silicate fractionation owing to the more incompatible behavior of W compared to Hf.

Positive deviations in $\mu^{182}W$ relative to the modern terrestrial reference are found in Eoarchean to Paleoproterozoic sequences of the Slave (Willbold et al. 2015) and Superior Cratons (Touboul et al. 2014) of Canada, the North Atlantic Craton of Canada (Liu et al. 2016) and Greenland (Willbold et al. 2011; Dale et al. 2016; Rizo et al. 2016), and the Baltic (Touboul et al. 2012) and Fennoscanidan (Puchtel et al. 2016a) Shields indicating the preservation of rocks that underwent a differentiation event in the Hadean. Furthermore, komatiites of the Schapenburg Greenstone Remnant of the Kaapvaal Craton preserved a negative $\mu^{182}W$ signature that likely formed by magma ocean differentiation in the Hadean (Puchtel et al. 2016b). Again, the Barberton komatiites do not record the involvement of Hadean material in their formation (Touboul et al. 2012).

Collectively, there is abundant evidence for the former existence of Hadean protocrust and Hadean mantle material within most Archean terrains. Hence, their contribution to Archean cratonic crust seems to have been a widespread phenomenon.

1.3 Structure and formation of the early continental crust

In the Archean, the Earth´s mantle was about 150 to 200 °C hotter than today (Herzberg et al. 2010), and hence the early Earth´s oceanic crust must have been was thicker (25 to 45 km), more magnesian, and more buoyant compared to toady's oceanic crust (Sleep and Windley 1982; Bickle 1986). Furthermore, the early Earth´s continental crust was characterized by granitoid-greenstone complexes that contain several unique features in comparison to recent continental crust (e.g., Hamilton 2003). For example, the strongly deformed and metamorphosed early Archean granitoid crust is dominated by sodic tonalite-trondhjemite-granodiorite (TTG) compositions, whereas post-Archean granitoid rocks are more potassic in composition (Moyen and Martin 2012). The greenstones usually consist of less deformed tholeiitic basalts, komatiitic basalts, and komatiites (Viljoen and Viljoen, 1969b). The latter are unique magmas with MgO contents above 18 wt.% that are interpreted to be derived from a hotter Archean mantle (Herzberg, 1992; Nisbett et al., 1993; Arndt et al., 1998), with one exception in the Tertiary on Gorgona Island (Echeverría 1980). These thick sequences of mafic to ultramafic magma flows are typically interlayered with thin units of felsic volcanic rocks and metasediments such as Banded Iron Formations (BIFs), chert, greywacke, shale, and quartzite (e.g., Kamo and Davis, 1994; Kröner et al., 2013; van Kranendonk et al., 2014).

However, the tectonic setting in which these granitoid-greenstone complexes formed remains a matter of debate.

Amongst the most studied sequences of Archean age is the 3.55 to 3.2 Ga Barberton Granite-Greenstone Terrain (Kamo and Davis, 1994; Kröner et al., 1996) of the eastern Kaapvaal Craton. However, the original field and genetic relationships between the granitoids and greenstones were often obliterated due to severe deformation, migmatization and multiple metamorphic events. Thus, the tectonic setting in which this supracrustal succession formed is highly debated. Opposing models for Archean continental crustal growth in the Barberton Granite-Greenstone Terrain include on the one hand subduction-accretion scenarios (Fig. 1.2a; De Wit et al. 1992, 2011, 2018; de Ronde and Kamo 2000; Moyen et al. 2006, 2007; Schoene et al. 2008; Kisters et al., 2010; Schoene and Bowring 2010; Furnes et al. 2012; Cutts et al. 2013), and on the other hand crustal growth as a result of plume activity (Fig. 1.2b; Anhaeusser 1984; Chavagnac 2004; Van Kranendonk et al. 2011b).

In the subduction-accretion models, the existence of thick (15-21 km), predominantly basaltic sequences have been interpreted as either accreted oceanic plateaux (Condie 1997; Martin et al., 2014) or as obducted slices of oceanic crust (Fig. 1.2a; de Wit et al. 1992, 2011; Furnes et al. 2012). Additionally, the calc-alkaline felsic volcanic rocks of the succession were interpreted as being subduction-related volcanic arc magmas (de Wit et al. 1992; de Ronde and Kamo 2000; Kohler and Anhaeusser 2002; Kisters et al. 2010). In such subduction-accretion models, TTGs have been interpreted as being analogues of modern adakites that form today by partial melting of subducted basaltic crust (Martin et al. 2005). However, several researchers (Smithies et al. 2005a, 2007; Bédard 2006, 2018; Van Kranendonk et al. 2010; Shirey and Richardson 2011; Van Kranendonk 2011a; Dhuime et al. 2012; Bédard et al. 2013) are convinced that modern-style plate tectonics, which today is characterized by steep subduction of old, cold oceanic lithosphere, did not commence earlier than ca. 3.2 to 3.0 Ga ago. Therefore, the operation of proto-plate tectonics involving shallow subduction of thick and buoyant oceanic lithosphere has been suggested by some authors as the predominant crustal growth process on the early Earth (Anhaeusser 1973; Bickle 1978; Davies 1995; Foley et al. 2003; Van Kranendonk 2010). Accretion of such small-scale proto-plate tectonics may then have formed the thick root of ancient lithospheric mantle beneath the Kaapvaal crust (e.g., Carlson et al. 2000; Byerly et al. in press).

Opposed to the formation of early continental crust by subduction-accretion processes on the Kaapvaal Craton, is the formation of an oceanic or continental volcanic plateau as a result of plume activity (Fig. 1.2b; Anhaeusser 1984; Van Kranendonk et al. 2009; Smithies et al. 2005b, 2009; Griffin and O'Reilly 2007a, b; Van Kranendonk 2011b). Arguments in favor of formation on a volcanic plateau are the upward younging of volcanic rocks, the geochemical variability up-stratigraphy, i.e. interlayering of mafic and felsic units, and the lack of large-scale tectonic duplication, i.e. tectonic stacking of oceanic lithosphere, in the 15 to 21 km-thick greenstone succession (Viljoen and Viljoen 1969b; Lowe et al., 1985; Byerly et al. 1996; Lowe and Byerly 2007). Furthermore, the komatiites within the succession were shown to be derived from large-scale, deep mantle melting within a mantle plume (Storey et al. 1991; Herzberg et al. 2007), and both the komatiites and basaltic rocks are similar in composition to ocean plateau basalts (Storey et al. 1991; Condie 2005; Smithies et al. 2005b; Herzberg et al. 2007; Van Kranendonk et al. 2009). Additionally, the felsic volcanic rocks are thought to have formed either by assimilation-fractional crystallization in large tholeiitic magma chambers or represent partial melts of older felsic continental crust (Van Kranendonk et al. 2009; Kröner et al. 2013, 2016). In such an intraplate volcanic plateau setting, TTG magmas are thought to have formed by melting of deep greenstone-belt roots (Fig. 1.2b; e.g., Smithies, 2000; Bédard 2006; Van Kranendonk et al. 2015; Johnson et al. 2016). Furthermore, crustal thickening is proposed to have been accompanied by the development of dome-and-keel structures due to partial convective overturn of buoyant granitoid melts and sinking of dense greenstone wedges (Anhaeusser 1984; Van Kranendonk et al. 2009, 2015; Sizova et al., in press), similar to what has been proposed for coeval units of the Pilbara Craton of Western Australia (e.g., Hickman 1981; Smithies et al. 2005b; Van Kranendonk et al. 2015).

An intermediate tectonic style between small-scale plate tectonics on the one hand and partial convective overturn on an oceanic plateau on the other hand is likely to have influenced the tectonic regime of the Barberton Granite-Greenstone Terrain (Byerly et al. in press). However, there is no evidence for major uplift or development of sedimentary basins before ca. 3230 Ma in the BGB which leads to the conclusion that until this time the BGB developed through magmatic accretion, probably on an oceanic plateau, rather than through subuction (Byerly et al. in press). After ca. 3230 Ma amalgamation, of small protocontinental nuclei occurred and lead to the formation and stabilization of the Kaapvaal Craton until about 3.1 Ga (Byerly et al. in press).

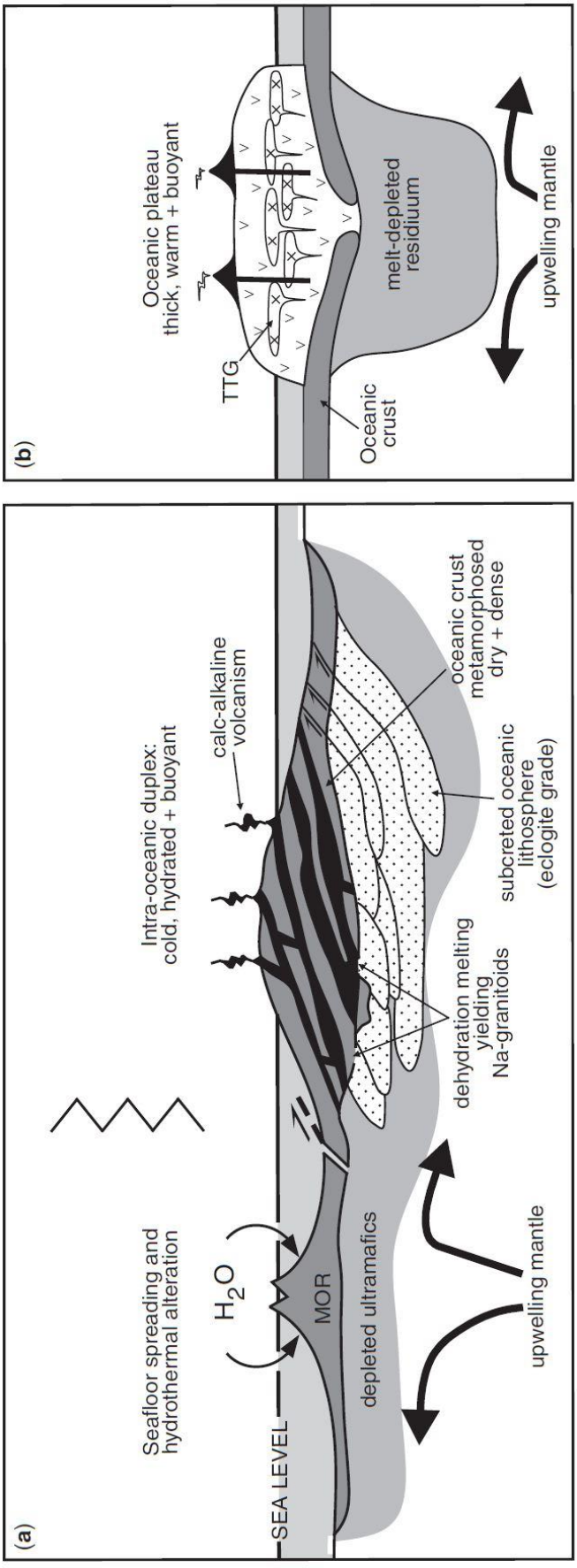

Figure 1.2: Opposing models for the formation of Paleoarchean crust in the eastern Kaapvaal Craton. A) Intra-oceanic subduction-accretion model with imbrication of oceanic lithosphere (black) leading to the formation of intra-oceanic crust-stacks. B) Volcanic plateau model with magmatic accretion and internal differentiation. (Van Kranendonk et al. 2015).

1.4 Development of the eastern Kaapvaal Craton throughout the Archean

The oldest rocks of the eastern Kaapvaal Craton are found in the ca. 3.66 to 3.2 Ga Ancient Gneiss Complex (AGC) of Swaziland (Fig. 1.3; Hoffmann and Kröner in press, and references herein), and mainly consist of foliated and partly migmatized gneisses of the TTG suite (Hunter 1974; Hunter et al., 1984). These granitoid gneisses overlap in age with the mafic to ultramafic metavolcanic rocks of the 3.55 to 3.2 Ga Barberton Greenstone Belt (BGB; Fig. 1.3) that forms the major part of the Barberton Granite-Greenstone Terrain (e.g., Kamo and Davis, 1994; Kröner et al., 1996) which was discussed above.

Two main crust-forming events with accompanying regional amphibolite-facies metamorphism affected the AGC and BGB (Kamo and Davies 1994). One early phase in the southern BGB terrain occurred at ca. 3436 Ma with peak P-T conditions of ~4.5 kbar and 550 °C (Cutts et al. 2013), and another more widespread phase occurred at ca. 3.23-3.22 Ga, and peak metamorphic conditions of 8-11 kbar and 650-700 °C were attained (Kisters et al. 2003). The latter tectono-metamorphic event at about 3.2 Ga extended from northern Swaziland into the central KwaZulu-Natal province and led to ductile deformation and migmatization of lower crustal TTGs (Hunter 1974; Kröner 2007; Reinhard et al. 2015), as well as tight folding in the upper crustal greenstones (e.g., Dziggel et al. 2005; Nédélec et al. 2012). Furthermore, during this 3.2 Ga event, granitoid rocks were emplaced and many of the original granitoid-greenstone relationships of the older sequences were obliterated. Tectonic models for the ca. 3.2 Ga crust-forming event vary from subduction-accretion scenarios (e.g., Moyen et al. 2006; Kisters et al., 2010; Schoene and Bowring, 2010) to models that include partial convective overturn of an over-thickened oceanic plateau (Van Kranendonk 2011b). The ca. 3.2 Ga event was accompanied by the deposition of the 3.26 to 3.22 Ga volcanoclastic and metasedimentary Fig Tree Group and the 3.22 to 3.20 Ga terrigenious clastic Moodies Group (Heubeck and Lowe 1994; Kamo and Davies 1994; Byerly et al. 1996).

During a later phase, at ca. 3.1 Ga (Kamo and Davis, 1994), a regionally extensive magmatic event may have been triggered by partial delamination of the lithospheric mantle (Moser et al. 2000) and produced the Mpuluzi-Piggs Peak batholiths. Based on Sr-Nd isotope evidence, these potassic granitoids were interpreted to have been derived from partial melting of an older TTG basement (Robb et al. 2006; Schoene et al. 2009), and mixing with juvenile mantle-derived melts (Murphy 2015). The heat provided by these

mantle-derived melts is proposed to have led to “draining” of fusible material from the lower crust, increasing its rigidity and limiting further tectonism (Murphy 2015).

The period of ca. 3.1 Ga plutonic activity in the eastern Kaapvaal Craton was followed by deposition of the volcano-sedimentary ca. 2.9 Ga Pongola Supergroup (Tankard et al. 1982; Hunter and Wilson 1988; Beukes and Cairncross, 1991), extending from south-central Swaziland into northern and central KwaZulu-Natal of southeastern South Africa. The Pongola Supergroup belongs to one of the oldest cratonic cover sequences in the world (Anhaeusser 1973), and was probably deposited in a volcanic rift setting, the Pongola basin (Bickle and Eriksson 1982), between contrasting crustal blocks of the AGC with generally older granitoids ranging in age from ca. 3.6 to 3.2 Ga in the northeast (Mukasa et al. 2013) and ca. 3.3 to 3.2 Ga in the southwest (Wilson and Zeh 2018). Contemporaneous to the Pongola Supergroup, the ca. 2.9 to 2.8 Ga Usushwana Igneous Complex (Hegner et al. 1984; Gumsley et al. 2015) was deposited that was interpreted to represent a feeder dike system to the Pongola Supergroup volcanic rocks (Gumsley et al. 2015).

In the Neoarchean, extensional deformation caused local metamorphism of the Pongola Supergroup (Hofmann et al. 2015) and terminated the Archean crust formation history in the eastern Kaapvaal Craton. Crustal extension during this period is also indicated by ca. 2.70 to 2.66 Ga dolerite dike swarms that crosscut the eastern Kaapvaal Craton (Klausen et al. 2010; Olsson et al. 2010, 2011; Gumsley et al. 2016).

The ca. 3.66 to 3.2 Ga geological history of the Barberton Granite-Greenstone Terrain shares many similarities with the geological history of the Eastern Pilbara Terrain of the Pilbara Craton of Western Australia (Van Kranendonk et al., 2015). For instance, both terrains contain 12 to 20 km thick, upward-younging greenstone successions of comparable age that comprise several cycles of bimodal volcanism (Viljoen & Viljoen 1969a; Lowe and Byerly 2007; Van Kranendonk et al. 2007a). Furthermore, both the Kaapvaal and Pilbara Cratons underwent widespread intrusion of granitoids at around ca. 3.3 to 3.2 Ga causing deformation and metamorphism with the development of dome-and-keel structures (Collins et al. 1998; Hickman and Van Kranendonk 2004; Van Kranendonk et al. 2004; Van Kranendonk et al. 2009; Van Kranendonk 2011b) and this metamorphic event was, in both cratons, accompanied by the deposition of coarse-grained clastic sediments (Anhaeusser 1976; Van Kranendonk et al. 2010; Heubeck et al. 2013). After ca. 3.2 Ga both cratons were affected by rifting and terrane accretion, possibly as a

result of modern-style subduction (Shirey et al. 2002; Eglington and Armstrong 2004; Smithies et al. 2005a; Van Kranendonk et al. 2007b; Shirey and Richardson 2011).

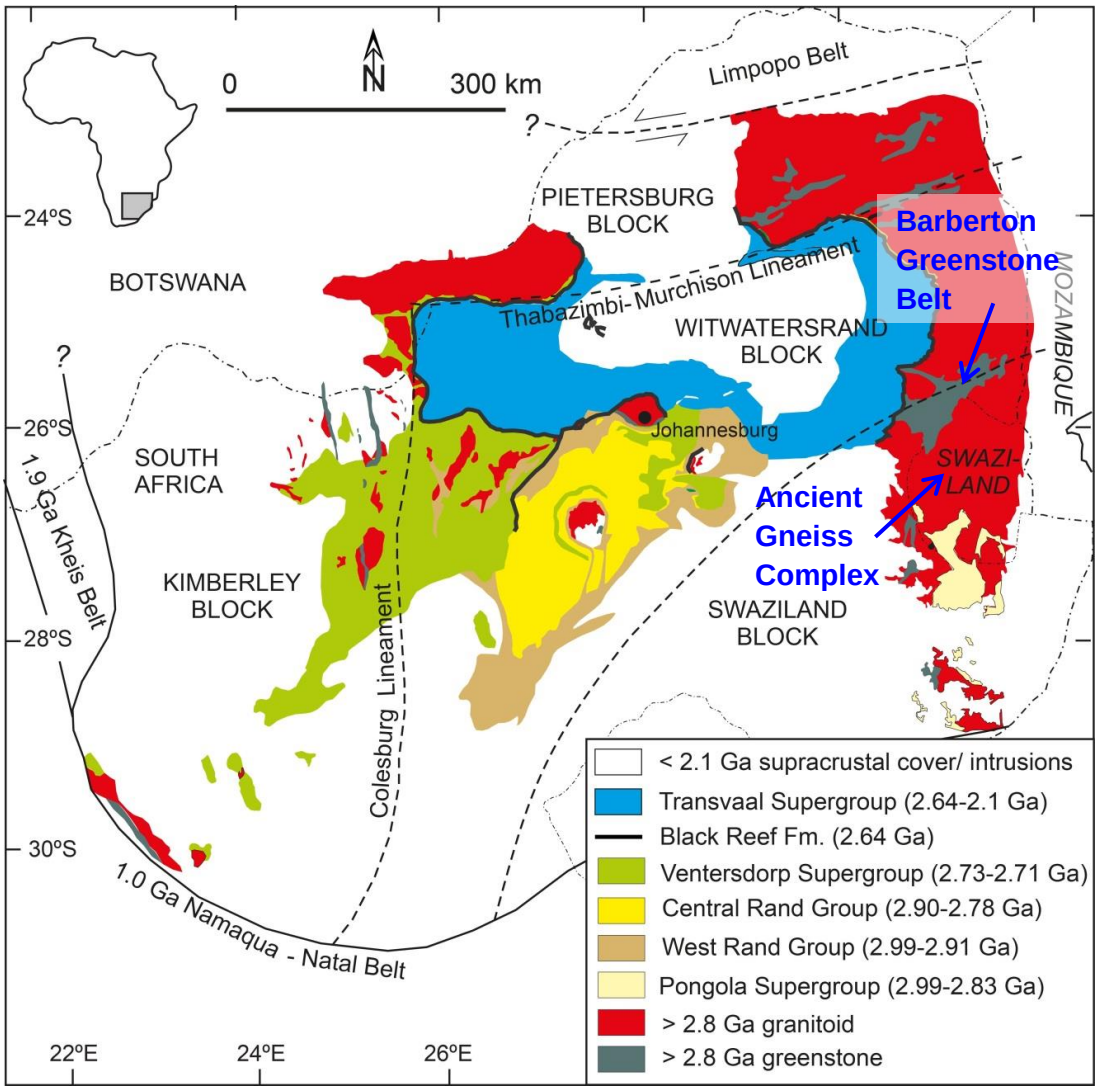

Figure 1.3: Overview of the main geological units of the Kaapvaal Craton, South Africa. Modified after Frimmel et al. (2009).

1.5 Scope of this thesis

The first objective of this thesis is to elucidate the differentiation and reworking history of rocks in the oldest part of the Kaapvaal Craton. In a next step, this thesis aims to constrain the evolution of the mantle sources of rocks from the Kaapvaal Craton throughout the Paleo- to Mesoarchean by constraining the geochemical characteristics of mantle-derived rocks that vary in age, composition, and petrography. Additionally, the interaction of parental melts with felsic crust of the AGC is evaluated.

Combining data derived from the short-lived ^{146}Sm-^{142}Nd decay system with existing geological, petrological and geochemical information on crustal and mantle-derived samples of the eastern Kaapvaal Craton leads to a deeper understanding of whether and when Hadean crustal components were incorporated into the sources of Archean crustal rocks. This enables us to understand the geodynamic processes such as mantle differentiation and crustal reworking operating in the early Archean. As explained above, crust-mantle differentiation in the Hadean resulted in positive (mantle-derived) and negative (crust-derived) μ^{142}Nd anomalies relative to the modern terrestrial μ^{142}Nd value that is, per definition, zero. Hence, the ^{146}Sm-^{142}Nd isotope system is a powerful tool to constrain the involvement of Hadean material in crust-formation processes. In the eastern Kaapvaal craton, so far only komatiites of the Komati Formation and the Schapenburg Greenstone Remnant were analyzed for their μ^{142}Nd. The Komati komatiites did not show any deviation from the terrestrial value (Caro et al. 2006; Puchtel et al. 2013), whereas the Schapenburg komatiites exhibit negative μ^{142}Nd anomalies (Puchtel et al. 2016b). However, no basaltic or other crustal rocks of the BGB or AGC have so far been analyzed for their ^{142}Nd isotope composition. Hence, constraining a possible contribution of Hadean crustal or mantle material to the basaltic and crustal rocks of the BGB and AGC is crucial for our understanding of crust-formation processes in the eastern Kaapvaal Craton. This research is reported in Chapter 2 and was published in the journal *Earth and Planetary Science Letters*.

Chapter 3 of this thesis deals with the characterization of the geochemical composition of the mantle sources that gave rise to the mafic and ultramafic rocks of the Paleoarchean lower Onverwacht Group of the Barberton Greenstone Belt (BGB) to constrain how the formation of basalts and komatiites may be linked. By employing Lu-Hf and Sm-Nd isotope analyses in conjunction with major and trace element compositional data on a large set of samples, I evaluate whether or not the parental mantle-derived melts of komatiites and tholeiites interacted with older crustal material during ascent. This information will be used to constrain the geodynamic setting in which the volcanic rocks of the lower Onverwacht Group formed.

In Chapter 4, I aim to characterize the tholeiitic basalts of the ca. 3.0 to 2.9 Ga volcanic rocks of the Kubuta area in the AGC by means of ^{176}Lu-^{176}Hf and ^{147}Sm-^{143}Nd isotope and trace element composition to constrain the relation of these rocks in terms of mantle source composition and contamination history of the parental magmas to other ca. 3.0 to 2.8 Ga volcanic sequences in this region. Furthermore, the reliability of the

petrogenetic model of Gumsley et al. (2015) for the Mesoarchean volcanic rocks of Swaziland and South Africa is tested. From a synthesis of previously published geochemical and isotopic data, I propose a refined petrogenetic model for the evolution of the Mesoarchean mantle-derived rocks of the AGC that considers both, age and geochemical data.

1.6 Main chapters of the thesis

This cumulative doctoral thesis summarizes my research in form of three manuscripts prepared for publication in international peer-reviewed scientific journals. One of these manuscripts has been published, and two are in final preparation stages for submission. The present work is based on a research project of Dr. J. Elis Hoffmann funded by the Deutsche Forschungsgemeinschaft (DFG) through grants HO4697/1-1 and HO4697/1-2. Below, I briefly summarize the individual chapters of this thesis and indicate the contribution from co-authors to the respective manuscripts.

Chapter 2 reports the first high-precision ^{142}Nd data for granitoids and amphibolites of the Ancient Gneiss Complex (AGC) and the Barberton Greenstone Belt (BGB), ranging in age from 3.66 to 3.22 Ga, in order to trace Hadean crust-mantle differentiation processes. This study was published in *Earth and Planetary Science Letters* (Schneider, K.P., Hoffmann, J.E., Boyet, M., Münker, C., Kröner, A., 2018), entitled "Coexistence of enriched and modern-like ^{142}Nd signatures in Archean igneous rocks of the eastern Kaapvaal Craton, southern Africa" (https://doi.org/10.1016/j.epsl.2018.01.022).

Negative μ^{142}Nd anomalies in mantle-derived rocks indicate the involvement of an early-enriched mantle reservoir in the formation of the AGC that differentiated in the Hadean during the lifetime of ^{146}Sm. Our results show that mantle-derived rocks tapped the early-enriched reservoir with negative μ^{142}Nd at least until 3.46 Ga. In contrast, the granitoids preserved a negative μ^{142}Nd signature that formed by incorporation of older AGC crust at least until 3.22 Ga. Additionally, the oldest gneisses of the AGC that are up to 3.66 Ga in age resemble the modern terrestrial μ^{142}Nd, indicating that a modern terrestrial ^{142}Nd reservoir was already present by early Archean times.

JEH, AK, and CM provided sample powders for analysis. JEH, AK, and I have sampled amphibolites in the field. Major elements were analyzed by Almut Katzemich in Cologne. Trace elements were analyzed by Dieter Garbe-Schönberg in Kiel and by me in

Berlin. Hf-^{143}Nd analyses were carried out by JEH and me. MB advised me on how to perform the ^{142}Nd chemistry that I conducted in her lab, and we jointly carried out MC-TIMS measurements in Clermond-Ferrand. The data were discussed amongst all co-authors, especially JEH, CM, and me. I interpreted the data and wrote the manuscript with input from all co-authors. The manuscript was internally reviewed by all co-authors and externally by two journal reviewers, namely Tsuyoshi Iizuka and an anonymous reviewer.

Chapter 3 deals with the petrogenetic history of metakomatiites and metabasalts of the lower Onverwacht Group of the BGB. To constrain the petrogenetic evolution of these rocks, major and trace element as well as Hf-Nd isotope compositions were determined. A manuscript on this research, entitled "Petrogenetic evolution of basalts and their relation to komatiites of the lower Onverwacht Group, Barberton Greenstone Belt (South Africa)" is in review with *Chemical Geology*. Co-authors of this manuscript are J. Elis Hoffmann, Carsten Münker, Magda Patyniak, Peter Sprung, Desiree Roerdink, Dieter Garbe-Schönberg, and Alfred Kröner.

Based on the current data set, and in combination with previously published data, a geodynamic evolution model for the lower Onverwacht Group of the BGB is proposed. The data are consistent with a continent-type setting for the older ca. 3.55 to 3.48 Ga Sandspruit and Theespruit Formations, involving partial melting of ambient mantle and subsequent assimilation-fractional crystallization. In contrast, the younger ca. 3.48 to 3.45 Ga Komati Formation formed in an oceanic setting involving magma generation in a deep mantle plume. The transition from a continent-type setting during deposition of the Sandspruit and Theespruit Formations to an oceanic-type setting during deposition of the Komati Formation likely occurred as a consequence of continental rifting.

JEH, AK, and I have sampled the amphibolites of the Sandspruit and Theespruit Formations in the field. DR provided some additional samples of the Theespruit Formation, and CM provided samples of the Komati Formation. MP provided data for the Komati Formation samples from her Bachelor thesis. Major element analysis by XRF was carried out by Almut Katzemich in Cologne. Trace element compositions for samples with the abbreviations LON, BA, and ZA were measured by quadrupole ICP-MS by DGS in Kiel. I carried out trace element analyses of the samples with the abbreviation KS-BA in Berlin, using an Element XR ICP-MS. PS and I carried out Hf-Nd isotope analyses by MC-ICP-MS in Cologne. The data were discussed amongst all co-authors, and

particularly by JEH, CM and me. I interpreted the data and wrote the manuscript with input from all co-authors. The manuscript was internally reviewed by JEH and CM.

Chapter 4 deals with the petrogenetic history of metabasalts sampled close to the Kubuta Ranch in south-central Swaziland. For this purpose, major and trace element as well as Hf-Nd isotope compositions were determined. A manuscript of this study, entitled "A refined petrogenetic model for a Mesoarchean large igneous province on the eastern Kaapvaal Craton (southern Africa)" is in preparation for publication. Co-authors of this manuscript are J. Elis Hoffmann, Alfred Kröner, Alexander Balduin, Peter Sprung, Anja M. Schleicher, and Carsten Münker.

Combining our geochemical results with age determinations of the literature leads to the proposition of a refined petrogenetic model for continental flood volcanism in a Mesoarchean large igneous province on the eastern Kaapvaal Craton. Our results show that the Nsuze and Mozaan Group were derived from a komatiitic parental magma that was sourced from a weakly depleted mantle reservoir, likely represented by a mantle plume. In contrast, the Usushwana, Hlagothi, and Kubuta units were sourced from a more incompatible element-depleted mantle source, likely represented by ambient upper mantle. Prior to eruption, the magmas from all volcanic units underwent assimilation-fractional crystallization, possibly involving felsic crustal rocks of the ca. 3.5 Ga crust-forming event in the AGC.

JEH, AK, and I sampled the metabasalts in the field. AB helped with crushing and milling of the sample material. Major element analysis by XRF was carried out by AMS in Potsdam. I carried out trace element analyses by XR ICP-MS at FU Berlin. PS and I carried out Hf-Nd isotope analyses by MC-ICP-MS in Cologne. The data were discussed amongst JEH, CM and me. I interpreted the data and wrote the manuscript with input from JEH and CM. The manuscript was internally reviewed by JEH and CM.

Chapter 2

Coexistence of enriched and modern-like ^{142}Nd signatures in Archean igneous rocks of the eastern Kaapvaal Craton, southern Africa

2.1 Abstract

The short-lived ^{146}Sm-^{142}Nd isotope system is an important tool for tracing Hadean crust-mantle differentiation processes and constraining their imprint on much younger rocks from Archean cratons. We report the first comprehensive set of high-precision ^{142}Nd analyses for granitoids and amphibolites of the Ancient Gneiss Complex (AGC; Swaziland) and the oldest metavolcanic units of the Barberton Greenstone Belt (BGB; South Africa). The investigated samples span an age range from 3.66 Ga to 3.22 Ga and are representative of major geological units of the AGC and the lower Onverwacht Group of the BGB. Measured samples yielded μ^{142}Nd values in the range from -8 ppm to +3 ppm relative to the JNdi-1 terrestrial standard, with typical errors smaller than 4.4 ppm. The distribution of the μ^{142}Nd values for these 17 measured samples is bimodal with ten samples showing a tendency towards slightly negative μ^{142}Nd anomalies, whereas seven samples have ^{142}Nd similar to the terrestrial reference. The only confidently resolvable μ^{142}Nd anomalies were found in a 3.44 Ga Ngwane Gneiss sample and in amphibolites of the ca. 3.45 Ga Dwalile Greenstone Remnant, revealing μ^{142}Nd values ranging from -7.9 ± 4.4 to -6.1 ± 4.3 ppm. The μ^{142}Nd deficits do not correlate with age, lithological unit, or sample locality. Instead, our results reveal that two distinct mantle domains were involved in the formation of the AGC crust. The two reservoirs can be distinguished by their μ^{142}Nd signatures. Mantle-derived rocks tapped the incompatible element enriched reservoir with negative μ^{142}Nd at least until 3.46 Ga, whereas the granitoids preserved a negative μ^{142}Nd signature that formed by incorporation of older AGC crust at least until 3.22 Ga. The oldest gneisses with no μ^{142}Nd anomaly are up to 3.64 Ga in age, indicating that a modern terrestrial ^{142}Nd reservoir was already present by early Archean times.

This chapter is published in

Earth and Planetary Science Letters Vol. 487, Pages 54-66

Schneider, K.P., Hoffmann, J.E., Boyet, M., Münker, C., Kröner, A. (2018);
https://doi.org/10.1016/j.epsl.2018.01.022

[1]Institut für Geologische Wissenschaften, Freie Universität Berlin, Germany
[2]Laboratoire Magmas et Volcans, Université Clermont Auvergne, France
[3]Institut für Geologie und Mineralogie, Universität zu Köln, Germany
[4]Beijing SHRIMP Center, Institute of Geology, Chinese Academy of Geological Sciences, Beijing, China, and Institut für Geowissenschaften, Universität Mainz, Germany

This chapter was modified for publication as doctoral thesis.

2.2 Introduction

Studying the first billion years of Earth´s evolution is crucial for understanding the early mantle and crustal differentiation history as well as crustal recycling processes. However, the lack of preservation of the Hadean (4.5-4.0 Ga) rock record hinders a direct study of early geodynamic processes. The earliest relicts of potential continental crustal origin are zircon detrital grains from the ca. 3.3 Ga Jack Hills metaquartzites in NW Australia, dating back to almost 4.4 Ga (e.g., Wilde et al. 2001). Metamorphosed felsic continental crust of Eo- and Paleoarchean age (4.0-3.2 Ga) is preserved as grey gneiss terranes in all cratonic nuclei. These predominantly consist of multiphase grey gneisses that comprise juvenile tonalite-trondhjemite-granodiorites (TTGs) and granitoids of various composition, depending on the exposed crustal level and pre-deformation history (e.g., Nutman et al. 1996; Moyen 2011; Anhaeusser 2014; Hoffmann and Kröner, in press). Associated with the granitoids s.l. are greenstone belts, consisting of ultramafic, mafic and felsic volcanic rocks, and their plutonic equivalents, as well as metasedimentary units. Often, only fragments of the original greenstone associations of various sizes are interlayered with the grey gneisses.

Currently it is under debate in which tectonic environment the early continental crust on Earth formed and stabilized (e.g., van Kranendonk, et al., 2015; Hoffmann et al. 2016 and references therein). Models invoke an initial phase of TTG formation, followed by reworking caused by collision between crustal terranes and involvement of mantle-derived magmas by intrusion and underplating. This led to formation of various types of granitoids that were subsequently strongly deformed and migmatized during post-magmatic metamorphic events. The most prominent relicts of early crustal terranes are the Acasta Gneiss Complex, the Nuvvuagittuq region, the Hudson Bay terrane, and the Eoarchean Labrador gneiss terranes of Canada, as well as the Itsaq Gneiss Complex of southern West Greenland, the Pilbara and northwestern Yilgarn Cratons of Australia, and the Ancient Gneiss Complex located in the eastern Kaapvaal Craton of southern Africa (e.g., Bennett et al. 2007; Van Kranendonk et al. 2007a; Roth et al. 2013, 2014a; Kröner et al. 2014; O´Neil and Carlson 2017; and references therein).

One key observation concerning early crust formation is the lack of Hadean (pre-4.0 Ga) crust in Archean terranes, raising the question whether such an ancient mafic protocrust was involved in the formation of Archean terranes or not (e.g., Kemp et al. 2010; Zeh et al. 2011; O'Neil et al. 2013; O'Neil and Carlson 2017). However, the

Hadean age of ~4.3 Ga proposed for the Ujaraaluk unit in the Nuvvuagittuq greenstone belt suggests that portions of protocrust survived since its formation (O'Neil et al. 2008). Moreover, based on Hf isotope compositions in zircons, reworking of a Hadean or Eoarchean protocrust has been proposed for different terranes (e.g., Iizuka et al. 2007; Kemp et al. 2010; Zeh et al. 2011; Kröner et al. 2014).

A powerful tool to test the involvement of Hadean crustal and mantle sources in the formation of Archean cratonic crust is the short-lived ^{146}Sm-^{142}Nd ($T_{1/2}$ = 103 Ma ± 5 Ma, Meissner et al. 1987) decay system. Due to its short half-life, the ^{146}Sm-^{142}Nd decay system was only active in the first ca. 500 million years of Earth´s evolution. Consequently, differentiation of crustal material from a mantle or crustal source before the extinction of ^{146}Sm will fractionate Sm and Nd because of the slightly more incompatible behavior of Nd compared to Sm during mantle and crustal melting, resulting in heterogeneities in the ^{142}Nd/^{144}Nd composition of early differentiated terrestrial reservoirs (e.g., Harper and Jacobsen 1992; Boyet et al. 2005; Caro et al. 2006; Rizo et al. 2012). During early crust-mantle differentiation, the continental crust developed towards low Sm/Nd isotope ratios, expressed as negative μ^{142}Nd (μ^{142}Nd = (^{142}Nd/^{144}Nd$_{sample}$ / ^{142}Nd/^{144}Nd$_{standard}$ − 1) x 10^6 in ppm) and the incompatible element depleted mantle developed with a high Sm/Nd isotope ratio, resulting in positive μ^{142}Nd values. Hence, an offset in μ^{142}Nd relative to younger rocks can be ascribed to early terrestrial fractionation. Such early terrestrial fractionation events may have included early magma ocean fractionation involving deep mantle phases such as bridgmanite and Ca-perovskite (Corgne et al. 2005) that would directly imprint on the ^{142}Nd composition of the mantle, leaving behind early ^{142}Nd enriched (high Sm/Nd) and depleted (low Sm/Nd) reservoirs (Boyet et al. 2005; Boyet and Carlson 2006; Caro et al. 2005, 2006). Furthermore, the formation of Hadean mafic crust and residual mantle is mirrored by the ^{142}Nd signature of Archean rocks (O'Neil et al. 2008).

So far, all terrestrial rocks younger than 2.70 Ga were found to have a uniform ^{142}Nd/^{144}Nd isotopic composition with μ^{142}Nd of approximately 0 ± 5 ppm (e.g., Boyet and Carlson 2006; Caro et al. 2006; Roth et al. 2014b). In contrast, some ancient terrains show both positive and negative derivations in μ^{142}Nd compared to the terrestrial average value for post-Archean rocks.

Positive μ^{142}Nd anomalies relative to the terrestrial standard have been reported for rocks of the early crustal terranes of Greenland, yielding maximum values of up to +20 ppm (e.g., Boyet and Carlson 2006; Caro et al. 2006; Bennett et al. 2007; Rizo et al.

2011, 2012, 2013; O´Neil et al. 2016). These μ^{142}Nd anomalies were interpreted to directly trace a Hadean mantle reservoir that differentiated between 4.32 Gyr and 4.51 Gyr ago. Complementary reservoirs with negative μ^{142}Nd were reported from the Hadean/Eoarchean Nuvvuagittuq Supracrustal Belt (-18 to +8 ppm; O´Neil et al. 2008, 2012; Roth et al. 2013), the 3.40-3.75 Ga Ukalik belt and Innuksuac complex, Canada (-9 to +1 ppm; Caro et al. 2017), the Acasta gneisses, Canada (μ^{142}Nd as low as -16 ppm; Roth et al. 2014a), as well as from the 3.4-3.5 Ga Ameralik dykes, Greenland (-11 to +16 ppm; Rizo et al. 2012). Similarly, komatiites from the ca. 3.55 Ga Schapenburg Greenstone Remnant (South Africa, Kaapvaal Craton) yielded negative μ^{142}Nd anomalies as low as -13 ppm and were interpreted to trace material from the crystallization of an early Hadean magma ocean (Puchtel et al. 2016b).

Due to the short half-life of the ^{146}Sm-^{142}Nd isotope system, it can be used as a tool for tracing early recycling and mantle stirring processes (Bennett et al. 2007). It has been recognized, that early signatures virtually disappear in magmatic rocks throughout the Archean, with one exception from 2.7 Ga komatiites of the Abitibi belt (Canada) that yielded a μ^{142}Nd anomaly of up to +9 (Debaille et al. 2013). Recently, O'Neil and Carlson (2017) obtained negative μ^{142}Nd anomalies for ca. 2.75 Ga granitoids from the Hudson Bay terrane (Canada), which indicate late Archean reworking of rocks with negative μ^{142}Nd signatures that were derived from ancient reservoirs which initially differentiated from the mantle in the Hadean.

In this study, we focus on Archean granitoids and mantle-derived rocks from the eastern Kaapvaal Craton (South Africa and Swaziland). We report the first high-precision ^{142}Nd/^{144}Nd analyses for well-characterized granitoids and meta-tholeiites (amphibolites) of the Ancient Gneiss Complex (AGC; Swaziland) and from the lower Onverwacht Group of the Barberton Greenstone Belt (BGB; South Africa). The investigated samples span an age range from 3.66 Ga to 3.22 Ga and represent the main lithological units of the AGC and the oldest rocks of the BGB. The data are used to elucidate the differentiation and reworking history of the oldest part of the Kaapvaal Craton. The combination of data derived from the short-lived ^{146}Sm-^{142}Nd system with existing geological, petrological and geochemical information for these samples lead to a deeper understanding of if and how Hadean crustal components were incorporated into the sources of Archean crustal rocks, enabling us to place general constraints on geodynamic processes operating in the early Archean.

2.3 Geology of the Ancient Gneiss Complex and Barberton Greenstone Belt

The 3.66-3.20 Ga AGC (Hoffmann and Kröner, in press, and references therein) is located in the eastern Kaapvaal Craton and predominantly comprises complexly deformed Paleo- to Mesoarchean grey gneisses of the TTG suite that are interlayered with rare amphibolites (Fig. 2.1; Hoffmann and Kröner, in press). The 3.66-3.45 Ga Ngwane Gneiss is the oldest component of the AGC (Hoffmann and Kröner, in press, and references therein) and is exposed in central and western Swaziland as well as in the Phophonyane Inlier of northwestern Swaziland. The Ngwane Gneiss underwent ductile amphibolite- to granulite-facies metamorphism (Kröner et al. 1993, 2014 and references theirein). The interlayered amphibolites represent mafic dykes (Jackson 1984; Hoffmann and Kröner, in press) as well as infolded greenstone remnants (e.g., Jackson 1984; Kröner and Tegtmeyer 1994). The Ngwane Gneiss is intruded by the 3.478-3.430 Ga homogeneous and variously foliated dioritic to tonalitic Tsawela Gneiss (e.g., Jackson 1984; Kröner et al. 1993; Hoffmann et al. 2016), granitoid gneisses of the ca. 3.23 Ga Usutu Intrusive Suite (Schoene et al. 2009), and the 3.1 Ga Pigg´s Peak batholith (Murphy 2015) which divides the AGC from the BGB in the north, as well as several other smaller plutons with ages up to 2.7 Ga (e.g., Zeh et al. 2011). The most prominent and largest supracrustal succession within the AGC is the ca. 3.45 Ga Dwalile Greenstone Remnant (DGR; Kröner and Tegtmeyer 1994) exposed west of Mankanyane town along the border with South Africa.

To the northwest the AGC is tectonically separated from the 3.53-3.20 Ga BGB and surrounding plutons (e.g., Kröner et al. 1991, 1996; Van Kranendonk et al. 2009) by a major faulted contact, the Phophonyane shear zone (Fig. 2.1). The oldest unit of the BGB is the Onverwacht Group, which comprises mafic and ultramafic volcanic rocks that are interlayered with subordinate felsic volcanic rocks. The BGB is surrounded by several plutons, namely the Steynsdorp, Theespruit, Stolzburg, Nelshoogte, and Kaap Valley plutons with ages of ca. 3.51 to 3.20 Ga. Their compositions range from tonalite to trondhjemite (e.g., Anhaeusser 2014).

The AGC and the southern BGB are characterized by regionally extensive medium-pressure and high-temperature metamorphism that occurred at ca. 3.2 Ga (e.g., Dziggel et al. 2005; Taylor et al. 2012). This metamorphic event led to lower granulite-facies ductile deformation, migmatization, and anatexis, followed by syntectonic emplacement of granitoids in the lower and mid-crustal domains represented by the AGC (e.g., Schoene et

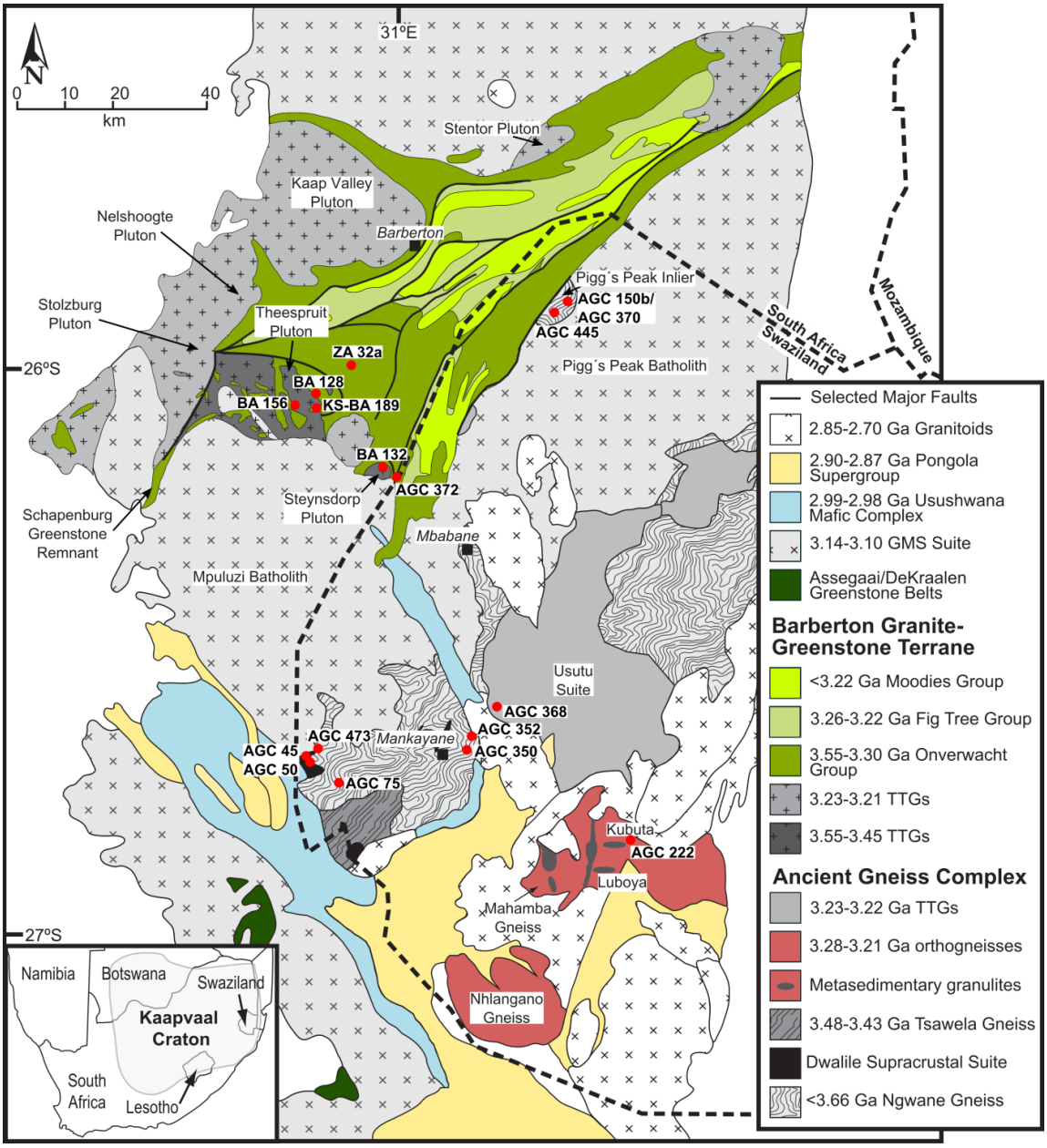

Figure 2.1: Simplified geological map of the Ancient Gneiss Complex (Swaziland) and Barberton Greenstone Belt (South Africa) in the eastern Kaapvaal Craton. Red dots mark sample localities of the investigated felsic, mafic, and ultramafic rocks. Map modified after Van Schijndel et al. (2017)

al. 2008). In the BGB, this metamorphism caused a greenschist- and upper amphibolite facies overprint, coupled with refolding and structural parallelism between granitoid gneisses and supracrustal rocks (e.g., De Ronde and De Wit 1994; Lowe and Byerly 1999; van Kranendonk et al. 2009, 2015; Kröner et al., 2016).

2.4 Samples and analytical techniques

2.4.1 Sample selection

The strategy of our sample selection was to cover a comprehensive range of rocks representative of the early Archean crust of the AGC and BGB that included different lithological units and ages, to gain structural and temporal resolution of possible changes in $^{142}Nd/^{144}Nd$ isotopic compositions. We selected six well-characterized and least altered granitoid gneisses from the AGC, including TTG compositions and grey gneisses of various origins, covering an age range from 3.66 Ga (grey gneiss AGC 150b; Kröner et al. 2014) to 3.22 Ga (grey gneiss AGC 445; age: personal communication A. Kröner 2017). Three of these samples, the 3.66 Ga Ngwane grey gneiss (AGC 150b), the 3.55 Ga tonalite from north of Pigg´s Peak town (AGC 370), and the 3.48 Ga tonalitic Tsawela gneiss from west-central Swaziland (AGC 75), reveal heterogeneous Hf-in-zircon isotope compositions implying involvement of older crustal components in the formation of these rocks (Kröner et al. 2014; Hoffmann et al. 2016). Additionally, the 3.26 Ga granodiorite from the Usutu Suite (AGC 368) contains inherited zircons that date back to 3.45 Ga which is in agreement with contribution from an older crustal source (ages: personal communication A. Kröner 2017). Furthermore, two amphibolites and one metagabbro from the AGC were selected, all dating back to ages between >3.40 Ga (AGC 222; Kröner et al. 1993; Taylor et al. 2012; Suhr et al. 2015) and 3.46 Ga (AGC 45; Kröner and Tegtmeyer 1994; AGC 350 dated to 3.46 Ga; personal communication A. Kröner 2016). In addition, we selected two ca. 3.45 Ga ultramafic rocks from the Dwalile Greenstone Remnant (Kröner and Tegtmeyer 1994) and one 3.24 Ga trondhjemitic gneiss which intruded into the grey gneisses structurally below the Dwalile Greenstone Remnant (age: personal communication A. Kröner 2017). The latter sample contains inherited zircon grains of 3.49 Ga and ca. 3.64 Ga (ages: personal communication A. Kröner 2017).

Rock types of the oldest supracrustal sequences of the BGB include one meta-tholeiite of the Sandspruit Formation (KS-BA 189; supplementary material 2.A) and two samples of the Theespruit Formation (meta-tholeiite BA 156, supplementary material 2.A; felsic metavolcanic rock AGC 372, Kröner et al. 2013) as well as one meta-tholeiite of the Komati Formation (ZA-32a, supplementary material 2.A). These samples span a narrower age range than the AGC granitoids from ca. 3.55 Ga to 3.48 Ga and are representative of the lower Onverwacht Group. In addition, $\mu^{142}Nd$ analyses were

conducted on a 3.46 Ga tonalite component of the Theespruit Pluton, containing heterogeneous Hf-in-zircon isotopic compositions (e.g., sample BA 115 from Kröner et al. 2016 that was taken at the same locality), and a 3.51 Ga sample of the Steynsdorp Pluton. More detailed descriptions are provided in Kröner and Tegtmeyer (1994), Kröner et al. (2013, 2014, 2016), and Hoffmann et al. (2016). Sample localities are shown in Figure 2.1.

2.4.2 Analytical methods

The chemical separation for Nd isotopes is described in detail in the supplementary material 2.B. Neodymium isotope measurements were performed using a Thermo-Scientific^{TM} Triton multi-collector thermal ionization mass spectrometer (MC-TIMS) at the Laboratoire Magmas et Volcans (LMV), University Clermont Auvergne, Clermont Ferrand, France. Neodymium fractions were dissolved in 2 µl of 2.5 N HCl and loaded onto outgassed zone-refined Re filaments. Neodymium was measured as Nd^+ using a second bare Re filament as ionization filament. Each measurement was performed in 27 blocks of 20 cycles each (~8 s integration) in dynamic mode using amplifier rotation. The background was measured before each block. After a series of 9 blocks, readjustment of the focus and a peak center were conducted. For the dynamic mode, one line of measurements was performed with the mass ^{145}Nd in the central faraday cup with ^{140}Ce being monitored in the L4 and ^{147}Sm in the H2 faraday cup. The second line was measured with the mass ^{143}Nd in the central faraday cup, monitoring ^{138}Ba in the L4 faraday cup to check if the ionization of Nd isotopes was not hampered due to a high Ba signal. If possible, samples were run repeatedly up to three times on the same filament, depending on the Nd content (notation #R1, #R2, and #R3 in Table 2.1, respectively).

Roth et al. (2014b) showed that rapid sample fractionation between the sequential measurement of $^{146}Nd/^{144}Nd$ and $^{142}Nd/^{144}Nd$ (2 lines acquisition) can induce large biases on dynamic $^{142}Nd/^{144}Nd$ ratios. The fractionation rates calculated for samples and standards during this study are on average 0.215 $ppm.s^{-1}$ and 0.175 $ppm.s^{-1}$, respectively. These values are far below the threshold limit of 0.4 $ppm.s^{-1}$. A fractionation rate that would produce a bias on dynamic $^{142}Nd/^{144}Nd$ ratios must be higher than 5 ppm.

Neodymium isotope ratios were corrected for mass fractionation using the exponential law and $^{146}Nd/^{144}Nd = 0.7219$. Data are reported relative to the JNdi-1 standard which was measured along with the samples, resulting in an average long-term

$^{142}Nd/^{144}Nd$ ratio of 1.141839 ± 1.33 ppm (95% confidence interval, n = 13) for the first analytical session (LMV Triton) and 1.141827 ± 1.10 ppm (95% confidence interval, n = 17) for the second session (LMV Triton Plus), using a student´s t distribution for our calculations. The use of a student´s t distribution is justified, because of the relatively limited number of JNdi-1 analyses within the two analytical sessions, i.e. 13 and 17 times (see supplementary material 2.C for a detailed explanation of our calculation). However, in the figures we report the 2s.d. external reproducibility of the corresponding JNdi-1 standard sessions 1 (i.e. ±4.4 ppm) and 2 (i.e. ±4.3 ppm) for samples that were only measured once. For repeated measurements (n = 2-3) a mean value of the repeated sample analyses was calculated and is also reported together with the 2s.d. of the corresponding standard sessions (i.e. ±4.4 ppm for samples of the first and ±4.3 ppm for samples of the second analytical session).

Available major and trace element as well as ^{147}Sm-^{143}Nd and ^{176}Lu-^{176}Hf isotope data for all samples are summarized in the supplementary material 2.A. A summary of the analytical methods for samples AGC 222, AGC 350, AGC 445, AGC 473, BA 132, BA 156, KS-BA 189, and ZA-32a is provided in the supplementary material 2.D.

2.5 Results

Table 2.1 summarizes the results for $^{142}Nd/^{144}Nd$, $^{143}Nd/^{144}Nd$, $^{145}Nd/^{144}Nd$, $^{146}Nd/^{144}Nd$, $^{148}Nd/^{144}Nd$, and $^{150}Nd/^{144}Nd$ measurements on seventeen samples from the BGB and AGC, respectively. The Hawaiian basalt BHVO-2 was measured as reference material, and the data as well as repeated analyses of the terrestrial standard JNdi-1 are listed in Table 2.1. Measurements have been performed during two different analytical sessions and using the two LMV thermal ionization mass spectrometers: Triton™ (session 1) and Triton Plus™ (session 2). The BHVO-2 standard yielded a $\mu^{142}Nd$ of 2.4 ± 3.9 ppm (2.s.e.), overlapping within error with the JNdi-1 terrestrial standard measured in session 1. The analytical uncertainties on $^{142}Nd/^{144}Nd$ for single internal sample runs were usually better than 3.9 ppm (2s.e.), except for two samples (AGC 350, KS-BA 189), which had internal reproducibilities between ± 4.0 ppm and ± 5.0 ppm (2s.e.; Table 2.1).

Measured $\mu^{142}Nd$ values in samples of the Kaapvaal Craton range from -7.9 ± 4.4 ppm (2s.d.) to +3.0 ± 4.3 ppm (2s.d.; Fig. 2.2). Confidently resolvable $\mu^{142}Nd$ anomalies were found in a 3.44 Ga Ngwane Gneiss (AGC 352) and two ca. 3.45 Ga (ultra-)mafic rocks from the Dwalile Supracrustal Suite (AGC 45 and 50), having $\mu^{142}Nd$

values of -7.9 ± 4.4 ppm (2s.d.), -6.2 ± 4.3 ppm (2s.d.), and -6.1 ± 4.3 ppm (2s.d.), respectively.

Table 2.1: Measured ^{142}Nd data for granitoids and (ultra-)mafic rocks from the Ancient Gneiss Complex and Barberton Greenstone Belt.

Samples	Age	^{142}Nd/^{144}Nd	± 2s.e. on last dec. pl.	μ^{142}Nd (µg/g)	±2s.e. (µg/g)	^{143}Nd/^{144}Nd	± 2s.e. on last dec. pl.	ε^{143}Nd*	^{145}Nd/^{144}Nd	± 2s.e. on last dec. pl.	μ^{145}Nd (µg/g)	± 2s.e. (µg/g)
1. analytical session												
AGC372	3552	1.141832	4	-5.6	3.7	0.510649	2	-0.6	0.348406	1	12.6	3.4
BA156	3530	1.141839	4	0.0	3.2	0.512711	2	0.8	0.348404	1	7.0	2.8
AGC75 #R1	3478	1.141833	4	-4.8	3.9	0.510531	2		0.348403	1	2.8	3.7
AGC75 #R2	3478	1.141832	4	-5.9	3.7	0.510532	2		0.348402	1	0.7	3.3
AGC75 average				-5.4				0.2				
AGC352	3442	1.141830	4	-7.9	3.1	0.510989	2	1.1	0.348403	1	4.1	2.9
AGC222	3400	1.141840	3	0.6	3.0	0.512396	2	1.6	0.348403	1	3.9	2.9
AGC368	3261	1.141835	3	-3.3	2.7	0.510369	2	-1.0	0.348403	1	3.8	2.8
AGC445	3216	1.141833	4	-5.4	3.2	0.510727	2	-1.1	0.348405	1	7.6	3.1
BHVO2		1.141842	5	2.4	3.9	0.512976	2		0.348404	1	6.5	3.9
2. analytical session												
AGC 150b #R1	3661	1.141827	3	0.2	2.8	0.510981	1		0.348400	1	2.6	2.8
AGC 150b #R2	3661	1.141825	4	-1.8	3.1	0.510981	2		0.348400	1	3.0	2.8
AGC 150b average				-0.8				0.7				
KS-BA189	3553	1.141827	6	0.4	5.0	0.511444	3	1.1	0.348401	2	5.4	5.0
AGC 370	3552	1.141822	4	-4.2	3.8	0.510128	2	1.4	0.348401	1	6.4	3.5
BA132 #R1	3509	1.141824	4	-2.6	3.3	0.510621	2		0.348400	1	3.3	2.9
BA132 #R2	3509	1.141823	4	-3.8	3.9	0.510621	2		0.348402	1	9.0	3.4
BA132 average				-3.2								
ZA32a	3480	1.141821	4	-5.4	3.7	0.512140	2	0.3	0.348402	1	7.5	3.1
BA128	3465	1.141827	3	0.1	2.6	0.511125	1	0.2	0.348400	1	2.2	2.9
AGC350 #R1	3455	1.141825	5	-1.9	4.5	0.511909	2		0.348401	1	4.4	3.9
AGC350 #R2	3455	1.141829	5	2.1	4.6	0.511913	2		0.348400	1	1.2	3.4
AGC350 #R3	3455	1.141825	5	-2.0	4.0	0.511911	2		0.348400	1	3.5	3.7
AGC350 average				-0.6				0.5				
AGC50 #R1	3458	1.141821	4	-5.4	3.9	0.511791	2		0.348401	1	4.6	3.9
AGC50 #R2	3458	1.141819	4	-6.7	3.7	0.511789	2		0.348400	1	1.9	3.4
AGC50 average				-6.1								
AGC 45	3445	1.141820	4	-6.2	3.1	0.512141	2	0.0	0.348399	1	-0.1	2.7
AGC473	3241	1.141830	3	3.0	3.0	0.510548	1	-1.0	0.348401	1	4.0	2.2

Table 2.1 continued.

Samples	Age	$^{146}Nd/^{144}Nd$	± 2s.e. on last dec. pl.	$^{148}Nd/^{144}Nd$	± 2s.e. on last dec. pl.	$\mu^{148}Nd$ (µg/g)	± 2s.e. (µg/g)	$^{150}Nd/^{144}Nd$	± 2s.e. on last dec. pl.	$\mu^{150}Nd$ (µg/g)	± 2s.e. (µg/g)
1. analytical session											
AGC372	3552	0.722331	100	0.241581	2	-7.5	6.2	0.236448	2	-35.7	7.9
BA156	3530	0.723225	60	0.241581	1	-5.8	5.0	0.236450	2	-26.4	7.2
AGC75 #R1	3478	0.721429	24	0.241580	1	-13.0	6.0	0.236449	2	-30.0	8.1
AGC75 #R2	3478	0.722741	53	0.241580	1	-12.3	5.9	0.236449	2	-29.5	7.8
AGC352	3442	0.722696	60	0.241581	1	-6.9	5.1	0.236449	2	-33.0	7.0
AGC222	3400	0.723633	87	0.241582	1	-2.3	5.3	0.236451	2	-25.0	6.8
AGC368	3261	0.723632	15	0.241579	1	-17.1	4.7	0.236448	1	-36.4	6.3
AGC445	3216	0.722131	93	0.241580	1	-11.5	5.3	0.236446	2	-44.3	7.2
BHVO2		0.721600	59	0.241582	2	-3.9	6.6	0.236446	2	-43.4	8.6
2. analytical session											
AGC 150b #R1	3661	0.721711	66	0.241577	1	-2.2	4.5	0.236448	1	-8.7	6.2
AGC 150b #R2	3661	0.723316	24	0.241578	1	4.2	5.0	0.236452	2	5.6	6.9
KS-BA189	3553	0.721973	47	0.241577	2	0.4	8.7	0.236451	3	1.7	11.1
AGC 370	3552	0.721285	94	0.241577	1	-0.6	6.1	0.236448	2	-11.4	8.5
BA132 #R1	3509	0.720851	52	0.241576	1	-2.4	5.0	0.236448	2	-10.2	7.3
BA132 #R2	3509	0.722296	19	0.241576	1	-4.5	5.9	0.236447	2	-15.7	8.3
ZA32a	3480	0.722807	176	0.241577	1	1.2	5.5	0.236446	2	-17.4	7.7
BA128	3465	0.723051	33	0.241579	1	8.0	4.1	0.236453	1	10.9	4.2
AGC350 #R1	3455	0.720526	68	0.241578	2	2.5	7.4	0.236450	2	-3.2	10.2
AGC350 #R2	3455	0.722572	32	0.241576	1	-5.7	5.9	0.236450	2	-0.8	7.7
AGC350 #R3	3455	0.724003	34	0.241578	2	4.0	6.7	0.236450	2	-2.0	9.2
AGC50 #R1	3458	0.720716	47	0.241577	2	-0.6	6.6	0.236447	2	-13.2	8.8
AGC50 #R2	3458	0.722796	50	0.241576	1	-2.4	6.0	0.236445	2	-24.8	7.4
AGC 45	3445	0.720788	89	0.241575	1	-7.4	4.9	0.236449	1	-7.1	6.3
AGC473	3241	0.722943	45	0.241577	1	-2.1	3.9	0.236449	1	-6.3	5.5

* Calculated with $^{147}Sm/^{144}Nd$ and initial $^{143}Nd/^{144}Nd$ of published isotope data. For published $^{147}Sm/^{144}Nd$ and initial $^{143}Nd/^{144}Nd$ isotope data please refer to Table S1 of the supplementary material.
#R1, #R2 means run 1, run 2

Table 2.1 continued.

Terrestrial standards	$^{142}Nd/^{144}Nd$	± 2s.e. on last dec. pl.	$\mu^{142}Nd$ (µg/g)	±2s.e. (µg/g)	$^{143}Nd/^{144}Nd$	± 2s.e. on last dec. pl.	$^{145}Nd/^{144}Nd$	± 2s.e. on last dec. pl.	$\mu^{145}Nd$ (µg/g)	±2s.e. (µg/g)
1. analytical session										
JNdi-1	1.141840	8	1.1	3.3	0.512103	3	0.348402	2	-0.5	5.5
JNdi-1	1.141835	6	-3.8	2.7	0.512101	2	0.348402	1	0.5	4.1
JNdi-1	1.141836	6	-2.5	2.8	0.512103	3	0.348402	2	-0.9	5.2
JNdi-1	1.141836	7	-2.2	3.1	0.512103	3	0.348402	2	1.4	5.6
JNdi-1	1.141843	8	3.6	3.7	0.512102	4	0.348402	2	0.8	6.0
JNdi-1	1.141839	8	0.5	3.6	0.512101	3	0.348401	2	-2.2	5.7
JNdi-1	1.141841	7	1.5	3.2	0.512104	4	0.348402	2	0.6	5.9
JNdi-1	1.141837	17	-1.6	7.2	0.512101	7	0.348400	4	-4.5	12.3
JNdi-1	1.141837	7	-1.4	3.3	0.512104	4	0.348401	2	-2.2	7.2
JNdi-1	1.141841	7	1.7	3.0	0.512104	3	0.348402	2	1.4	5.6
JNdi-1	1.141839	7	0.3	3.1	0.512104	4	0.348402	2	0.1	6.7
JNdi-1	1.141842	7	2.9	3.1	0.512104	3	0.348403	2	1.8	5.6
JNdi-1	1.141839	9	0.0	3.8	0.512104	5	0.348403	3	3.5	8.3
JNdi-1 avg. 1. session	1.141839	5	0.0	4.4 (2s.d.)						
2. analytical session										
JNdi-1	1.141823	6	-3.4	5.0	0.512107	3	0.348399	2	-0.7	4.4
JNdi-1	1.141823	3	-3.5	3.0	0.512107	2	0.348398	1	-4.8	2.6
JNdi-1	1.141828	4	0.5	3.1	0.512105	2	0.348402	1	8.8	2.9
JNdi-1	1.141824	3	-2.7	2.8	0.512103	1	0.348402	1	9.2	2.3
JNdi-1	1.141823	4	-3.5	3.2	0.512104	2	0.348399	1	-0.1	2.5
JNdi-1	1.141826	3	-0.8	2.9	0.512105	1	0.348398	1	-2.2	2.4
JNdi-1	1.141826	3	-1.0	2.5	0.512106	1	0.348399	1	-1.5	2.2
JNdi-1	1.141827	3	0.3	2.4	0.512106	1	0.348399	1	-0.1	2.1
JNdi-1	1.141828	3	0.7	3.0	0.512106	2	0.348399	1	-0.1	2.8
JNdi-1	1.141828	4	0.9	3.2	0.512105	2	0.348398	1	-4.1	2.9
JNdi-1	1.141830	3	2.7	2.8	0.512106	1	0.348400	1	1.4	2.4
JNdi-1	1.141830	3	2.7	2.8	0.512106	1	0.348400	1	1.4	2.4
JNdi-1	1.141829	3	2.2	3.1	0.512107	2	0.348399	1	-0.8	2.8
JNdi-1	1.141828	5	0.5	4.0	0.512108	2	0.348399	1	-1.6	3.5
JNdi-1	1.141828	4	1.0	3.7	0.512108	2	0.348399	1	-0.1	3.2
JNdi-1	1.141828	5	1.2	4.0	0.512108	2	0.348397	1	-5.0	3.7
JNdi-1	1.141829	4	2.1	3.7	0.512110	2	0.348399	1	0.1	3.0
JNdi-1 avg. 2. session	1.141827	5	0.0	4.3 (2s.d.)						

Table 2.1 continued.

Terrestrial standards	$^{146}Nd/^{144}Nd$	± 2s.e. on last dec. pl.	$^{148}Nd/^{144}Nd$	± 2s.e. on last dec. pl.	$\mu^{148}Nd$ (µg/g)	±2s.e. (µg/g)	$^{150}Nd/^{144}Nd$	± 2s.e. on last dec. pl.	$\mu^{150}Nd$ (µg/g)	±2s.e. (µg/g)
1. analytical session										
JNdi-1	0.723837	17	0.241582	2	-3.9	10.3	0.236455	3	-4.5	14.2
JNdi-1	0.722755	88	0.241583	2	1.4	7.7	0.236457	2	4.3	10.3
JNdi-1	0.722290	65	0.241583	2	1.6	8.6	0.236459	3	10.6	11.7
JNdi-1	0.722718	15	0.241583	2	-0.5	9.6	0.236456	3	-3.3	14.0
JNdi-1	0.722830	62	0.241583	3	-1.0	10.6	0.236457	3	1.8	14.8
JNdi-1	0.721677	76	0.241582	2	-3.0	10.0	0.236455	3	-7.9	14.5
JNdi-1	0.722316	95	0.241582	2	-5.2	10.0	0.236455	3	-4.1	14.2
JNdi-1	0.721402	110	0.241585	6	9.7	24.6	0.236458	8	7.0	32.8
JNdi-1	0.722926	35	0.241582	3	-2.4	12.0	0.236456	4	-1.7	16.0
JNdi-1	0.722075	69	0.241584	2	3.5	10.0	0.236457	3	2.9	14.6
JNdi-1	0.722491	12	0.241583	3	2.3	11.2	0.236458	4	4.6	15.3
JNdi-1	0.723389	98	0.241583	3	-0.4	10.6	0.236455	3	-6.4	13.9
JNdi-1	0.722572	61	0.241584	3	3.5	13.5	0.236459	5	12.5	19.8
2. analytical session										
JNdi-1	0.720617	65	0.241575	2	-9.3	7.7	0.236446	3	-19.7	10.8
JNdi-1	0.720659	61	0.241574	1	-11.2	4.9	0.236445	2	-24.2	6.8
JNdi-1	0.720515	32	0.241578	1	5.9	5.0	0.236454	2	15.3	6.6
JNdi-1	0.721589	24	0.241579	1	7.7	4.0	0.236454	1	16.1	5.5
JNdi-1	0.720704	48	0.241578	1	2.4	4.9	0.236451	2	4.3	6.9
JNdi-1	0.723311	67	0.241577	1	1.4	4.6	0.236451	1	1.8	6.1
JNdi-1	0.720810	55	0.241576	1	-5.0	3.9	0.236449	1	-5.0	5.3
JNdi-1	0.723915	74	0.241576	1	-2.8	3.6	0.236449	1	-4.4	5.2
JNdi-1	0.721511	51	0.241577	1	1.3	4.7	0.236451	2	2.0	6.7
JNdi-1	0.723244	48	0.241578	1	5.0	5.2	0.236453	2	10.6	6.8
JNdi-1	0.721490	65	0.241578	1	3.6	4.2	0.236450	1	-1.9	5.9
JNdi-1	0.721490	65	0.241578	1	3.6	4.2	0.236450	1	-1.9	5.9
JNdi-1	0.723453	52	0.241577	1	-0.3	5.1	0.236451	2	4.4	7.1
JNdi-1	0.721598	56	0.241578	1	4.0	5.8	0.236452	2	8.2	8.6
JNdi-1	0.723597	36	0.241579	1	7.1	5.8	0.236454	2	15.9	7.3
JNdi-1	0.721057	50	0.241575	2	-9.0	6.4	0.236448	2	-10.0	8.7
JNdi-1	0.724330	45	0.241576	1	-4.6	5.2	0.236448	2	-11.6	7.6

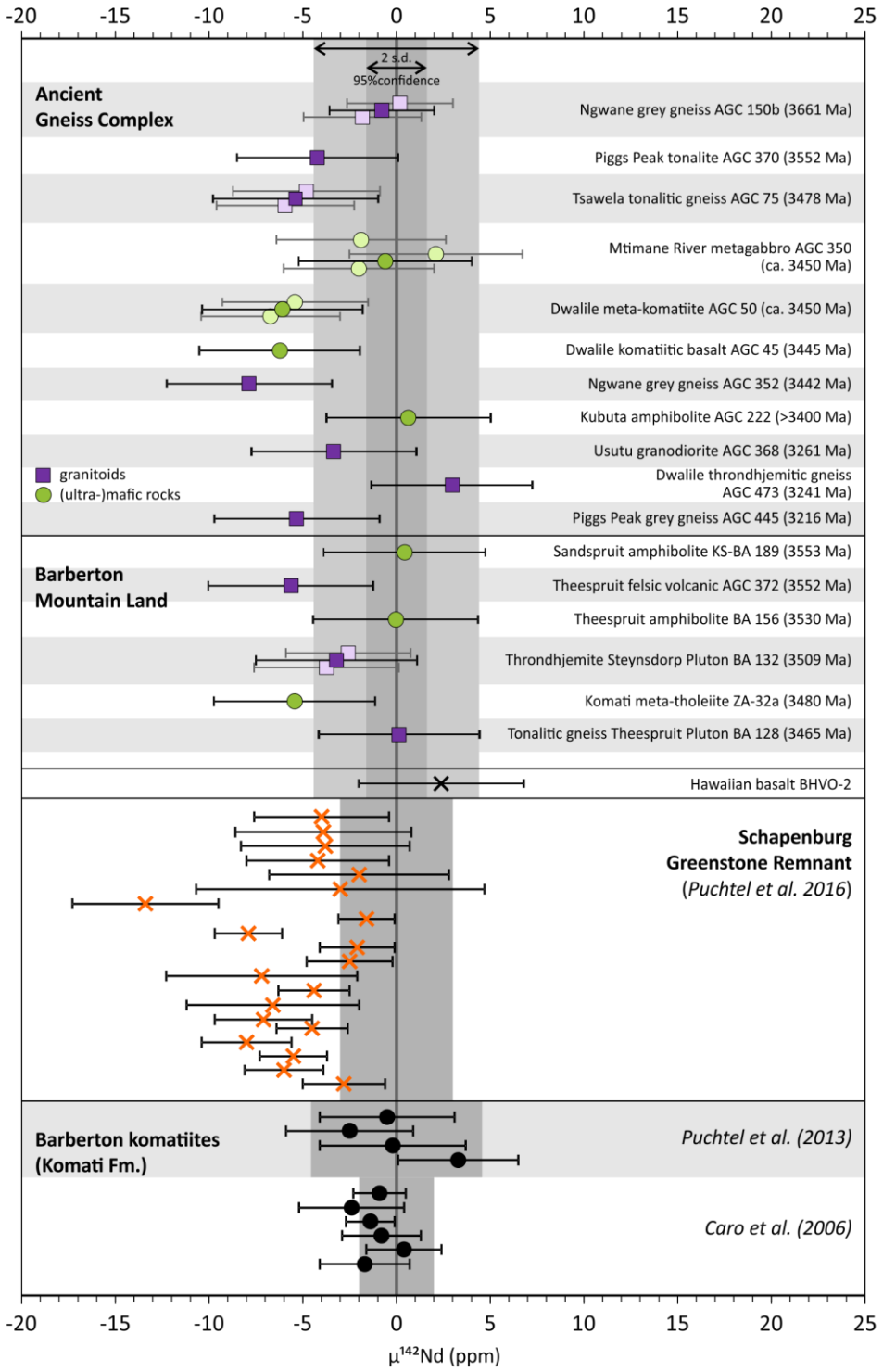

Figure 2.2: Measured μ^{142}Nd values for the studied AGC and BGB rocks reported together with the 2s.d. of the corresponding standard sessions. Usually single measurements of granitoids (purple) and (ultra-)mafic rocks (green) are reported except for samples AGC 150b, AGC 75, AGC 350, AGC 50, BA 132, and BA 128 where single measurements are represented by lighter symbols and the mean values are represented by the dark filled symbols. Samples AGC 352, AGC 45, and AGC 50 show resolvable negative anomalies relative to the terrestrial JNdi-1 standard (95% conf. int., grey vertical box). Additionally, four samples (AGC 75, 372, 445, and ZA-23a) show a tendency to slightly negative μ^{142}Nd values that are, however, within error not unambiguously resolvable from the JNdi-1 terrestrial standard. The 95% confidence interval of the JNdi-1 standard was ±1.3 ppm for the first analytical session (n = 13) and ±1.1 ppm for the second analytical session (n = 17). The 2s.d. of the JNdi-1 reference of ±4.4 ppm is shown for comparison (lighter grey vertical box). Additionally, literature data for Barberton and Schapenburg komatiites is shown.

2.6 Discussion

2.6.1 Evaluation of metamorphic disturbance

All samples from the AGC and BGB underwent metamorphic overprint up to amphibolite-facies conditions. Such metamorphic events could cause element migration and, hence, disturbance of the Nd isotope compositions by metamorphic fluids. However, our samples do not show any correlation of their μ^{142}Nd signatures with, for example, enrichment in light rare earth or large ion lithophile elements (Supplement 2.E). Consequently, we consider the μ^{142}Nd anomalies in the AGC and BGB rocks as reflecting undisturbed signatures that are inherited from the source compositions.

2.6.2 Significance of negative ^{142}Nd signatures in Archean rocks of the Ancient Gneiss Complex

The first μ^{142}Nd data reported for the AGC provide evidence for the preservation of a negative μ^{142}Nd isotope signature throughout different lithological units of the AGC (Fig. 2.2). However, only three samples can be readily distinguished in terms of μ^{142}Nd compared to the modern terrestrial reference material. Furthermore, as illustrated in Figure 2.3a,b, a bimodal distribution can be observed with one population of ten samples having generally negative μ^{142}Nd anomalies with an average of -5.3 ± 2.8 ppm (2s.d.) relative to the terrestrial standard and another population of seven samples showing no deviation from the JNdi-1 terrestrial standard with a mean μ^{142}Nd of 0.4 ± 2.5 ppm (2s.d.). The presence of negative μ^{142}Nd values requires the involvement of an older crustal or incompatible element enriched mantle reservoir in their petrogenesis. This could have occurred either by direct melting of a Hadean incompatible element enriched protocrust that remained unaffected by melting or crustal recycling since its differentiation (e.g., O'Neil et al. 2008; O'Neil and Carlson 2017) or by inheritance of a Hadean μ^{142}Nd signature from older granitoids that formed after the extinction of ^{146}Sm and were contaminated by Hadean crustal material, ultimately resulting from Hadean mantle-derived mafic melts. Alternatively, the negative μ^{142}Nd anomalies were inherited from the mantle source that underwent a differentiation event in the Hadean accompanied by a decrease of Sm/Nd and may have interacted with the early cratonic nuclei to produce granitoids with variably negative μ^{142}Nd values.

Preserved Archean continental crust is interpreted to consist, to large degrees, of juvenile TTGs, which represent direct melts of metamorphosed mafic crust (e.g., Moyen and Martin 2012 and refs. therein). However, many Archean crustal terranes are now composites of grey gneisses that have diverse origins and complex formation histories involving crustal reworking processes (e.g., Moyen 2011; Hoffmann et al. 2011). Here, interaction of mantle-derived magmas with older felsic crust may have been common, leading to further differentiation and diversification of the Archean crust and, ultimately, to stabilization of the crust (e.g., Laurent et al. 2014; Hoffmann et al. 2016). This is the case for the early Archean crust of the eastern Kaapvaal craton where, on the basis of heterogeneous Hf isotope signatures of zircons from grey gneiss samples, different studies argued for interaction of juvenile mantle-derived magmas with older felsic crust (Zeh et al. 2011; Kröner et al. 2014; Hoffmann et al. 2016) or melting of older felsic crust in the presence of zircon (e.g., Tang et al. 2014). Moreover, rare inherited Eoarchean zircon grains were found in rocks of the AGC (e.g., Kröner and Tegtmeyer 1994), thus providing additional support for the involvement of older crustal rocks in the genesis of the exposed crust. Interestingly, incompatible element depleted mantle Lu-Hf model ages for zircons from the Ngwane gneisses were calculated to be up to 4.1 Ga (e.g., Zeh et al. 2011; Kröner et al. 2014). However, the complex intra-crustal differentiation processes make one-stage model ages unlikely, and the calculated ages would only provide minimum ages for the initial extraction of melt from a hypothetical incompatible element depleted mantle reservoir.

Juvenile crustal additions to the AGC were largely restricted to the mid-Paleoarchean (e.g., Zeh et al. 2011; Kröner et al. 2014; Hoffmann et al. 2016). The granitoids measured here for their $^{142}Nd/^{144}Nd$ isotope compositions cover an age range from ca. 3.66 to ca. 3.22 Ga. The only clearly resolvable negative ^{142}Nd anomaly was found in a 3.44 Ga Ngwane grey gneiss from the Mankanyane region. In this sample, the zircon Hf isotope compositions were heterogeneous (Hoffmann et al. 2016), in support of the conclusions of Kröner et al. (2014) and Hoffmann et al. (2016) that these rocks formed by melting of older crustal material. Furthermore, the youngest 3216 Ma grey gneiss investigated in this study has a negative $\mu^{142}Nd$ value that is not resolvable from the terrestrial standard. This indicates that back-mixing of crustal components into the mantle or, alternatively, mantle reservoirs carrying the ^{142}Nd anomaly lasted at least until 3.2 Ga, and this process can potentially be traced in various granitoids of different ages.

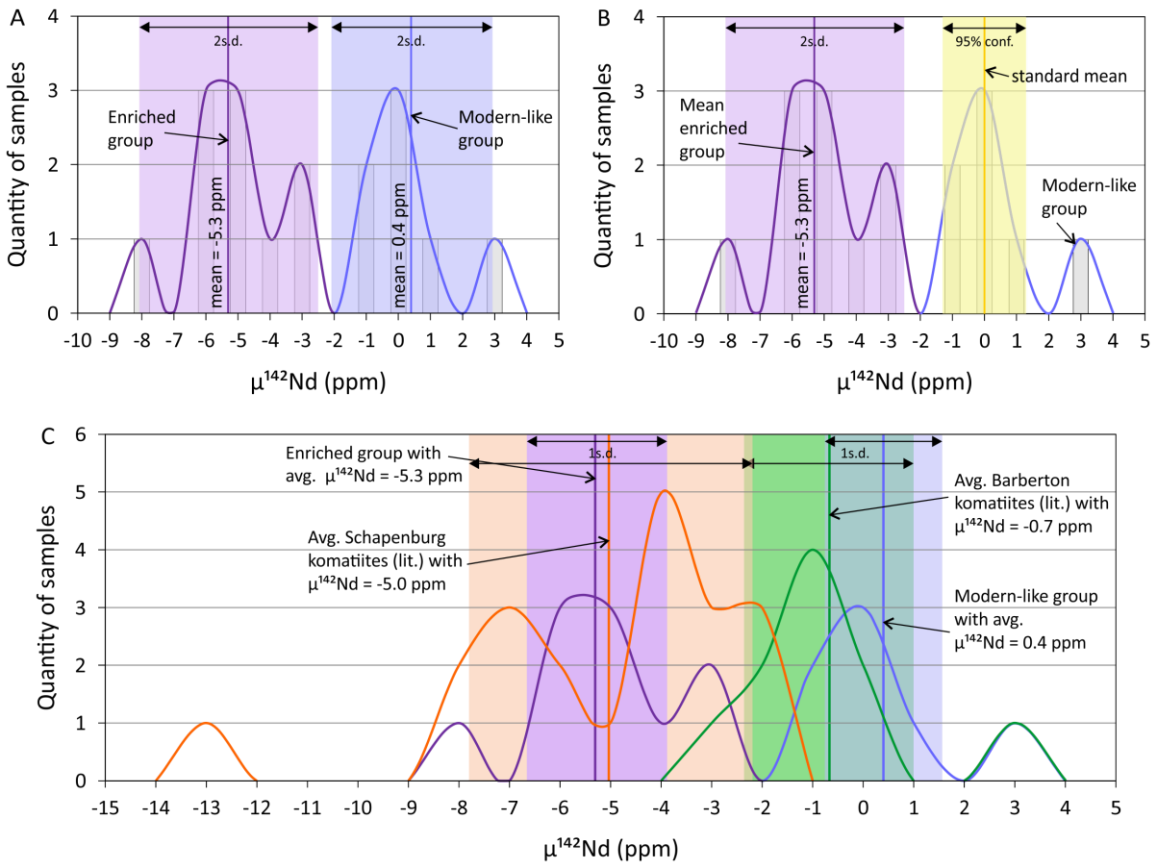

Figure 2.3: Histograms of μ^{142}Nd data. A) Distribution of analyzed samples (grey bars) divided into a bimodal distribution with an enriched group having an average μ^{142}Nd of -5.3 ± 2.8 ppm (2s.d., n = 10; purple line and shaded area) and a modern-like group averaging +0.4 ± 2.5 ppm (2s.d., n = 7; blue line and shaded area). A student´s t-test of the two groups resulted in a t value of -4.31, i.e. t (-4.31) < $t_{critical}$ (-2.131) which means that the two groups are statistically significantly different form each other (see calculation in supplementary material 2.F). B) Distribution of analyzed samples compared to the population of JNdi-1 terrestrial standards having an average μ^{142}Nd of 0 ± 1.3 ppm (95% conf.int.; yellow line and yellow shaded area). A student´s t-test of the enriched group and the standard populations of the first and second analytical sessions resulted in t values of -6.54 and -6.89, respectively. For the fist analytical session this results in t (-6.54) < $t_{critical}$ (-2.08) and for the second analytical session this results in t (-6.89) < $t_{critical}$ (-2.06), i.e. the enriched group is statistically significantly different from the standard populations (see calculation in supplementary material 2.F). C) Comparison of our data to literature data of the Schapenburg komatiites (orange line and shaded area; Puchtel et al. 2016b) and Barberton komatiites (green line and shaded area; Caro et al. 2006, Puchtel et al. 2013). The Schapenburg komatiites have an average μ^{142}Nd of -5.0 ± 2.8 ppm (1s.d.) resembling our enriched group of samples, and the Barberton komatiites have an average μ^{142}Nd of -0.7 ± 1.7 ppm (1s.d.) resembling our modern-like group of samples, which confirms our interpretation of the involvement of two mantle sources in the formation of these rocks.

Except for two samples of the Dwalile Greenstone Remnant (AGC 45, 50) that bear resolvable negative μ^{142}Nd anomalies, two other Palaeoarchean amphibolites (AGC 222; AGC 350) from Kubuta in central Swaziland and the Mtimane River NE of Mankayane do not show any discernable offset from the modern terrestrial μ^{142}Nd value (Fig. 2.2). These two amphibolites without anomalies may constitute end members during complex

crustal assimilation and mixing processes, involving melts derived from older Ngwane gneiss basement as suggested by Hoffmann et al. (2016) for the 3.48-3.43 Ga Tsawela gneiss suite. Hence, the most negative μ^{142}Nd values in the Ngwane and Tsawela gneisses may still represent intermediate values, provided that the two modern-like amphibolites measured in this study are indeed representatives of juvenile mafic melts. Unfortunately, these two amphibolites are infolded in the Ngwane gneiss, and intrusive relationships between the two components are not preserved at these localities.

For the Dwalile Greenstone Remnant, Kröner and Tegtmeyer (1994) reported initial ε^{143}Nd data for amphibolites, hornblende-schists, and metasediments ranging from positive to negative $\varepsilon^{143}Nd_{(t)}$ values that are in agreement with variable degrees of crustal contamination as well as incorporation of older crustal detritus in sedimentary rocks of the belt. Moreover, inherited zircon grains, up to 3.7 Ga in age, were reported in the gneissic basement structurally below the Dwalile Geenstone Remnant (Kröner and Tegtmeyer 1994), indicating an older felsic crustal basement. So far, there are no detailed studies on the geochemical composition of the AGC mafic rocks, but we consider crustal contamination of our two amphibolite samples from Dwalile as unlikely, on the basis of flat trace element patterns and depleted to chondritic Hf-Nd isotopic compositions. The observed negative μ^{142}Nd anomalies of Dwalile samples AGC 45 and AGC 50 may thus be representative of the tapped mantle source. Interestingly, enriched (i.e., negative) μ^{142}Nd and μ^{182}W deviations have been reported for komatiites of the 3.55 Ga Schapenburg Greenstone remnant ca. 65 km away (Puchtel et al. 2016b). These signatures were interpreted by the authors as being of mantle origin, likely related to fractionation processes involving Ca-Mg perovskite in an early magma ocean. Decoupling of ^{142}Nd and ^{143}Nd systematics in Schapenburg komatiites with mean negative μ^{142}Nd (μ^{142}Nd = -5 ± 2.8 ppm) and positive ε^{143}Nd (ε^{143}Nd = +2.4 ± 0.1) was interpreted to reflect a melt depletion event within the source of the komatiites at the end of the lifetime of ^{146}Sm at ca. 4027 Ma. Hence, both the mafic precursor rocks of AGC crust and the mantle-derived rocks in the Schapenburg area may have tapped the same mantle reservoirs.

2.6.3 Relation between the Ancient Gneiss Complex and the Barberton Greenstone Belt

The AGC is tectonically separated from the supracrustal BGB by the Phoponyane shear zone northwest of Pigg´s Peak town, possibly indicating that the two terranes were

originally separated and amalgamated either around 3.3 to 3.2 Gyr (De Ronde and De Wit, 1994) or around 3.55 to 3.42 Gyr ago (Kröner et al., 1996). In contrast to the AGC, the majority of rock units of the BGB terrane, namely the 3.55 to 3.53 Ga amphibolites of the lowermost Onverwacht Group as well as the 3.51 Ga Steynsdorp and 3.46 Ga Theespruit plutons, do not show any deviation in μ^{142}Nd from the terrestrial standard (Fig. 2.2). Hence, these units have not inherited a Hadean crustal or mantle reservoir that differentiated during the lifetime of ^{146}Sm. However, two samples of the lower Onverwacht Group, a 3.55 Ga felsic volcanic rock (AGC 372; Theespuit Fm.) and a 3.48 Ga meta-tholeiite (ZA-32a; Komati Fm.) show a tendency towards negative μ^{142}Nd anomalies (Fig. 2.2) that are not fully resolvable from the JNdi-1 terrestrial standard. Yet, we consider these features as being important for the interpretation of the geodynamic setting in which the BGB formed.

Kröner et al. (2013, 2016) proposed that the felsic metavolcanic rocks of the lower Onverwacht Group originated from interaction of an older crustal source with juvenile, underplated material. These authors based their conclusions on heterogeneous Hf isotope compositions in zircons and calculated crustal model ages for the precursor ranging from 3.60 to 3.95 Ga. However, the negative μ^{142}Nd signature (μ^{142}Nd = -5.6 ± 4.4 ppm) of the felsic volcanic rock (AGC 372) investigated in this study is not very pronounced, and it is likely that the ca. 3.60 to 3.95 Ga precursors only carried a diluted Hadean isotope signature because they formed after the lifetime of ^{146}Sm. Such a model would be in agreement with the contribution of AGC-like basement beneath the lower Onverwacht Group as a source for felsic volcanism within the BGB. This hypothesis is also supported by ca. 3.7 Ga inherited zircon grains reported from Theespruit felsic volcanic rocks (Roerdink et al. 2016) and from the adjacent 3.2 Ga Vlakplaats pluton (Kröner et al. 1996). Therefore, it is likely that felsic volcanic rocks of the BGB were initially fed by magma chambers that are elsewhere represented by second generation granitoids such as the Tsawela gneiss suite that carry a diluted Hadean μ^{142}Nd signature, as they are exposed at crustal levels of the AGC (Hoffmann et al. 2016).

Another interesting observation of this study is the tendency towards negative μ^{142}Nd in the younger meta-tholeiite sample of the ca. 3.48 Ga Komati Formation (sample ZA 32a) with a μ^{142}Nd value of -5.4 ± 4.3 ppm (Fig. 2.2). Previous studies focused exclusively on komatiites from the Barberton type locality and from the 3.26 Ga Weltevreden Fm. that do not preserve any resolvable μ^{142}Nd deviation (Caro et al. 2006; Puchtel et al. 2016b). Yet, initial ε^{176}Hf and initial ε^{143}Nd compositions for rocks from the

Komati Fm. are predominantly positive, showing no evidence of contamination by older crust (Blichert-Toft and Arndt 1999; Blichert-Toft et al. 2015). In contrast, trace element compositions of some spinifex-textured komatiites of the Komati Fm. were interpreted to reflect contamination with older continental crust (Robin-Popieul et al. 2012). The flat trace element pattern (La_{CN}/Yb_{CN} = 1.6) as well as the juvenile to slightly depleted Hf-Nd isotope signature of meta-tholeiite ZA 32a ($\varepsilon Hf_{(t)}$ of 2.6 and $\varepsilon Nd_{(t)}$ of 0.3; supplementary material 2.A) are not in agreement with crustal contamination. Hence, two different mantle reservoirs may have been tapped by Komati Fm. magmas producing komatiites with modern-like $\mu^{142}Nd$ on the one side and tholeiites with negative $\mu^{142}Nd$ on the other side. These two mantle reservoirs possibly reflecting mixing between ascending mantle plume magmas and ambient upper mantle or lithospheric mantle (e.g., Sossi et al. 2016, and references therein) that bear a small ^{142}Nd deficit.

2.6.4 Origin of the negative $\mu^{142}Nd$ signatures in rocks of the AGC and BGB

In Figure 2.3a, the samples investigated in this study plot in a bimodal distribution. One group comprises seven samples with no $\mu^{142}Nd$ anomalies and the other group includes ten samples having a tendency to negative $\mu^{142}Nd$ signatures. The groups may reflect derivation of two separate mantle reservoirs. Interestingly, both reservoirs must have been tapped concurrently, independent of magmatic age and lithological unit. Collectively, both $\mu^{142}Nd$ reservoirs are represented by samples spanning an age range from 3.66 Ga to 3.23 Ga (for the $\mu^{142}Nd$ = +0.4 reservoir) and 3.55 Ga to 3.22 Ga (for the negative $\mu^{142}Nd$ reservoir). Notably, both reservoirs are represented by samples of the AGC and BGB.

2.6.4.1 Origin of the negative $\mu^{142}Nd$ signatures in mantle-derived rocks

The enriched ^{142}Nd end member, as represented by the Dwalile amphibolites, was likely mantle-derived, analogous to the negative $\mu^{142}Nd$ of the Schapenburg komatiites, and interacted with differentiated AGC crust. Since some (ultra-)mafic Dwalile rocks were potentially crustally contaminated (e.g., Kröner and Tegtmeyer 1994) the measured value may thus not represent the true negative $\mu^{142}Nd$ value of the incompatible element enriched reservoir, provided that the contaminating crust had positive or modern-like $\mu^{142}Nd$. The original values for this reservoir may be represented by the mantle source tapped by the 3.55 Ga Schapenburg komatiites, which yielded negative $\mu^{142}Nd$ values as

low as -13.4 ppm compared to the terrestrial standard (Puchtel et al. 2016b; Fig. 2.3c). This may indicate that the negative μ^{142}Nd values of the Dwalile amphibolites and the Komati Fm. tholeiite may represent intermediate values which already reflect mixing between ^{142}Nd enriched and modern-like mantle reservoir end members. However, it is difficult to estimate the exact mixing parameters and whether the two reservoirs were genetically related to each other. Furthermore, when assuming a crustal end member with a negative μ^{142}Nd signature for mixing, a quantification of mixing would be even more difficult.

For mantle derived rocks, the combined use of ^{142}Nd and ^{143}Nd isotope systematics can be applied as a tool for the calculation of model ages reflecting Hadean mantle differentiation events (e.g., Harper and Jacobsen 1992; Caro et al. 2006; Rizo et al. 2011). However, for granitoids with complex histories such as those of the AGC, this method is not applicable due to multiple metamorphic resetting and mixing of the ^{147}Sm-^{143}Nd system during crustal reworking, which occurred after extinction of the ^{146}Sm-^{142}Nd system, leading to decoupling of the two systems.

As the (ultra-)mafic samples from Dwalile and the tholeiite from Barberton seem to be derived from an incompatible element enriched reservoir, it is likely that their mantle source already carried an enriched ^{142}Nd signature. Assuming that the (ultra-)mafic Dwalile rocks and the Komati Fm. tholeiite represent mantle source compositions, and provided that metamorphism did not disturb their ^{147}Sm/^{144}Nd, a minimum age for the differentiation of their mantle sources can be calculated (Figure 2.4). As shown in Figure 2.4, the mantle source from which the Dwalile komatiites and the Komati tholeiite were derived may have differentiated at 4.3 Gyr ago.

The ultimate origin of the negative μ^{142}Nd anomaly in the Dwalile komatiites and the Komati tholeiite may therefore be related to early magma ocean differentiation (e.g., Puchtel et al. 2016b). Alternatively, the mantle source could have been re-enriched in incompatible elements by recycling of Hadean protocrust back into the mantle that carried a negative μ^{142}Nd signature (Guitreau et al. 2012; Caro et al. 2017). However, it is not possible to confidently constrain which of these two possibilities is applicable to the AGC and BGB (ultra-)mafic rocks.

In summary, our study reveals that two mantle reservoirs were involved in the formation of the AGC and BGB rocks in the eastern Kaapvaal Craton that can be distinguished by means of their μ^{142}Nd signatures. The enriched ^{142}Nd reservoir likely has a minimum mantle differentiation age of ca. 4.3 Ga (Fig. 2.4), provided that

metamorphism did not disturb the $^{147}Sm/^{144}Nd$. This enriched ^{142}Nd reservoir and was incorporated into the (ultra-)mafic Dwalile and some Komati Fm. rocks since some 3.45 Gyr ago. In contrast, the modern-like reservoir is trapped in mafic AGC and BGB rocks ranging in age from 3.55 to ca. 3.40 Ga.

2.6.4.2 Origin of the negative $\mu^{142}Nd$ signatures in granitoids

Constraining the origin of the enriched ^{142}Nd signature in the AGC granitoids is similarly challenging. A direct contribution of incompatible element enriched mafic Hadean protocrust to the TTG precursors of the AGC, sporadically occurring over a time period of ca. 1 billion years, is likely. Such a process has recently been suggested for the Hudson Bay terrane by O'Neil and Carlson (2017). Alternatively, the negative $\mu^{142}Nd$ anomalies in the granitoids could also be the result of repeated re-melting of granitoid crust that inherits a negative $\mu^{142}Nd$ signature, ultimately derived from recycled incompatible element enriched Hadean protocrust, and mixing with mafic melts that formed after the extinction of ^{146}Sm. This hypothesis is based on the fact that the Nd budget would be dominated by the crustal rocks during crustal reworking. For example, the Dwalile mafic and ultramafic rocks have Nd contents of 5.56 and 8.19 ppm, respectively, whereas the Nd concentrations of the granitoids carrying the negative ^{142}Nd signature range from 12.2 to 37.5 ppm (Table S 2.1). Additionally, repeated re-melting of protocrustal material and mixing with juvenile mafic melts is indicated by a trend toward more radiogenic Hf-in-zircon isotope compositions with time in the AGC granitoids (Zeh et al. 2011; Kröner et al. 2014; Hoffmann et al. 2016; Hoffmann and Kröner in press). The ^{142}Nd isotopes in AGC granitoids are decoupled from this process and appear to be independent of age or sample locality which confirms that both the incompatible element enriched protocrustal and modern-like mantle reservoirs contributed to the formation of AGC rocks since at least the early Archean.

Collectively, the negative $\mu^{142}Nd$ signature in granitoids of the AGC is likely derived from repeated re-melting of Hadean protocrustal material. However, it cannot be resolved whether the negative $\mu^{142}Nd$ signature in this Hadean protocrustal material was ultimately derived from crust-mantle differentiation of a modern-like or from an already incompatible element enriched mantle source, comparable to the two mantle reservoirs that formed the mafic rocks of the AGC and BGB.

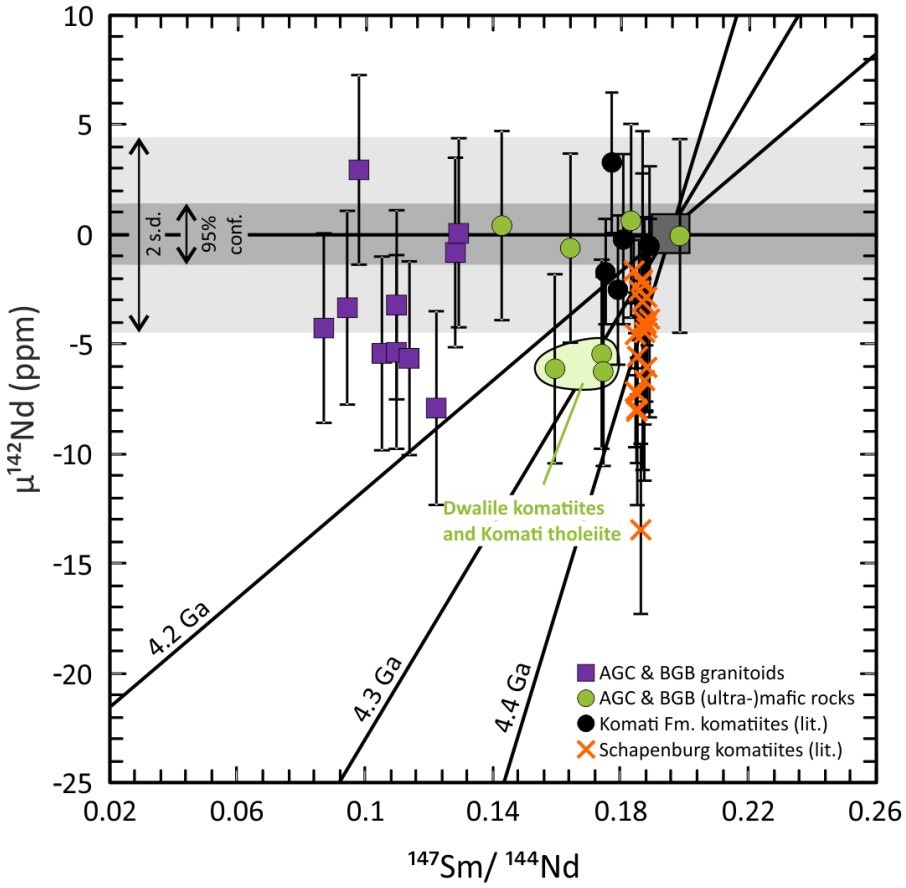

Figure 2.4: $\mu^{142}Nd$ vs. $^{147}Sm/^{144}Nd$. The Dwalile komatiites and Komati Fm. tholeiite analyzed in this study yielded a mantle source differentiation age of ca. 4.3 Ga, provided that their $^{147}Sm/^{144}Nd$ ratio was not disturbed by secondary alteration. However, given the sample uncertainties, the source differentiation age could vary between 4.1 and 4.4 Ga. The granitoids showing negative $\mu^{142}Nd$ signatures inherited a contribution from the incompatible element enriched mantle reservoir. Another group of granitoids and mafic rocks of the AGC and BGB did not tap the incompatible element enriched mantle reservoir. The dark grey square represents the chondritic Sm/Nd ratio of 0.196. The dark grey horizontal box represents the 95% confidence interval of 1.3 ppm obtained for measurements of the JNdi-1 terrestrial standard, and the light grey horizontal box represents the 2 s.d. of 4.4 ppm obtained for measurements of the JNdi-1 terrestrial standard for comparison. The figure is modified after O´Neil and Carlson (2017), who calculated reference isochrones for 4.4-, 4.3-, and 4.2-billion years old crustal reservoirs that were derived from a mantle with a chondritic Sm/Nd ratio. Literature data are from Caro et al. (2006), Puchtel et al. (2013, 2016b).

2.6.5 Worldwide sources of early enriched and depleted ^{142}Nd signatures through time

Decreasing negative and positive Hadean $\mu^{142}Nd$ anomalies through time (Figure 2.5a,b) have been interpreted to represent increasing homogenization of early differentiated reservoirs (e.g., Boyet and Carlson 2005; Caro et al. 2006; Bennett et al. 2007; Rizo et al. 2012). However, it is ambiguous as to whether this homogenization of early-differentiated reservoirs is only seen in mantle-derived rocks through time or also in

the stabilized cratons. Figure 2.5a shows all published $\mu^{142}Nd$ data for rocks directly derived from mantle melts, and Figure 2.5b depicts $\mu^{142}Nd$ data for felsic crustal rocks with ages of ca. 4.3 to ca. 2.65 Ga. The compilation of all published data in Figure 2.5a indicates that enriched and depleted ^{142}Nd mantle reservoirs were only partially homogenized by 2.65 Ga and that incompatible element enriched and depleted sources were, in fact, tapped by mantle-derived rocks throughout the Archean. Felsic crustal rocks, however, can preserve the anomaly over longer time scales than mafic-ultramafic rocks since they are reworked from older rocks that share enriched or depleted ^{142}Nd signatures ultimately derived from stabilized mafic precursors (e.g., Roth et al. 2014a; O'Neil and Carlson 2017). Alternatively, the signatures in felsic rocks may indicate protocrustal material that was recycled back into the mantle (Guitreau et al. 2012; Caro et al. 2017). In the former case, enriched or depleted ^{142}Nd signatures are tapped directly from a Hadean protocrust, whereas in the latter case the ^{142}Nd anomalies are traced by basaltic crust that was formed by re-enriched mantle material. Our study on the eastern Kaapvaal Craton reveals that ancient incompatible element enriched mantle reservoirs were likely present until at least 3.45 Ga, as represented by the Dwalile amphibolites, thus confirming earlier studies from Greenland (Rizo et al. 2012) and Schapenburg (Puchtel et al. 2016b), as well as Acasta where the most negative $\mu^{142}Nd$ values are found in samples with low SiO_2 (Roth et al. 2014a). Further melting of such mafic material, as well as of older felsic crust, incorporated negative $\mu^{142}Nd$ signatures in crustal rocks of the AGC until at least 3.22 Ga. This indicates that re-mixing of components containing inherited enriched ^{142}Nd crustal or mantle reservoirs in the eastern Kaapvaal Craton lasted for more than 1 Gyr from the initial differentiation events in the Hadean at ca. 4.3 Ga to the Mesoarchean at about 3.2 Ga.

Our study reveals that crustal nuclei may have tapped two different mantle sources – one modern-like and one incompatible element enriched source – that were present throughout most of the Archean. Mixing between the two sources may have taken place, but cannot be resolved by our dataset (Fig. 2.5a,b). Nevertheless, the large range in complementary enriched and depleted ^{142}Nd isotope signatures in other Archean cratons such as in Canada or Greenland (Fig. 2.5a) possibly reflects multiple mantle reservoirs that may have mixed with each other instead of preserving single-stage processes, i.e., direct tapping of Hadean crustal or mantle material.

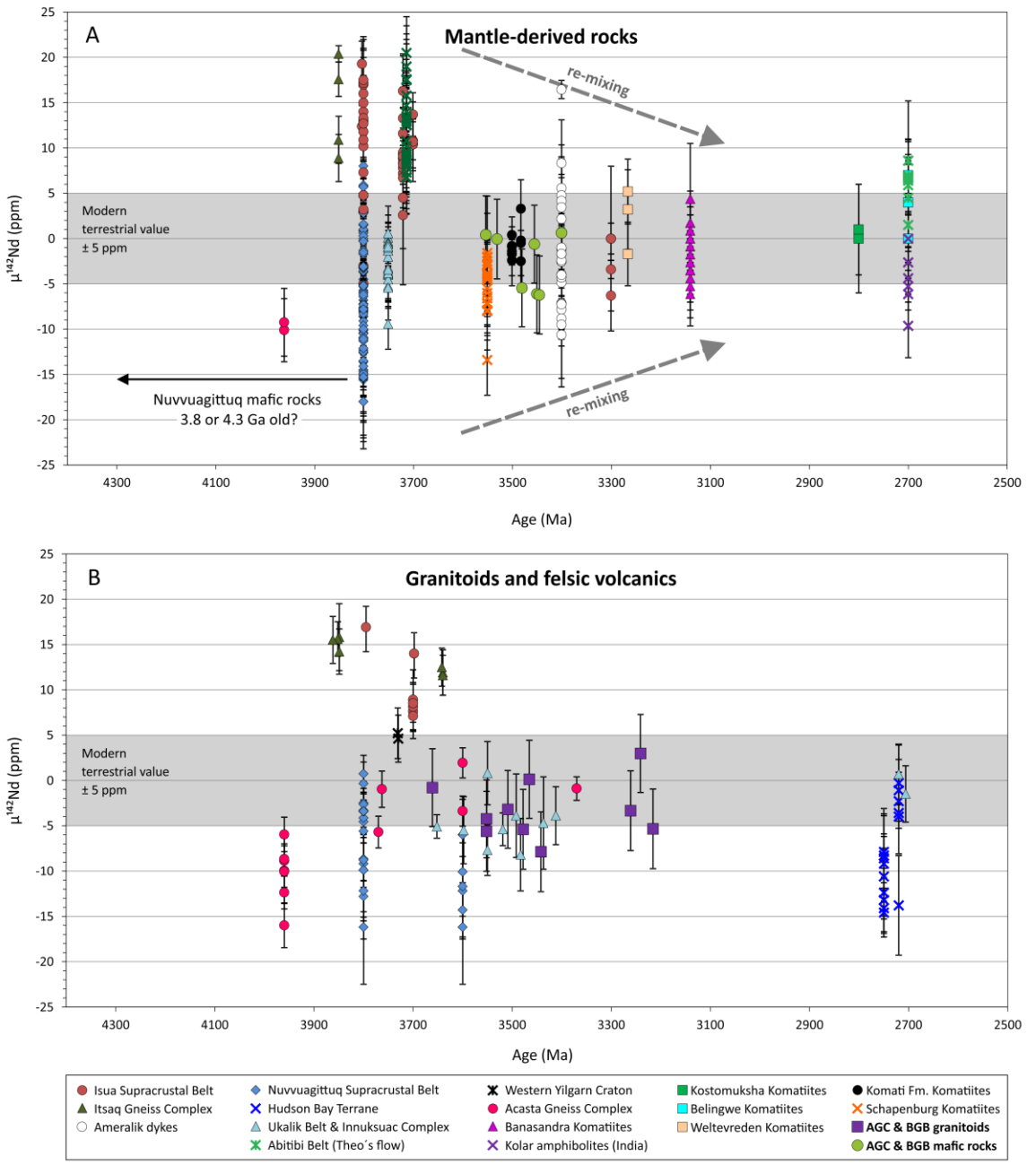

Figure 2.5: Compilation of published μ^{142}Nd data against age for Archean cratons worldwide, including literature and our data for the Kaapvaal Craton. A) Mantle-derived rocks against age. B) Granitoid rocks against age. The compiled μ^{142}Nd anomalies for mantle-derived rocks indicate re-mixing of reservoirs with positive and negative μ^{142}Nd signatures with time. A similar trend is overserved for the granitoids, but the mechanism may be different for different tectonic environments (see text). The age of mafic Nuvvuagittuq rocks is currently under debate. References: Boyet and Carlson 2006; Caro et al. 2006, 2017; Bennett et al. 2007; O`Neil et al. 2008, 2012, 2016; Rizo et al. 2011, 2012, 2013; Debaille et al. 2013; Puchtel et al. 2013, 2016b; Roth et al. 2013, 2014a; Maya et al. 2016; O´Neil and Carlson 2017.

2.7 Conclusions

We report the first high-precision $^{142}Nd/^{144}Nd$ analyses for well characterized granitoids and meta-tholeiites (amphibolites) of the Ancient Gneiss Complex (Swaziland) and the lower Onverwacht Group of the Barberton Greenstone Belt (South Africa). Our study reveals that representative well-preserved crustal and mantle-derived rocks of the AGC and BGB show variable $\mu^{142}Nd$ values ranging from -7.9 ± 4.4 ppm to +3.0 ± 4.3 ppm. As reflected by their $^{142}Nd/^{144}Nd$ isotope compositions, two different mantle reservoirs must have been involved in crust-forming processes between 3.66 and 3.22 Ga. The metamorphic rocks that sample these two reservoirs are indistinguishable in terms of age, lithology or sample locality. Instead, the two mantle reservoirs can be distinguished by means of their $\mu^{142}Nd$ signatures. Negative $\mu^{142}Nd$ anomalies indicate the involvement of an early-enriched mantle reservoir in the formation of the AGC that differentiated in the Hadean during the lifetime of ^{146}Sm. This incompatible element enriched mantle reservoir likely formed by Ca-Mg-perovskite fractionation in the early magma ocean, analogous to the Schapenburg mantle source, and was likely reworked throughout the Archean. This mantle source possibly differentiated at ca. 4.3 Ga. The presence of negative $\mu^{142}Nd$ anomalies in mantle-derived rocks as late as 3.45 Ga confirms the presence of enriched ^{142}Nd reservoirs in the Paleoarchean mantle. Reworking of crustal rocks by re-melting of incompatible element enriched mantle-derived protocrust may have transferred the enriched signature to granitoids of the AGC that are as young as 3.22 Ga. Parallel to AGC crust that was derived from incompatible element enriched mantle domains, other mantle-derived rocks and complementary granitoids of the AGC and the BGB were derived from mantle domains that do not show evidence for early differentiation events during the lifetime of ^{146}Sm. Our finding of enriched and modern-like mantle reservoirs by means of ^{142}Nd in the Kaapvaal Craton raises the question of whether other Archean cratons such as in West Greenland, Canada or Western Australia underwent a similar complex reservoir mixing history instead of single-stage processes. Such parallel behavior of enriched and depleted ^{142}Nd mantle and crustal domains may have played a more pronounced role in the formation of Archean cratons around the world than previously thought.

2.8 Acknowledgements

JEH and KS thank the Deutsche Forschungsgemeinschaft (DFG) for financial support through grants HO4697/1-1 and HO4697/1-2. AK acknowledges DFG grant KR590/92-1. CM acknowledges funding by DFG grants Mu 1406/8 and Mu 1406/18. MB thanks the Excellence initiative N° ANR-10-LABX-0006, the Région Auvergne, the European Regional Development. We thank Tsuyoshi Iizuka and a second anonymous reviewer for their constructive and helpful comments that improved our manuscript. We thank Monika Feth for laboratory support and Alexander Balduin for help with sample preparation and the geological map. KS thanks the LMV in Clérmont-Ferrand for hospitality during her visit for analytical work. This is a contribution to the SPP1833 Project '*Building a habitable Earth*' funded by the DFG. This project has received funding from the European Union´s Horizon 2020 research and innovation program under Grant Agreement N° 682778.

2.9 Supplementary information

Supplement 2.A: Summary of major and trace element as well as Sm-Nd and Lu-Hf isotope data.

	Ancient Gneiss Complex								
Sample	**AGC 150b[a]**	**AGC 370[a]**	**AGC 75[b]**	**AGC 50[c]**	**AGC 350[#]**	**AGC 45[c]**	**AGC 352[b]**	**AGC 222[b]**	**AGC 368[#]**
Lithology	grey gneiss	tonalite	tonalitic gneiss	meta-komatiite	foliated metagabbro	amph. - komatiitic balsalt	grey gneiss	amphibolite	granodiorite
Age (Ma)	3661	3552	3478	3458	3455	3445	3442	>3400	3261
Formation	Ngwane Gneiss (Piggs Peak)	Piggs Peak	Tsawela Gneiss	Dwalile	Mtimane River	Dwalile	Ngwane Gneiss	Kubuta	Usutu Suite
Major elements (wt.%)									
SiO_2	69.7	78.1	63.5	49.6	55.4	49.1	70.1	46.8	64.9
TiO_2	0.39	0.16	0.58	0.46	1.08	0.77	0.49	1.66	0.79
Al_2O_3	12.6	12.4	15.9	4.56	15.0	9.76	14.7	14.6	16.7
Fe_2O_3	5.69	1.47	5.71	6.14	9.89	3.18	4.19	15.4	5.45
FeO	-	-	-	7.04	n.d.	9.98	-	-	n.d.
MnO	0.07	0.04	0.09	0.25	0.13	0.24	0.06	0.20	0.06
MgO	2.43	0.450	3.07	23.3	6.38	15.3	1.48	7.16	1.59
CaO	1.41	1.22	5.35	8.40	7.00	9.80	2.49	10.9	4.25
K_2O	2.54	1.64	1.50	0.03	1.46	0.09	1.44	2.11	1.19
Na_2O	1.71	4.78	4.14	0.13	3.49	1.35	4.92	0.80	4.83
P_2O_5	0.09	0.04	0.12	0.05	0.16	0.12	0.13	0.30	0.26
Trace elements (µg/g)				*					
Li	241	-	45.1	-	17.2	-	14.0	12.2	n.d.
Sc	4.82	1.72	12.2	16.6	25.2	25.5	5.91	41.0	n.d.
V	21.6	-	96.3	116	152	225	54.8	404	n.d.
Cr	17.5	6.70	73.4	1891	205	1765	28.8	127	n.d.
Co	11.1	4.32	21.0	-	41.6	90.0	10.6	62.1	n.d.
Ni	12.2	18.3	60.4	1231	139	403	17.9	127	n.d.
Cu	109	-	37.9	54.8	25.3	51.0	3.09	100	n.d.
Zn	164	-	65.9	86.0	125	121	77.7	121	n.d.
Ga	23.5	-	18.6	-	22.8	-	20.7	18.8	n.d.
Rb	229	61.5	76.9	4.98	56.3	10.0	38.5	69.4	n.d.
Sr	121	215	393	24.6	418	23.0	595	143	n.d.
Y	59.4	4.5	15.5	8.57	39.5	22.0	16.2	27.4	n.d.
Zr	340	134	147	40.4	139	66.0	176	-	n.d.
Nb	33.8	6.57	6.95	2.02	9.34	5.00	6.95	3.90	n.d.
Mo	-	-	1.19	-	0.170	-	0.254	0.304	n.d.
Cd	-	-	0.124	-	0.200	-	0.132	0.167	n.d.
Sn	-	-	-	-	1.69	-	1.55	0.370	n.d.
Sb	-	-	0.0612	-	0.0400	-	0.0689	0.0691	n.d.
Cs	21.2	-	1.19	2.16	0.850	3.91	0.760	2.67	n.d.
Ba	537	633	296	6.79	234	-	376	45.0	n.d.

Supplement 2.A continued.

	Ancient Gneiss Complex								
Sample	**AGC 150b[a]**	**AGC 370[a]**	**AGC 75[b]**	**AGC 50[c]**	**AGC 350[#]**	**AGC 45[c]**	**AGC 352[b]**	**AGC 222[b]**	**AGC 368[#]**
Trace elements (µg/g)									
La	51.2	20.8	28.2	3.84	12.2	4.06	20.1	5.30	n.d.
Ce	93.8	40.8	56.9	9.05	32.7	10.8	36.5	13.8	n.d.
Pr	11.2	3.49	6.45	1.24	4.97	1.72	4.65	2.06	n.d.
Nd	41.8	12.2	24.0	5.56	24.1	8.19	18.1	10.2	n.d.
Sm	8.88	1.55	4.16	1.50	6.54	2.36	3.73	3.06	n.d.
Eu	1.37	0.760	1.14	0.404	1.66	0.700	1.04	1.25	n.d.
Gd	9.15	1.22	3.77	1.70	7.02	2.82	3.37	4.01	n.d.
Tb	1.55	0.150	0.492	0.269	1.15	0.490	0.510	0.690	n.d.
Dy	9.88	0.880	2.70	1.60	7.10	3.42	2.96	4.58	n.d.
Ho	2.04	0.160	0.525	0.321	1.41	0.760	0.580	0.970	n.d.
Er	5.76	0.440	1.45	0.916	3.81	2.3	1.60	2.72	n.d.
Tm	0.83	0.070	0.221	0.130	0.54	0.311	0.229	0.406	n.d.
Yb	5.24	0.460	1.45	0.826	3.39	1.87	1.49	2.68	n.d.
Lu	0.760	0.080	0.227	0.117	0.488	0.360	0.222	0.418	n.d.
Hf	9.65	3.39	3.64	0.975	3.15	1.91	4.47	2.02	n.d.
Ta	2.54	0.420	0.459	0.138	0.483	0.263	0.544	0.230	n.d.
W	-	-	0.142	-	0.250	-	0.144	2.306	n.d.
Tl	-	-	0.39	-	0.280	-	0.285	0.331	n.d.
Pb	9.60	10.6	6.03	0.551	3.94	0.379	4.78	5.17	n.d.
Th	14.5	3.00	4.01	0.520	0.680	0.476	3.86	0.440	n.d.
U	3.73	0.980	0.743	0.135	0.260	0.125	0.625	0.153	n.d.
Isotopic composition				*				#	
Sm (µg/g)	9.01	1.97	3.80	1.36	6.09	2.21	3.71	2.85	4.90
Nd (µg/g)	42.5	13.7	21.8	5.16	22.4	7.68	18.4	9.41	30.2
$^{147}Sm/^{144}Nd$	0.1280	0.0868	0.1050	0.1592	0.1642	0.1743	0.1220	0.1830	0.0979
$^{143}Nd/^{144}Nd_0$	0.511019	0.510137	0.510548	0.511775	0.511922	0.512138	0.511004	0.512410	0.510422
±	14	13	11	9	10	9	16	8	8
$\varepsilon^{143}Nd_{(t)}$	0.72	1.44	0.22	-0.30	0.50	0.05	1.15	1.62	-1.85
Lu (µg/g)	0.778	0.0988	0.216	0.120	0.488	0.289	0.222	0.414	0.157
Hf (µg/g)	8.39	4.47	3.64	0.952	3.12	1.74	4.47	2.22	7.18
$^{176}Lu/^{177}Hf_0$	0.0132	0.00314	0.00843	0.0179	0.0222	0.0236	0.00705	0.0265	0.0031
$^{176}Hf/^{177}Hf_0$	0.281410	0.280755	0.281164	0.281786	0.282105	0.282186	0.281174	0.282472	0.280896
±	7	7	5	22	5	10	6	7	7
$\varepsilon Hf_{(t)}$	2.53	2.09	2.41	1.70	2.80	2.33	5.39	6.00	0.92
Sm/Nd	0.212	0.143	0.174	0.264	0.272	0.288	0.202	0.302	0.162

Supplement 2.A continued.

	Ancient Gneiss Complex		Barberton Greenstone Belt					
Sample	**AGC 473[#]**	**AGC 445[#]**	**KS-BA 189[#]**	**AGC 372[d]**	**BA 156[#]**	**BA 132[#]**	**ZA-32a[#]**	**BA 128[e]**
Lithology	throndhjemitic gneiss	grey gneiss	tholeiitic basalt	felsic volcanic rock	amph. - tholeiitic pillow basalt	throndhjemite	tholeiite	tonalitic gneiss
Age (Ma)	3241	3216	3553	3552	3530	3509	3480	3465
Formation	Dwalile	Piggs Peak	Sandspruit Fm	Theespruit Fm.	Theespruit Fm.	Steynsdorp Pluton	Komati Fm.	Theespruit Pluton
Major elements (wt.%)								
SiO_2	68.7	58.0	52.1	62.8	53.7	71.9	53.2	69.1
TiO_2	0.49	1.15	0.50	0.80	0.96	0.30	0.77	0.27
Al_2O_3	16.4	18.4	13.8	17.0	13.9	15.3	12.1	15.0
Fe_2O_3	3.18	7.46	10.6	5.76	11.8	2.59	11.6	2.95
FeO	n.d.	n.d.	n.d.	-	n.d.	n.d.	n.d.	-
MnO	0.04	0.08	0.16	0.08	0.18	0.05	0.19	0.03
MgO	0.86	1.93	10.0	2.05	6.20	0.57	8.94	1.35
CaO	2.96	5.76	10.3	4.91	10.8	2.24	9.65	2.79
K_2O	1.76	1.59	0.54	3.17	0.04	2.10	0.17	1.47
Na_2O	5.50	5.31	1.81	3.16	2.39	4.94	3.27	5.35
P_2O_5	0.15	0.35	0.08	0.24	0.09	0.06	0.09	0.09
Trace elements (µg/g)								
Li	63.4	178	n.d.	-	7.55	111	5.76	41.0
Sc	2.10	3.27	30.3	-	35.9	1.86	27.1	3.47
V	27.2	104	165	-	326	14.9	218	62.5
Cr	7.97	4.10	n.d.	-	147	5.16	691	438
Co	5.23	15.7	58.6	-	46.1	3.00	52.1	7.76
Ni	3.80	5.23	n.d.	-	101	4.09	173	39.8
Cu	10.5	37.9	67.4	-	155	8.16	123	4.86
Zn	68.4	128	74.5	-	83.5	48.5	74.4	50.0
Ga	21.0	22.9	12.7	-	15.2	20.2	11.4	18.2
Rb	28.8	50.6	n.d.	-	0.416	33.0	2.71	53.1
Sr	367	499	182	-	116	312	198	574
Y	11.2	11.7	16.7	-	23.2	13.4	18.5	5.93
Zr	183	218	65.5	-	62.5	170	66.5	131
Nb	8.85	9.25	3.10	-	2.65	9.20	3.66	4.68
Mo	0.243	0.565	0.513	-	0.272	0.117	0.336	-
Cd	0.157	0.325	0.0949	-	n.d.	0.155	0.111	-
Sn	1.77	3.52	0.568	-	0.164	0.184	0.623	-
Sb	0.0367	0.0442	n.d.	-	0.220	0.295	0.0631	-
Cs	2.46	13.8	n.d.	-	0.116	6.38	0.272	2.58
Ba	384	446	89.1	-	24.3	479	53.9	322

Supplement 2.A continued.

	Ancient Gneiss Complex		Barberton Greenstone Belt					
Sample	**AGC 473[#]**	**AGC 445[#]**	**KS-BA 189[#]**	**AGC 372[d]**	**BA 156[#]**	**BA 132[#]**	**ZA-32a[#]**	**BA 128[e]**
Trace elements (µg/g)								
La	28.8	37.3	8.71	-	3.28	19.6	4.40	9.02
Ce	37.8	47.6	18.0	-	8.87	25.4	11.34	16.2
Pr	6.20	9.21	2.22	-	1.38	4.11	1.66	2.00
Nd	23.2	37.5	9.08	-	7.21	15.2	7.94	8.20
Sm	4.02	6.80	2.18	-	2.38	2.91	2.29	1.82
Eu	1.07	1.90	0.600	-	0.887	0.735	0.756	0.64
Gd	3.14	5.26	2.52	-	3.17	2.58	2.84	1.59
Tb	0.391	0.626	0.405	-	0.570	0.390	0.496	0.21
Dy	1.92	2.70	2.71	-	3.90	2.29	3.28	1.15
Ho	0.337	0.390	0.586	-	0.836	0.454	0.688	0.21
Er	0.865	0.857	1.69	-	2.38	1.29	1.94	0.57
Tm	0.119	0.103	0.255	-	0.364	0.193	0.290	0.0810
Yb	0.725	0.611	1.68	-	2.43	1.30	1.92	0.51
Lu	0.101	0.0844	0.251	-	0.356	0.221	0.298	0.0720
Hf	4.48	5.23	1.78	-	1.61	4.34	1.63	3.23
Ta	0.786	0.486	0.202	-	0.165	0.921	0.216	0.400
W	0.120	0.293	0.294	-	0.127	0.392	0.105	-
Tl	0.402	0.631	n.d.	-	0.0361	0.336	0.0280	-
Pb	9.87	9.69	2.43	-	0.552	6.795	0.707	7.33
Th	4.71	4.75	1.43	-	0.252	3.73	0.403	1.88
U	0.838	2.55	0.203	-	0.0868	0.705	0.101	-
Isotopic composition								
Sm (µg/g)	4.93	6.80	1.99	6.16	2.14	3.44	2.10	1.85
Nd (µg/g)	30.5	37.5	8.42	32.8	6.54	18.9	7.31	8.67
$^{147}Sm/^{144}Nd$	0.0978	0.1095	0.1426	0.1135	0.1983	0.1097	0.1738	0.1290
$^{143}Nd/^{144}Nd_0$	0.510545	0.510736	0.511431	0.510660	0.512728	0.510609	0.512134	0.511105
±	6	7	7	9	7	13	8	20
$\varepsilon^{143}Nd_{(t)}$	-1.00	-1.10	1.13	-0.62	0.87	-0.40	0.29	0.20
Lu (µg/g)	0.111	0.0840	0.257	0.393	0.368	0.221	0.295	0.0766
Hf (µg/g)	4.62	5.23	1.77	5.55	1.69	4.27	1.70	3.68
$^{176}Lu/^{177}Hf_0$	0.00343	0.00229	0.0206	0.0100	0.0310	0.00735	0.0246	0.00296
$^{176}Hf/^{177}Hf_0$	0.280894	0.280854	0.281991	0.281139	0.282689	0.281014	0.282255	0.280738
±	7	11	11	6	6	5	5	7
$\varepsilon Hf_{(t)}$	-0.30	0.23	3.50	-1.07	2.98	-4.30	2.60	0.10
Sm/Nd	0.162	0.181	0.236	0.188	0.328	0.182	0.288	0.213

[a]Kröner et al. 2014; [b]Hoffmann et al. 2016; [c]Kröner & Tegtmeyer 1994; [d]Kröner et al. 2013; [e]Sample BA 115 from Kröner et al. 2016; *AGC 50: TE and Isotopes by Hoffmann et al in prep.; [#]this study, ages: pers. comm. A. Kröner 2016; n.d. = not detected

Supplement 2.B: Sample digestion and chemical separation for $^{142}Nd/^{144}Nd$ analyses

Sample powders were digested in a mixture of concentrated HF-HNO_3 in Parr® pressure vessels for 48 hours and dried down with one additional milliliter of $HClO_4$. Subsequently, 5 ml conc. HNO_3 was added to the samples and dried down immediately. After evaporation, the samples were dissolved in 6 ml 6 N HCl overnight. After full equilibration was reached, the samples were evaporated to dryness.

For purifying Nd from the whole rock sample solutions, four chemical separations were implemented. The first separation was performed on ca. 20 cm long and 6 mm wide Teflon columns filled with AG-50W-x8 200-400 µm mesh resin. Samples were loaded in 2.5 N HCl. Major elements were eluted with 44 ml of 2.5 N HCl and heavy REE were eluted in 10 ml 4 N HCl. The remaining REE fraction was collected in 29 ml of 6 N HCl and subsequently dried down. In a second stage, the REE fraction was diluted in 0.2 ml of a mixture of 10 N HNO_3 and 20 mM $NaBrO_3$ and loaded on 12 mm long and 7 mm wide PET columns filled with 1 ml of Eichrom Ln-Spec 50-100 µm resin to remove Ce from the REE fraction. Details are given in Tazoe et al. (2007). After elution of the REE fraction, a mixture of 6 N HCl and H_2O_2 was added to the columns to reduce Ce and ensure that no Ce^{4+} is present. This chemical separation was done twice to reduce the Ce content to negligible levels. In a third step 6 cm long and 4 mm wide quartz columns filled with 300 mg of Eichrom Ln-Spec 25-50 µm resin were used to purify the Nd from all other REE. In order to do that, the samples were loaded in 0.2 ml of 0.2 N HCl. The light REE were eluted with 10.5 ml of 0.2 N HCl. Subsequently, the Nd fraction was collected in 3 ml of 0.25 N HCl. However, after checking the elemental content in the samples at the ICP-MS, some samples still showed comparatively high Ba concentrations. Consequently, a fourth separation was applied to remove Ba from the samples. For this separation, columns filled with 1 ml of AGW50-X8 200-400 µm mesh resin were used. The samples were loaded in 2.5 N HCl. The Ba was eluted with 2 N HNO_3 and the pure Nd fraction was subsequently collected in 6 N HCl. The total procedural blank determined by ICP-MS for Nd is 300 pg, The blank contribution was negligible in comparison to the Nd fractions for analyzed samples (> 500 ng).

Supplement 2.C: Calculation of 95% confidence intervals of the JNdi-1 standard sessions.

For calculation of the 95% confidence interval we used a student´s t distribution, because the quantity of analyzed JNdi-1 standards was relatively low, i.e. 13 and 17 analyses in the first and second analytical session, respectively. Therefore, the distribution of analyses of the JNdi-1 standard does likely not follow a typical Gauß normal distribution, but a so called t distribution that has broader tails and a lower peak center than a normal distribution:

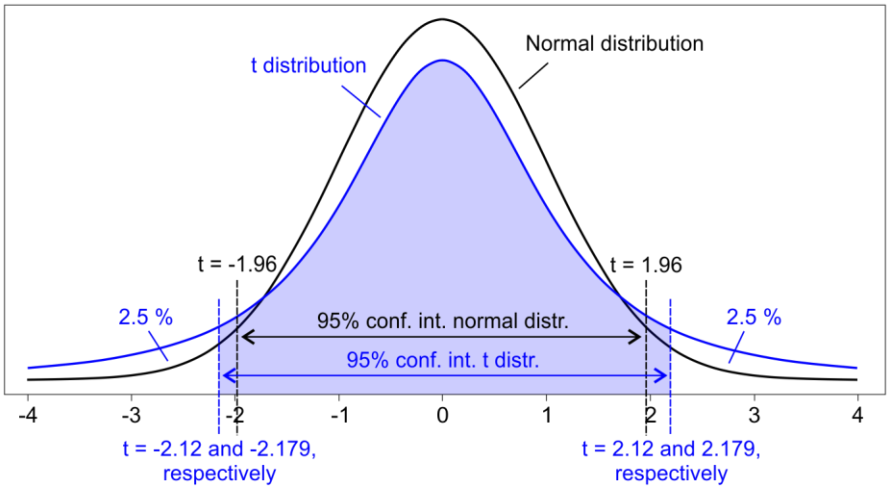

Figure 2.A: Sketch of the 95% confidence intervals of a normal (black line) and a t distribution (blue line). The t distribution has a lower peak center and broader tails than the normal distribution. As a consequence, the 95% confidence interval of the t distribution is broader, in our case at t = 2.12 (n = 17) and t = 2.178 (n = 13), than that of a normal distribution (t = 1.96 for n = 30 to ∞).

The formula for the t distribution is given as

$$\overline{x} \pm t \times \frac{s}{\sqrt{n}}$$

where $\overline{x}$ is the arithmetic mean of the JNdi-1 analyses, t is the value for the 95% confidence interval, s is the standard deviation of the JNdi-1 analyses, and n is the number of analyzed JNdi-1 standards.

For our first JNdi-1 standard session the values are: n = 13, $\overline{x}$ = 0.0 ppm, s = 2.2 ppm. The value for t can be inferred from a t table for n-1 degrees of freedom for a two-tailed distribution. In the case for the 13 analyses, so 12 degrees of freedom, we get $t_{0.025}$ = 2.179. If the values are set in the above formula we get:

$$0.0 \text{ ppm} \pm 2.179 \times \frac{2.2 \text{ ppm}}{\sqrt{13}} \approx 0.0 \text{ ppm} \pm 1.3 \text{ ppm}$$ 95% confidence interval for the first analytical session.

For the second analytical session of the JNdi-1 terrestrial standard, this calculation can be done with n = 17, $\bar{x}$ = 0.0 ppm, s = 2.14 ppm, $t_{0.025}$ = 2.12 which results in a 95% confidence interval of ± 1.10 ppm.

Supplement 2.D: Analytical methods BA 132, BA 156, ZA-32a, KS-BA 189, AGC 222, AGC 350, AGC 445, AGC 473

Samples BA 132, BA 156, KS-BA 189, ZA-32a, AGC 350, AGC 368, AGC 445, and AGC 473 were analyzed for their whole rock major element compositions by X-ray fluorescence spectrometry (XRF) on $Li_2B_4O_7$-flux fusion discs using a PANalytical Axios X-ray spectrometer at the University of Cologne, Germany (Table S 2.1). The loss on ignition (LOI) for each sample was determined by baking 1 g of rock powder in a muffle type furnace at 1000°C for 24 hours.

Samples BA 132, BA 156, KS-BA 189, ZA-32a, AGC 350, AGC 445, and AGC 473 were also analyzed for their trace element compositions. Sample powders were digested in Parr® pressure vessels in concentrated HF-HNO_3 for 72 hours and dried down with adding one milliliter of $HClO_4$. Subsequently 2 ml concentrated HNO_3 was added to the samples and dried down immediately. After evaporation to dryness, the samples were diluted in 3 % HNO_3 for trace element analysis. Samples BA 132, BA 156, and ZA-32a were analyzed at the University of Kiel, Germany, using an AGLIENT 7500cs quadrupole inductively coupled plasma mass spectrometer (ICP-MS). The analytical procedures followed Garbe-Schönberg (1993). Sample KS-BA 189 was analyzed at the Freie Universität Berlin using a Thermo Finnigan Element XR ICP-MS. Samples were diluted by dilution factors of 14000 to 64000 depending on the trace element concentrations of the samples. In order to calibrate the measured intensities of the low, middle and high masses, an internal standard solution of 1 ppb Ge-In-Re was added to the end dilution. The end dilutions were measured against a calibration curve of several dilutions of BHVO-2 ranging from 11.000- to 600.000-fold dilutions that were also doped with a 1 ppb Ge-In-Re solution. Furthermore, two REE solutions containing 1 ppb and 0.4 ppb Ba, La, Ce, Pr, Nd, and Sm were measured along with the samples in order to determine the oxide ratio that was produced within the plasma during measurements. Following this procedure, relative errors for the REEs were usually around 5 % and range from 4 to 19 % for the HFSE, LILE, and Sc, V, Cr, Co, Ni, Cu, Zn (Table S 2.1).

Samples BA 132, BA 156, KS-BA 189, ZA-32a, AGC 222, AGC 350, AGC 368, AGC 445, and AGC 473 were analyzed for their Hf and Nd isotopic compositions and Lu, Hf, Sm, Nd concentrations (Table S 2.1). The analyses were obtained by isotope dilution using mixed ^{176}Lu-^{180}Hf and ^{149}Sm-^{150}Nd tracers following the protocols of Münker et al. (2001) and Weyer et al. (2002). Measurements were carried out using a Thermo Scientific Neptune multi-collector ICP-MS at the joint facility of the Cologne and Bonn universities (Germany), operated in static mode. Chemical separation of Hf and Nd followed the procedures outlined in Pin and Zalduegui (1997) and Münker et al. (2001). Reference materials AGV-2 and BHVO-2 were measured along with the samples to determine the accuracy of the results.

Measured values of ^{176}Hf/^{177}Hf and ^{143}Nd/^{144}Nd were corrected for mass fractionation using the exponential law and ^{179}Hf/^{177}Hf = 0.7325 and ^{146}Nd/^{144}Nd = 0.7219, respectively. All values are given relative to a ^{176}Hf/^{177}Hf of 0.282160 for the AMES solution that is isotopically indistinguishable from JMC-475, and relative to a ^{143}Nd/^{144}Nd of 0.511859 for the La Jolla Nd standard. Samples were analyzed at the same concentrations as the standards, i.e. 24 ppb for AMES and 20 ppb for La Jolla. Typical external reproducibilities for Nd and Hf isotope measurements were ±0.3 ε-units. CHUR parameters used to calculate epsilon values are from Bouvier et al. (2008).

Supplement 2.E

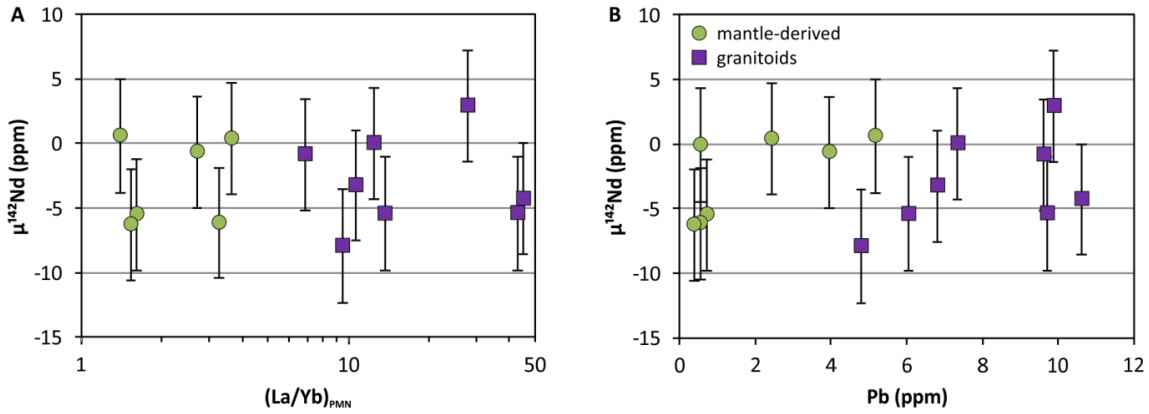

Supplement 2.E: Evaluation of metamorphic disturbance. A) μ^{142}Nd anomalies vs. $(La/Yb)_{PMN}$. B) μ^{142}Nd anomalies vs. Pb content. No correlation can be observed between the μ^{142}Nd anomalies and elevated LREE or LILE. Consequently, we assume that metamorphic effects did not disturb the μ^{142}Nd anomalies of our AGC and BGB samples.

Supplement 2.F: t-test for enriched and modern-like groups of samples

To test if our enriched and modern-like groups of samples show a statistical offset from each other, we carried out a two-sample t-test for a two-tailed t distribution. The formula for t is given as

$$t = \frac{\bar{x}1 - \bar{x}2}{\sqrt{\frac{(n1-1)*s1^2+(n2-1)*s2^2}{n1+n2-2}} * \sqrt{\frac{1}{n1}+\frac{1}{n2}}}$$

where $\bar{x}$ is the mean μ^{142}Nd anomaly of the two groups, *s* is the standard deviation of the mean of the two groups, and *n* is the number of samples in each group. We test the hypotheses H0: $\bar{x}_1 = \bar{x}_2$ or H1: $\bar{x}_1 \neq \bar{x}_2$.

The values for the enriched group are: $\bar{x}_1$ = -5.3 ppm, n_1 = 10, s_1 = 2.8 ppm (2s.d.), and the values for the modern-like group are: $\bar{x}_2$ = 0.4 ppm, n_2 = 7, s_2 = 2.5 ppm (2s.d.). If we set these values in the formula above, we get t = -4.31. Our calculated t value has to be compared with $t_{critical}$, which can be inferred from the t table for 15 degrees of freedom (i.e. 7+10-2 = 15) and is ±2.131 for a two-tailed distribution at a 95% confidence interval. As a result t (-4.31) < $t_{critical}$ (-2.131), which means that the H1 hypothesis is valid and our enriched and modern-like groups of samples show a statistical offset from each other.

The same t-test can be carried out for the enriched group of samples compared to the first and second analytical sessions of the JNdi-1 terrestrial standard. The values for the enriched group are as stated above, and the values for the first analytical JNdi-1 session are $\bar{x}_2$ = 0.0 ppm, n_2 = 13, s_2 = 4.4 ppm (2s.d.). Applied in the formula for t, we get t = -6.54. Compared to a $t_{critical}$ of ±2.080 (21 degrees of freedom), a statistically significant offset between the enriched group of samples and the first analytical JNdi-1 session can be observed.

This calculation can be done analogous for the second analytical session of the JNdi-1 standard. The values are $\bar{x}_2$ = 0.0 ppm, n_2 = 17, s_2 = 4.3 ppm (2s.d.) and applied in the above formula for t, this results in a t value of -6.89. Compared to a $t_{critical}$ of ±2.060 (25 degrees of freedom), a statistically significant offset between the enriched group of samples and the second analytical JNdi-1 session can be observed.

Chapter 3

Petrogenetic evolution of metabasalts and metakomatiites of the lower Onverwacht Group, Barberton Greenstone Belt (South Africa)

3.1 Abstract

A well-preserved sequence, by Archean standards, of mantle-derived metabasalts and metakomatiites forms large parts of the lower Onverwacht Group of the Barberton Greenstone Belt (South Africa). To elucidate the origin of mafic and ultramafic rocks from this 3.55 to 3.45 Ga sequence, we present a comprehensive geochemical dataset including major and trace elements as well as Lu-Hf and Sm-Nd isotope compositions for a variety of metavolcanic rocks. These include metabasalts of the amphibolite-facies Sandspruit and Theespruit Formations as well as metabasalts and metakomatiites of the lower greenschist-facies Komati Formation.

Based on their incompatible trace element patterns, the basalts of the Sandspruit and Theespruit Formations can be subdivided into a light rare earth element (LREE) depleted group, a LREE-undepleted group, and a LREE-enriched group. Positive $\varepsilon Hf_{(t)}$ and $\varepsilon Nd_{(t)}$ values of ca. +3 to +4 and 0 to +2, respectively, together with depletions in Th and La_{CN}/Yb_{CN} indicate derivation of the LREE-depleted basalts from a depleted mantle source. However, chondritic $\varepsilon Hf_{(t)}$ and $\varepsilon Nd_{(t)}$ values combined with positive Th and La_{CN}/Yb_{CN} of the LREE-enriched samples indicate a contribution from older granitoid crust in the petrogenesis of these samples.

Trace element patterns of komatiites and basalts of the Komati Formation are generally flat relative to primitive mantle with slight depletions in heavy rare earth elements and Th and overall positive $\varepsilon Hf_{(t)}$ of +2.5 ± 3.5 (2s.d.) and $\varepsilon Nd_{(t)}$ of +0.5 ± 2.2 (2s.d.). The coherence in trace element characteristics suggests a common magmatic origin for basalts and komatiites. However, this study reveals that the two lavas were derived from different sources, i.e. komatiites were formed by high degrees of melting of a depleted mantle source containing residual garnet in a plume setting and the basalts were formed by low-degree partial melting of the upper mantle.

Based on the current dataset, combined with published data, we propose a geodynamic model for the oldest units of the Barberton Greenstone Belt that describes the development from a submerged continental setting (for the Sandspruit and Theespruit Formations) to an oceanic setting (for the Komati Formation) as a consequence of continental rifting.

This chapter is in revision with *Chemical Geology* as

Schneider, K.P.[1,2,3], Hoffmann, J.E.[1], Münker, C.[2,3], Patyniak, M.[4], Sprung, P.[2,3], Roerdink, D.[5], Garbe Schönberg, D.[6], Kröner, A.[7,8]

[1]Institut für Geologische Wissenschaften, Freie Universität Berlin, Germany

[2]Institut für Geologie und Mineralogie, Universität zu Köln, Germany

[3]Steinmann Institut für Geologie, Mineralogie und Paläontologie, Rheinische Friedrich-Wilhelms Universität Bonn, Germany

[4]Institute of Earth and Environmental Sciences, University of Potsdam, Germany

[5]Department of Earth Science, University of Bergen, Norway.

[6]Institut für Geowissenschaften, Universität Kiel, Germany

[7]Beijing SHRIMP Center, Institute of Geology, Chinese Academy of Geological Sciences, Beijing, China

[8]Institut für Geowissenschaften, Universität Mainz, Germany

3.2 Introduction

The occurrence of komatiites is mostly restricted to the Archean and early Proterozoic Eons, with two Phanerozoic exceptions including the occurrence on Gorgona Island (Echeverría 1980) and the Tortugal lavas of Costa Rica (Trela et al., 2017). Several studies have proposed that komatiite melts formed by high-degrees of mantle melting (>30%; e.g., Sun and Nesbitt 1978, Herzberg 1992) at high pressures of about 18 GPa, and temperatures exceeding 1600 °C (Green 1981; Nisbet et al. 1993; Puchtel et al. 2013). Three different types of komatiites have been recognized worldwide based on their major and trace element compositions (Sun and Nesbitt 1978; Jahn et al., 1979, 1982; Nesbitt et al., 1979): (1) Al-depleted komatiites, with low Al/Ti ratios, enriched concentrations of incompatible elements, and depletion in heavy rare earth elements (HREE); (2) Al-undepleted komatiites, having chondritic Al/Ti ratios and flat HREE patterns; and (3) Al-enriched komatiites, having high Al/Ti ratios, low concentrations of incompatible elements, enrichment in HREE, and depletion in light REE. All three types of komatiites can occur in the same volcanic sequence, possibly indicating synchronous evolution in a hot anhydrous mantle plume (Sun and Nesbitt 1978; Nesbitt et al. 1979; Jahn et al. 1982; Campbell et al. 1989; Ohtani et al. 1989; Robin-Popieul et al. 2012). In contrast, other authors (Allègre et al., 1982; Parman et al. 1997; Grove et al. 1997; Stone et al. 1997) favored a subduction origin for komatiites on the basis of the chemical composition of fresh clinopyroxene in Barberton komatiites that would indicate the presence of 3-6 wt.% of dissolved water in a komatiite melt. Conversely, more recent studies suggest that plume-sourced komatiites contained up to 0.6 wt. % of water that was possibly entrained from water-bearing minerals in the mantle transition zone (Sobolev et al. 2016; Asafov et al. 2018).

However, komatiites are volumetrically minor and represent only less than 5 % of the volcanic rocks in most Archean greenstone belts (de Wit and Ashwal 1997). Hence, the major part of Archean greenstone successions were formed by basaltic volcanism, occasionally interlayered with felsic volcanic rocks (e.g., Viljoen and Viljoen 1969a Armstrong et al. 1990; Kröner et al. 1991, 2013; Smithies et al. 2007; Van Kranendonk et al. 2007a,b). These basalts are mostly tholeiitic in composition and are interpreted to represent melts derived from moderate degrees of upper mantle melting (10-20 %; Nesbitt and Sun 1976; Jochum et al. 1991; Xie et al. 1993; Herzberg et al. 2010) or, alternatively, represent differentiates of komatiitic melts (Jochum et al. 1991; Xie et al. 1993). Hence,

tholeiitic magmatism contributed significantly to the thickening of oceanic plateaux on the early Earth (e.g., Herzberg et al. 2010).

Furthermore, all Archean greenstone successions were deposited on an older crustal basement (e.g., Campbell and Davies, 2017 and refs. therein), and evidence for interaction of primary magmas with older continental crust is thus abundant from the chemical record of greenstone belts and their zircon heritage, which occasionally reveals inheritance (e.g., Chauvel et al. 1983, 1985; Polat et al. 2005; Cattell et al. 1984; Kröner and Tegtmeyer 1994; Bolhar et al. 2002, 2003; Boily et al. 2009; Maurice et al. 2009). Thus, interaction of mantle-derived melts with early continental crust is likely to have been an important process of Archean tectonics.

In this study, we aim to characterize the geochemical composition of the mantle sources that gave rise to the mafic and ultramafic rocks of the Paleoarchean lower Onverwacht Group of the Barberton Greenstone Belt (BGB) to constrain how the formation of basalts and komatiites may be linked. Furthermore, we evaluate whether the parental mantle-derived melts interacted with older crustal material during ascent, employing Lu-Hf and Sm-Nd isotope analyses in conjunction with major and trace element compositional data on a large set of samples.

Based on field observations the lower Onverwacht Group was originally subdivided into the Sandspruit, Theespruit, and Komati Formations (Viljoen and Viljoen 1969b). However, more recent studies have shown that the Sandspruit and Theespruit Formations are geochemically and geochronologically indistinguishable (Kröner et al. 2013; 2016). Thus, the two formations are discussed as one unit in the following chapters. Based on chemical composition, the meta-tholeiites of the ca. 3.55 to 3.48 Ga amphibolite-facies Sandspruit and Theespruit Formations can be subdivided into three groups: (1) light rare earth element (LREE) depleted, (2) LREE-undepleted, and (3) LREE-enriched. Furthermore, we sampled the full compositional spectrum of mantle-derived rocks of the ca. 3.48 to 3.45 Ga greenschist-facies Komati Formation including (a) komatiites, (b) komatiitic basalts, and (c) tholeiitic basalts. From our results and a synthesis of previously published geochemical and isotopic data, we propose a petrogenetic model for the evolution of the lower Onverwacht Group.

3.3 Geological background and sample petrography

Amongst the Archean crustal exposures, the 3.55-3.20 Ga Barberton Granitoid-Greenstone terrane (BGGT), located in the eastern part of the Kaapvaal Craton of southern Africa, contains a well-preserved record, by Archean standards, of volcanic sequences and tonalite-trondhjemite-granodiorite (TTG) plutons (Anhaeusser 2014). The volcanic sequences show a wide compositional range (felsic, mafic, and ultramafic) with well constrained stratigraphical relationships (e.g., Armstrong et al. 1990; Kröner et al. 1991, 2013, 2016; Kamo and Davies 1994; Byerly et al. 1993, 1996). Two distinctive geodynamic models for the BGGT have been proposed: Formation by (1) subduction-accretion (De Wit et al. 1992, 2011, 2018; Moyen et al. 2006; Furnes et al. 2012; Cutts et al. 2013), where TTGs as well as felsic volcanic rocks were generated in a subduction setting (De Wit et al. 1992, 2011, 2018; de Ronde and Kamo 2000; Moyen et al. 2006, 2007; Schoene et al. 2008; Schoene and Bowring 2010; Furnes et al. 2012; Cutts et al. 2013), or in (2) a volcanic plateau setting, accompanied by the development of dome-and-keel structures due to partial convective overturn of buoyant granitoid melts and sinking of dense greenstone wedges (Anhaeusser 1984; Van Kranendonk et al. 2009, 2014), similar to what has been proposed for coeval units of the Pilbara Craton of Western Australia (e.g., Hickman 1981; Smithies et al. 2005; Van Kranendonk et al. 2014). In such intraplate settings, TTG magmas are thought to have formed by melting of deep greenstone-belt roots (e.g., Smithies, 2000; Bédard 2006; Van Kranendonk et al. 2014; Johnson et al. 2016).

The 3.55-3.20 Ga Barberton Greenstone Belt (BGB) is part of the BGGT and is located in the eastern part of the Kaapvaal Craton of eastern South Africa and northwestern Swaziland (Armstrong et al. 1990; Kröner et al. 1991; Byerly et al. 1993, 1996). It is widely accepted that the BGB consists of a 15 to 21 km thick tightly folded volcano-sedimentary sequence known as the Barberton Supergroup (Viljoen and Viljoen 1969a; Brandl et al. 2006; Lowe and Byerly 2007). However, other authors (e.g., de Wit et al. 2018) interpreted the Barberton Supergroup to represent a package of tectonic thrusts rather than representing a continuous stratigraphy. Nevertheless, the Barberton Supergroup is intruded by four different generations of granitoid plutons at ca. 3.51 Ga, 3.45 Ga, 3.22 Ga, and 3.10 Ga (Kamo and Davis 1994; Moyen et al. 2007).

The Barberton Supergroup comprises three supracrustal successions, the basal, predominantly volcanic 3.55-3.26 Ga Onverwacht Group, the overlying volcanoclastic

and metasedimentary 3.26-3.22 Ga Fig Tree Group, and the uppermost terrigenous clastic 3.22 to 3.20 Ga Moodies Group (Viljoen and Viljoen 1969a, 1969b; Viljoen and Viljoen 1969; Armstrong et al. 1990; Kröner et al. 1991, 1996; Heubeck and Lowe 1994; Kamo and Davis 1994; Lowe and Byerly 1999, 2007). The Onverwacht Group is subdivided by a chert layer known as the Middle Marker into the lower Onverwacht Group comprising the Sandspruit, Theespruit, and Komati Formations, and into the upper Onverwacht Group including the Hooggenoeg, Noisy, Mendon, and Kromberg Formations (Armstrong et al. 1990). All units located northeast of the Komati Fault including the Komati Formation of the lower Onverwacht Group and the formations of the upper Onverwacht Group (Fig. 3.1) were affected by greenschist-facies metamorphism. In contrast, the coeval Sandspruit and Theespruit Formations (Kröner et al. 2016) located to the southwest of the Komati fault (Fig. 3.1) were overprinted at amphibolite-facies conditions (Anhaeusser and Robb 1980; Anhaeusser 1984; De Ronde and De Wit 1994; Lowe and Byerly 1999; Dziggel et al. 2005; Cutts et al. 2013), with peak metamorphic conditions ranging from 640 to 700 °C and 8 to 13 kbar (Dziggel et al. 2002; Lana et al. 2010; Van Kranendonk et al. 2014; Cutts et al. 2013; Roerdink 2013).

We focus on the oldest mafic and ultramafic rocks of the lower Onverwacht Group from the 3.55 to 3.48 Ga Sandspruit and Theespruit Formations and the 3.48 to 3.45 Ga Komati Formation (Armstrong et al. 1990; Lopez-Martinez et al. 1992; Kamo and Davis 1994; Kröner et al. 1996; Dunn 2000). All sample locations are shown on the geological map (Fig. 3.1) and, where available, GPS coordinates are listed in Tables 1 and 2. Rock types sampled from the Sandspruit and Theespruit Formations include amphibolites and garnet-amphibolites. Major mineral phases are amphibole, epidote, and plagioclase. Minor phases are quartz, relict clinopyroxene, alkali feldspar, muscovite, and biotite as well as accessory apatite, ilmenite, and titanite. The samples are slightly affected by sericitization or chloritization, both resulting from post-depositional hydrothermal activity or retrograde greenschist-facies overprint. The majority of amphibolites show a preferred orientation of minerals as a consequence of deformation during amphibolite-facies metamorphism. The samples from the somewhat younger Komati Formation include komatiites, komatiitic basalts, tholeiitic basalts, and one metagabbro. The komatiites exhibit typical spinifex textures consisting of 1-5 cm long and 0.5 cm wide clinopyroxene needles and a matrix of fine-grained crystalline clinopyroxene, plagioclase, quarz, olivine, Cr-spinel, and glass. Some samples also contain minor amounts of amphibole, serpentine, and chlorite. The tholeiitic basalts are rich in plagioclase which is usually found in the

groundmass but can also occur as phenocrysts. Other mineral phases are phenocrystic clinopyroxene and minor amphibole and chlorite. The metagabbro sample mostly consists of twinned clinopyroxene and plagioclase with minor amounts of chlorite, epidote, amphibole, and apatite inclusions in plagioclase. The tholeiitic and metagabbroic samples preserved their magmatic textures.

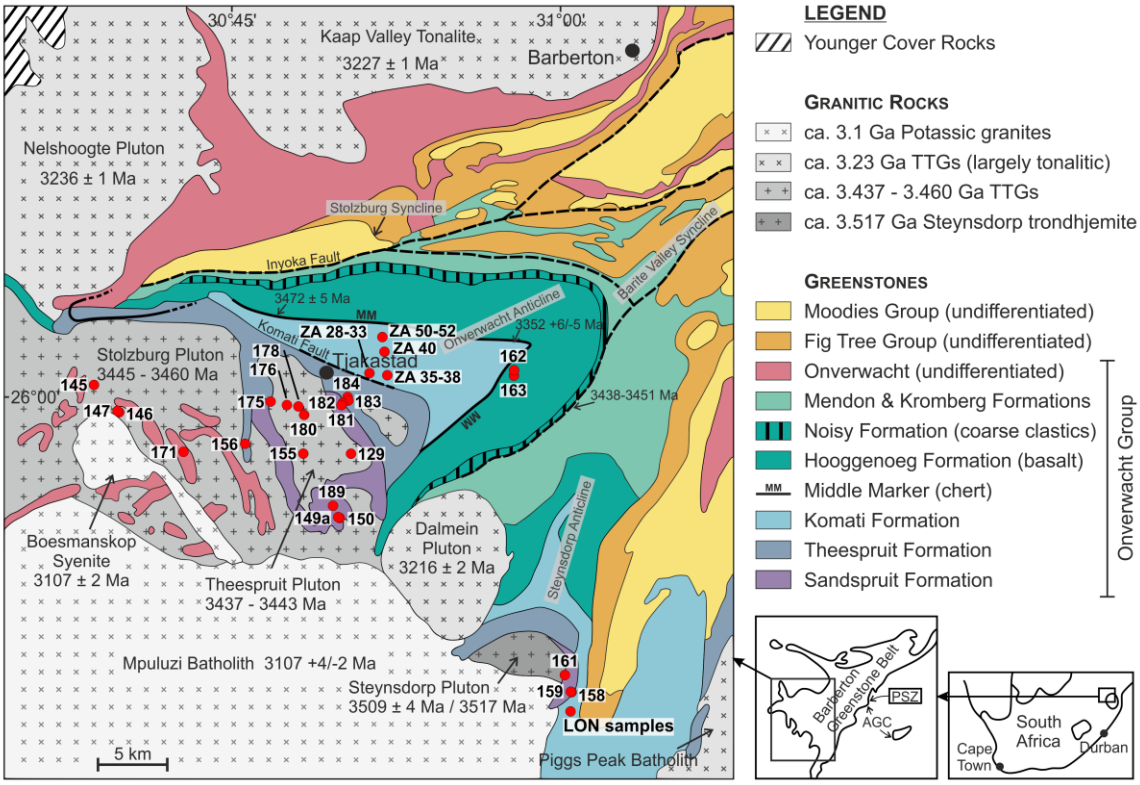

Figure 3.1: Geological map of the southern Barberton Greenstone Belt after Grosch et al. (2011). Sample localities of the Sandspruit, Theespruit, and Komati Formations are indicated by red dots. Numbers are for BA, KS-BA, and ZA samples.

3.4 Analytical techniques

Three sets of samples were analyzed in this study. The first set comprises seven amphibolites of the Theespruit Formation from the study of Roerdink (2013; samples LON-11-12 to LON-11-15, LON-11-18, LON-11-20, LON-11-22). These samples were collected from the Londozi Prospect at the southeastern margin of the BGB in Swaziland near the border with South Africa (Roerdink 2013; Roerdink et al. 2016 Fig. 3.1; Table 3.1). Additionally, twenty new samples of the Sandspruit and Theespruit Formations as well as thirteen samples of the Komati Formation were collected from the southern BGB (Fig. 3.1; Tables 3.1, 3.2). The newly collected rock samples were cut with a diamond

blade saw to remove alteration rims. The remaining material was crushed in a stainless-steel jaw crusher and milled in an agate ball mill. The powders were used for major and trace element as well as for whole-rock Nd and Hf isotope analyses.

Samples with abbreviations BA, KS-BA, and ZA, as well as samples LON-11-12 and LON-11-13 were analyzed for their whole-rock major element compositions by X-ray fluorescence (XRF) on $Li_2B_4O_7$-flux fusion discs at the University of Cologne and at the Steinmann Institute of Bonn University (Germany) using a PANalytical Axios XRF spectrometer (Tables 3.1, 3.2). The volatile content was determined as loss on ignition (LOI) by heating 1 g of rock powder in a muffle type furnace for 1 hour at 1000 °C.

All samples were analyzed for their trace element compositions. Sample powders were digested in Parr® pressure vessels in concentrated HF-HNO_3 for 72 hours at 180 °C and subsequently dried down. The evaporation step was repeated with 2 ml concentrated HNO_3. After evaporation to dryness, samples were diluted in 3 % HNO_3 for trace element measurements. Samples with the abbreviations LON, BA, and ZA were analyzed using an AGILENT 7500cs quadrupole inductively coupled plasma mass spectrometer (ICP-MS) at the University of Kiel, Germany. The accuracy of the results can be inferred from the measured values for the BHVO-2 basalt reference material that was analyzed alongside the samples (Table 3.1). Analytical procedures followed those reported in Garbe-Schönberg (1993). Samples abbreviated as KS-BA were analyzed using a Thermo Finnigan Element XR ICP-MS at Freie Universität Berlin. Detailed analytical procedures for trace element analysis are given in supplement 3.A. Relative total errors (1 RSD) for the REEs were usually around 3 to 9 %, except for Dy (up to 17 %) and span 4 to 20 % for the HFSE, LILE, and Sc, V, Cr, Co, Ni, Cu, Zn (Table 3.2).

All samples were analyzed for their Hf and Nd isotope compositions and Lu, Hf, Sm, Nd concentrations (Table 3.3). The data were obtained using combined isotope dilution isotope composition analyses using mixed ^{176}Lu-^{180}Hf and ^{149}Sm-^{150}Nd tracers following Münker et al. (2001). Samples ZA 28a, b, and ZA 29a, b, c were analyzed for their Lu-Hf systematics at the Westfälische Wilhelms-Universität Münster using a Micromass IsoProbe multi-collector ICP-MS. Replicates of samples ZA 28a, b, and ZA 29b and all other investigated samples were analyzed using a Thermo Scientific Neptune MC-ICP-MS at the joint facility of Cologne/Bonn Universities (Germany), operated in static mode. Chemical separation of Lu, Hf, Sm, and Nd followed Münker et al. (2001) and Pin and Zalduegui (1997). Reference materials AGV-2, BHVO-2, and the in-house standard NZ 557 were measured alongside the samples to determine the accuracy of our results.

Values of $^{176}Hf/^{177}Hf$ and $^{143}Nd/^{144}Nd$ were corrected for mass bias using the exponential law and normalizing to $^{179}Hf/^{177}Hf = 0.7325$ and $^{146}Nd/^{144}Nd = 0.7219$, respectively. Repeated analyses of the in-house AMES Hf solution standard yielded an external reproducibility of ±6 ppm (2 s.d.; n = 26), whereas repeated analyses of the AMES Nd and JNdi-1 standards yielded external reproducibilities of ±56 ppm (2 s.d.; n = 18) and ±38 ppm (2 s.d.; n = 37), respectively, over the course of the four analytical sessions in which samples with abbreviations BA, KS-BA, and LON were analyzed. The external reproducibilites for samples with the abbreviation ZA for both Ames Hf and LaJolla Nd were ±40 ppm, analyzed in the same analytical session. Reported values are given relative to $^{143}Nd/^{144}Nd = 0.512115$ for JNdi (i.e., $^{143}Nd/^{144}Nd = 0.511858$ for La Jolla Nd, Tanaka et al. 2000) and $^{176}Hf/^{177}Hf = 0.282160$ for our AMES Hf solution that is isotopically indistinguishable from the JMC-475 standard (Scherer et al., 2000). Repeated analysis of the andesite reference AGV-2 and the basalt reference BHVO-2 normalized to the LaJolla standard resulted in $^{143}Nd/^{144}Nd$ values of 0.512801 ± 0.000009 (2 s.d., n=7) and 0.512994 ± 0.000029 (2 s.d., n=8), respectively, in perfect agreement with previously determined values (e.g., Weis et al. 2006). Analysis of the in-house basalt reference NZ 557 normalized to AMES Hf resulted in $^{176}Hf/^{177}Hf = 0.282961 \pm 0.000011$, identical to previous analyses by Sprung et al. (2007). Normalization of the andesite and basalt reference materials was carried out following Sprung et al. (2010). All procedural blanks obtained alongside the sample data were insignificant and <16 pg for Lu, <57 pg for Hf, <80 pg for Sm, and <100 pg for Nd. Furthermore, three replicate analyses were carried out for samples BA 155, KS-BA 171, and LON-11-20. External reproducibilities for $^{143}Nd/^{144}Nd$ yielded 6 ppm (2 s.d., n = 2) for BA 155, 36 ppm (2 s.d., n = 2) for KS-BA 171, and 205 ppm (2 s.d., n = 2) for LON-11-20. Additionally, the external reproducibilites for $^{176}Hf/^{177}Hf$ were 9 ppm (2 s.d., n = 2) for BA 155, 61 ppm (2 s.d., n = 2) for KS-BA 171, and 48 ppm (2 s.d., n = 2) for LON-11-20. The CHUR parameters used to calculate epsilon Hf and Nd values are from Bouvier et al. (2008). In all calculations, values of 1.867×10^{-11} a^{-1}(Scherer et al. 2001, Söderlund et al. 2004) and 6.54×10^{-12} a^{-1} (Lugmair and Marti 1977) for the ^{176}Lu decay constant and that of ^{147}Sm were used.

Table 3.1: Major and trace element concentrations for Sandspruit/Theespruit and Komati samples with the abbreviations BA, LON, and ZA.

Sample	**BA 147**	**BA 149 a**	**BA 129**	**BA 145**	**BA 146**	**BA 155 A**	**Ba 155 B**
Formation	Sandspruit	Sandspruit	Theespruit	Theespruit	Theespruit	Theespruit	Theespruit
Rock type	Garnet-Amphibolite	Amphibolite	Amphibolite	Garnet-Amphibolite	Amphibolite	Amphibolite	Amphibolite
Age (Ma)	3553	3553	3530	3530	3530	3538	3538
Location	S 26°00'26.6" E 30°39'46.7"	S 26°04'12.0" E 30°49'55.1"	S 26°01'59.9" E 30°50'23.8"	S 25°59'27.4" E 30°38'37.7"	S 26°00'26.0" E 30°39'44.0"	S 26°01'58.5" E 30°48'14.1"	
Major elements (wt.%)							
SiO_2	52.1	55.0	53.1	52.6	51.8	52.3	
TiO_2	1.39	0.66	0.52	1.44	1.24	0.60	
Al_2O_3	13.7	9.39	14.2	13.4	12.2	14.6	
Fe_2O_3	13.5	11.6	9.31	13.6	12.1	10.3	
MnO	0.17	0.19	0.15	0.18	0.18	0.17	
MgO	5.78	9.82	8.32	5.74	7.57	7.42	
CaO	10.1	9.96	10.6	10.5	12.1	12.3	
K2O	0.41	0.28	0.22	0.33	0.64	0.28	
Na_2O	2.42	2.47	3.08	1.93	1.54	2.20	
P_2O_5	0.16	0.07	0.05	0.18	0.15	0.05	
LOI	0.84	0.77	n.d.	0.76	0.94	1.16	
Total	100.5	100.2	99.5	100.6	100.5	101.4	
Trace elements (µg/g)							
Li	24.0	5.38	14.4	27.0	8.98	18.9	18.8
Sc	32.3	29.7	40.7	32.7	35.2	38.3	38.6
V	384	212	267	392	342	267	272
Cr	104	857	370	78.6	518	183	172
Co	46.3	61.7	47.1	48.6	54.0	50.1	50.1
Ni	91.0	194	136	83.6	183	150	153
Cu	90.0	42.0	132	147	51.5	1.61	1.64
Zn	101	82.3	84.0	106	87.9	61.8	61.9
Ga	18.2	9.60	12.2	17.2	15.9	13.6	13.7
Rb	6.57	5.86	11.2	9.55	7.65	6.34	6.39
Sr	192	152	108	155	125	131	132
Y	33.8	15.4	13.1	35.8	32.3	15.4	15.3
Zr	98.2	51.5	29.1	98.3	87.1	35.5	35.8
Nb	5.07	3.05	1.22	5.51	5.73	1.41	1.42
Mo	0.506	0.211	0.158	0.454	0.772	0.150	0.150
Sn	0.192	0.102	0.130	0.250	0.277	0.254	0.218
Sb	0.0554	0.0787	0.0444	0.0478	0.0663	0.0780	0.0744
Cs	0.204	0.204	0.557	0.302	1.09	0.584	0.592
Ba	32.0	33.2	18.2	19.5	33.1	26.2	26.4
La	4.77	4.77	1.70	7.62	7.74	1.81	1.82
Ce	15.4	10.7	4.48	19.2	19.0	5.00	5.05
Pr	2.36	1.66	0.697	2.91	2.83	0.811	0.814
Nd	12.2	7.68	3.62	14.2	13.9	4.31	4.33
Sm	3.85	2.14	1.24	4.27	4.02	1.52	1.53
Eu	1.39	0.728	0.566	1.51	1.42	0.586	0.587
Gd	4.87	2.49	1.72	5.25	4.88	2.08	2.08

Table 3.1 continued.

Sample	BA 147	BA 149 a	BA 129	BA 145	BA 146	BA 155 A	Ba 155 B
Trace elements (µg/g)							
Tb	0.867	0.434	0.314	0.933	0.850	0.383	0.383
Dy	5.77	2.81	2.16	6.08	5.56	2.63	2.62
Ho	1.21	0.579	0.468	1.29	1.18	0.567	0.568
Er	3.39	1.62	1.33	3.61	3.30	1.62	1.61
Tm	0.512	0.245	0.206	0.536	0.498	0.253	0.251
Yb	3.35	1.59	1.35	3.56	3.26	1.65	1.68
Lu	0.486	0.234	0.211	0.511	0.474	0.252	0.251
Hf	2.43	1.27	0.799	2.46	2.26	0.947	0.957
Ta	0.305	0.196	0.0736	0.337	0.352	0.0967	0.0960
W	0.103	0.184	0.132	0.137	0.130	0.147	0.154
Tl	0.0744	0.0513	0.0737	0.107	0.0868	0.0728	0.0724
Pb	1.52	1.41	1.16	1.35	1.84	2.08	2.02
Th	0.553	0.381	0.101	0.628	0.578	0.155	0.155
U	0.182	0.143	0.0500	0.189	0.183	0.0698	0.0693
$Ta/Ta^*_{(PM)}$	0.92	0.75	0.76	0.77	0.78	0.89	0.88
$Nb/Nb^*_{(PM)}$	1.25	1.13	1.41	1.22	1.28	1.17	1.18
$Eu/Eu^*_{(PM)}$	1.09	1.09	1.27	1.09	1.13	1.11	1.11
$Sm/Sm^*_{(PM)}$	1.08	1.15	0.94	1.14	1.16	1.05	1.05
La_{CN}/Yb_{CN}	1.00	2.10	0.88	1.50	1.66	0.77	0.76
Gd_{CN}/Yb_{CN}	1.19	1.28	1.04	1.20	1.22	1.03	1.01

Sample	BA 156	BA 158	BA 159	BA 161	LON-11-12 A	LON-11-12 B	LON-11-13
Formation	Theespruit	Theespruit	Theespruit	Theespruit	Theespruit	Theespruit	Theespruit
Rock type	Amphibolite	Amphibolite	Amphibolite	Amphibolite	Amphibolite	Amphibolite	Amphibolite
Age (Ma)	3530	3530	3530	3530	3521	3521	3521
Location	S 26°01'29.4" E 30°45'40.1"	S 26°10'40.2" E 31°00'31.0"	Next to BA 158	S 26°10'03.4" E 31°00'11.9"	S 26°11'20" E 31°0'28"		S 26°11'20" E 31°0'28"
Major elements (wt.%)							
SiO_2	52.2	53.8	55.8	47.2	67.1		57.0
TiO_2	0.94	2.25	1.30	0.92	0.78		0.52
Al_2O_3	13.5	12.5	14.7	15.2	4.51		3.06
Fe_2O_3	11.5	15.8	9.92	13.9	6.52		8.96
MnO	0.17	0.15	0.14	0.25	0.60		0.51
MgO	6.03	5.46	5.13	4.86	5.72		8.55
CaO	10.5	4.11	9.10	13.3	10.5		16.6
K2O	0.04	0.11	0.35	0.53	1.32		0.78
Na_2O	2.32	3.87	3.32	2.67	0.421		0.396
P_2O_5	0.08	0.24	0.22	0.13	0.06		0.05
LOI	3.79	2.20	0.65	2.15	0.47		0.82
Total	101.2	100.5	100.6	101.1	98.0		97.3

Table 3.1 continued.

Sample	BA 156	BA 158	BA 159	BA 161	LON-11-12 A	LON-11-12 B	LON-11-13
Trace elements (µg/g)							
Li	7.55	23.9	29.9	17.2	31.1	31.5	51.7
Sc	35.9	32.9	30.2	29.2	25.0	24.7	17.2
V	326	382	192	219	146	144	96
Cr	147	22.97	54.93	159	1329	1353	1000
Co	46.1	44.6	27.6	46.1	144	142	142
Ni	101	55.79	28.08	111	725	724	717
Cu	155	155	38.5	111	95.0	93.9	30.3
Zn	83.5	102	80.4	84.5	141	138	88.64
Ga	15.2	20.1	17.9	28.1	7.05	7.03	6.18
Rb	0.416	1.43	6.99	6.93	46.5	46.2	30.6
Sr	116	54.5	176	238	84.9	83.6	69.8
Y	23.2	58.8	25.3	28.8	10.6	10.5	11.5
Zr	62.5	205	142	154	51.0	50.6	34.3
Nb	2.65	9.15	11.1	9.93	3.98	3.73	2.91
Mo	0.272	0.246	0.490	0.443	0.670	0.653	0.418
Sn	0.164	0.931	0.373	0.522	0.300	0.321	0.262
Sb	0.220	3.21	0.0627	0.428	0.0949	0.0932	0.0884
Cs	0.116	0.386	0.656	0.704	1.49	1.49	0.973
Ba	24.3	20.5	57.8	93.2	2601	2574	1869
La	3.28	13.2	12.2	14.4	4.42	4.37	6.76
Ce	8.87	30.1	30.1	28.4	11.2	11.1	16.4
Pr	1.38	4.47	4.07	4.13	1.72	1.72	2.40
Nd	7.21	21.8	17.5	18.2	8.35	8.44	11.3
Sm	2.38	6.44	4.22	4.57	2.20	2.22	2.49
Eu	0.887	2.25	1.29	2.00	0.941	0.933	0.994
Gd	3.17	8.27	4.47	5.06	2.21	2.20	2.42
Tb	0.570	1.47	0.732	0.842	0.339	0.340	0.374
Dy	3.90	9.80	4.55	5.32	2.00	2.01	2.20
Ho	0.836	2.08	0.927	1.09	0.404	0.403	0.436
Er	2.38	5.94	2.57	3.01	1.10	1.09	1.18
Tm	0.364	0.894	0.384	0.448	0.169	0.170	0.183
Yb	2.43	5.93	2.51	2.89	1.07	1.08	1.16
Lu	0.356	0.867	0.368	0.420	0.157	0.159	0.172
Hf	1.61	5.11	3.13	3.41	1.29	1.28	0.892
Ta	0.165	0.572	0.716	0.609	0.279	0.262	0.234
W	0.127	0.743	0.531	0.359	459	436	598
Tl	0.0361	0.0380	0.0658	0.0373	0.181	0.189	0.178
Pb	0.552	0.563	5.16	4.30	5.16	5.23	2.97
Th	0.252	0.762	3.41	2.04	0.385	0.385	0.255
U	0.0868	0.215	1.04	0.510	0.125	0.127	0.123
$Ta/Ta^*_{(PM)}$	0.83	0.77	0.91	0.75	0.99	0.96	0.74
$Nb/Nb^*_{(PM)}$	1.31	1.38	0.66	0.87	1.21	1.18	1.16
$Eu/Eu^*_{(PM)}$	1.07	1.06	0.98	1.61	1.28	1.26	1.44
$Sm/Sm^*_{(PM)}$	1.03	0.97	1.07	0.90	1.02	1.04	1.28
La_{CN}/Yb_{CN}	0.94	1.55	3.39	3.49	2.89	2.83	4.08
Gd_{CN}/Yb_{CN}	1.06	1.14	1.45	1.42	1.68	1.66	1.71

Table 3.1 continued.

Sample	LON-11-14	LON-11-15	LON-11-18	LON-11-20 A	LON-11-20 B	LON-11-22	BA 162	ZA 29 a
Formation	Theespruit	Theespruit	Theespruit	Theespruit	Theespruit	Theespruit	Komati	Komati
Rock type	Amphibolite	Amphibolite	Amphibolite	Amphibolite	Amphibolite	Amphibolite	Metagabbro	Tholeiite
Age (Ma)	3521	3521	3521	3521	3521	3521	3481	3482
Location	S 26°11'20" E 31°0'28"	S 26°11'20" E 31°0'28"	S 26°11'20" E 31°0'28"	S 26°11'20" E 31°0'28"		S 26°11'20" E 31°0'28"	S 25°58'54.9" E 30°57'55.5"	S 25°59'30.87" E 30°51'16.08"
Major elements (wt.%)								
SiO_2	52.4	68.6	52.1	55.7		52.3	53.3	52.4
TiO_2	1.01	1.15	1.15	1.06		1.15	0.426	0.78
Al_2O_3	13.6	14.4	16.5	13.8		13.4	16.3	10.4
Fe_2O_3	15.2	5.50	14.7	13.0		16.5	7.98	12.5
MnO	0.20	0.40	0.42	0.39		0.21	0.12	0.21
MgO	5.83	1.92	5.61	4.68		5.95	7.14	8.83
CaO	10.7	6.70	8.16	10.2		9.67	9.03	9.70
K_2O	0.45	1.16	1.84	1.08		0.22	1.47	0.64
Na_2O	2.12	0.60	0.78	1.08		2.32	2.42	3.14
P_2O_5	-	-	-	-		-	0.11	0.09
LOI	-	-	-	-		-	2.76	1.11
Total	101.5	100.5	100.2	101.1		101.6	101.0	99.9
Trace elements (µg/g)								
Li	70.7	171	255	54.6	55.2	36.9	20.2	n.d.
Sc	36.7	37.5	43.0	39.2	39.7	22.8	23.7	32.0#
V	293	287	363	304	307	190	116	211#
Cr	138	147	160	140	141	67.7	644	529#
Co	80.1	103	135	99.6	99.7	122	39.6	47.0#
Ni	120	92.4	245	149	150	70.2	245	113#
Cu	55.3	49.9	212	268	270	33.7	32.1	n.d.
Zn	118	65.0	143	146	146	28.4	61.9	92.0#
Ga	15.8	16.0	21.1	16.7	16.8	10.4	16.0	14.0#
Rb	5.57	46.5	90.0	30.1	30.4	45.3	45.8	8.96
Sr	51.4	95.0	96.4	90.5	91.2	42.9	212	208
Y	21.8	9.51	57.8	24.0	24.1	17.5	18.2	23.1
Zr	65.4	70.0	73.7	67.5	68.6	43.0	105	77.9
Nb	3.43	3.95	3.69	3.76	3.78	2.38	8.86	4.53
Mo	0.204	0.496	0.154	0.474	0.489	0.613	1.16	0.679
Sn	0.169	0.0916	0.515	0.176	0.101	0.647	0.779	n.d.
Sb	0.104	0.102	0.0956	0.0859	0.0858	0.0780	0.279	0.121
Cs	0.461	6.16	11.1	1.86	1.86	2.16	0.708	0.242
Ba	145	679	2045	2164	2172	1172	225	155
La	3.99	5.07	5.79	4.42	4.38	3.36	20.0	6.57
Ce	10.6	13.0	14.9	11.5	11.4	9.07	39.2	16.2
Pr	1.64	2.02	2.28	1.79	1.77	1.46	4.43	2.31
Nd	8.34	10.3	11.6	9.29	9.12	7.57	16.3	10.7
Sm	2.60	3.14	4.29	2.84	2.83	2.47	3.11	3.00
Eu	1.01	1.15	1.79	1.35	1.34	1.13	0.863	0.933
Gd	3.30	2.86	7.45	3.62	3.58	3.14	3.04	3.64
Tb	0.594	0.397	1.48	0.637	0.636	0.535	0.483	0.647
Dy	3.93	2.18	10.5	4.22	4.22	3.37	3.05	4.25
Ho	0.844	0.423	2.22	0.904	0.903	0.668	0.651	0.899
Er	2.39	1.18	6.10	2.59	2.58	1.73	1.90	2.58
Tm	0.368	0.196	0.889	0.405	0.403	0.245	0.300	0.376
Yb	2.41	1.43	5.64	2.70	2.69	1.46	1.97	2.50
Lu	0.361	0.234	0.781	0.403	0.402	0.195	0.293	0.375

Table 3.1 continued.

Sample	LON-11-14	LON-11-15	LON-11-18	LON-11-20 A	LON-11-20 B	LON-11-22	BA 162	ZA 29 a
Trace elements (µg/g)								
Hf	1.74	1.87	1.94	1.77	1.76	1.12	2.43	2.24
Ta	0.236	0.316	0.275	0.273	0.274	0.236	0.463	0.339
W	235	628	271	407	413	931	0.318	0.482
Tl	0.0618	0.205	0.498	0.176	0.166	0.204	0.253	0.063
Pb	3.17	2.05	2.90	2.53	2.53	0.946	5.66	0.634
Th	0.318	0.341	0.455	0.330	0.328	0.241	3.32	0.605
U	0.100	0.145	0.123	0.0978	0.0949	0.129	0.725	0.147
$Ta/Ta^*_{(PM)}$	0.95	1.04	0.87	0.99	1.00	1.23	0.49	0.91
$Nb/Nb^*_{(PM)}$	1.25	1.17	1.05	1.23	1.24	0.96	0.60	1.01
$Eu/Eu^*_{(PM)}$	1.13	1.09	1.40	1.40	1.39	1.22	1.13	1.05
$Sm/Sm^*_{(PM)}$	1.01	1.10	1.15	0.94	0.94	1.08	1.08	1.06
La_{CN}/Yb_{CN}	1.16	2.48	0.72	1.14	1.14	1.61	7.08	1.83
Gd_{CN}/Yb_{CN}	1.12	1.63	1.08	1.09	1.09	1.76	1.26	1.18

Sample	ZA 29 b	ZA 29 c	ZA 31a	ZA 32a	BA 163	ZA 28 a	ZA 28aR
Formation	Komati	Komati	Komati	Komati	Komati	Komati	Komati
Rock type	Tholeiite	Tholeiite	Tholeiite	Tholeiite	Komatiite	Komatiite	Komatiite
Age (Ma)	3482	3482	3482	3482	3481	3482	3482
Location	S 25°59'30.87" E 30°51'16.08"	S 25°59'30.87" E 30°51'16.08"	S 25°59'30.87" E 30°51'16.08"	S 25°59'30.87" E 30°51'16.08"	A few meters south of BA 162	S 25°59'30.87" E 30°51'16.08"	S 25°59'30.87" E 30°51'16.08"
Major elements (wt.%)							
SiO_2	51.4	54.7	52.6	52.8	49.9	42.0	41.8
TiO_2	0.79	0.71	0.66	0.77	0.321	0.18	0.19
Al_2O_3	10.8	9.83	8.56	12.1	4.84	3.15	3.17
Fe_2O_3	12.2	11.1	12.8	11.5	10.1	11.0	11.5
MnO	0.21	0.19	0.18	0.19	0.12	0.15	0.16
MgO	11.2	8.8	11.8	8.88	23.2	31.1	30.5
CaO	10.0	9.66	9.79	9.59	6.83	3.99	4.01
K_2O	0.23	1.34	0.09	0.16	0.01	0.11	0.11
Na_2O	2.61	3.08	2.43	3.25	0.005	0.16	0.05
P_2O_5	0.09	0.08	0.07	0.09	0.03	0.03	0.03
LOI	1.29	1.11	1.15	0.92	5.07	8.61	8.61
Total	101.0	100.8	100.1	100.2	100.4	101.0	100.1
Trace elements (µg/g)							
Li	n.d.	n.d.	6.92	5.76	11.1	n.d.	n.d.
Sc	32.0#	29.0#	28.2	27.1	22.2	17.0#	n.d.
V	187#	202#	198	218	139	72#	71.2#
Cr	708#	673#	2167	691	3261	2508#	2699#
Co	51.0#	47.0#	60.8	52.1	92.8	125#	76.1#
Ni	194#	139#	251	173	1059	2000#	2029#
Cu	n.d.	n.d.	133	122.8	29.4	n.d.	n.d.
Zn	92.0#	77.0#	85.4	74.4	60.9	53.0#	65.3#
Ga	10.0#	11.0#	10.7	11.4	6.04	5.00#	n.d.
Rb	4.87	15.3	2.73	2.71	0.212	1.72	n.d.
Sr	154	130	140	198	8.25	20.5	n.d.
Y	19.0	20.5	15.6	18.5	6.70	2.97	n.d.
Zr	64.3	69.3	61.0	66.5	16.4	7.88	n.d.
Nb	3.59	4.04	3.58	3.66	0.695	0.561	n.d.
Mo	1.40	0.549	0.536	0.336	0.193	0.357	n.d.

Table 3.1 continued.

Sample	ZA 29 b	ZA 29 c	ZA 31a	ZA 32a	BA 163	ZA 28 a	ZA 28aR
Trace elements (µg/g)							
Sn	n.d.	n.d.	0.522	0.623	0.131	n.d.	n.d.
Sb	0.0357	0.208	0.181	0.0631	0.114	1.32	n.d.
Cs	0.111	0.183	0.306	0.272	0.118	0.629	n.d.
Ba	29.3	357	65.3	53.9	85.9	6.09	n.d.
La	4.76	5.16	4.66	4.40	0.947	0.509	n.d.
Ce	12.2	13.3	11.9	11.34	2.40	1.43	n.d.
Pr	1.78	1.94	1.743	1.659	0.378	0.208	n.d.
Nd	8.37	9.12	8.19	7.94	1.87	1.03	n.d.
Sm	2.45	2.61	2.23	2.29	0.682	0.341	n.d.
Eu	0.916	0.818	0.769	0.756	0.252	0.120	n.d.
Gd	2.97	3.18	2.61	2.84	0.945	0.453	n.d.
Tb	0.529	0.565	0.443	0.496	0.176	0.0867	n.d.
Dy	3.52	3.72	2.83	3.28	1.21	0.576	n.d.
Ho	0.745	0.787	0.588	0.688	0.261	0.124	n.d.
Er	2.11	2.24	1.63	1.94	0.736	0.358	n.d.
Tm	0.312	0.331	0.240	0.290	0.117	0.0532	n.d.
Yb	2.08	2.19	1.56	1.92	0.754	0.359	n.d.
Lu	0.309	0.325	0.239	0.298	0.114	0.0549	n.d.
Hf	1.84	1.95	1.47	1.63	0.484	0.260	n.d.
Ta	0.249	0.271	0.217	0.216	0.057	0.0412	n.d.
W	0.589	0.479	0.179	0.105	0.119	0.328	n.d.
Tl	0.031	0.087	0.0250	0.0280	0.031	0.0134	n.d.
Pb	0.482	0.591	0.486	0.707	0.141	0.197	n.d.
Th	0.456	0.534	0.495	0.403	0.104	0.0330	n.d.
U	0.113	0.130	0.106	0.101	0.048	0.0145	n.d.
$Ta/Ta^*_{(PM)}$	0.89	0.88	0.79	0.80	1.03	1.14	
$Nb/Nb^*_{(PM)}$	1.08	1.08	1.11	1.26	0.92	1.40	
$Eu/Eu^*_{(PM)}$	1.17	1.05	1.11	1.02	0.98	0.84	
$Sm/Sm^*_{(PM)}$	0.97	1.05	1.08	1.06	1.01	0.99	
La_{CN}/Yb_{CN}	1.60	1.65	2.09	1.60	0.88	0.99	
Gd_{CN}/Yb_{CN}	1.17	1.19	1.36	1.21	1.02	1.03	

Sample	ZA 28 b	ZA 28bR	ZA 30a	ZA 33	ZA 35	ZA 36	ZA 38
Formation	Komati	Komati	Komati	Komati	Komati	Komati	Komati
Rock type	Komatiite	Komatiite	Komatiite	Komatiite	Komatiite	Komatiite	Komatiite
Age (Ma)	3482	3482	3482	3482	3482	3482	3482
Location	S 25°59'30.87" E 30°51'16.08"	S 25°59'30.87" E 30°51'16.08"	S 25°59'30.87" E 30°51'16.08"	S 25°59'30.87" E 30°51'16.08"	S 25°59'29.52" E 30°51'58.66"	S 25°59'29.17" E 30°52'00.68"	S 25°59'31.73" E 30°52'00.52"
Major elements (wt.%)							
SiO_2	41.7	41.7	45.1	44.1	44.1	43.9	46.0
TiO_2	0.24	0.24	0.41	0.36	0.33	0.32	0.38
Al_2O_3	2.49	2.49	5.04	4.03	3.34	3.36	4.03
Fe_2O_3	10.2	10.2	12.3	12.1	12.0	11.4	11.1
MnO	0.15	0.15	0.17	0.18	0.18	0.17	0.16
MgO	32.6	32.6	23.2	26.9	27.9	28.2	25.1
CaO	4.59	4.59	8.04	5.56	5.48	5.30	7.46
K_2O	0.02	0.02	0.01	0.01	0.01	0.02	0.03
Na_2O	0.05	0.05	0.17	0.19	0.14	0.09	0.38
P_2O_5	0.03	0.03	0.05	0.03	0.03	0.03	0.04
LOI	8.69	8.69	4.80	6.64	7.15	7.32	5.51
Total	101.2	101.2	99.22	100.1	100.7	100.2	100.2

Table 3.1 continued.

Sample	ZA 28 b	ZA 28bR	ZA 30a	ZA 33	ZA 35	ZA 36	ZA 38
Trace elements (µg/g)							
Li	n.d.	n.d.	0.664	1.90	3.69	4.30	12.3
Sc	16.0#	16.0#	18.6	18.1	18.0	11.4	13.4
V	58.0#	58.0#	125	114	111	104	71.6
Cr	1816#	1816#	2998	2132	2203	2068	1563
Co	118#	118#	86.3	100	101	97.5	108
Ni	1872#	1872#	935	1288	1467	1467	1717
Cu	n.d.	n.d.	90.0	41.7	54.2	35.3	23.7
Zn	54.0#	54.0#	63.4	73.8	70.6	66.7	55.8
Ga	n.d.	n.d.	6.18	5.01	4.42	4.30	3.05
Rb	1.44	1.44	0.341	0.302	0.561	0.865	2.23
Sr	19.8	19.8	28.7	17.3	37.6	37.3	8.1
Y	3.69	3.69	9.03	7.14	7.19	6.96	4.77
Zr	11.3	11.3	36.8	23.0	22.0	22.3	14.7
Nb	0.656	0.656	2.14	1.39	1.34	1.31	0.827
Mo	0.796	0.796	0.384	0.191	0.170	0.137	0.172
Sn	n.d.	n.d.	0.325	0.241	0.266	0.251	0.145
Sb	0.0498	0.0498	0.0319	0.119	0.0548	0.0703	0.7614
Cs	0.672	0.672	0.297	0.313	0.209	0.442	1.106
Ba	1.97	1.97	5.78	3.98	25.6	23.5	15.3
La	0.630	0.630	2.76	1.80	1.77	1.63	1.07
Ce	2.06	2.06	7.13	4.81	4.68	4.39	2.78
Pr	0.310	0.310	1.03	0.722	0.700	0.665	0.408
Nd	1.65	1.65	4.76	3.55	3.45	3.32	1.98
Sm	0.555	0.555	1.29	1.03	1.01	0.986	0.605
Eu	0.199	0.199	0.404	0.371	0.358	0.346	0.226
Gd	0.701	0.701	1.51	1.23	1.22	1.18	0.763
Tb	0.124	0.124	0.255	0.207	0.206	0.198	0.133
Dy	0.787	0.787	1.64	1.32	1.32	1.27	0.860
Ho	0.162	0.162	0.339	0.271	0.270	0.260	0.177
Er	0.449	0.449	0.943	0.741	0.738	0.711	0.482
Tm	0.0646	0.0646	0.139	0.109	0.108	0.105	0.0709
Yb	0.422	0.422	0.911	0.709	0.692	0.679	0.454
Lu	0.0628	0.0628	0.139	0.108	0.105	0.104	0.0686
Hf	0.368	0.368	0.856	0.587	0.560	0.557	0.379
Ta	0.0579	0.058	0.129	0.0825	0.0778	0.0766	0.0494
W	0.561	0.561	0.179	0.0722	0.177	0.243	0.197
Tl	0.00733	0.00733	0.0212	0.00456	0.00984	0.00974	0.0465
Pb	0.161	0.161	0.328	0.334	0.284	0.268	0.302
Th	0.0417	0.0417	0.284	0.145	0.137	0.130	0.0842
U	0.0176	0.0176	0.0709	0.0389	0.0373	0.0361	0.0233
$Ta/Ta^*_{(PM)}$	1.33	1.33	0.79	0.77	0.75	0.78	0.78
$Nb/Nb^*_{(PM)}$	1.20	1.20	1.13	1.29	1.31	1.33	1.30
$Eu/Eu^*_{(PM)}$	0.95	0.95	0.97	1.06	1.07	1.06	0.82
$Sm/Sm^*_{(PM)}$	1.06	1.06	1.13	1.14	1.17	1.16	1.06
La_{CN}/Yb_{CN}	1.04	1.04	2.11	1.77	1.79	1.68	1.65
Gd_{CN}/Yb_{CN}	1.35	1.35	1.35	1.41	1.44	1.42	1.37

Table 3.1 continued.

Sample	**ZA 40**	**ZA 50**	**ZA 51**	**ZA 52**	**BIR-1 Kiel A**	**BIR-1 Kiel B**	**BHVO-2 Kiel**
Formation	Komati	Komati	Komati	Komati	Reference	Reference	Reference
Rock type	Komatiite	Komatiitic basalt	Komatiitic basalt	Komatiitic basalt	Icelandic Basalt	Icelandic Basalt	Hawaiian Basalt
Age (Ma)	3482	3482	3482	3482			
Location	S 25°58'41.07" E 30°51'52.55"	S 25°58'14.82" E 30°51'49.32"	S 25°58'14.82" E 30°51'49.32"	S 25°58'14.82" E 30°51'49.32"			
Major elements (wt.%)							
SiO_2	43.3	53.2	52.2	53.7			
TiO_2	0.25	0.50	0.54	0.53			
Al_2O_3	2.20	8.56	9.12	9.09			
Fe_2O_3	11.1	9.40	10.2	9.96			
MnO	0.14	0.14	0.13	0.14			
MgO	33.2	13.1	14.2	13.5			
CaO	0.98	8.68	8.61	7.53			
K_2O	0.02	0.24	0.20	0.31			
Na_2O	n.d.	2.62	2.17	2.46			
P_2O_5	0.03	0.05	0.05	0.05			
LOI	9.81	3.87	2.98	3.03			
Total	101.0	100.3	100.4	100.3			
Trace elements (µg/g)							
Li	1.96	12.4	13.2	13.7	3.42	3.38	4.69
Sc	22.0	37.2	37.8	33.7	44.1	43.5	32.0
V	136	227	229	219	321	315	313
Cr	2448	1058	1125	1038	375	372	284
Co	102	56.4	57.3	56.0	51.3	51.3	44.5
Ni	1377	251	267	261	161	160	118
Cu	28.8	39.7	70.1	34.3	121	119	132
Zn	68.2	56.8	54.6	58.4	67.5	67.2	101
Ga	5.55	10.1	10.7	10.6	15.8	15.7	21.72
Rb	0.419	2.41	3.23	4.60	0.208	0.205	9.17
Sr	60.5	88.7	59.4	52.1	107	105	376
Y	8.91	13.0	13.3	13.4	15.8	15.4	25.5
Zr	28.6	37.5	40.8	38.5	15.2	14.9	170
Nb	1.69	1.70	1.86	1.77	0.543	0.536	18.0
Mo	0.137	0.124	0.109	0.188	0.0725	0.0658	4.69
Sn	0.496	0.262	0.322	0.342	0.729	0.701	1.74
Sb	0.123	0.0220	0.0177	0.0221	0.514	0.482	0.138
Cs	0.188	0.302	0.089	0.169	0.00890	0.00852	0.106
Ba	37.7	67.2	118	129	6.71	6.66	130
La	2.08	2.10	2.14	2.61	0.630	0.618	15.4
Ce	5.55	5.53	5.59	6.43	1.94	1.91	37.7
Pr	0.840	0.810	0.814	0.913	0.382	0.381	5.35
Nd	4.17	3.89	3.91	4.29	2.49	2.46	25.1
Sm	1.25	1.19	1.22	1.27	1.16	1.14	6.23
Eu	0.443	0.402	0.376	0.483	0.544	0.542	2.12
Gd	1.49	1.66	1.69	1.75	1.86	1.85	6.29
Tb	0.252	0.311	0.319	0.326	0.368	0.364	0.953
Dy	1.62	2.16	2.21	2.26	2.64	2.63	5.39
Ho	0.331	0.470	0.477	0.491	0.585	0.579	0.993
Er	0.908	1.33	1.37	1.40	1.68	1.66	2.46
Tm	0.133	0.198	0.205	0.210	0.253	0.251	0.335
Yb	0.861	1.30	1.34	1.37	1.68	1.67	2.02
Lu	0.132	0.201	0.209	0.211	0.247	0.244	0.281

Table 3.1 continued.

Sample	ZA 40	ZA 50	ZA 51	ZA 52	BIR-1 Kiel A	BIR-1 Kiel B	BHVO-2 Kiel
Trace elements (µg/g)							
Hf	0.712	0.945	1.00	0.997	0.575	0.574	4.20
Ta	0.0989	0.0984	0.107	0.106	0.0424	0.0415	1.10
W	0.363	0.0394	0.0403	0.0489	0.0295	0.0330	0.287
Tl	0.00865	0.0154	0.0193	0.0229	0.0116	0.0134	0.0670
Pb	0.320	1.07	0.608	0.977	3.11	2.99	1.57
Th	0.172	0.200	0.217	0.217	0.0403	0.0436	1.23
U	0.0470	0.0519	0.0650	0.0552	0.0241	0.0291	0.476
$Ta/Ta^*_{(PM)}$	0.78	0.77	0.79	0.72			
$Nb/Nb^*_{(PM)}$	1.31	1.23	1.24	1.19			
$Eu/Eu^*_{(PM)}$	1.28	0.93	0.83	1.05			
$Sm/Sm^*_{(PM)}$	1.15	0.99	1.00	0.94			
La_{CN}/Yb_{CN}	1.69	1.13	1.11	1.33			
Gd_{CN}/Yb_{CN}	1.41	1.04	1.02	1.04			

[#]RFA data; *Jochum et al. (2005); n.d. = not determined

Table 3.2: Major and trace element concentrations of Sandspruit/Theespruit samples with the abbreviation KS-BA.

Sample	KS-BA 171 A	KS-BA 171 B	KS-BA 175	KS-BA 176	KS-BA 178	KS-BA 180	KS-BA 181	KS-BA 182
Formation	Sandspruit	Sandspruit	Sandspruit	Sandspruit/ Theespruit	Sandspruit/ Theespruit	Sandspruit/ Theespruit	Theespruit	Theespruit
Rock type	Amphibolite	Amphibolite	Amphibolite	Amphibolite	Amphibolite	Amphibolite	Amphibolite	Amphibolite
Age (Ma)	3553	3553	3553	3530	3530	3530	3530	3530
Location	S 26°01'52.1" E 31°42'51.3"		S 26°00'06.2" E 30°46'46.2"	S 26°00'13.6" E 30°47'29.2"	S 26°00'17.3" E 30°47'58.9"	S 26°00'33.7" E 30°48'15.0"	S 26°00'06.7" E 30°49'59.0"	S 26°00'03.6" E 30°50'00.6"
Major elements (wt.%)								
SiO_2	54.7	54.7	48.9	52.9	50.9	48.6	50.8	49.6
TiO_2	0.93	0.91	0.73	0.32	0.23	1.22	1.31	1.39
Al_2O_3	13.2	13.2	3.46	2.69	12.4	14.2	10.9	10.2
Fe_2O_3	11.9	11.9	15.5	9.22	8.60	13.3	13.7	14.0
MnO	0.30	0.30	0.23	0.16	0.14	0.19	0.21	0.21
MgO	4.53	4.52	16.2	16.2	12.5	7.40	7.85	10.8
CaO	9.63	9.64	11.9	14.9	8.26	10.4	10.9	9.85
K_2O	1.82	1.80	0.10	0.04	1.63	0.35	0.37	0.05
Na_2O	0.95	0.94	0.58	0.52	0.85	2.02	2.21	2.06
P_2O_5	0.10	0.10	0.05	0.03	0.06	0.13	0.15	0.20
LOI	1.04	1.04	1.52	1.14	3.97	2.19	1.24	1.04
Total	99.1	99.1	99.0	98.1	99.5	100.1	99.7	99.4
Trace elements (µg/g)								
Li	n.d.	n.d.	n.d.	6.12	n.d.	n.d.	n.d.	n.d.
Be	n.d.	n.d.	n.d.	n.d.	0.754	n.d.	1.15	1.83
Sc	28.1	31.3	58.6	33.3	25.9	36.7	44.1	25.8
V	275	290	169	129	131	248	255	158
Cr	119	127	2974#	2591#	1454#	257	592	1197#
Co	44.2	49.5	82.0#	47.0#	63.3	57.3	63.9	69.0
Ni	73.9	84.0	611#	221#	552	144	178	453#
Cu	84.6	94.1	89.8	54.6	n.d.	77.5	135	125
Zn	121	133	94.4	54.0#	73.0#	91.9	164	145
Ga	15.3	15.7	4.3	3.1	12.5	15.2	17.5	14.5
Rb	59.0#	59.0#	n.d.	n.d.	88.0#	27.0#	6.07	n.d.
Sr	85.7	87.2	n.d.	n.d.	209	138	142	396
Y	20.2	20.6	13.3	6.93	17.4	25.5	40.5	34.0
Zr	61.1	62.0	34.0	15.1	71.9	69.4	158	155
Nb	2.66	2.73	2.60	n.d.	n.d.	2.99	10.0	13.26
Mo	0.912	1.03	0.154	0.121	0.524	0.352	0.788	1.12
Cd	n.d.	n.d.	0.128	n.d.	n.d.	0.101	0.187	0.191
Sn	0.913	0.897	0.710	0.387	0.894	0.549	1.70	3.44
Sb	0.0466	0.0443	0.0464	n.d.	n.d.	n.d.	0.0964	0.164
Cs	n.d.	n.d.	n.d.	n.d.	n.d.	n.d.	n.d.	0.163
Ba	73.9	72.9	9.75	11.0	211	54.2	32.4	10.9
La	4.46	4.38	7.46	2.03	15.8	5.42	12.9	17.8
Ce	11.4	11.1	9.90	4.68	29.0	13.8	30.1	40.9
Pr	1.64	1.61	2.18	0.699	3.13	2.05	4.16	5.57
Nd	7.53	7.47	10.2	3.38	11.1	9.84	18.4	24.1
Sm	2.24	2.20	2.67	1.05	2.17	2.92	5.12	5.78
Eu	0.899	0.887	0.771	0.378	0.553	1.08	1.41	1.75
Gd	2.38	2.33	2.18	0.972	3.29	2.77	5.14	6.01

Table 3.2 continued.

Sample	KS-BA 171 A	KS-BA 171 B	KS-BA 175	KS-BA 176	KS-BA 178	KS-BA 180	KS-BA 181	KS-BA 182
Trace elements (µg/g)								
Tb	0.532	0.532	0.457	0.209	0.360	0.609	0.993	0.958
Dy	3.60	3.58	2.78	1.37	2.37	4.13	6.38	5.84
Ho	0.771	0.766	0.556	0.287	0.542	0.887	1.36	1.21
Er	2.16	2.17	1.48	0.79	1.59	2.50	3.73	3.24
Tm	0.329	0.325	0.208	0.112	0.232	0.380	0.553	0.477
Yb	2.10	2.09	1.33	0.73	1.57	2.49	3.52	3.02
Lu	0.315	0.308	0.195	0.108	0.227	0.376	0.508	0.435
Hf	1.93	1.92	1.23	0.52	1.80	2.06	4.06	3.89
Ta	0.210	0.211	0.202	0.0683	0.362	0.218	0.592	0.819
W	0.420	0.393	0.287	0.072	0.381	0.0708	0.743	0.297
Pb	2.35	2.30	1.66	0.388	7.11	1.46	4.02	n.d.
Th	0.481	0.473	0.439	0.192	4.98	0.454	1.76	2.12
U	0.107	0.112	0.0843	0.0604	1.14	0.0992	0.400	0.505
$Ta/Ta^*_{(PM)}$	0.89	0.89	0.61	1.07	0.73	0.78	0.77	0.79
$Nb/Nb^*_{(PM)}$	0.85	0.88	0.89	-	-	0.96	0.98	1.01
$Eu/Eu^*_{(PM)}$	1.12	1.12	0.96	1.14	1.08	1.03	0.94	1.05
$Sm/Sm^*_{(PM)}$	0.87	0.87	1.41	1.22	1.07	1.01	1.08	1.13
La_{CN}/Yb_{CN}	1.48	1.47	3.93	1.94	7.04	1.52	2.57	4.13
Gd_{CN}/Yb_{CN}	0.92	0.91	1.34	1.08	1.71	0.91	1.19	1.62
Nb/Ta	12.64	12.95	12.87	-	-	13.70	16.97	16.20
Zr/Hf	31.65	32.30	27.59	29.23	39.97	33.62	39.01	39.72

Sample	**KS-BA 183**	**KS-BA 184**	**KS-BA 189**
Formation	Theespruit	Theespruit	Theespruit
Rock type	Amphibolite	Amphibolite	Amphibolite
Age (Ma)	3530	3530	3553
Location	S 25°59'59.6" E 30°50'07.5"	S 25°59'58.1" E 30°50'07.4"	S 26°03'53.3" E 30°49'38.0"
Major elements (wt.%)			
SiO_2	50.2	49.5	51.1
TiO_2	1.40	1.66	0.49
Al_2O_3	11.4	13.2	13.6
Fe_2O_3	14.4	14.9	10.4
MnO	0.22	0.29	0.16
MgO	7.23	4.52	9.81
CaO	10.6	9.32	10.2
K_2O	0.26	0.28	0.53
Na_2O	2.27	4.14	1.78
P_2O_5	0.16	0.19	0.08
LOI	0.42	0.69	1.64
Total	98.5	98.6	99.7

Table 3.2 continued.

Sample	KS-BA 183	KS-BA 184	KS-BA 189	BHVO-2 mean (4 analytical sessions)	2s.d. (µg/g)	BHVO-2 reference*	2s.d. (µg/g)*
Trace elements (µg/g)							
Li	n.d.	n.d.	n.d.	4.33	1.54	4.50	0.09
Be	0.981	1.98	n.d.	1.03	0.20	1.08	0.05
Sc	38.0	27.8	30.3	31.2	3.2	31.8	0.3
V	262	196	165	295	93.9	318	2.3
Cr	389	65.0#	1011#	266	98.9	287	3.1
Co	59.3	54.8	58.6	43.0	9.2	44.9	0.3
Ni	172	96.7	267#	122	26.5	120	1.2
Cu	90.1	485	67.4	128	20.6	129	1.4
Zn	149	170	74.5	107	54.7	104	1.0
Ga	17.8	18.4	12.7	20.2	3.5	21.4	0.2
Rb	4.60	n.d.	35.0#	9.25	3.01	9.26	0.10
Sr	114	210	182	366	84.9	394	1.7
Y	40.8	41.9	16.7	25.3	4.7	25.9	0.3
Zr	168	202	65.5	157	36.3	171	1.3
Nb	10.5	19.2	3.10	16.4	3.8	18.1	0.2
Mo	n.d.	n.d.	0.513	4.15	0.47	4.07	0.16
Cd	0.174	0.211	0.0949	0.150	0.016	0.152	0.049
Sn	2.22	2.05	0.568	1.75	0.09	1.78	0.06
Sb	0.0892	0.0811	n.d.	0.102	0.014	0.103	0.008
Cs	n.d.	0.0828	n.d.	0.0974	0.0089	0.0996	0.0022
Ba	24.5	40.3	89.1	130	6.0	131	1.0
La	8.21	27.6	8.71	15.2	0.7	15.2	0.1
Ce	21.3	60.8	18.0	37.5	1.7	37.5	0.2
Pr	3.28	7.99	2.22	5.31	0.25	5.34	0.03
Nd	15.4	32.8	9.08	24.1	1.0	24.3	0.3
Sm	4.84	7.05	2.18	6.00	0.27	6.02	0.06
Eu	1.75	1.96	0.750	2.03	0.09	2.04	0.01
Gd	4.43	8.06	2.52	6.15	0.48	6.21	0.04
Tb	1.00	1.15	0.405	0.932	0.044	0.939	0.006
Dy	6.59	7.03	2.71	5.28	0.23	5.28	0.03
Ho	1.40	1.46	0.586	0.987	0.039	0.989	0.005
Er	3.79	4.02	1.69	2.50	0.10	2.51	0.01
Tm	0.576	0.603	0.255	0.335	0.025	0.335	0.003
Yb	3.67	3.80	1.68	1.99	0.18	1.99	0.03
Lu	0.525	0.558	0.251	0.272	0.028	0.275	0.002
Hf	4.27	5.01	1.78	4.44	0.21	4.47	0.03
Ta	0.626	1.19	0.202	1.15	0.06	1.15	0.02
W	0.868	1.04	0.294	0.249	0.013	0.251	0.035
Pb	3.40	4.41	2.43	1.63	0.11	1.65	0.04
Th	1.87	3.05	1.43	1.21	0.11	1.22	0.02
U	0.319	0.555	0.203	0.413	0.043	0.412	0.035

Table 3.2 continued.

Sample	KS-BA 183	KS-BA 184	KS-BA 189
Ta/Ta*$_{(PM)}$	0.98	0.76	0.52
Nb/Nb*$_{(PM)}$	0.96	1.02	0.48
Eu/Eu*$_{(PM)}$	1.17	0.97	1.22
Sm/Sm*$_{(PM)}$	0.90	1.14	0.96
La$_{CN}$/Yb$_{CN}$	1.56	5.08	3.63
Gd$_{CN}$/Yb$_{CN}$	0.99	1.73	1.22
Nb/Ta	16.73	16.19	15.29
Zr/Hf	39.28	40.32	36.89

#RFA data; *Jochum et al. (2005); n.d. = not determined; PM = primitive mantle-normalized; CN = chondrite-normalized

3.5 Results

The major and trace element compositions of the Sandspruit and Theespruit Formations as well as the Komati Formation are reported in Tables 3.1 and 3.2. Major element data for most "LON" samples of the Theespruit Formation are from Roerdink (2013), except of LON-11-12 and LON-11-13. All other major and the trace element data were analyzed in this study. Additionally, the Lu-Hf and Sm-Nd isotope compositions of all samples analyzed in this study are listed in Table 3.3.

3.5.1 Sandspruit and Theespruit Formations

3.5.1.1 Major element conentrations

Most samples of the Sandspruit and Theespruit Formations exhibit SiO_2 and MgO contents ranging from 47.2 to 55.8 wt.% and 4.7 to 9.8 wt.%, respectively, and Al_2O_3/TiO_2 values range from 4.8 to 27.7. However, one amphibolite (LON-11-15) with pillow structures sampled at the contact to silicified schists (Roerdink 2013), yielded a high SiO_2 (68.6 wt.%) and a low MgO content (1.9 wt.%). The major element abundances of this sample have most likely been modified by silicification.

In element vs. MgO plots (Harker diagrams), the samples follow typical mineral fractionation trends of oceanic basalts. Fractionation of olivine is indicated by the negative correlation of Al_2O_3 vs. MgO and the positive correlation of Ni and MgO for samples with MgO contents below 30 wt.% (Fig. 3.2a, c). Furthermore, literature data

include samples exceeding MgO contents of 30 wt.% that likely represent admixture with olivine, causing the development of these high MgO contents. Likewise, in TiO_2 vs. MgO space, fractionation of olivine and clinopyroxene is indicated for MgO contents below 30 wt.%. However, above 30 wt.% MgO the trend is dominated by admixture of olivine (Fig. 3.2b). Fractionation of clinopyroxene is also suggested by positive correlations of Cr and Sc with MgO contents for MgO below 30 wt.% (Fig. 3.2d).

3.5.1.2 Trace element concentrations

Trace element data for amphibolites of the Sandspruit and Theespruit Formations overlap with data from Jahn et al. (1982; Fig. 3.3). The primitive mantle (PM) normalized trace element patterns of most samples of the two formations are generally flat (Fig. 3.3a) at two- to eleven-fold enriched contents relative to primitive mantle. However, some samples show an enrichment in light rare earth elements (LREEs) and elevated Th. The Sandspruit and Theespruit samples of this study can be subdivided into three groups, based on their petrological and geochemical characteristics: (1) a LREE depleted group having low La_{CN}/Yb_{CN} ranging from 0.72 to 0.88, uniform Gd_{CN}/Yb_{CN} of around one, high Zr/Th (162-288, with depleted mantle values being ca. 557, and PM values ca. 120, and those of continental crust ca. 20, Chavagnac 2004), negative anomalies for Th and Ti, and positive $Nb/Nb^*_{(PM)}$ anomalies (Tables 3.1, 3.2); (2) a LREE-undepleted group having relatively flat REE (La_{CN}/Yb_{CN} = 0.94-1.94), uniform Gd_{CN}/Yb_{CN} of around one, moderate to high Zr/Th (78-269), negative anomalies for Th and Ti, and positive $Nb/Nb^*_{(PM)}$ anomalies; (3) a LREE-enriched group with high La_{CN}/Yb_{CN} ranging from 1.56 to 5.08, elevated Gd_{CN}/Yb_{CN} ranging from 1.0 to 1.7, low Zr/Th (41.5-90.1), and negative $Nb/Nb^*_{(PM)}$ anomalies below one and down to 0.48 (Fig. 3.3a; Tables 3.1, 3.2). All samples show slightly negative Ta anomalies down to Ta/Ta_{PM}^* of 0.52.

Figure 3.2: Co-variation diagrams for major and trace elements of the Sandspruit/Theespruit (A-D) and Komati Formations (E-H). A) Al2O3 wt.% vs. MgO wt.%; B) TiO2 wt.% vs. MgO wt.%; C) Ni ppm vs. MgO wt.%; D) Cr ppm vs. MgO wt.%; E) Al2O3 wt.% vs. MgO wt.%; F) TiO2 wt.% vs. MgO wt.%; G) Ni ppm vs. MgO wt.%; H) Cr ppm vs. MgO wt.%. Fractionation of olivine and pyroxene is indicated for MgO contents below 30 wt.%. However, above 30 wt.% MgO the trend indicates admixture of olivine and Cr-rich phases. Literature data are from Vilijoen and Vilijoen (1969); Jahn et al. (1982); Lécuyer et al. 1994; Parman et al. (2001); Chavagnac (2004); Robin-Popieul et al. (2012); Kröner et al. (2013, 2016); Puchtel et al. (2013); Sossi et al. (2016).

Sandspruit and Theespruit Formations :

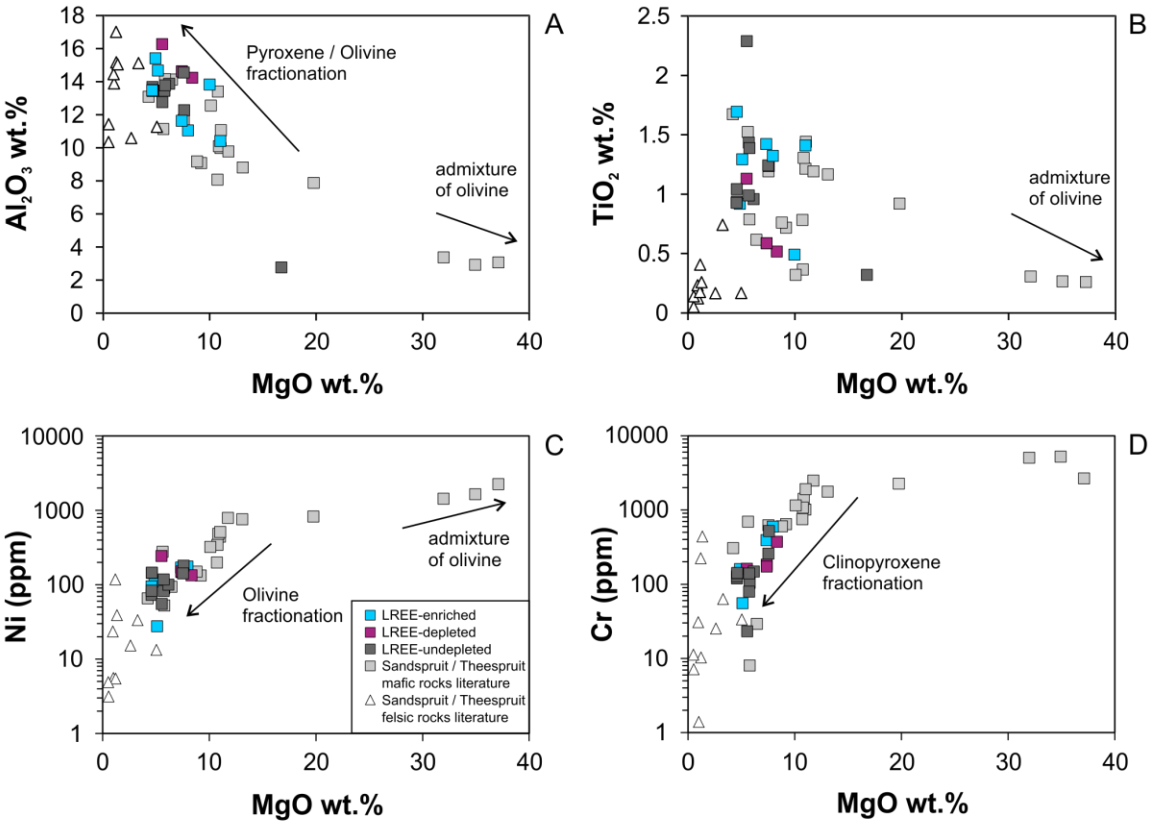

Komati Formation :

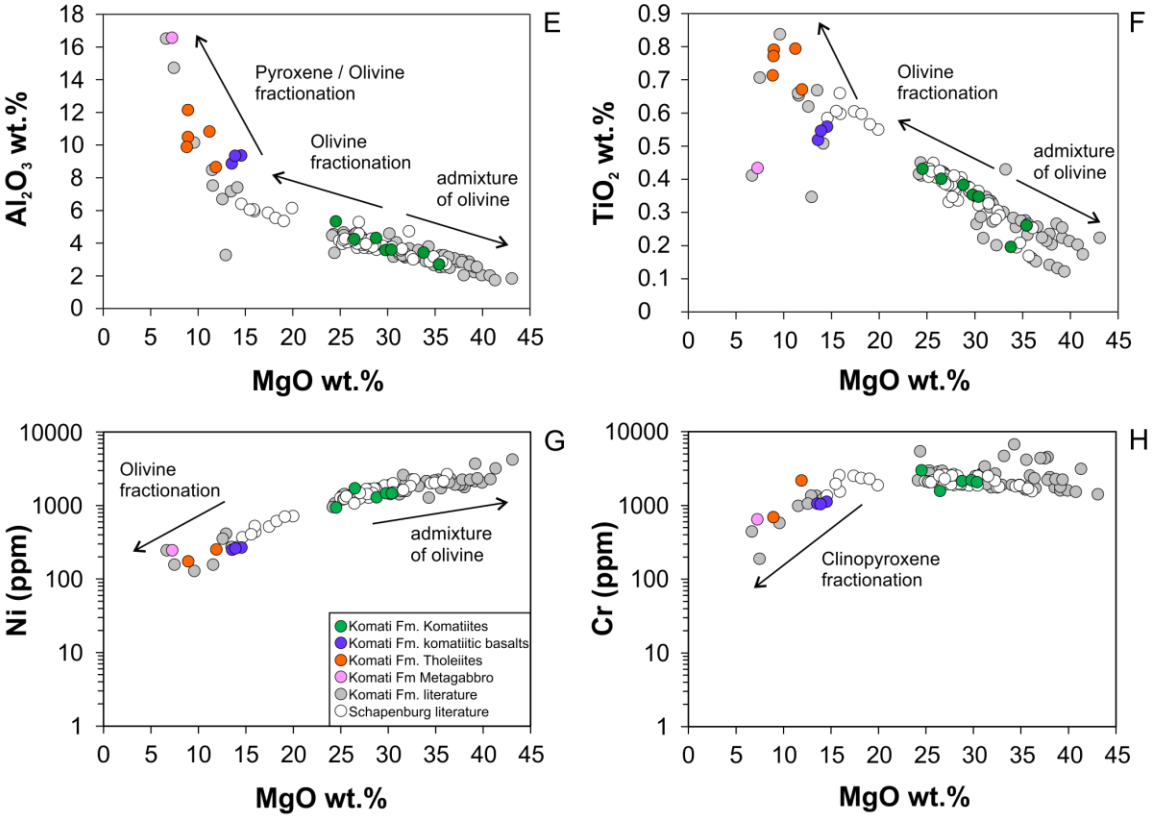

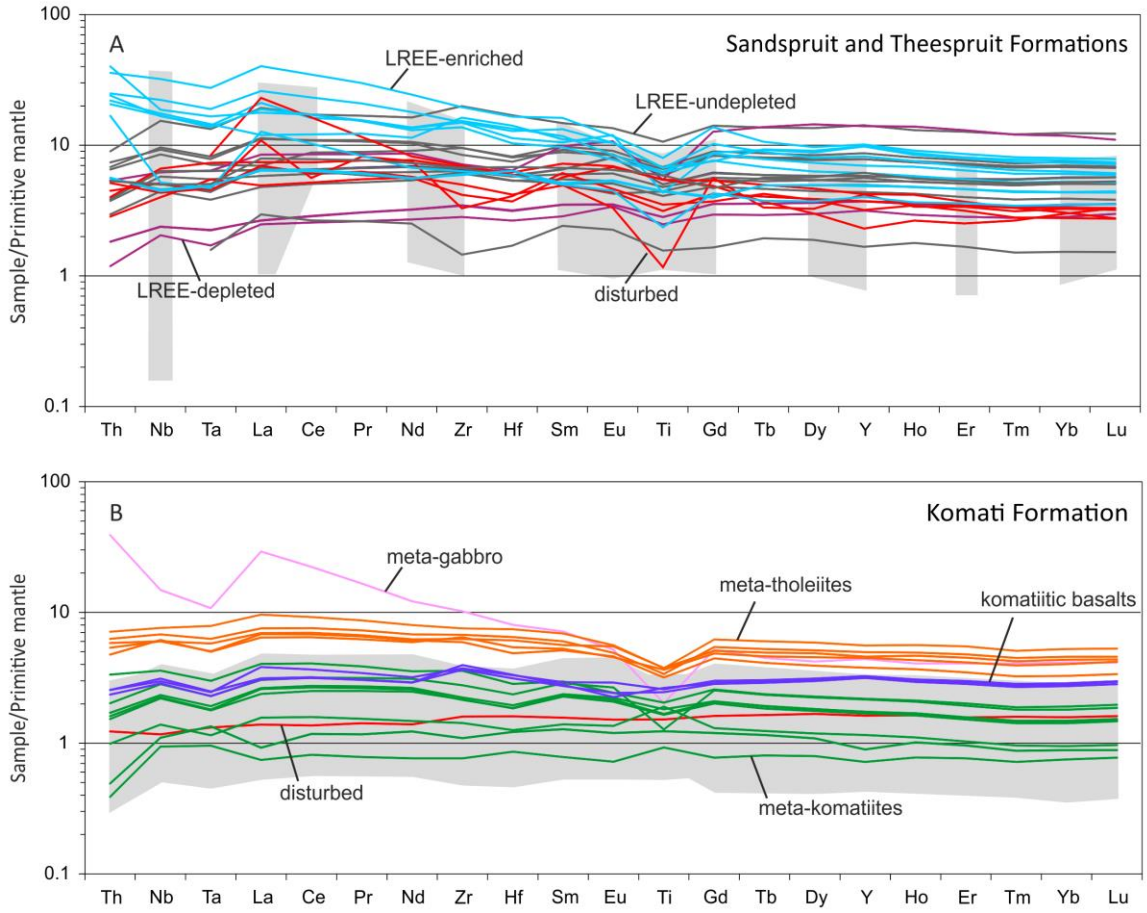

Figure 3.3: Primitive mantle-normalized extended trace element patterns for the Sandspruit/Theespruit Formations (A) and Komati Formation (B) compared to published literature data (gray boxes). Literature data are from Jahn et al. (1982); Parman et al. (2003); Chavagnac (2004); Robin-Popieul et al. (2012); Puchtel et al. (2013); Sossi et al. (2016). Primitive mantle values for normalization are from Palme and O´Neill (2014).

3.5.1.3 Whole-rock Hafnium-Neodymium isotope systematics

The LREE-undepleted samples exhibit $^{176}Lu/^{177}Hf$ and $^{147}Sm/^{144}Nd$ ratios ranging from 0.02339 to 0.03119 and 0.1740 to 0.1984, respectively. Ages used for calculation of $\varepsilon Hf_{(t)}$ and $\varepsilon Nd_{(t)}$ values are reported in Table 3.3. The $\varepsilon Hf_{(t)}$ values for these samples range from +2.6 to +7.5, $\varepsilon Nd_{(t)}$ values are between +0.3 and +1.9. The LREE-enriched and LREE-depleted samples show lower ($^{176}Lu/^{177}Hf$ = 0.01534-0.02059, $^{147}Sm/^{144}Nd$ = 0.1291-0.1869) and higher ($^{176}Lu/^{177}Hf$ = 0.03612-0.05709, $^{147}Sm/^{144}Nd$ = 0.2033-0.2278) ratios, respectively, at consistent $\varepsilon Hf_{(t)}$ ($\varepsilon Hf_{(t)}$ = 0.0 to +4.0) and $\varepsilon Nd_{(t)}$ ($\varepsilon Nd_{(t)}$ = -3.3 to +1.1; Table 3.3).

Most Sandspruit and Theespruit samples plot on the modern terrestrial array of Vervoort et al. (2011) in $\varepsilon Hf_{(t)}$ vs. $\varepsilon Nd_{(t)}$ space (Fig. 3.4a), except for the LREE-enriched

amphibolite KS-BA 183 which has a strongly negative $\varepsilon Nd_{(t)}$ of -3.3 and the LREE-undepleted amphibolite KS-BA 180 which has a very positive $\varepsilon Hf_{(t)}$ of +7.5. However, the epsilon values of the Sandspruit and Theespruit Formations overlap those of the ca. 3.48 Ga Komati Formation, albeit revealing a remarkably smaller scatter compared to the literature data of the Komati Formation (Fig. 3.4b). On average, the Sandspruit and Theespruit units display slightly superchondritic $\varepsilon Hf_{(t)}$ and $\varepsilon Nd_{(t)}$ values. Interestingly, five samples belonging to the LREE-enriched group follow a trend towards subchondritic $\varepsilon Nd_{(t)}$ at chondritic $\varepsilon Hf_{(t)}$. When compared to the felsic volcanic rocks of the same formations (Kröner et al. 2013), the Sandspruit and Theespruit mafic volcanic rocks from this study show less radiogenic $\varepsilon Hf_{(t)}$ at similar $\varepsilon Nd_{(t)}$. When compared to granitoid gneiss samples from the Ancient Gneiss Complex (AGC) of Swaziland (Kröner et al. 2014), our amphibolites of the mafic Sandspruit and Theespruit Formation exhibit similar initial $\varepsilon Nd_{(t)}$ and $\varepsilon Hf_{(t)}$ (Fig. 3.4).

3.5.2 Komati Formation

3.5.2.1 Major element concentrations

The tholeiites and the metagabbro from the Komati Formation show SiO_2 and MgO contents of 51.4-54.7 wt.% and 7.1-11.8 wt.%, respectively. Tholeiites exhibit Al_2O_3/TiO_2 ranging from 12.9 to 15.7. The metagabbro has a much higher Al_2O_3/TiO_2 ratio of 38.2. In comparison to these samples, the komatiites, including the komatiitic basalts, display similar to slightly lower SiO_2 (41.7-53.7 wt.%), and much higher MgO contents (13.1-33.2 wt.%; Fig. 3.2). The komatiites generally display lower-than-chondritic Al_2O_3/TiO_2 values ranging between 9.0 and 12.4 and can therefore be classified as Al-depleted komatiites. However, sample ZA 28a represents a notable exception revealing an Al_2O_3/TiO_2 ratio of 17.5 and is therefore classified as Al-undepleted Munro-type komatiite. In combination with literature data, the komatiites follow an olivine accumulation trend for MgO contents above 30 wt.%, illustrated by the negative correlations of Al_2O_3 and TiO_2 with MgO contents and the positive correlation of Ni with MgO contents (Fig. 3.2e-g). The komatiitic basalts, the tholeiites, and the metagabbro follow an olivine and pyroxene fractionation trend, as indicated by their negative correlations of Al_2O_3 and TiO_2 with MgO contents (Fig. 3.2e, f) and their positive correlations of Ni, Sc, and Cr contents with MgO (Fig. 3.2g, h).

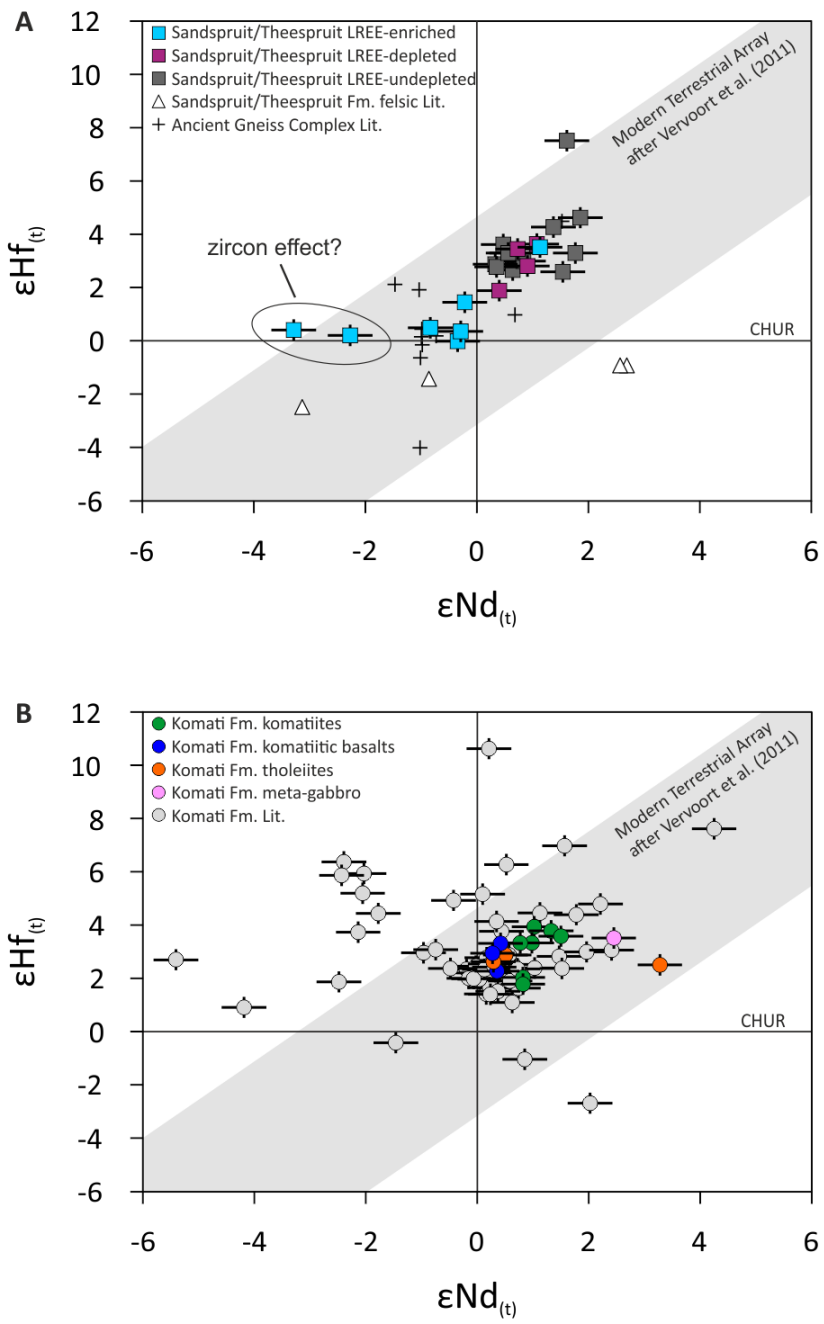

Figure 3.4: A) εHf(t) vs. εNd(t) diagram for mafic and ultramafic rocks of the Sandspruit and Theespruit Formations, grouped in LREE-enriched, LREE-depleted, and LREE-undepleted patterns. The LREE-enriched samples show a trend from more depleted towards chondritic initial εHf(t) and subchondritic initial εNd(t) values. However, two LREE-enriched samples having chondritic εHf(t) at negative εNd(t) could have been affected by a "zircon effect". For comparison, literature data are for granitoid gneisses of the Ancient Gneiss Complex calculated to 3.5 Ga (black symbols; Kröner et al. 2014) and from felsic volcanic rocks of the Sandspruit and Theespruit Formations (white triangles; Kröner et al. 2013). B) εHf(t) vs. εNd(t) diagram for komatiites, komatiitic basalts, tholeiites, and a metagabbro of the Komati Formation. Literature data for the Komati Formation are from Lahaye et al. (1995), Blichert-Toft and Arndt (1999), Puchtel et al. (2013), Blichert-Toft et al. (2015). The majority of analyzed samples follow the modern terrestrial array of Vervoort et al. (2011).

Table 3.3: Hafnium-Neodymium isotope compositions of samples of the Sandspruit, Theespruit, and Komati Formations.

Fm.	Sample	Age* (Ma)	Lu (µg/g)	Hf (µg/g)	$^{176}Lu/^{177}Hf$ (mes.)	$^{176}Hf/^{177}Hf$ (mes.)	±2s.d.	$\varepsilon Hf_{(t)}$	Sm (µg/g)	Nd (µg/g)	$^{147}Sm/^{144}Nd$ (mes.)	$^{143}Nd/^{144}Nd$ (mes.)	±2s.d.	$\varepsilon Nd_{(t)}$
Sandspruit Fm.	**BA 147**	3553	0.5033	2.620	0.02726	0.282470	±6	4.3	3.509	11.08	0.19150	0.512594	±8	1.4
	BA 149 a	3553	0.2316	1.320	0.02491	0.282255	±5	2.3	0.917	6.87	0.08070	0.511988	±8	40.7
	KS-BA 171 A	3553	0.311	1.84	0.02397	0.282202	±8	2.8	2.07	7.01	0.17836	0.512234	±8	0.4
	KS-BA 171 B	3553	0.311	1.86	0.02375	0.282190	±11	2.9	2.07	6.96	0.17953	0.512260	±11	0.3
	KS-BA 175	3553	0.196	1.21	0.02298	0.282052	±11	-0.1	2.48	9.37	0.15974	0.511823	±7	0.9
Sandspruit/ Theespruit Fm.	**KS-BA 176**	3530	0.110	0.511	0.03045	0.282645	±9	2.7	0.951	3.14	0.18288	0.512356	±10	0.6
	KS-BA 178	3530	0.231	1.77	0.01851	0.281766	±9	0.3	1.94	10.19	0.11480	0.510713	±7	-0.4
	KS-BA 180	3530	0.384	2.09	0.02607	0.282483	±12	7.5	2.65	9.03	0.17772	0.512285	±8	1.6
Theespruit Fm.	**BA 129**	3530	0.2068	0.804	0.03652	0.283086	±4	3.6	1.131	3.36	0.20333	0.512856	±9	1.1
	BA 145	3530	0.5375	2.842	0.02684	0.282454	±6	4.6	3.884	12.99	0.18080	0.512370	±7	1.9
	BA 146	3530	0.4870	2.639	0.02619	0.282372	±5	3.3	3.630	12.61	0.17404	0.512207	±5	1.8
	BA 155 A	3538	0.2500	0.9825	0.03612	0.283054	±8	3.4	1.339	3.90	0.20783	0.512944	±7	0.7
	BA 155 B	3538	0.251	0.979	0.03637	0.283052	±9	2.8	1.34	3.91	0.20735	0.512942	±8	0.9
	BA 156	3530	0.368	1.69	0.03096	0.282689	±6	3.0	2.14	6.53	0.19836	0.512728	±7	0.8
	BA 158	3530	0.894	5.43	0.02339	0.282162	±7	2.6	5.94	20.08	0.17884	0.512308	±7	1.5
	BA 159	3530	0.382	3.53	0.01534	0.281547	±7	0.2	3.86	16.16	0.14435	0.511309	±6	-2.3
	BA 161	3530	0.430	3.66	0.01664	0.281629	±7	0.0	4.17	16.69	0.15099	0.511562	±6	-0.3
	LON-11-12	3521	0.150	1.12	0.01897	0.281429	±6	-12.9	1.94	7.61	0.15427	0.511687	±10	0.6
	LON-11-13	3521	0.165	0.763	0.03066	0.282119	±6	-16.6	2.16	10.02	0.13017	0.511141	±9	0.9
	LON-11-14	3521	0.366	1.85	0.02815	0.282515	±6	3.6	2.32	7.57	0.18561	0.512412	±9	0.5
	LON-11-15	3521	0.231	2.00	0.01638	0.281728	±7	4.0	2.84	9.44	0.18178	0.512336	±9	0.7
	LON-11-18	3521	0.815	2.03	0.05709	0.284434	±7	1.9	3.63	9.64	0.22783	0.513392	±8	0.4
	LON-11-20 A	3521	0.410	1.88	0.03104	0.282704	±7	3.3	2.47	8.09	0.18496	0.512402	±9	0.6
	LON-11-20 B	3521	0.411	1.87	0.03119	0.282713	±8	3.3	2.53	8.41	0.18164	0.512327	±8	0.6
	LON-11-22	3521	0.195	1.10	0.02526	0.281953	±6	-9.4	2.32	7.23	0.19425	0.512630	±8	0.8
	KS-BA 181	3530	0.515	4.01	0.01824	0.281752	±7	0.5	4.58	16.94	0.16342	0.511827	±8	-0.8
	KS-BA 182	3530	0.444	3.85	0.01637	0.281651	±9	1.4	5.27	22.24	0.14312	0.511384	±6	-0.2

Table 3.3 continued.

Fm.	Sample	Age* (Ma)	Lu (µg/g)	Hf (µg/g)	$^{176}Lu/^{177}Hf$ (mes.)	$^{176}Hf/^{177}Hf$ (mes.)	±2s.d.	$\varepsilon Hf_{(t)}$	Sm (µg/g)	Nd (µg/g)	$^{147}Sm/^{144}Nd$ (mes.)	$^{143}Nd/^{144}Nd$ (mes.)	±2s.d.	$\varepsilon Nd_{(t)}$
Theespruit Fm.	**KS-BA 183**	3530	0.537	4.25	0.01792	0.281728	±10	0.4	4.44	14.36	0.18685	0.512250	±7	-3.3
	KS-BA 184	3530	0.561	4.93	0.01617	0.281608	±10	0.4	6.44	30.17	0.12911	0.511053	±6	-0.3
	KS-BA 189	3553	0.257	1.77	0.02059	0.281991	±11	3.5	1.99	8.42	0.14256	0.511431	±7	1.1
Komati Fm.	**BA 162** (Gabbro)	3481	0.293	2.44	0.01702	0.281770	±8	3.5	2.77	14.92	0.11236	0.510830	±6	2.5
	BA 163 (Thol.)	3481	0.106	0.467	0.03210	0.282670	±5	-0.5	0.531	1.614	0.19886	0.512750	±8	1.1
	ZA 29 a (Thol.)	3482	0.337	1.63	0.02927	0.282554	±15	2.1						
	ZA 29 b (Thol.)	3482	0.280	1.48	0.02695	0.282391	±15	1.9						
	Za 29bR	3482	0.291	1.67	0.02468	0.282267	±5	2.9	2.10	7.38	0.17200	0.512103	±7	0.5
	ZA 29 c (Thol.)	3482	0.304	1.46	0.02960	0.282589	±19	2.6						
	Za 31a (Thol.)	3482	0.235	1.52	0.02184	0.282065	±6	2.5	1.92	7.38	0.15723	0.511904	±9	3.3
	Za 32a (Thol.)	3482	0.295	1.70	0.02463	0.282255	±5	2.6	2.10	7.31	0.17380	0.512134	±8	0.3
	ZA 28 a (Kom.)	3482	0.059	0.238	0.03534	0.282959	±38	2.0						
	ZA 28aR	3482							0.354	1.11	0.19262	0.512594	±7	0.8
	ZA 28 b (Kom.)	3482	0.067	0.363	0.02616	0.282419	±24	4.8						
	Za 28bR	3482	0.067	0.359	0.02644	0.282414	±8	3.9	0.573	1.78	0.19449	0.512647	±10	1.0
	Za 30a (Kom.)	3482	0.136	0.892	0.02157	0.282083	±3	3.8	1.16	4.30	0.16260	0.511928	±7	1.3
	Za 33 (Kom.)	3482	0.105	0.609	0.02448	0.282265	±5	3.3	0.924	3.23	0.17278	0.512145	±8	1.0
	Za 35 (Kom.)	3482	0.103	0.582	0.02506	0.282312	±8	3.6	0.918	3.17	0.17525	0.512228	±10	1.5
	Za 36 (Kom.)	3482	0.104	0.583	0.02531	0.282278	±4	1.8	0.894	3.04	0.17774	0.512251	±7	0.8
	Za 38 (Kom.)	3482	0.120	0.700	0.02432	0.282254	±4	3.3	1.05	3.57	0.17824	0.512261	±5	0.8
	Za 50 (KB)	3482	0.193	0.981	0.02788	0.282493	±4	3.3	1.04	3.42	0.18399	0.512375	±7	0.4
	Za 51 (KB)	3482	0.215	1.07	0.02862	0.282532	±3	2.9	1.17	3.77	0.18712	0.512440	±7	0.3
	Za 52 (KB)	3482	0.207	1.02	0.02862	0.282514	±4	2.3	1.13	3.84	0.17819	0.512238	±7	0.4
	Reference material													
	AGV-2 (mean)											0.512567 (n=7)		
	BHVO-2 (mean)											0.512836 (n=8)		

*3521 Ma: Roerdink et al. (2013); 3530 Ma: Vilijoen & Vilijoen (1969); Kröner et al. (1996); Van Kranendonk et al. (2009); 3538 Ma: Armstrong et al. (1990); Kamo and Davis (1994); 3553 Ma: Kröner et al. (1996); Thol. = Tholeiite, Kom. = Komatiite, KB = Komatiitic basalt.

3.5.2.2 Trace element concentrations

Our trace element data for the Komati Formation samples agree well with data from Parman et al. (2003), Chavagnac (2004), Robin-Popieul et al. (2012), Puchtel et al. (2013), and Sossi et al. (2016; Fig. 3.3). The PM-normalized incompatible trace element patterns are generally flat with minor depletion of the HREE relative to the LREE and MREE. The values of Gd_{CN}/Yb_{CN} of komatiites, komatiitic basalts, and tholeiites range from 1.0 to 1.4. In contrast, the metagabbro shows enrichment in highly incompatible elements. The Komati Formation samples analyzed in this study can be subdivided into (a) komatiites showing spinifex-texture and MgO contents >24 wt.% with flat REE patterns that are up to four times enriched relative to PM; (b) komatiitic basalts being in composition similar to komatiites, albeit having lower MgO abundances of ~13 to 14 wt.%, and are about four times enriched relative to PM; and (c) tholeiitic basalts showing negative Ti anomalies, low MgO concentrations, and relatively flat REE that are five- to eightfold enriched relative to PM (Fig. 3.3b). Negative anomalies for Th and Ti as well as slightly negative Ta anomalies with Ta/Ta_{PM}* of 0.72 to 0.91 are generally observed for tholeiites and komatiites of the Komati Formation (Table 3.1). However, two komatiites show distinctly positive Ti anomalies. Four komatiites lack a Ti anomaly. Tholeiites and komatiites display slightly positive Nb anomalies with Nb/Nb_{PM}* ranging from 1.01 to 1.40. The metagrabbro also shows negative Ti and Ta anomalies (Ta/Ta_{PM}* = 0.49), a negative Nb anomaly (Nb/Nb_{PM}* = 0.60), and a positive Th anomaly. Komatiite BA 163 shows no anomalies and displays an incompatible element composition similar to primitive mantle values. Values of La_{CN}/Yb_{CN} for tholeiites, komatiitic basalts, and komatiites range from 0.9 to 2.1, that of the metagabbro is 7.1 (Table 3.1).

3.5.2.3 Whole-rock Hafnium-Neodymium isotope systematics

Our samples from the Komati Formation agree well with published $\varepsilon Hf_{(t)}$ and $\varepsilon Nd_{(t)}$ values (Lahaye et al. 1995, Blichert-Toft and Arndt 1999, Puchtel et al. 2013, Blichert-Toft et al. 2015), but show a significantly lower spread in both values (Fig. 3.4b). Tholeiites show typical $^{176}Lu/^{177}Hf$ and $^{147}Sm/^{144}Nd$ values of 0.02184 to 0.02960 and 0.1572 to 0.1738, respectively. Ages used for calculation of $\varepsilon Hf_{(t)}$ and $\varepsilon Nd_{(t)}$ values are reported in Table 3.3. The calculated $\varepsilon Hf_{(t)}$ and $\varepsilon Nd_{(t)}$ values are +1.9 to +2.9 and +0.3 to +0.5, respectively (Fig. 3.4b). The komatiites show a wide range of $^{176}Lu/^{177}Hf$ from 0.02157 to 0.03534 and $^{147}Sm/^{144}Nd$ from 0.1626 to 0.1987, respectively, with $\varepsilon Hf_{(t)}$

ranging from -0.5 to +4.8, and $\varepsilon Nd_{(t)}$ ranging from -0.1 to +1.5 (Fig. 3.4b). The komatiitic basalts show a much narrower range in $^{176}Lu/^{177}Hf$ and $^{147}Sm/^{144}Nd$ with $^{176}Lu/^{177}Hf$ ranging from 0.02788 to 0.02862 and $^{147}Sm/^{144}Nd$ ranging from 0.1782 to 0.1871. Their $\varepsilon Hf_{(t)}$ are +2.3 to +3.3, their $\varepsilon Nd_{(t)}$ are +0.3 to +0.4 (Fig. 3.4b). The metagabbro sample has lower $^{176}Lu/^{177}Hf$ (0.01702) and $^{147}Sm/^{144}Nd$ (0.1122) and a higher $\varepsilon Nd_{(t)}$ value of +2.5, yet an $\varepsilon Hf_{(t)}$ of +3.5 that is higher than those of the tholeiites and komatiites of the same formation.

3.6 Discussion

3.6.1 Effects of alteration and metamorphism

The influence of alteration and metamorphism on pristine geochemical compositions of Archean volcanic sequences such as rocks from the lower Onverwacht Group of the BGB is a major concern in geochemical studies of such sequences. Alteration in these rocks was likely caused by post-magmatic element mobility during metamorphism or hydrothermal fluid infiltration during metamorphism or seafloor alteration (Lahaye et al. 1995; Hofmann and Harris 2008). The volcanic sequences of the Sandspruit and Theespruit Formations have undergone amphibolite-facies metamorphism with subsequent greenschist-facies overprint. Amphibolite-facies metamorphism is expressed in the petrographic properties of these rocks, in particular addition of water and the breakdown of pyroxene into amphibole, epidote, titanite and garnet. In contrast, the rocks of the Komati Formation were only affected by a greenschist-facies overprint which is mostly indicated by addition of water and chloritization of magmatic minerals. SiO_2 was likely mobile during alteration, whereas elements like Ti, Zr, Y, Nb, and Sc commonly behave as immobile elements during aqueous alteration processes (Polat et al. 2002). Hofmann and Harris (2008) recognized that silica alteration is a common feature in almost all BGB sequences, typically accompanied by specific elemental depletion and enrichment patterns. According to these authors, silica alteration is accompanied by the enrichment of elements like K, Rb, and Ba and the depletion of elements like Ni, Co, Cu, and Zn (Hofmann and Harris 2008).

3.6.1.1 Sandspruit and Theespruit Formations

In thin section, the samples of the Sandspruit and Theespruit Formations show major to minor evidence of chloritization or carbonatization. However, the originally mafic volcanic rock LON-11-15, sampled from below a silicified schist zone (Roerdink 2013), has been effected by silicification, now displaying an elevated SiO_2 content of 68.6 wt.%. In addition, this sample shows many characteristics of silicified volcanic rocks from the BGB as described by Hofmann and Harris (2008), namely depletions of Cu, Zn, and Y and elevated La_{CN}/Yb_{CN} values (La_{CN}/Yb_{CN} = 2.5; Table 3.1). Thus, sample LON-11-15 shows signs of extensive subseafloor hydrothermal alteration, and its major and trace element as well as Hf-Nd isotope compositions are excluded from interpretation in the following sections.

The ^{176}Lu-^{176}Hf systematics of LON-11-22 and the ^{147}Sm-^{143}Nd systematics of BA 149a are disturbed, yielding unrealistically negative $\varepsilon Hf_{(t)}$ of -9.4 and positive $\varepsilon Nd_{(t)}$ of +40.7, respectively (Table 3.3). Additionally, disturbed trace element compositions were observed for amphibolites LON-11-22, KS-BA 175 and KS-BA 178, as indicated by 'spiky', non-coherent trace element patterns (Fig. 3.3, Tables 3.1, 3.2). As a result, these samples are also excluded from further interpretation in this manuscript.

Although the above-mentioned samples show clear signs of hydrothermal alteration, the majority of investigated samples of this study inherited relatively unperturbed geochemical signatures. These can be observed as relatively smooth incompatible trace element patterns relative to PM (Fig. 3.2). The trends in the Harker diagrams correspond broadly with fractionation trends, suggesting that the major geochemical characteristics of most investigated samples from the Sandspruit and Theespruit Formations were preserved throughout amphibolite- and/or greenschist-facies metamorphism. In a study of boninite-like rocks of the 3.7-3.8 Ga Isua Greenstone Belt from western Greenland, Polat et al. (2002) defined some criteria that pristine igneous features of Archean volcanic rocks need to meet: (1) Concentrations of incompatible elements show clear correlations with Zr contents in binary diagrams, for example Zr-Nd and Zr-Nb; (2) no Ce anomalies are present; (3) the samples show less than 2 % enrichment in carbonate and silica; and (4) the LOI is below 6 wt.%. Combined, our least altered samples from the ca. 3.53 Ga Sandspruit and Theespruit Formations all meet the above criteria and are therefore regarded as metamorphosed Archean volcanic rocks that have preserved largely

undisturbed igneous major and immobile trace element as well as correlated initial Hf-Nd isotope compositions of most samples (Fig. 3.4).

3.6.1.2 Komati Formation

We note that LOI values of some komatiites can reach as high as 8.7 wt.%. Such high values are a common feature of komatiite suites and is a consequence of serpentinization of olivine (Arndt et al. 2008). Samples of the Komati Formation also show extensive chloritization or serpentinization in thin section, and primary minerals have been replaced by secondary phases. However, our samples still have well preserved igneous textures and generally retained relatively undisturbed geochemical signatures. A notable exception is komatiite sample BA 163. This sample is highly serpentinized and shows a slight enrichment in SiO_2 (49.9 wt.%) compared to the other komatiites that usually have SiO_2 contents below 48.6 wt.%. Additionally, the content of Ba (85 ppm) in BA 163 is higher than in unaltered samples that usually have Ba contents below ca. 38 ppm. Also, the Hf-Nd isotope characteristics of this sample are disturbed (Table 3.3). This compositional modification can be linked to serpentinization during later greenschist-facies overprint rather than to sea-floor silica alteration as observed for samples of the older Sandspruit and Theespruit Formations. This is because the disturbed komatiites of the Komati Formation lack characteristic sea-floor related element enrichment and depletion patterns such as enrichment in SiO_2, K_2O, Ba and Rb and depletion in Y and Sr as described by Hofmann and Harris (2008). As a result, sample BA 163 is not considered further for interpretation.

In element versus MgO content space, the selected elements show clear correlations for all remaining samples of the Komati Formation (Fig. 3.2e-h). This indicates that neither major nor trace elements were significantly mobilized during greenschist-facies overprint. Furthermore, the Hf and Nd isotopes in these samples define regression lines in isochron diagrams (Fig. 3.8) that correspond to the actual age of emplacement of the Komati Formation, indicating that the Hf-Nd isotope composition of our samples was not significantly disturbed (see discussion in chapter 5.2). Collectively, most of our samples from the Komati Formation preserve relatively undisturbed geochemical characteristics and meet the criteria for unperturbed igneous rocks as defined by Polat et al. (2002) and Hofmann and Harris (2008).

3.6.2 Age constraints on samples from the Sandspruit, Theespruit, and Komati Formations

The LREE-depleted and LREE-undepleted groups of samples of the Sandspruit and Theespruit Formations are characterized by $\varepsilon Hf_{(t)}$ of generally +3 to +4 (Fig. 3.5a) defining a Lu-Hf regression line corresponding to an age of 3599 ± 83 Ma (MSWD = 13; Fig. 3.6b). The LREE-enriched group is characterized by overall chondritic $\varepsilon Hf_{(t)}$ values (Fig. 3.5a), one exception is sample KS-BA 189 that has an $\varepsilon Hf_{(t)}$ of +3.5. This group of samples yielded a Lu-Hf regression line corresponding to the same age of 3599 ± 91 Ma (MSWD = 1.7; Fig. 3.6a) as the LREE-depleted and LREE-undeleted groups of samples. The corresponding Sm-Nd regression line including the samples of all three groups yielded a slope equivalent to an age of 3560 ± 82 Ma (MSWD = 43; Fig. 3.6c). The three age data overlap, within uncertainty, and also agree with the published eruption age of 3.55 to 3.48 Ga for the Sandspruit and Theespruit Formations, based on U-Pb zircon dating (Armstrong et al. 1990; Kröner et al., 2016).

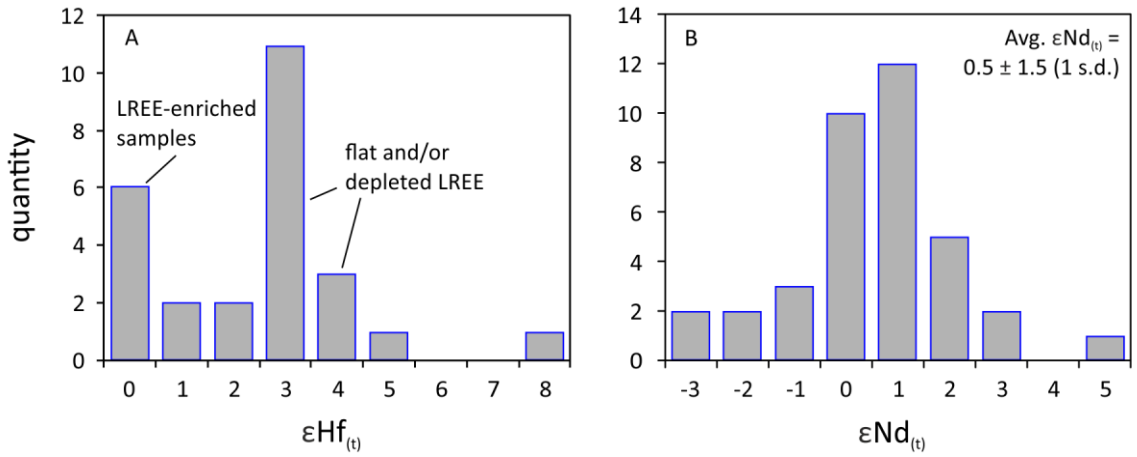

Figure 3.5: Histograms of εHf(t) (A) and εNd(t) (B) for published data and data of this study for mafic and ultramafic rocks of the Sandspruit and Theespruit Formations. On the basis of εHf(t), two groups of samples can be distinguished: The LREE-enriched rocks generally have εHf(t) ≈ 0, and samples with undepleted to depleted LREE have εHf(t) of 3 to 4. In contrast, the most frequently observed range in εNd(t) is from 0 to 2. The calculated average εNd(t) is 0.5 ± 1.5 (1 s.d.), respectively. Literature data are from Jahn et al. (1982), Gruau et al. (1990), Blichert-Toft and Arndt (1999), Van Kranendonk et al. (2009).

The Komati Formation samples of all three groups analyzed in this study generally have $\varepsilon Hf_{(t)}$ of +2 to +4 and $\varepsilon Nd_{(t)}$ of 0 to +3 (Fig. 3.7a,b) yielding Lu-Hf and Sm-Nd regression lines that correspond to ages of 3424 ± 73 Ma (MSWD = 37) and 3466 ± 76 Ma (MSWD = 50; Fig. 3.8a, b), respectively, overlapping with the accepted eruption

age of 3.48-3.45 Ga (Armstrong et al. 1990). In addition, one metagabbro (BA 162) was sampled that has a LREE-enriched pattern distinct from all other samples of the Komati Formation (Fig. 3.3b), possibly reflecting crustal contamination. However, the high average $\varepsilon Hf_{(t)}$ value of +3.5 indicates a more juvenile origin. The gabbros in the Komatii Formation are intrusive into the effusive volcanic rocks, and some of these gabbroic bodies yielded zircon ages ranging from 3351 to 3482 Ma (e.g., Armstrong et al. 1990). Hence, it is possible that sample BA 162 may represent one of the younger generation gabbros, leading to overestimated radiogenic $\varepsilon Nd_{(t)}$ and $\varepsilon Hf_{(t)}$ values, because of incorrect age assignment.

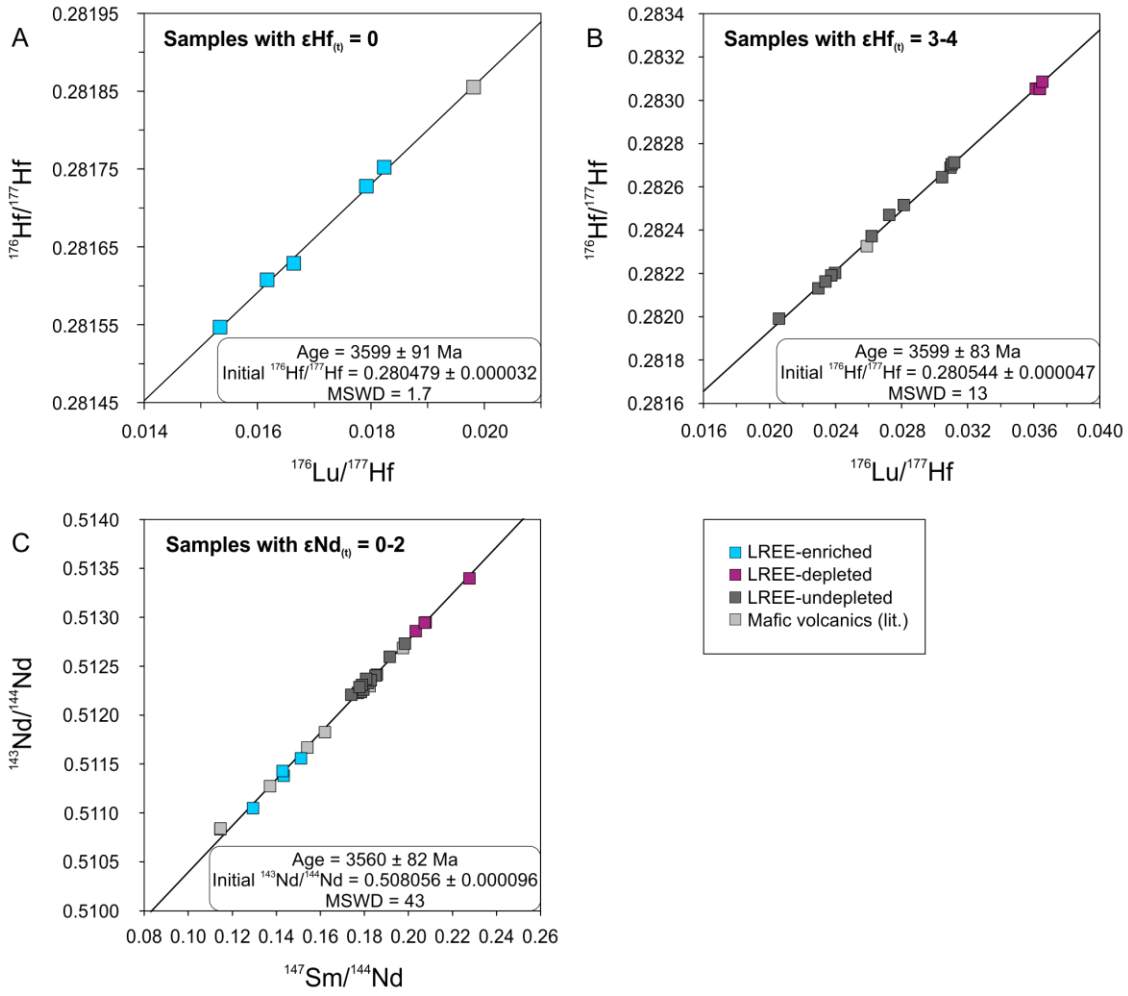

Figure 3.6: Whole-rock regression lines for mafic and ultramafic rocks of the Sandspruit and Theespruit Formations including our data and data from the literature (Gruau et al. 1990; Blichert-Toft and Arndt 1999; Van Kranendonk et al. 2009). A) Lu-Hf regression line for LREE-enriched samples with εHf(t) = 0 corresponding to an age of 3599 ± 91 Ma (MSWD = 1.7). B) Lu-Hf regression line for LREE-undepleted and LREE-depleted samples with εHf(t) = +3 to +4 corresponding to an age of 3599 ± 83 Ma (MSWD = 13). C) Sm-Nd regression line for samples with εNd(t) = 0 to +1 corresponding to an age of 3560 ± 82 Ma (MSWD = 43). All ages are in agreement, within error, with the emplacement ages of 3.55 to 3.48 Ga for the Sandspruit and Theespruit Formations (Kröner et al., 2013; 2016; Roerdink et al, 2016).

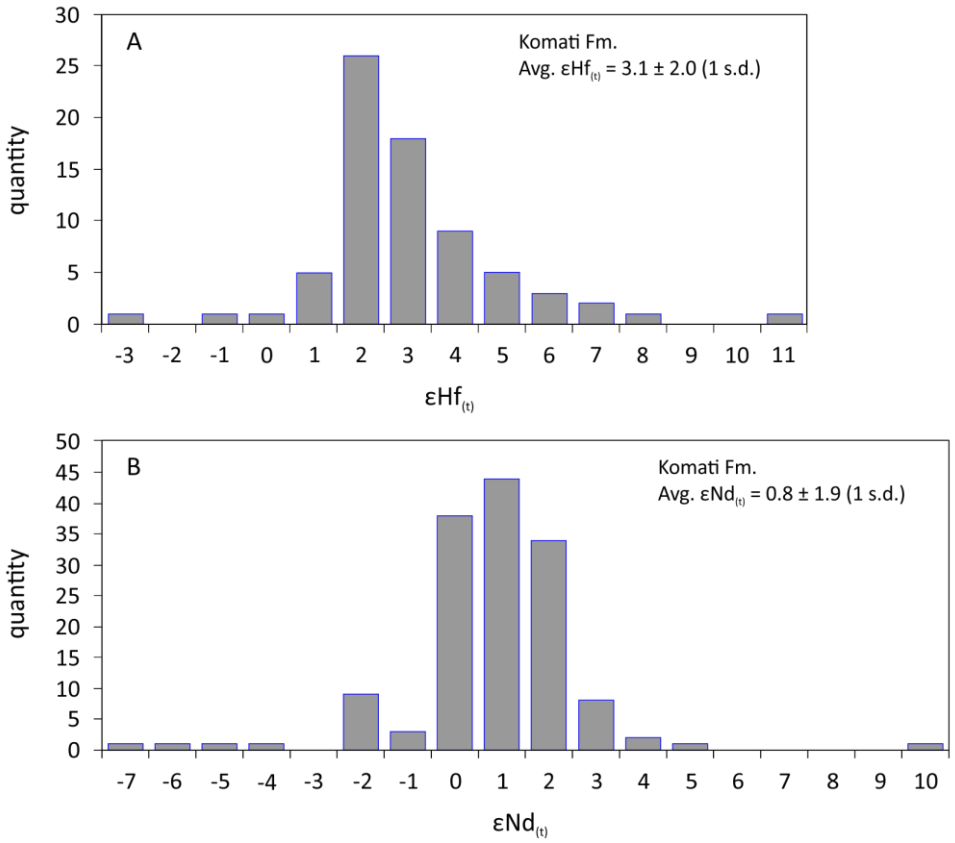

Figure 3.7: Histograms of εHf(t) (A) and εNd(t) (B) for published data and data of this study for mafic and ultramafic rocks of the Komati Formation. The most frequently observed ranges in εHf(t) and εNd(t) is from +2 to +4 and 0 to +3, respectively. Calculated average values for εHf(t) and εNd(t) are 3.1 ± 2.0 (1 s.d.) and 0.8 ± 1.9 (1 s.d.), respectively. Literature data are from Hamilton et al. (1979), Gruau et al. (1990), Lahaye et al. (1995), Blichert-Toft and Arndt (1999), Blichert-Toft et al. (2015), Chavagnac (2004), Puchtel et al. (2013).

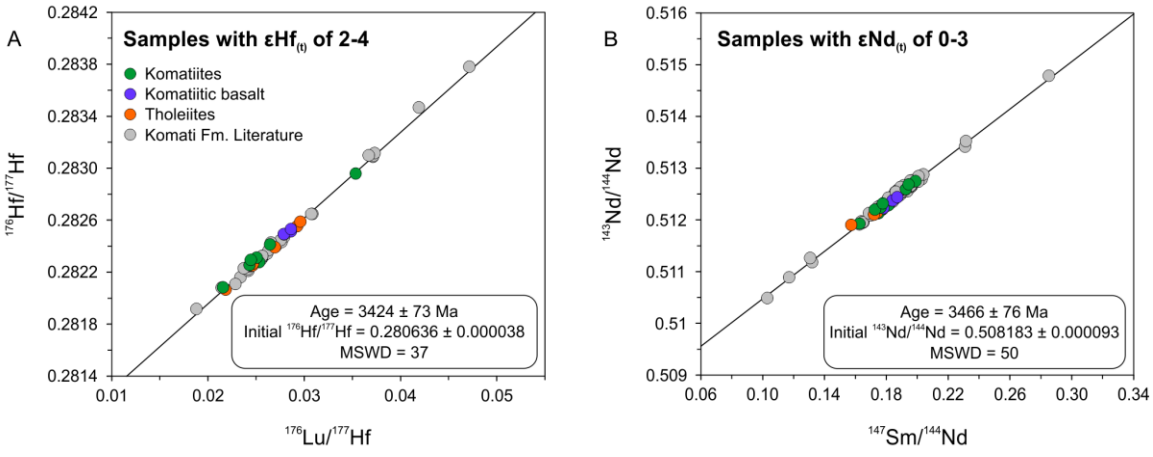

Figure 3.8: Whole-rock regression lines for samples of the Komati Formation with (A) εHf(t) of +2 to +4 and (B) εNd(t) of 0 to +3. For the Lu-Hf system the regression line corresponds to an age of 3424 ± 73 Ma (MSWD = 37) and for the Sm-Nd system to an age of 3466 ± 76 Ma (MSWD = 50). Both ages are in agreement, within error, with the published age of 3.48-3.45 Ga for the Komati Formation (Armstrong et al. 1990), indicating that these rocks are relatively pristine and were not affected by crustal contamination or mixing with felsic magma. Literature data are from Hamilton et al. (1979), Gruau et al. (1990), Lahaye et al. (1995), Blichert-Toft and Arndt (1999), Chavagnac (2004); Blichert-Toft et al. (2015).

3.6.3 Evaluation of crustal contamination

Archean greenstone belts were deposited on an older crustal basement (e.g., Campbell and Davies, 2017 and refs. therein). Evidence for interaction of primary magmas with older continental crust is thus abundant from the chemical properties of greenstone belts and their zircon record that often reveals inheritance (e.g., Chauvel et al. 1983, 1985; Arndt and Jenner, 1986; Polat et al. 2005; Cattell et al. 1984; Kröner and Tegtmeyer 1994; Bolhar et al. 2002; Boily et al. 2009; Maurice et al. 2009). In case of the Barberton Greenstone Belt, evidence for an older basement is based on the presence of ca. 3702 Ma old inherited zircon xenocrysts in the 3.45 Ga Vlakplaats granodiorite that intruded the Theespruit Formation close to the 3.51 Ga Steynsdorp Pluton (Kröner et al. 1996). However, not only plutonic rocks carry inherited zircons but also some felsic volcanic rocks of the Theespruit Formation that are interlayered with mafic units (Roerdink et al. 2016). Moreover, heterogeneous initial Hf isotope compositions in magmatic zircons from felsic volcanic rocks of the Sandspruit, Theespruit, and the ca. 3.45 Ga Hooggenoeg Formations of the Onverwacht Group have been reported (Kröner et al. 2013; 2016), and Lu-Hf crustal model ages of zircons from felsic volcanic rocks of the Sandspruit and Theespruit Formations range from 3.6 to 3.9 Ga (Kröner et al. 2016). The inherited zircon record and the heterogeneous Hf-in-zircon isotope compositions of plutonic and effusive rocks of the BGB have been taken as evidence for interaction with older AGC crust (Kröner et al. 1996, 2013, 2016). In contrast, de Wit et al. (2018) interpret the heterogeneous Hf-in-zircon isotope signatures in the felsic volcanic rocks of the BGB as being the result of a contribution from older subducted clastic sediments. However, we reject this hypothesis, because no field evidence in form of unidirectional asymmetry that could be related to subduction in the southern Barberton granite-greenstone terrane has so far been found (e.g. Anhaeusser 1984; Van Kranendonk 2011, Brown, 2015). Thus, interaction of felsic volcanic rocks with an older basement may have been a common process, hinting also towards the presence of a crustal contaminant in the mafic volcanic rocks of the lower Onverwacht Group.

Crustal contamination of komatiites, komatiitic basalts, and tholeiites of the Komati Formation has so far not been reported in the literature (e.g., Robin-Popieul et al. 2012), and our study confirms the absence of crustal contamination as indicated by overall positive $\varepsilon Hf_{(t)}$ and $\varepsilon Nd_{(t)}$, as well as slightly positive Nb anomalies, and high Zr/Th (130-

270) in our sample set. Consequently, in the following we only discuss the contamination process of Sandspruit and Theespruit mafic amphibolites by crustal material.

The amphibolite samples of the Sandspruit and Theespruit Formations analyzed in this study are interlayered with felsic volcanic rocks, indicating synchronous bimodal volcanism (e.g., Viljoen and Viljoen 1969a; Kröner et al. 1991, 2013, 2016). These felsic volcanic rocks carry inherited zircons resulting from interaction with or formation from continental crust (Kröner et al. 2013; Roerdink et al. 2016). Hence, it is likely that the mafic rocks also interacted with crustal material. In Th/Yb vs Nb/Yb space (Fig. 3.9a), the LREE-depleted and LREE-undepleted groups of samples overlap the field of komatiites and the present-day MORB-OIB array of Pearce (2008), indicating a relatively unaltered geochemical composition that was not substantially altered by crustal contamination. In contrast, the samples from the LREE-enriched group lie on an array toward the >3.55 Ga AGC granitoids (Kröner et al. 2014) and their partial melting products, represented by the felsic volcanic rocks of the Sandspruit and Theespruit Formations (Van Kranendonk et al. 2009; Kröner et al. 2013). Both the >3.55 Ga AGC granitoids and felsic volcanic rocks may constitute an end member composition for contamination. The other end member is on the MORB-OIB array after Pearce (2008) at slightly depleted Th/Yb and Nb/Yb compositions, indicating a depleted mantle-like (DM) source for the parental melts (Fig. 3.9a). From this observation we conclude that two different scenarios for contamination of the Sandspruit/Theespruit samples could apply: (1) assimilation-fractional crystallization (AFC) of >3.55 Ga AGC crust or (2) magma mixing with crustally-derived felsic melts of the same formation. The latter scenario was already proposed for felsic volcanic rocks within the Pilbara Craton (Van Kranendonk et al. 2015), Yilgarn Craton (Barnes and van Kranendonk 2014), Northeastern Superior Province (Maurice et al. 2009), Abitibi Greenstone Belt (Leclerc et al. 2011), and Mesoarchean andesites from southern West Greenland (Szilas et al. 2017). However, although magma mixing of felsic and mafic components could approximate most trace element characteristics of the LREE-enriched samples, simple magma mixing fails to reproduce the SiO_2 content of some LREE-enriched amphibolites, which would be too high. Hence, it is more likely that AFC processes have played a role in the formation history of the LREE-enriched Sandspruit and Theespruit lavas as also indicated by the olivine and pyroxene fractionation trends in Al_2O_3, Ni, and Cr vs. MgO spaces (Fig. 3.2a, c, d).

To evaluate the dominant process and to quantify the amount of contamination, we carried out AFC and mixing calculations using the Microsoft Excel calculation spreadsheet of Ersoy and Helvaci (2010). As crustal contaminant, a 3645 ± 5 Ma Ngwane Gneiss with tonalitic composition from the study of Kröner et al. (2014; sample AGC01-5) was used. This sample belongs to the first generation TTG gneisses in the AGC, exposed near the Phophonyane shear zone in northwestern Swaziland at the margin to the BGGT (Kröner et al. 2014). As "parental melt", the LREE-depleted sample BA 129 was chosen, because this sample shows the highest depletion in incompatible elements compared to all other Sandspruit and Theespruit samples from this study and, therefore, this is the sample that should be least disturbed by crustal contamination. Our calculations are illustrated in Figures 3.9b and 3.9c. With this approach the LREE-enriched samples from the Sandspruit and Theespruit Formations are best explained by 12 % AFC in Sc vs. La/Yb space (Fig. 3.9a) or 24 % AFC in Nb vs. La/Yb space (Fig. 3.9b). The discrepancy between the two calculated AFC percentages is likely a consequence of the difference in compatibility of Sc and Nb. Whereas Sc is moderately compatible, Nb behaves as an incompatible element, and its concentration in the LREE-enriched samples would mainly be controlled by the crustal contaminant. Likewise, the Hf and Nd budget, and hence the Hf and Nd isotope composition of the LREE-enriched samples, would also be mainly controlled by the crustal contaminant. This is because of the difference in Hf and Nd concentrations between older AGC crust (sample AGC01-5 has Hf of 7.1 ppm and Nd of 31.7 ppm) and mafic magma ("parental magma" BA 129 has Hf of 0.80 ppm and Nd of 3.62 ppm), where the mixed compositions should be dominated by the admixed AGC gneiss. Interestingly, our calculations also show that the LREE-undepleted samples can be explained by up to 36 % of fractional crystallization of the parental melt, involving olivine and pyroxene fractionation. Additionally, some LREE-undepleted samples seem to have undergone a very small amount of AFC before fractional crystallization became the dominant process. However, it has to be noted that our AFC calculations are only minimum estimates, because the chosen "parental magma" contains only 8.32 wt.% MgO. This is lower than estimated MgO contents in primary melts from modern ocean plateaux, like the Ontong Java Plateau, ranging from 15.6 to 20.4 wt.% MgO (Fitton and Godard 2004) as well as lower than modeled primary magma compositions of non-arc basalts ranging in MgO from 18 to 24 wt.% (Herzberg et al. 2010). Hence, this indicates that fractionation processes prior to contamination must have taken place, likely represented by olivine and pyroxene fractionation.

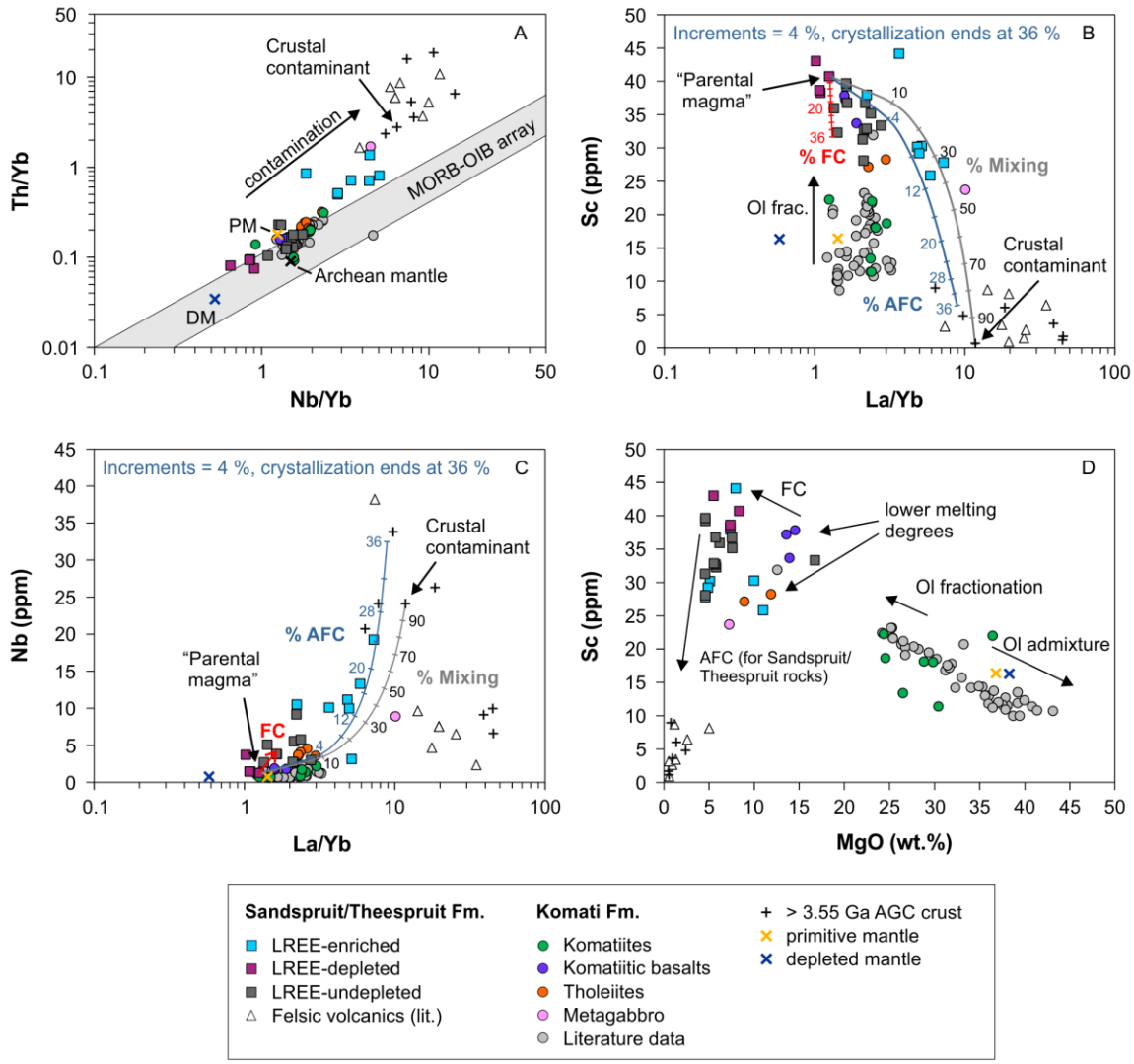

Figure 3.9: Crustal contamination of LREE enriched rocks of the Sandspruit and Theespruit Formations. A) Th/Yb vs. Nb/Yb space. The development of LREE-enriched samples of the Sandspruit and Theespruit Formations is likely the result of contamination with crustal material from the ca. 3.66-3.55 Ga Ancient Gneiss Complex (AGC). B) and C) Assimilation – fractional crystallization (AFC) and mixing modeling. Sample BA 129 of this study was used as "parental melt" and sample AGC01-5 from the study of Kröner et al. (2014) was used as crustal contaminant composition: B) Sc (ppm) vs. La/Yb. The modeling shows that the Sandspruit/Theespruit LREE-enriched samples can be reproduced by a maximum of 12 % AFC or by up to 30 % mixing of a tonalite from the AGC. In contrast, the samples characterized by flat REE patterns likely originate from fractional crystallization (FC) of either the parental melt or of a hybrid AFC melt. Rocks from the Komai Formation (own and literature data) are shown for comparison. Note that the Sc concentration in the tholeiites is much higher than in the komatiites, likely resulting from olivine fractionation and/or a lower degree of mantle melting. C) Nb (ppm) vs. La/Yb. This diagram shows that the contamination process was most likely dominated by AFC rather than by mixing. With this approach, the LREE-enriched samples of the Sandspruit and Theespruit Formations can be reproduced by up to 24 % AFC. Again, the modeling shows that the samples characterized by flat REE patterns likely resulted from fractional crystallization. D) Sc (ppm) vs. MgO (wt.%). The komatiitic and tholeiitic basalts of the Komati Formation result from lower degrees of partial melting compared to the komatiites of the same formation that show an olivine (Ol) fractionation trend. The LREE-depleted and LREE-undepleted basalts of the Sandspruit and Theespruit Formations could have formed by fractional crystallization of olivine from a more Mg-rich parental magma. The LREE-enriched samples develop to lower Sc and MgO contents, likely resulting from AFC processes.

Literature data: >3.55 Ga AGC crust (Kröner et al. 2014), Sandspruit/Theespruit felsic volcanic rocks (Kröner et al. 2013, 2016), Sandspruit Theespruit mafic rocks (Viljoen and Viljoen 1969; Jahn et al. 1982), primitive mantle (Plame and O´Neill 2014), depleted mantle (Salters and Stracke 2004), Komati Formation (Jahn et al. 1982, Chavagnac 2004, Parman et al. 2001, Robin-Popieul et al. 2012, Puchtel et al. 2013, Sossi et al. 2016).

Another argument in favor of crustal assimilation via AFC is the possible "zircon effect" that can be observed in two LREE-enriched samples having chondritic $\varepsilon Hf_{(t)}$ at negative $\varepsilon Nd_{(t)}$ (Fig. 3.4a). Such a feature could be the result of disequilibrium melting of zircon during crustal anatexis in which zircon may be retained if the crustal contaminant has a relatively high Zr concentration or the partial melt is rapidly ascending (e.g., Tang et al. 2014). The residual zircons may then retain ^{177}Hf at the crustal source and this process would lead to isotopically distinct batches of melts (e.g., Tang et al. 2014).

Yet, AFC of >3.55 Ga AGC crust alone cannot account for the remarkable coherence of trace element patterns of samples belonging to the LREE-enriched group of the Sandspruit and Theespruit Formations (Fig. 3.3a). This feature is likely a consequence of magma chamber processes as described by O´Hara (1977), where periodically refilled magma chambers that undergo continuous fractional crystallization are capable of producing magmas with coherent trace element patterns that are variably enriched relative to PM, as observed for the rocks of the Sandspruit and Theespruit Formations. An analogue for the crystals that might have formed by such a process could be represented by the Stolzburg layered ultramafic intrusion in the BGB (Anhaeusser 2001).

In the following, the mantle source composition of the LREE-depleted samples of the Sandspruit and Theespruit Formations will be constrained. The results will be discussed in relation to the nature of the mantle sources that gave rise to the komatiites, komatiitic basalts, and tholeiites of the Komati Formation.

3.6.4 Characterization of mantle sources of tholeiites and komatiites

The tholeiites of the Sandspruit/Theespruit Formations and the komatiites, komatiitic basalts, and tholeiites of the Komati Formation share similar geochemical characteristics such as relatively flat coherent primitive mantle normalized trace element patterns (Fig. 3.3a, b) and depleted mantle-like Hf-Nd isotope compositions (Fig. 3.4a, b). This geochemical resemblance may hint at a similar magmatic history for the mafic and ultramafic rocks of the lower Onverwacht Group. However, the geodynamic settings in which the Sandspruit/Theespruit and Komati Formations formed must have differed from

each other because crustal interaction occurred in the ca. 3.55 Ga Sandspruit/Theespruit basalts, and there exist interlayered felsic volcanic rocks in these formations. These features are not observed in the ca. 3.48 Ga Komati Formation lavas. Hence, in the following, we separately discuss the likely magmatic origin for tholeiites of the Sandspruit and Theespruit Formations and for komatiites, komatiitic and tholeiitic basalts of the Komati Formation.

3.6.4.1 Tholeiites of the Sandspruit and Theespruit Formations

The metavolcanic rocks of the Sandspruit and Theespruit Formations mostly consist of tholeiitic and minor pricritic basalts (our data; Viljoen and Viljoen 1969; Jahn et al. 1982). However, there are some literature data that reported "peridotitic komatiites" having MgO contents above 18 wt.%, and reaching up to 37 wt.% (Fig. 3.2a-d; Viljoen and Viljoen 1969; Jahn et al. 1982). These samples have been classified mainly based on their major element composition and are in some cases highly altered to serpentinite (e.g., Jahn et al. 1982). Hence, we presume that these MgO-rich rocks were originally olivine-rich cumulates, and we therefore conclude that the Sandspruit and Theespruit Formations only contain tholeiites and picrites, and no komatiites.

In Th/Yb vs Nb/Yb space (Fig. 3.9a) the LREE-depleted samples plot to lower Th/Yb and Nb/Yb than the LREE-undepleted samples of the same formations and to lower Th/Yb and Nb/Yb than the komatiites and basalts of the Komati Formation. This indicates that the source for the Sandspruit and Theespruit basalts was more depleted than for the komatiites and basalts of the Komati Formation. A more incompatible element-depleted mantle source for the Sandspruit and Theespruit Formations is also indicated by the lower La/Yb ratios of the LREE-depleted samples (Fig. 3.9b, c) compared to komatiites of the Komati Formation. Furthermore, in Sc vs. La/Yb (Fig. 3.9b) and Sc vs. MgO (Fig. 3.9d) spaces the LREE-depleted and LREE-undepleted Sandspruit and Theespruit samples plot to much higher Sc concentrations than komatiites of the Komati Formation, most likely resulting from lower degrees of mantle melting. Additionally, the LREE-depleted samples have relatively low MgO contents ranging from 5.61 to 8.32 wt.% and, therefore, do not represent the parental magmas of the Sandspruit and Theespruit lavas. Hence, we conclude that the LREE-depleted samples represent low degree melts of an incompatible element-depleted mantle source, and the magma

underwent olivine fractionation prior to AFC, which both resulted in an increase in Sc concentrations and decrease in MgO contents.

The melting depth of basalts from the Sandspruit and Theespruit Formations can be constrained based on their Gd_{CN}/Yb_{CN} ratios. The LREE-depleted and LREE-undepleted samples of this study have uniform Gd_{CN}/Yb_{CN} indicating melting in the spinel stability field. However, basalts from the literature (Jahn et al. 1982) show higher than chondrite Gd_{CN}/Yb_{CN} indicating melting in the garnet stability field. Combined, we propose that the basalts from the Sandspruit and Theespruit Formations formed by moderate degrees of melting in the spinel/garnet transition zone of the upper incompatible element-depleted mantle. This hypothesis is confirmed by other studies on basalts in greenstone belts of the Kaapvaal, Pilbara, and Superior Cratons where basalts that formed independently of komatiites were found (Jochum et al. 1991; Xie et al. 1993).

Another interesting feature of the Sandspruit/Theespruit basalts is their scatter in TiO_2 content. Our contamination modeling in the previous chapter shows that the LREE-undepleted and LREE-enriched samples can be explained by AFC processes. However, in TiO_2 vs. MgO space (Fig. 3.2b) no clear correlation that would indicate mineral fractionation can be observed. In contrast, for basalts of the Komati Formation, a clear olivine fractionation trend for the basalts is visible (Fig. 3.2f). This indicates that the Sandspruit/Theespruit basalts must have undergone a process different from simple fractional crystallization prior to eruption. A process that is capable of enriching the Sandspruit/Theespruit magmas in Ti could be dissolution of clinopyroxene of the lithospheric mantle, because this mineral is the main carrier of Ti in the mantle (e.g., Sossi et al. 2016). Dissolution of lithospheric mantle clinopyroxene would also drive the Hf-Nd isotope composition of the magma towards more depleted signatures, as also proposed for the depleted Hf-Nd isotope signatures of volcanic rocks from the ca. 2.8 Ga Windimurra igneous complex of the Yilgarn Craton (Nebel et al. 2013). Alternatively, the scatter in TiO_2 concentration in the Sandspruit and Theespruit tholeiites could be the result of variable fractionation of titano-magnetite, as proposed for more evolved tholeiites of the younger Kromberg Formation of the BGB (e.g. Vennemann and Smith 1999).

3.6.4.2 Komatiites, komatiitic and tholeiitic basalts of the Komati Formation

Different melting models have previously been suggested for the Komati Formation komatiites. Most of these invoke high degrees of melting (>30 %) of a primitive mantle source in the garnet stability field at great depths down to 400 km (Green 1975; Sun and Nesbitt 1978; Ohtani 1984; Campbell et al. 1989; Ohtani et al. 1989; Herzberg 1992; Nisbet et al. 1993; Zhang and Herzberg 1994; Arndt 2003; Sossi et al. 2016). Moreover, on the basis of radiogenic $^{176}Hf/^{177}Hf$ and $^{143}Nd/^{144}Nd$ isotope compositions and elemental characteristics, several studies suggested derivation from an isotopically depleted source (Arndt 1977; Blichert-Toft and Arndt 1999; Blichert-Toft et al. 1999; Robin-Popieul et al. 2012; Puchtel et al. 2013). The involvement of an incompatible element-depleted mantle component in the formation of ultramafic rocks has also been suggested for several other Archean sequences, for example, the 3.52-3.24 Ga low-Ti basalts of the lower Pilbara Supergroup (e.g., Smithies et al. 2005), the 2.8 Ga Windimurra Igneous Complex of the Yilgarn Craton (Nebel et al. 2013), the 2.8-2.7 Ga Taishan komatiites of China (Polat et al. 2006), the ca. 2.06 Ga Jeesiörova komatiites of Finnish Lapland (Hanski et al. 2001), the 3.72 Ga boninite-like metabasalts from Isua (Hoffmann et al. 2010), and the 3.33 Ga Commondale komatiites, South Africa (Wilson and Carlson 1989; Hoffmann and Wilson, 2017).

A significant contribution of incompatible element-depleted mantle material to the sources of komatiites is consistent with the observed isotope compositions of komatiites of the Komati Formation that generally have radiogenic $\varepsilon Hf_{(t)}$ and $\varepsilon Nd_{(t)}$ values of around +2 to +4 and 0 to +2, respectively (Fig. 3.7). In some cases, reported $\varepsilon Hf_{(t)}$ and $\varepsilon Nd_{(t)}$ values can reach as high as +11 (Blichert-Toft et al. 2015) and +10 (Chavagnac 2004), if not caused by disturbance. To explain the flat trace element patterns relative to PM, combined with the depleted Hf-Nd isotope compositions of komatiites, Robin-Popieul et al. (2012) proposed a depleted mantle source for their melting model. These authors suggested that Barberton komatiites formed in a plume setting at high pressures (~13 GPa) by equilibrium melting of a depleted peridotite mantle source. At such great depths, komatiite melts and solid peridotite have similar densities, causing retention of high melt fractions in the source during progressive rising of the plume. At shallower levels, the melt is able to escape from its source due to an increase in density difference, leaving behind a garnet-bearing residue (Robin-Popieul et al. 2012). The depletion event of the mantle source must have occurred relatively short before the melting event (Robin-

Popieul et al. 2012), because no anomalies in μ^{142}Nd were so far observed for komatiites of the Komati Formation (Caro et al. 2006; Puchtel et al. 2013), yet leaving enough time for the development of depleted Hf-Nd isotope signatures. The melting model of Robin-Popieul et al. (2012) is capable of explaining many characteristics of komatiites, and we therefore favor that the komatiites of the Komati Formation formed by plume melting at great depths and separated from the source at shallower levels, leaving behind a garnet-bearing residue, which is consistent with their positive Gd_{CN}/Yb_{CN}.

In contrast to komatiites, the associated basalts were not as extensively studied, even though they make up most of the Archean mafic crust (de Wit and Ashwal 1997). From studies of basalts from the Kaapvaal, Zimbabwe, Pilbara, and Superior Cratons that are associated with komatiites three different formation mechanisms of associated basalts can be identified: (1) formation by melting within the same plume as komatiites, but at lower degrees of melting, (2) formation by moderate degrees of melting of upper mantle material, and (3) formation by fractionation of olivine from a komatiitic parental magma (Campbell et al. 1989; Jochum et al. 1991; Xie et al. 1993; Herzberg et al. 2010; Mole et al. 2018).

Parallel trace element patterns, similar elemental anomalies, similar positive Gd_{CN}/Yb_{CN} ratios, and similar isotope compositions of komatiitic and tholeiitic basalts compared to komatiites of the Komati Formation (Fig. 3.3a, b; Fig. 3.4a, b) possibly indicate a common magmatic origin. This, in turn, would hint towards a similar mantle source for komatiites, komatiitic, and tholeiitic basalts. Fractionation trends of olivine in komatiites can be observed in the variation diagrams in Figures 3.2e-h, but also in Sc vs. La/Yb (Fig. 3.9b) and Sc vs. MgO (Fig. 3.9d) spaces. At about 15 wt.% MgO, fractionation of pyroxene commences in the tholeiites and basaltic komatiites (Figures 3.2e, h; 3.9d). However, if the basalts were the result of olivine fractionation of a komatiitic parental magma, one would expect to have a continuous fractionation line instead of a gap in MgO concentrations between komatiites and basalts as reflected by the Komati Formation lavas (Fig. 3.2e-h; 3.10; e.g., Nisbet 1982). Hence, it is likely that the basalts and basaltic komatiites reflect lower melting degrees of the same or a different mantle source compared to komatiites of the same formation. This hypothesis is supported by the slightly negative μ^{142}Nd value of basalt ZA 32a (Schneider et al. 2018) indicating that the mantle source of the basalts contained a contribution of a long-term isolated reservoir in contrast to the source of the komatiites. Therefore, the basalts might have formed by partial melting of ambient upper mantle as a consequence of conductive

heating of the komatiite plume (e.g., Herzberg et al. 2010; Sossi et al. 2016; Schneider et al 2018). However, our hypothesis of a possibly heterogeneous upper mantle only rests on one μ^{142}Nd data point, and further investigation of the ^{142}Nd isotope composition of Komati Formation basalts would be needed.

3.6.5 Geodynamic setting for the lower Onverwacht Group

Trace elemental and isotope characteristics of the mafic and ultramafic volcanic rocks of the lower Onverwacht Group of the BGB have been interpreted to be the result of eruption within an early Archean oceanic plateau setting (e.g., Anhaeusser 1984; Chavagnac 2004; Van Kranendonk et al. 2009, 2014). This hypothesis is based on the resemblance of primitive mantle-normalized trace element patterns of uncontaminated mafic and ultramafic volcanic rocks of the lower Onverwacht Group (Sandspruit, Theespruit, and Komati Formations) with those of volcanic rocks of Phanerozoic large igneous provinces (LIPs; e.g., Storey et al. 1991; Kerr et al. 1996; Chavagnac 2004; Fitton and Godard 2004). Other studies attributed the geochemical characteristics of the lower Onverwacht volcanic rocks to derivation from a metasomatized mantle source, possibly related to subduction processes (e.g., Parman et al. 1997; Furnes et al. 2012). However, the production of voluminous amounts of volcanic material during a very short time period is more characteristic of LIPs than of less voluminous subduction volcanism (e.g., Coffin and Eldholm 1993).

An oceanic plateau setting for the lower Onverwacht Group volcanic rocks is, however, not consistent with the chemistry of interlayered felsic volcanic rocks in the Sandspruit and Theespruit Formations and the inherited zircon record. The felsic volcanic rocks of the Sandspruit and Theespruit Formations are interpreted to have formed by partial melting of AGC crust (Van Kranendonk et al. 2009; Kröner et al. 2013; 2016), which is a strong indication for older continental rather than oceanic lithosphere. Hence, the geodynamic setting for the Sandspruit and Theespruit basalts more likely resembles a submerged continental flood basalt setting (e.g., Arndt 1999; Kröner et al. 2013), comparable to the continental setting proposed for volcanic rocks of the Belingwe Greenstone Belt of the Zimbabwe Craton (Bolhar et al. 2002), the Superior Craton of Canada (Boily et al. 2009; Maurice et al. 2009), the Pilbara Craton (Smithies et al. 2007), and the Yilgarn Craton of Western Australia (Mole et al. 2014). In such a continental setting (Fig. 3.10a), the basalts of the Sandspruit and Theespruit Formations may have

formed by melting of the upper mantle, either by adiabatic decompression melting as a consequence of continental rifting (e.g., Anhaeusser et al. 1969), or by heating through an arriving mantle plume (e.g., Campbell et al., 1989). In a next step, the primary pricritic magma became trapped beneath the lithospheric mantle, and contemporaneous olivine (increase in Sc concentrations in the magma) and titano-magnetite fractionation, possibly coupled with pyroxene dissolution (variable TiO_2 in the magma), occurred. After sufficient fractionation, the density of the magma decreased and the magma could have risen through the lithospheric mantle into the continental crust and filled crustal magma chambers. In these crustal magma chambers, the magma developed to more evolved compositions by AFC together with a combination of periodically refilling of fresh mafic magma and eruption of evolved magma. Contemporaneously, some magma could have passed directly through the AGC crust with minor assimilation and produced the less contaminated basalts of the Sandspruit and Theespruit Formations (Fig. 3.10a).

In contrast to the basalts of the Sandspruit and Theespruit Formations, the komatiites, komatiitic, and tholeiitic basalts of the Komati Formation show no signs of interaction with crustal material (e.g., Robin-Popieul et al. 2012; Puchtel et al. 2013; this study). Consequently, the continental lithosphere may have thinned in response to progressive continental rifting (e.g., Anhaeusser et al. 1969) and would then have resembled an oceanic setting, as previously suggested (e.g., Anhaeusser 1984; Storey et al. 1991; Arndt 1999; Chavagnac 2004; Arndt et al. 2008; Van Kranendonk et al. 2009, 2014; Fig. 3.10b). Unfortunately, tectonic signs of continental rifting are not preserved in the field, because the original geological relationships were obliterated during deformation and metamorphism, and the different crustal levels of the Sandspruit/Theespruit and Komati Formations were juxtaposed along the Komati fault. Nevertheless, the volcanism (basaltic and komatiitic) of the Komati Formation shares similar geochemical and Hf-Nd isotope characteristics, but different ^{142}Nd systematics, which would be in favor of derivation from different mantle regions. In such an oceanic setting (Fig. 3.10b), the plume-derived komatiites could have erupted fast and without significant contamination through the oceanic lithosphere onto the surface. In addition, the basalts of the Komati Formation may have formed by moderate degrees of partial melting of a heterogeneous upper mantle and also erupted without significant contamination.

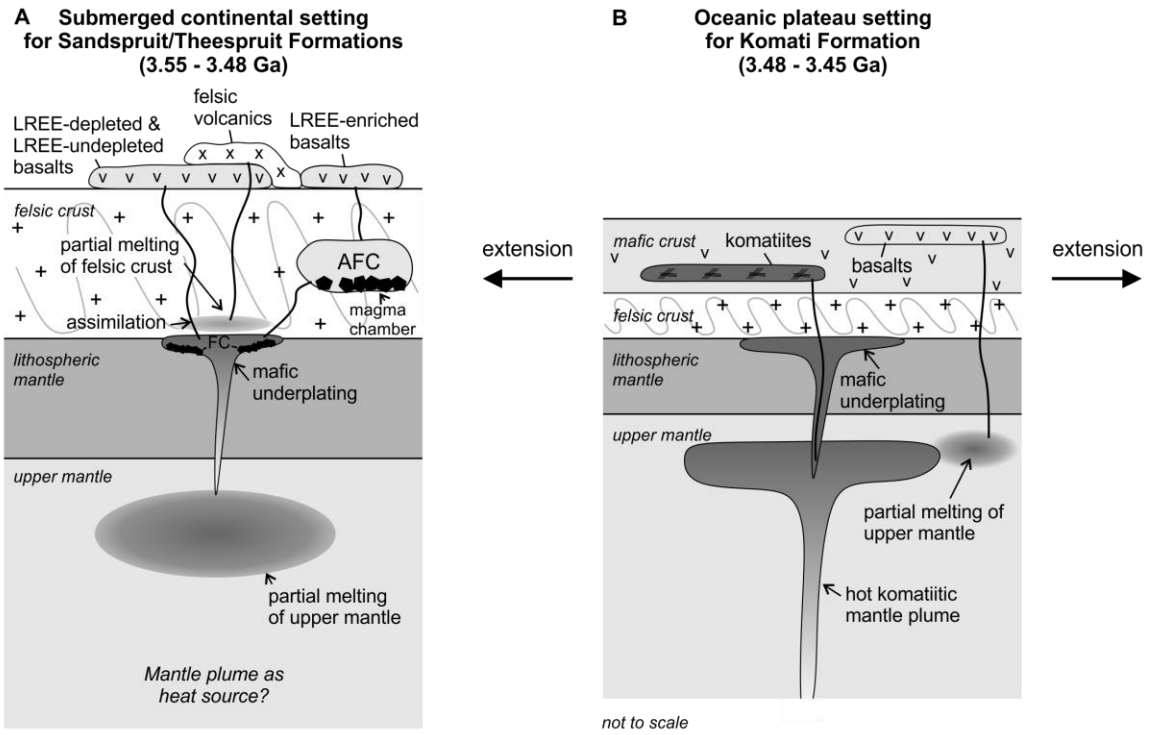

Figure 3.10: Schematic model for the geodynamic evolution of the lower Onverwacht Group. A) Continental setting for the 3.55 to 3.48 Ga Sandspruit and Theespruit Formations. Mafic underplating of partial melts of the upper mantle caused partial melting of felsic crust to form felsic volcanic rocks. During underplating fractional crystallization of the mafic magma occurred. When ascending to the surface, the fractionated magma underwent small assimilation of partial melts of the crust to form the LREE-depleted and LREE-undepleted basalts. Other mafic melts filled crustal magma chambers and underwent AFC processes and formed the LREE-enriched rocks. B) Oceanic setting for the 3.48 to 3.45 Ga Komati Formation. Komatiites are sourced from the central hot zone of a mantle plume, whereas the basalts are the products of partial melting of the heterogeneous upper mantle. AFC = assimilation – fractional crystallization, FC = fractional crystallization. The schematic oceanic setting (B) was modified after Van Kranendonk et al. (2012).

In summary, the volcanic rocks of the lower Onverwacht Group record a change in geological setting from a primarily submerged continental-type flood basalt scenario with bimodal volcanism that, as a consequence of rifting, gradually developed to a more oceanic plateau-like setting with mafic to ultramafic volcanism.

3.7 Conclusions

The Sandspruit and Theespruit Formations of the lower Onverwacht Group can be subdivided into three groups based on their trace element and Hf-Nd isotope characteristics: A LREE-depleted, a LREE-undepleted, and a LREE-enriched group. The depleted trace element characteristics, combined with positive $\varepsilon Hf_{(t)}$ and $\varepsilon Nd_{(t)}$ of the LREE-depleted group of samples, are consistent with low degree melting of an

incompatible element-depleted mantle source, likely represented by depleted upper mantle. Assimilation-fractional crystallization modeling indicates that the LREE-undepleted samples and the LREE-enriched samples can be explained by a combination of fractional crystallization and assimilation of older crustal material, likely represented by Ancient Gneiss Complex crust. The interaction of mafic magmas with felsic crust and the interlayered stratigraphy of mafic and felsic volcanic units of the Sandspruit and Theespruit Formations likely represent a submerged continental flood basalt setting for the formation of these rocks.

In contrast, the positive Gd_{CN}/Yb_{CN} ratios, overall positive $\varepsilon Hf_{(t)}$ and $\varepsilon Nd_{(t)}$, and flat PM-normalized trace element patterns of komatiites hint towards deep melting of a depleted mantle source, possibly by a mantle plume, in agreement with previous studies. However, the komatiitc and tholeiitic basalts formed by lower degrees of partial melting of upper mantle material, likely as a result of conductive heating by the komatiite mantle plume. The geodynamic setting of the volcanic rocks of the Komati Formation most likely reflects an ocean plateau setting, in agreement with the literature.

Collectively, the geodynamic setting for the formation of basalts and komatiites of the lower Onverwacht Group developed from a submerged continental platform setting to an oceanic plateau setting within ca. 100 Ma, possibly as a consequence of continental rifting.

3.8 Acknowledgements

JEH, KPS, CM, and AK thank the Deutsche Forschungsgemeinschaft (DFG) for grants HO4794/1-1, HO4794/1-2, Mu1406/8, Mu1406/19-1, KR590/94-1, and KR590/94-2. Paul Mason is thanked for support with samples from the Londozi valley and Axel Hofmann for logistic support in the field and sample shipping. We thank Ulrike Westernstroer for ICP-MS measurements at Kiel University and Philipp Gleissner, Yogita Kadlag and Chunhui Li for support with the ICP-MS. Monika Feth is thanked for laboratory assistance. We are indebted to Nick Arndt for his helpful comments on our revised version of the manuscript. This is a contribution to SPP1833 Project '*Building a habitable Earth*' funded by the DFG.

3.9 Supplementary information

Supplement 3.A: Analytical procedures for trace element analysis at FU Berlin

A stock solution of 600-fold diluted sample material was further diluted to obtain dilution factors ranging from 14000 to 64000, depending on the trace element concentrations of the samples. An internal standard solution of 1 ppb Ge-In-Re was added to the final dilution in order to correct measured intensities of the low, middle and high masses for signal drift. The final dilutions were calibrated against several dilutions of BHVO-2 ranging from 11000- to 600000-fold dilutions and which were also doped with 1 ppb Ge-In-Re solution. Furthermore, two REE solutions containing 1 ppb and 0.4 ppb Ba, La, Ce, Pr, Nd, and Sm were measured along with the samples in order to determine the oxide ratio that was produced within the plasma during measurements. We noted that oxide formation in the plasma seemed to be suppressed by the sample´s matrix. Thus, an oxide correction for REEs was not necessary. Following this procedure, total blanks were 0.37 ppb for REEs, 4.28 ppb for HFSEs, 0.16 ppm for LILEs, and 0.87 ppm for all other elements (Li, Be, Ga, Mo, Cd, Sn, Sb, Sc, V, Cr, Co, Ni, Cu, Zn). Detection limits were better than 0.06 ppb for REEs, 0.2 ppb for HFSEs, 0.4 ppb for LILEs, and 0.5 ppb for all other elements, except Zn, which had a detection limit of 1 ppb. The precision of concentration determinations is estimated based on blank contribution, signal error (1s.d.), and error of the calibaration curve. Estimated relative total uncertainties (1 RSD) for the REEs were usually around 3 to 9 %, except for Dy (up to 17 %) and span 4 to 20 % for the HFSE, LILE, and Sc, V, Cr, Co, Ni, Cu, Zn.

Chapter 4

A refined petrogenetic model for a Mesoarchean large igneous province on the eastern Kaapvaal Craton (southern Africa)

4.1 Abstract

We analyzed major and trace elements as well as Hf-Nd isotopes of greenstones and amphibolites sampled close to the Kubuta Ranch in South-Central Swaziland to characterize the mantle source composition of these volcanic rocks and, hence, to constrain their genetic relation to other volcanic sequences in Swaziland and South Africa. Based on coherent trace element patterns relative to primitive mantle and similar Nd isotope characteristics, the Kubuta volcanic rocks can be genetically related to the ca. 3.0 Ga Usushwana Igneous Complex in West-Central Swaziland and the ca. 2.9 Ga Hlagothi Complex located in the KwaZulu-Natal province. The coeval ca. 3.0 Ga Nsuze and ca. 2.9 Ga Mozaan Groups (Pongola Supergroup) of South-Central Swaziland and northern KwaZulu-Natal province have similar elemental anomalies, albeit slightly elevated compositions compared to the newly sampled Kubuta volcanic rocks.

Our study shows that the Nsuze and Mozaan Group were sourced from a komatiitic mantle reservoir, whereas the Usushwana, Hlagothi, and Kubuta units were sourced from a more depleted mantle source comparable to modern depleted MORB. Furthermore, our AFC calculations reveal that the crustal contaminants possibly represent felsic rocks from the ca. 3.5 Ga crust-forming event in the Ancient Gneiss Complex.

Combining our geochemical observations with the age determinations of the literature data leads to the proposition of a refined petrogenetic model, based on the model of Gumsley et al. (2013, 2015), for the continental flood volcanism in a Mesoarchean large igneous province on the eastern Kaapvaal Craton.

This chapter is in preparation for publishing as

Schneider, K.P.[1,2], Hoffmann, J.E.[1,2], Kröner, A.[3], Balduin, A.[1], Sprung, P.[2], Schleicher, A.M.[4], Münker, C.[2]

[1]Institut für geologische Wissenschaften, Geochemie, Freie Universität Berlin, Malteserstraße 74-100, 12249 Berlin

[2]Institut für Geologie und Mineralogie, Universität zu Köln, Zülpicher Straße 49b, 50674 Köln

[3]Institut für Geowissenschaften, Johannes Gutenberg-Universität Mainz, J.-J. Becherweg 21, 55128 Mainz

[4]Helmholz Center Potsdam, Deutsches GeoForschungsZentrum (GFZ), Telegrafenberg, 14473 Potsdam

4.2 Introduction

The Archean eon covers much of Earth´s history and was a period of major crust forming events (e.g., Armstrong 1981; Taylor and McLennan 1985; Belousova et al. 2010; Dhuime et al. 2012) that led to stabilization of the ancient cratons. One major crust forming event possibly occurred in the Mesoarchean (ca. 3.0 to 2.9 Ga) on the eastern Kaapvaal Craton in southern Africa producing large volumes of continental flood basalts in an intracratonic rift basin (e.g., Hegner et al. 1984; Gumsley et al. 2013, 2015). These Mesoarchean basalts have well-preserved magmatic textures and preserve their primary geochemical composition, which can be used to place constraints on the genetic relationships of these rocks across the Kaapvaal Craton.

The correlation of lavas of the eastern Pongola basin and western Witwatersrand basin in terms of age and composition led Gumsley et al. (2013, 2015) to the conclusion of the existence of a so far unknown Mesoarchean large igneous province. Mainly based on precise age determinations and field observations, these authors proposed that the large igneous province was formed by two magma pulses derived from a short-lived mantle plume. In their petrogenetic model, the first magma pulse formed the basaltic lavas of the ca. 3.0 Ga Nsuze Group (Pongola Supergroup) and the gabbros of the Usushwana Igneous Complex (Fig. 4.1; Gumsley et al. 2015). After some time of subsidence and sedimentation, the second pulse of magma formed the ca. 2.9 Ga lavas of the Mozaan Group (Pongola Supergroup; Fig. 4.1) and the mafic sills of the Hlagothi Complex (Gumsley et al. 2013).

However, there is some disagreement on the nature of the parental magmas that formed the Nsuze volcanic rocks. While Hegner et al. (1984) proposed an ultramafic komatiitic parental magma for Nsuze volcanic rocks, Armstrong et al. (1986) suggested a primitive basaltic parental magma. Likewise, the proposed crustal contamination processes that affected these parental magmas vary from bulk assimilation (Hegner et al. 1984) and assimilation-fractional crystallization (Armstrong et al. 1986) to magma mixing of basaltic and felsic melts (Nhleko 2003). All aforementioned authors agree that the contaminant is represented by felsic crustal rocks from the Ancient Gneiss Complex (AGC) of Swaziland.

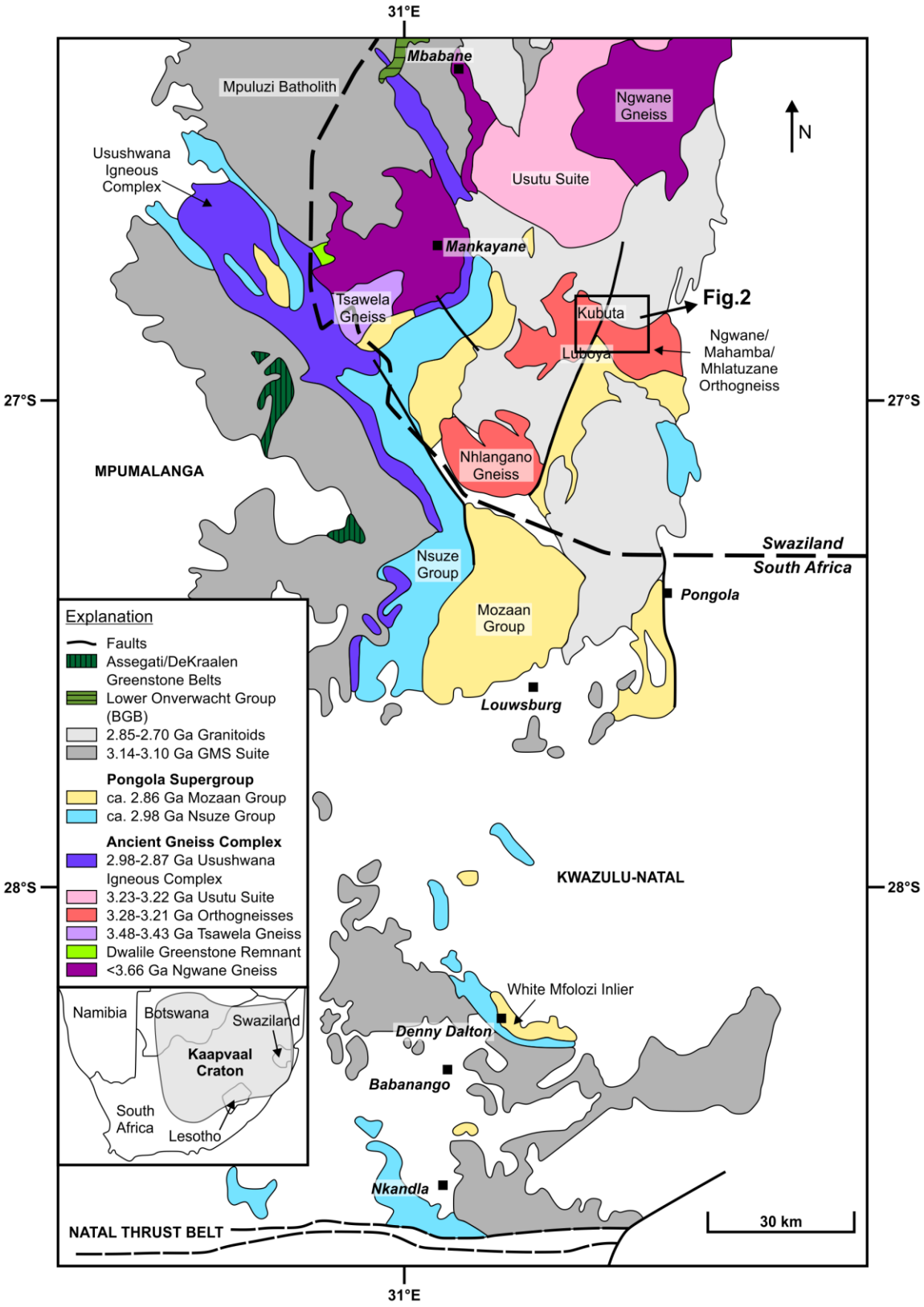

Figure 4.1: Geological overview map of the main supracrustal units of the Ancient Gneiss Complex and the Pongola Supergroup. The black box marks our sample localities which are shown in detail in the geological map in Figure 4.2. Modified after Ossa Ossa et al. (2016) and van Schijndel et al. (2017).

In this study, we carried out major and trace element, as well as Lu-Hf and Sm-Nd isotope analyses on volcanic rocks from the Kubuta area (Fig. 4.2). The Kubuta samples could either belong to volcanic rocks of the 2.98-2.84 Ga Pongola Supergroup (Fig. 4.1; Hegner et al. 1994; Walraven and Pape 1994; Gutzmer et al. 1999; Nhleko 2003; Mukasa et al. 2013) or the ca. 2.99 to 2.87 Ga Usushwana Igneous Complex (Fig. 4.1; Hegner et al. 1984; Gumsley et al. 2015) and ca. 2.86 Ga Hlagothi Complex (Gumsley et al 2013). Alternatively, the Kubuta volcanic rocks could be related to the ca. 2.66 Ga White Mfolozi Dike Swarm (WMDS; Gumsley et al 2016) further south in the KwaZulu-Natal province.

In this study, we aim to better constrain the composition of the mantle sources and the contamination history of the aforementioned sequences to test the reliability of the petrogenetic model of Gumsley et al. (2015) that was mostly based on age data. In combination with literature data, we propose a refined petrogenetic model for the Nsuze, Mozaan, Usushwana, Hlagothi, and Kubuta volcanic rocks that also takes geochemical evidence into account.

4.3 Geological overview and sample petrography

4.3.1 Geological overview

The eastern Kaapvaal Craton, located in Swaziland and eastern South Africa, records a continuous geological history from the early Archean to the Neoarchean recording the stabilization of continental lithosphere in this region. The first stabilized continental crust is represented by the 3.66-3.20 Ga Ancient Gneiss Complex (AGC; Compston and Kröner 1988; Schoene et al. 2008; Zeh et al. 2011; Kröner et al. 2014) that predominantly contains complexly deformed Paleo- to Mesoarchean grey gneisses that are rarely interlayered with amphibolites (e.g., Hunter et al. 1984; Kröner, 2007; Hoffmann and Kröner, in press). The oldest component of the AGC is the ca. 3.66-3.45 Ga Ngwane Gneiss (Fig. 4.1) that underwent ductile metamorphism under amphibolite to granulite conditions (Kröner et al. 1993, 2014). The Ngwane Gneiss is intruded by the genetically linked 3.478-3.430 Ga Tsawela Gneiss (Jackson 1984; Kröner et al. 1993; Hoffmann et al. 2016) as well as by several younger gneisses and granitoids like the 3.23-3.22 Ga Usutu Intrusive Suite in northern and central Swaziland (Schoene et al. 2009), and the 3.28-3.24 Ga Nhlangano and Mahamba Gneisses in south-central Swaziland (Fig. 4.1;

Schoene and Bowring, 2010). The ca. 3.1 Ga Pigg´s Peak and Mpuluzi Batholiths (Kamo and Davis, 1994; Murphy 2015) were the last major intrusions exposed in the eastern Kaapvaal Craton (Poujol et al. 2003; Schoene et al. 2008; Schoene and Bowring 2010). These intrusions separated the AGC in the Southeast from the Barberton Greenstone Belt in the Northwest. In its most southerly occurrence, the Mpuluzi Batholith forms the basement to the ca. 2.98-2.84 Ga Pongola Supergroup (Fig. 4.1; Hegner et al. 1994; Walraven and Pape 1994; Gutzmer et al. 1999; Nhleko 2003; Mukasa et al. 2013).

The Pongola Supergroup was deposited in an area of about 24000 km^2 extending from south-central Swaziland into northern and central KwaZulu-Natal in East South Africa, and belongs to one of the oldest cratonic cover sequences in the world (Anhaeusser 1973). The succession was deposited in a volcanic rift setting (Bickle and Eriksson 1982) between contrasting crustal blocks of the AGC with generally older granitoids ranging in age from ca. 3.6 to 3.2 Ga to the Northeast (Mukasa et al. 2013) and ca. 3.3 to 3.2 Ga to the Southwest (Wilson and Zeh 2018) of the Pongola basin. In the northern and central areas of the basin, the metamorphic grade of the volcanic and sedimentary rocks of the Pongola Supergroup ranges from largely greenschist up to granulite in some areas (Mukasa et al. 2013).

The Pongola Supergroup is divided into the lower, mostly volcanic, ca. 2.98 Ga Nsuze Group and the upper, predominantly sedimentary, ca. 2.86 Ga Mozaan Group (Fig. 4.1; Tankard et al. 1982; Hunter and Wilson 1988; Beukes and Cairncross, 1991). The volcanic rocks of the Nsuze Group range from metabasalt to metarhyolite (Tankard et al. 1982) that were deposited in an intracontinental environment (Burke et al. 1985) under subaerial to locally subaqueous conditions (Armstrong et al. 1986; Wilson and Grant 2006). The Mozaan Group rests unconformably on the Nsuze Group and mostly contains sandstone, shale, mudstone, and locally banded iron formations and stromatolites indicating deposition in a shallow marine environment (Von Brunn and Hobday 1976; Beukes and Lowe 1989; Beukes and Cairncross, 1991; Gold 2006; Hicks et al. 2011). Towards the top of the succession, volcanic rocks become more dominant again (Gold 2006).

The Nsuze and Mozaan Groups were intruded by the Usushwana Igneous Complex (UIC; Fig. 4.1), the Thole Complex, and the Hlagothi Complex. The UIC has an age of emplacement of 2871 ± 30 Ma (Hegner et al. 1984). However, recent U-Pb baddeleyite age dating by Gumsley et al. (2015) on gabbroic samples from the Piet Retief Suite that is part of the UIC yielded significantly older ages up to 2989 Ma falling in the age range of

Nsuze volcanic rocks. Based on their new ages, Gumsley et al. (2015) interpreted the Usushwana Igneous Complex as being a feeder dike system for Nsuze lavas. The 2874 ± 2 Ma Thole and 2866 ± 2 Ma Hlagothi Complexes consist of several gabbroic sills that are found in the KwaZulu-Natal province and are interpreted to be the feeder dikes for the Mozaan flood basalts (Gumsley et al 2013). Based on the similarity of ages and composition, Gumsley et al. 2013 proposed that the UIC, the Thole and Hlagothi Complexes, and the Mozaan volcanic rocks form part of a Mesoarchean large igneous province located in the south-eastern part of the Kaapvaal Craton and possibly extending into the eastern Witwatersrand block.

Later intrusions of ca. 2.85-2.70 Ga granitoids (Schoene and Bowring, 2010) were triggered by extensional deformation that also caused local deformation of the Pongola Supergroup (Hofmann et al. 2015). Following this event, ca. 2.70 to 2.66 Ga extensional dolerite dike swarms cross cut the eastern Kaapvaal Craton terminating the Archean crust formation history in the eastern Kaapvaal Craton (e.g., Klausen et al. 2010; Olsson et al. 2010, 2011; Gumsley et al. 2016).

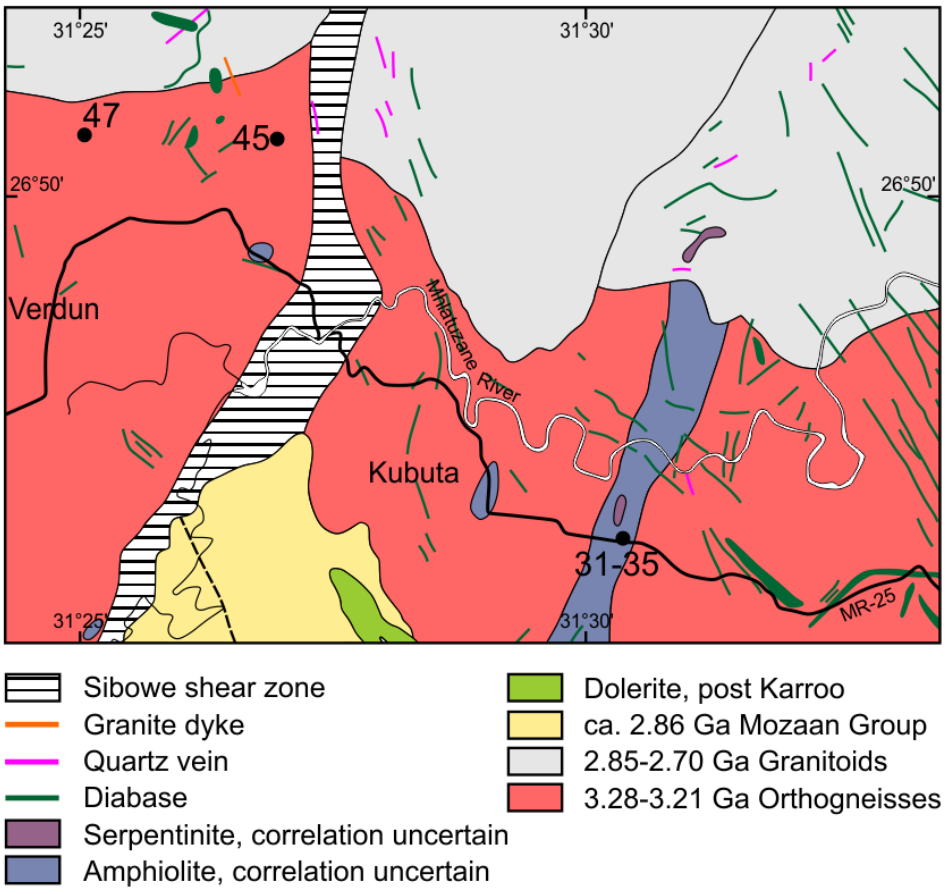

Figure 4.2: Detailed geological map with sample localities (KS-SW) marked as black dots with sample numbers (modified after Hunter 1965).

4.3.2 Sampling and sample petrography

Seven samples have been collected from the area of the Kubuta Ranch in South-Central Swaziland (Fig. 4.2). These samples are referred to as `Kubuta volcanic rocks` in the following. The samples were chosen, because the correlation of these rocks is uncertain according to the geological map of Swaziland (Hunter 1965; Fig. 4.2). Hence, one of the aims of this study is to constrain the relation of these rocks in terms of mantle source and contamination history to other volcanic sequences in this region, i.e. the 2.98-2.84 Ga Pongola Supergroup (Fig. 4.1; Hegner et al. 1994; Walraven and Pape 1994; Gutzmer et al. 1999; Nhleko 2003; Mukasa et al. 2013), the ca. 2.99 to 2.87 Ga Usushwana Igneous Complex (Fig. 4.1; Hegner et al. 1984; Gumsley et al. 2015), the ca. 2.86 Ga Hlagothi Complex (Gumsley et al 2013), or the ca. 2.66 Ga White Mfolozi Dike Swarm (WMDS; Gumsley et al 2016) further south in the KwaZulu-Natal province. Samples KS-SW 31 to 35 have been collected east of the Sibowe shear zone at the MR 25 (Fig. 4.2) in a geologic succession that was mapped by the geological survey of Swaziland as “amphibolite of uncertain correlation” (e.g., Hunter 1965). In contrast, samples KS-SW 45 and 47 have been collected west of the Sibowe shear zone as boulders in the river bed of the Matsanjeni River (Fig. 4.2).

All samples appear relatively fresh, with primary magmatic mineral textures preserved. However, when taking a closer look at the samples in thin section, the samples can be identified to have undergone greenschist-facies metamorphism expressed by variably chloritized mineral assemblages and formation of epidote. Sample KS-SW 31 has a micro-gabbroic texture containing minor olivine, and abundant clinopyroxene and plagioclase (Fig. 4.3a, b), indicating a moderate cooling rate. Samples KS-SW 32 to 35 exhibit an intergranular texture with usually bigger needle-shaped amphibole crystals and a medium-grained matrix of clinopyroxene, orthopyroxene, plagioclase, and epidote. Samples KS-SW 33 and 35 have radiating and branching fibrous plagioclase crystals preserved (Fig. 4.3c, d) that likely indicate crystallization in the center of a rapidly cooling pillow basalt, where cooling was slower than at the rims of the pillow (Philpotts and Ague, 2009). Carbonatization along mineral cracks is low in most samples, except for KS-SW 32, which shows relatively strong carbonatization and chloritization. However, the original magmatic texture of this sample is still preserved.

In contrast, samples KS-SW 45 and 47 show a porphyric texture having either 1-2 mm amphibole prisms and clinopyroxene crystals floating in a fine-grained plagioclase-

bearing matrix (KS-SW 45; Fig. 4.3e) or plagioclase and clinopyroxene crystals floating in a fine-grained orthopyroxene-bearing matrix (KS-SW 47). These two samples show almost no carbonatization. Furthermore, apatite can be found in plagioclase phenocrysts and secondary growth of accessory phases is common.

4.4 Analytical techniques

The rock samples were cut with a diamond blade saw to remove alteration rims and were subsequently prepared for thin sections. The remaining sample material was crushed to rock chips in a steel jaw crusher and milled to powder in an agate mill. The rock powders were used for major and trace element as well as whole rock Sm-Nd and Lu-Hf isotope analyses.

The whole rock major element compositions including the contents of H_2O and CO_2 were analyzed by X-ray fluorescence (XRF) on $Li_2B_4O_7$-flux fusion discs using a PANalytical Axios X-ray spectrometer at the German Research Centre for Geosciences (GFZ) in Potsdam, Germany (Table 4.1).

Furthermore, the trace element compositions were analyzed using a Thermo Finnigan Element XR ICP-MS at Freie Universität Berlin. Sample powders were digested in Parr® pressure vessels in concentrated HF-HNO_3 for 72 hours and were subsequently dried down. The evaporation step was repeated with 2 ml concentrated HNO_3. After evaporation to dryness, samples were diluted in 3 % HNO_3 for the trace element measurements. A stock solution of 600-fold diluted sample material was further diluted to an end dilution with a dilution factor ranging from ca. 23500 to 27500, depending on the trace element concentrations in the samples. An internal standard solution of 1 ppb Ge-In-Re was added to the end dilution in order to calibrate signal drift of the measured intensities of the low, middle and high masses. The end dilutions were measured against a calibration curve of several dilutions of BHVO-2 spanning from ca. 11000- to 600000-fold dilutions and were as well doped with 1 ppb Ge-In-Re standard solution. Following this procedure, relative total uncertainties (1s.d.) for all measured elements usually range from 4% to 18% with Nb having relative uncertainties up to 24%. The accuracy of our measurements can be inferred from the analyses of the BHVO-2 standard (Table 4.2). Additionally, the total procedural uncertainty can be inferred from sample replicates that were analyzed in four analytical sessions (Table 4.2).

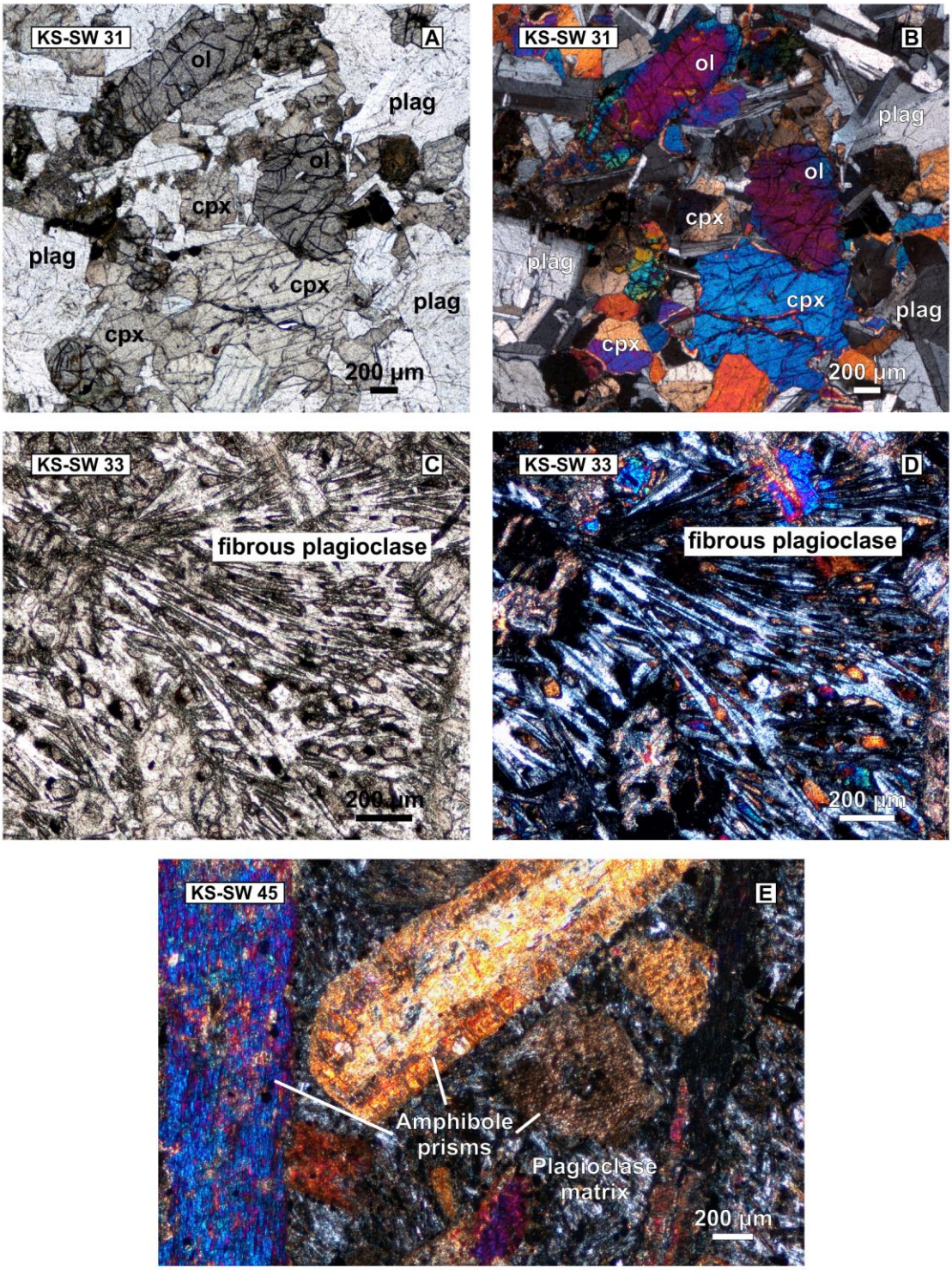

Figure 4.3: Thin section pictures of Kubuta volcanic rocks. A) and B) Typical intergranular texture preserved in Kubuta sample KS-SW 31 including minor olivine (ol), and abundant clinopyroxene (cpx) and plagioclase (plag) as the main components (A in plane-polarized light and B in cross-polarized light). C) and D) Fibrous plagioclase in sample KS-SW 33 in plane-polarized light (C) and cross-polarized light (D). E) Crystals of amphibole in a fine-grained plagioclase matrix of sample KS-SW 45 in cross-polarized light.

Table 4.1: Major element concentrations of Kubuta volcanic rocks.

Sample	**KS-SW 31**	**KS-SW 32**	**KS-SW 33**	**KS-SW 34**	**KS-SW 35**	**KS-SW 45**	**KS-SW 47**
Rock type	micro-gabbro	meta-basalt	meta-basalt	meta-basalt	meta-basalt	meta-basalt	meta-basalt
Location	S 26°53.08,4 E 31°30.25,9	S 26°53.06,6 E 31°30.27,1	S 26°53.06,6 E 31°30.27,1	3 m further NE of KS-SW 33	6 m further NE of KS-SW 34	S 26°49.23,0 E 31°26.54,2	S 26°49.18,7 E 31°25.03,6
Major elements (wt.%)							
SiO_2	48.8	44.4	53.2	51.4	53.1	52.0	46.9
TiO_2	0.99	0.43	0.37	0.54	0.37	1.29	0.39
Al_2O_3	16.0	6.00	10.2	13.7	10.5	8.07	11.8
Fe_2O_3	12.0	12.7	10.7	9.53	10.8	12.6	11.7
MnO	0.17	0.84	0.17	0.14	0.18	0.18	0.20
MgO	7.17	22.9	14.1	9.78	13.6	11.1	16.4
CaO	11.4	3.94	7.47	8.89	7.67	7.84	9.38
K_2O	0.29	0.03	0.41	0.60	0.44	0.64	0.42
Na_2O	1.96	0.01	1.52	2.24	1.50	2.25	0.93
P_2O_5	0.11	0.06	0.06	0.10	0.06	0.14	0.04
H_2O	0.91	7.15	1.27	2.64	1.48	2.67	1.11
CO_2	n.d.	0.74	0.03	0.06	0.01	0.62	0.11
Sum	99.8	99.1	99.5	99.5	99.6	99.4	99.3
Mg#	54.2	78.1	72.3	67.0	71.3	63.5	73.5

n.d. = not detected

Table 4.2: Trace element concentrations of Kubuta volcanic rocks.

Sample	KS-SW 31	KS-SW 32	KS-SW 33	KS-SW 33R	KS-SW 34	KS-SW 35	KS-SW 35R
Trace elements (µg/g)							
Be	n.d.	n.d.	n.d.	n.d.	n.d.	n.d.	n.d.
Ga	18.5	7.20	9.37	11.5	13.8	9.87	11.8
Rb	8.11	<10[#]	26.0[#]	n.d.	80.0[#]	29.0[#]	n.d.
Sr	161	n.d.	131	n.d.	181	143	n.d.
Y	21.1	12.5	9.98	8.25	19.2	10.7	8.62
Zr	64.0	41.4	38.1	n.d.	89.0	40.7	n.d.
Nb	2.57	2.33	1.05	n.d.	4.88	1.12	n.d.
Mo	0.293	0.564	0.235	0.283	0.539	0.725	0.420
Cd	n.d.	n.d.	n.d.	n.d.	n.d.	n.d.	n.d.
Sn	1.01	0.597	0.393	0.490	1.39	0.710	0.794
Sb	n.d.	n.d.	n.d.	n.d.	n.d.	n.d.	n.d.
Ba	88.8	n.d.	127	124	140	126	124
La	5.34	8.20	5.28	5.08	11.8	5.29	5.23
Ce	12.7	16.1	11.0	11.0	24.1	11.1	11.1
Pr	1.81	1.89	1.36	1.35	2.90	1.38	1.37
Nd	8.74	7.49	5.49	5.58	11.5	5.54	5.67
Sm	2.60	1.60	1.20	1.30	2.54	1.26	1.31
Eu	0.969	0.317	0.453	0.432	0.846	0.443	0.446
Gd	2.58	2.00	1.47	1.59	2.95	1.58	1.66
Tb	0.576	0.322	0.258	0.252	0.484	0.251	0.255
Dy	3.76	1.98	1.74	1.69	3.07	1.70	1.74
Ho	0.785	0.414	0.392	0.375	0.674	0.383	0.392
Er	2.18	1.15	1.15	1.15	1.94	1.14	1.18
Tm	0.310	0.164	0.178	0.179	0.293	0.178	0.185
Yb	1.96	1.00	1.20	1.15	1.88	1.18	1.19
Lu	0.293	0.158	0.193	0.182	0.290	0.191	0.183
Hf	1.93	1.24	1.16	1.11	2.34	1.14	1.13
Ta	0.172	0.207	0.0944	0.081	0.416	0.0946	0.085
W	n.d.	0.496	0.119	0.120	0.459	n.d.	0.120
Pb	2.09	1.08	2.52	1.09	n.d.	2.67	1.15
Th	0.695	1.46	0.705	0.685	2.36	0.725	0.699
U	0.171	0.443	0.203	0.193	0.492	0.212	0.200
Sc	34.9	19.3	32.0	26.4	27.1	32.9	27.3
V	280	113	148	124	125	152	129
Cr	244	n.d.	n.d.	n.d.	n.d.	n.d.	n.d.
Co	54.7	n.d.	82.4	75.3	61.3	81.3	75.1
Ni	143	n.d.	n.d.	n.d.	n.d.	n.d.	n.d.
Cu	138	148	51.5	42.9	51.0	54.4	45.7
Zn	168	n.d.	n.d.	64.4	n.d.	n.d.	64.5
$(Ta/Ta^*)_{PMN}$	0.66	0.80	0.57	-	0.76	0.57	-
$(Nb/Nb^*)_{PMN}$	0.71	-	-	-	0.44	-	-
$(Eu/Eu^*)_{CN}$	1.15	0.54	1.03	-	0.93	0.95	-
$(La/Yb)_{PMN}$	1.90	5.73	3.06	-	4.41	3.14	-
$(Gd/Yb)_{PMN}$	1.07	1.63	1.00	-	1.28	1.09	-

Table 4.2 continued.

Sample	KS-SW 45	KS-SW 47	BHVO-2 mean (4 analytical sessions)	2s.d. (µg/g)	BHVO-2 ref."	2s.d. (µg/g)"
Trace elements (µg/g)						
Be	n.d.	n.d.	1.10	0.54	1.08	0.05
Ga	12.4	10.2	20.0	4.5	21.4	0.2
Rb	50.0[#]	32.0[#]	9.24	2.48	9.26	0.10
Sr	190	62.2	367	83.5	394	1.7
Y	22.8	13.6	24.4	4.9	25.9	0.3
Zr	133	22.5	163	39.5	171	1.3
Nb	7.04	1.04	16.0	3.8	18.1	0.2
Mo	0.695	0.813	4.20	0.52	4.07	0.16
Cd	n.d.	0.0738	0.154	0.027	0.152	0.049
Sn	1.25	0.703	1.75	0.17	1.78	0.06
Sb	0.0426	0.0421	0.103	0.009	0.103	0.008
Ba	93.8	56.1	131	4.5	131	1
La	16.9	1.97	15.1	1.0	15.2	0.1
Ce	37.0	4.19	37.5	1.1	37.5	0.2
Pr	4.78	0.581	5.35	0.22	5.34	0.03
Nd	20.141	2.69	24.4	2.3	24.3	0.3
Sm	4.76	0.938	6.05	0.23	6.02	0.06
Eu	1.43	0.404	2.02	0.17	2.04	0.01
Gd	5.21	1.65	6.21	0.19	6.21	0.04
Tb	0.740	0.293	0.932	0.077	0.939	0.006
Dy	4.28	2.07	5.26	0.27	5.28	0.03
Ho	0.837	0.483	0.983	0.057	0.989	0.005
Er	2.26	1.41	2.53	0.15	2.51	0.01
Tm	0.313	0.219	0.344	0.087	0.335	0.003
Yb	1.92	1.43	1.95	0.39	1.99	0.03
Lu	0.286	0.221	0.275	0.024	0.275	0.002
Hf	3.63	0.723	4.47	0.13	4.47	0.03
Ta	0.451	0.043	1.15	0.05	1.15	0.02
W	0.227	0.125	0.254	0.039	0.251	0.035
Pb	2.79	0.924	1.66	0.11	1.65	0.04
Th	2.56	0.236	1.27	0.28	1.22	0.02
U	0.429	n.d.	0.410	0.019	0.412	0.035
Sc	22.8	34.8	30.8	4.4	31.8	0.3
V	171	175	308	45.5	318	2.3
Cr	n.d.	n.d.	277	95.4	287	3.1
Co	66.2	88.0	44.2	8.2	44.9	0.3
Ni	n.d.	n.d.	115	25.5	120	1.2
Cu	109	35.6	124	25.3	129	1.4
Zn	n.d.	73.6	102	49.8	104	1
$(Ta/Ta^*)_{PMN}$	0.58	0.44				
$(Nb/Nb^*)_{PMN}$	0.58	0.92				
$(Eu/Eu^*)_{CN}$	0.87	0.98				
$(La/Yb)_{PMN}$	6.15	0.96				
$(Gd/Yb)_{PMN}$	2.21	0.94				

[#]values determined by XRF; "Jochum et al. (2005); R = replicate; PMN = primitive mantle normalized; CN = chondrite normalized; n.d. = not detected

Table 4.3: Hafnium-Neodynium isotope composition of Kubuta volcanic rocks.

Sample	**KS-SW 31**	**KS-SW 32**	**KS-SW 33**	**KS-SW 34**	**KS-SW 35**	**KS-SW 45**	**KS-SW 47**
Rock type	micro-gabbro	meta-basalt	meta-basalt	meta-basalt	meta-basalt	meta-basalt	meta-basalt
Age (Ma)*	2980	2980	2980	2980	2980	2980	2980
Lu (µg/g)	0.289	0.151	0.182	0.289	0.186	0.305	0.224
Hf (µg/g)	1.88	1.23	1.12	2.31	1.15	3.91	0.736
^{176}Lu/^{177}Hf (mes.)	0.021821	0.017371	0.023003	0.017758	0.023030	0.011042	0.043232
^{176}Hf/^{177}Hf (mes.)	0.282858	0.281721	0.282274	0.281834	0.282272	0.281593	0.283338
± 2s.d.	0.000004	0.000007	0.000006	0.000006	0.000008	0.000007	0.000009
$\varepsilon Hf_{(t)}$	26.6	-4.8	3.4	-1.6	3.3	3.5	0.1
Sm (µg/g)	2.46	1.63	1.17	2.43	1.16	4.77	0.862
Nd (µg/g)	8.20	7.18	4.99	10.7	4.96	20.3	2.51
^{147}Sm/^{144}Nd (mes.)	0.181296	0.137473	0.141383	0.137376	0.141246	0.141764	0.207448
^{143}Nd/^{144}Nd (mes.)	0.512660	0.511410	0.511610	0.511351	0.511604	0.511586	0.512737
± 2s.d.	0.000008	0.000006	0.000008	0.000008	0.000009	0.000007	0.000008
$\varepsilon Nd_{(t)}$	6.3	-1.3	1.1	-2.5	1.0	0.5	-2.3

*Mukasa et al. (2013)

Hafnium and Nd isotope compositions and Lu, Hf, Sm, Nd concentrations of our samples were analyzed (Table 4.3) using a Thermo Scientific Neptune multi-collector ICP-MS at the University of Cologne (Germany), operated in static mode. The analyses were obtained by isotope dilution using mixed ^{176}Lu-^{180}Hf and ^{149}Sm-^{150}Nd tracers following the protocols of Münker et al. (2001) and Weyer et al. (2002). Chemical separation of Lu, Hf, Sm, and Nd follows the procedures outlined in Pin and Zalduegui (1997) and Münker et al. (2001).

Values of ^{176}Hf/^{177}Hf and ^{143}Nd/^{144}Nd were corrected for mass bias using the exponential law and ^{146}Nd/^{144}Nd = 0.7219 and ^{179}Hf/^{177}Hf = 0.7325, respectively. Repeated analyses of the Cologne AMES Hf solution standard yielded an external reproducibility of 41 ppm (2s.d., n = 4) for ^{176}Hf/^{177}Hf, whereas repeated analysis of the AMES Nd and JNdi-1 standards yielded external reproducibilities of 21 ppm (2s.d., n = 4) and 70 ppm (2s.d., n = 10) for ^{143}Nd/^{144}Nd, respectively, over the course of the analytical session. Reported values are given relative to ^{143}Nd/^{144}Nd = 0.512115 for JNdi (i.e., ^{143}Nd/^{144}Nd = 0.511858 for La Jolla Nd, Tanaka et al. 2000) and ^{176}Hf/^{177}Hf = 0.282160 for our AMES Hf solution, which is isotopically indistinguishable from the JMC-475 standard for Hf Scherer et al. (2000). All procedural blanks handled along with the sample batches during the course of this study were better than <3 pg for Lu, <37 pg

for Hf, <22 pg for Sm, and <132 pg for Nd and therefore were insignificant. Parameters used to calculate epsilon values are from Bouvier et al. (2008) and an age of 2980 Ma was assumed.

4.5 Results

4.5.1 Major elements

The SiO_2 and MgO contents in the samples range from 44.4 to 53.2 wt.% and from 7.17 to 22.9 wt.%, respectively (Table 4.1). Magnesium numbers (Mg#) range from 54 to 78 corresponding to the variability in MgO concentrations. Compared to the literature data, our samples have much higher MgO concentrations than the Nsuze Group volcanic rocks (Pongola Supergroup; Fig. 4.4a-d; Armstrong et al. 1986; Nhleko 2003; Klausen et al. 2010; Mukasa et al. 2013) and volcanic rocks from the WMDS (Gumsley et al. 2016). However, our Kubuta samples agree in MgO content with the volcanic rocks of the Mozaan Group (Pongola Supergroup; Nhleko 2003; Dlamini et al. 2017) and the Hlagothi Complex (Gumsley et al. 2013).

In Fe_2O_3 vs. MgO space, a positive correlation of samples of the Nsuze and Mozaan suites below 5 wt.% MgO (Fig. 4.4a) suggest fractionation of pyroxene and titano-magnetite. In addition, fractionation trends of pyroxene and plagioclase can be identified at MgO contents below 5 wt.% by the positive correlations of Al_2O_3 and CaO vs. MgO (Fig. 4.4b, c, d), respectively. Furthermore, the positive correlation of Eu anomaly vs. CaO content indicates plagioclase fractionation. Fractionation of apatite is indicated by the negative correlation of P_2O_5 above a SiO_2 content of 60 to 65 wt.% (Fig. 4.4e) and fractionation of zircon is indicated by the negative correlation of Zr and SiO_2 above a SiO_2 concentration of around 70 wt.% (Fig. 4.4f). However, there is another trend in Figure 4.4f which is irrespective of zircon fractionation where Zr increases with increasing SiO_2, possibly representing partial melts of continental crust. Compared to the fractionation trends observed from literature data, our samples mostly plot at the high-Mg ends of these trends resembling the high-Mg samples from the UIC and Hlagothi Complex. Samples from the White Mfolozi Dike Swarm (WMDS; Gumsley et al. 2016) are lower in MgO concentration than the Kubuta volcanic rocks.

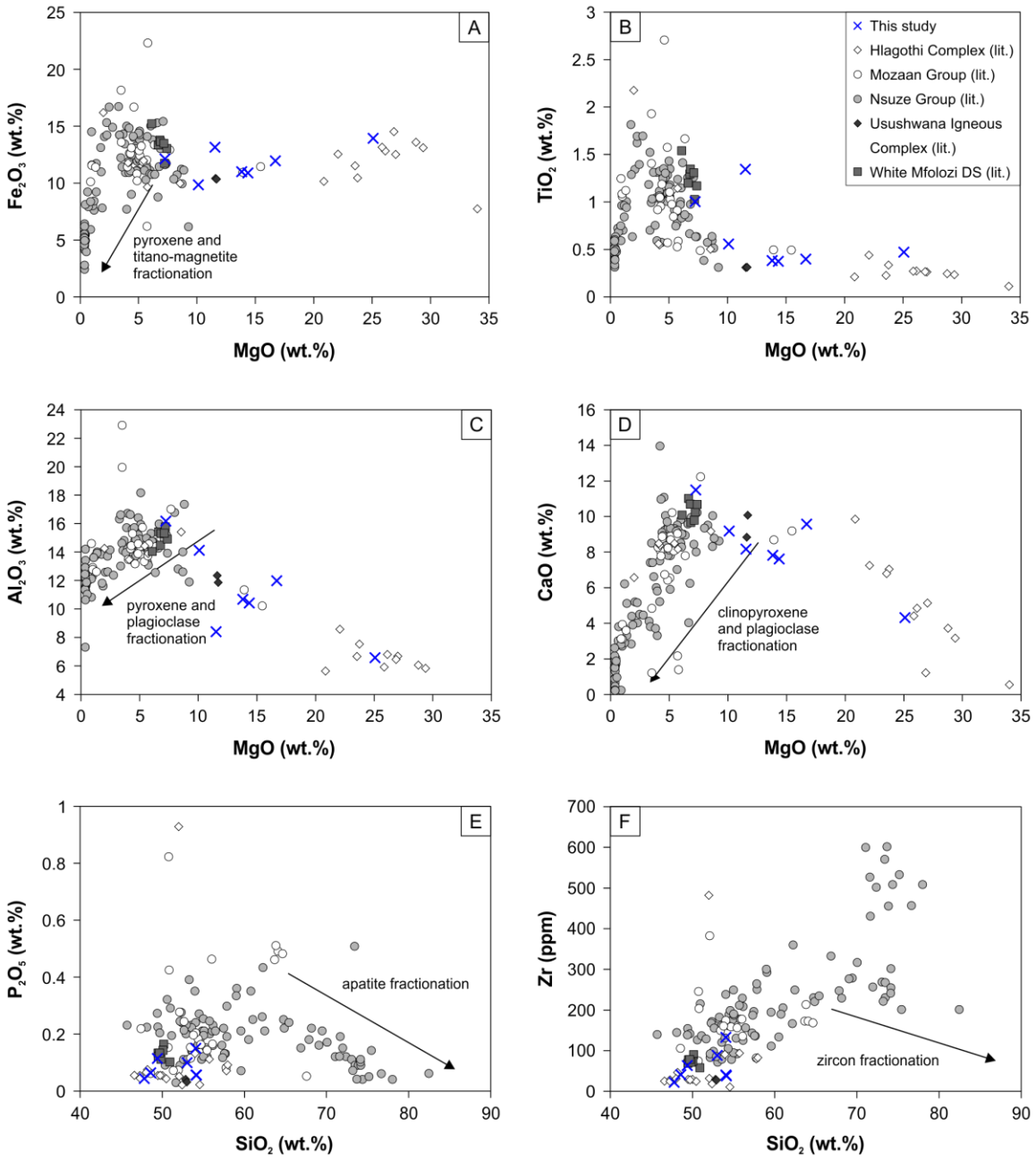

Figure 4.4: A) Fe2O3 vs. MgO. B) TiO2 vs. MgO. C) Al2O3 vs. MgO. D) CaO vs. MgO. E) P2O5 vs. SiO2. F) Zr vs. SiO2. Fractionation of pyroxene, plagioclase, apatite, and zircon is indicated for Nsuze and Mozaan volcanic rocks in plots A to F. Our Kubuta samples (blue crosses), and the samples from the Hlagothi Complex and Usushwana Igneous Complex are generally more primary in composition. Literature data is from Armstrong et al. (1986), Nhleko (2003), Klausen et al. (2010), Gumsley et al. (2013, 2016), Mukasa et al. (2013), and Dlamini et al. (2017).

4.5.2 Trace elements

The trace element concentrations of the samples are summarized in Table 4.2. The primitive mantle-normalized trace element patterns for our samples show an enrichment of light rare earth elements (LREE) and flat to slightly depleted heavy REEs relative to

primitive mantle (Fig. 4.5a, b). Most samples exhibit $(La/Yb)_{PMN}$ values greater than one, ranging from 1.90 to 6.15, except sample KS-SW 47 that has $(La/Yb)_{PMN}$ of around one. Four samples have $(Gd/Yb)_{PMN}$ values around one and in three samples the $(Gd/Yb)_{PMN}$ values range from 1.28 to 2.21. Pronounced negative anomalies are observed for Nb ($(Nb/Nb^*)_{PMN}$ = 0.44-0.92), Ta ($(Ta/Ta^*)_{PMN}$ = 0.44-0.80), and Ti. In contrast, prominent positive anomalies are present for Th, La, and Gd. Th/U ranges from 3.3 to 6.0 in

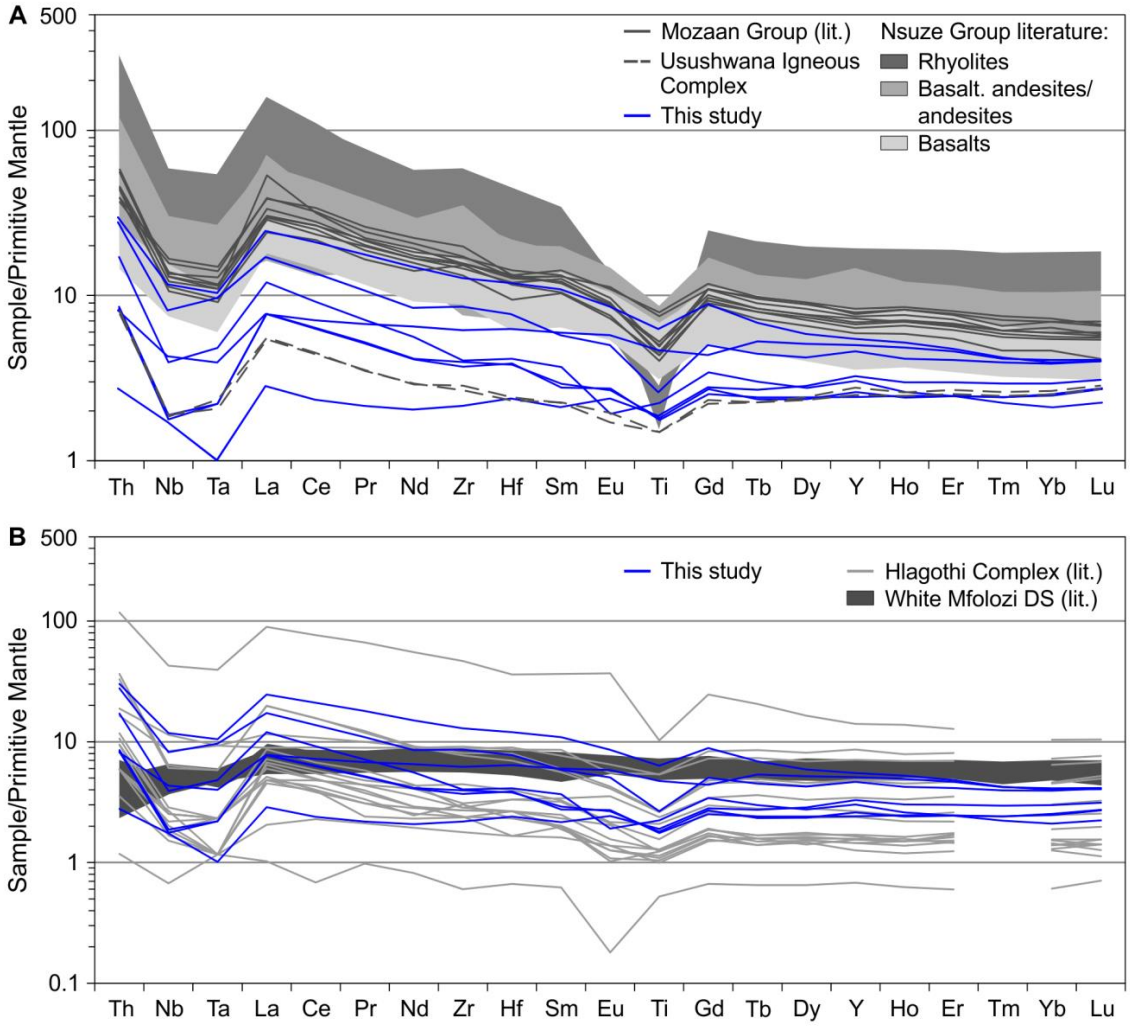

Figure 4.5: Primitive mantle (Palme and O´Neill 2014) normalized trace element patterns. A) Our samples (blue) compared to literature data for Nsuze (basalts: light grey, basaltic andesites: grey, and rhyolites: dark grey) and Mozaan (grey lines) lavas of the Pongola Supergroup, as well as two samples from the Usushwana Igneous Complex (UIC; dashed grey lines). The samples analyzed in this study are generally less enriched in REEs and some HFSEs compared to the literature data for Nsuze and Mozaan volcanic rocks (Nhleko 2003; Klausen et al. 2010; Mukasa et al. 2013). However, they broadly resemble the PM-normalized trace element patterns of the UIC (Nhleko 2003). B) Our samples (blue lines) compared to literature data for the Hlagothi Complex (light grey lines; Gumsley et al. 2013) and volcanic rocks from the White Mfolozi Dyke Swarm (White Mfolozi DS Gumsley et al. 2016). The incompatible trace element patterns of the Hlagothi Complex resemble quite well the trace element compositions of our samples. However, the incompatible trace element patterns of the White Mfolozi Dyke Swarm do not match the compositions our Kubuta samples.

agreement with Archean upper crustal values (e.g. McLennan and Taylor, 1991). Furthermore, negative Eu anomalies are present for four samples ranging from $(Eu/Eu)^*_{CN}$ = 0.54 to 0.95 indicating fractionation of plagioclase, whereas sample KS-SW 31 shows a small positive $(Eu/Eu)^*_{CN}$ of 1.15. All other samples lack Eu anomalies. Furthermore, all samples show elevated concentrations of fluid mobile elements like Rb, Ba, and Pb.

When compared to the literature data for Nsuze Group (Armstrong et al. 1986; Nhleko 2003; Klausen et al. 2010; Mukasa et al. 2013) and Mozaan Group (Nhleko 2003; Dlamini et al. 2017) volcanic rocks, our samples are generally less enriched relative to primitive mantle, yet exhibit similar $(La/Yb)_{PMN}$ and $(Gd/Yb)_{PMN}$ values and elemental anomalies (Fig. 4.5a). When compared to samples from the UIC (Nhleko 2003) and Hlagothi Complex (Gumsley et al. 2013), our samples match well the elemental abundances and exhibit similar $(La/Yb)_{PMN}$ and $(Gd/Yb)_{PMN}$ values and elemental anomalies (Fig. 4.5b). However, compared to volcanic rocks from the WMDS (Gumsley et al. 2016), the Kubuta samples have slightly less enriched HREE and much more enriched LREE than the WMDS, which are depleted in LREE.

4.5.3 Hafnium-Neodynium isotopes

The Lu-Hf and Sm-Nd isotopic compositions and Lu, Hf, Sm, and Nd concentrations of our sample suite are summarized in Table 4.3. For calculation of initial εHf and εNd values an age of 2980 Ma was assumed (Mukasa et al. 2013; see discussion in section 4.6.2). Most of our samples plot on the modern terrestrial array after Vervoort et al. (2011) in $\varepsilon Hf_{(t)}$ vs. $\varepsilon Nd_{(t)}$ space, except of sample KS-SW 31 that has much higher $\varepsilon Hf_{(t)}$ at $\varepsilon Nd_{(t)}$ values (Table 4.3). Therefore, this sample was not included in the plot in Figure 4.6. All other samples have $\varepsilon Hf_{(2980)}$ and $\varepsilon Nd_{(2980)}$ values ranging from -4.8 to +3.5 and from -2.5 to +1.1, respectively.

Literature data for Nsuze Group rocks and Usushwana Igneous Complex yielded $\varepsilon Nd_{(t)}$ values ranging from -1.8 to -7.8 (Hegner et al. 1984; Mukasa et al. 2013) and -3.7 to -1.6, respectively. These values are in well agreement with three of our samples having negative $\varepsilon Nd_{(t)}$ (and negative $\varepsilon Hf_{(t)}$) values. However, the other three Kubuta samples have chondritic to slightly elevated $\varepsilon Nd_{(t)}$ (and $\varepsilon Hf_{(t)}$) values at comparable neodymium concentrations (Fig. 4.6). Unfortunately, whole rock Lu-Hf isotope compositions were not available in the literature. Also, no Hf-Nd isotope data

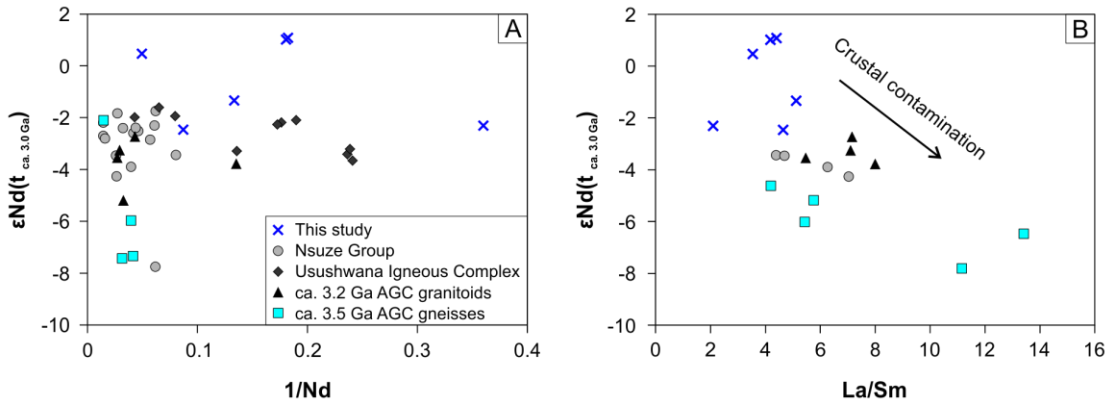

Figure 4.6: A) $\varepsilon Nd(t_{ca.\ 3.0\ Ga})$ vs. 1/Nd. B) $\varepsilon Nd(t_{ca.\ 3.0\ Ga})$ vs. La/Sm. Comparison of our Kubuta samples to samples of the ca. 2.9 Ga Nsuze Group and Usushwana Igneous Complex (Hegner et al. 1984; Mukasa et al. 2013) and samples of the ca. 3.2 Ga and ca. 3.5 Ga AGC (Kröner et al. 2014; Kröner et al. in press). Three of our Kubuta samples plot to higher $\varepsilon Nd_{(t)}$ at comparable 1/Nd and La/Sm than the rest of the ca. 2.9 Ga old volcanic rocks. When compared to felsic crust of the AGC, our samples generally have higher $\varepsilon Nd_{(t)}$ and 1/Nd and lower La/Sm. From diagram B) a crustal contamination trend towards higher La/Sm at lower $\varepsilon Nd_{(t)}$ can be inferred. The $\varepsilon Nd_{(t)}$ for AGC samples was calculated at 3.0 Ga.

were available for the Mozaan volcanic rocks, the Hlagothi Complex, and the WMDS to compare with our Kubuta samples.

4.6 Discussion

4.6.1 Effects of alteration and metamorphism

Great care must be taken when interpreting the geochemistry of Archean volcanic rocks, because these rocks underwent metamorphism that likely caused mobility of some elements which lead to alteration of the element inventory of these rocks. Relatively mobile elements during metamorphism in Archean volcanic rocks include Rb, K, Na, Sr, Ba, Ca, Fe, P, and Pb (Arndt et al. 1989; Arndt 1994) and should be used with caution to constrain magmatic processes. In contrast, the effects of metamorphic alteration on high field strength elements (HFSE), REEs, Al, Cr, and Ni are minor and therefore these elements are considered to be immobile at the whole-rock scale (Ludden et al. 1982; Jochum et al. 1991; Xie et al. 1993; Arndt 1994).

To distinguish whether an Archean greenstone is relatively undisturbed or not, Polat et al. (2002) developed five requirements that need to be met. Most of our investigated greenschist-facies meta-basalts meet all five criteria of Polat et al. (2002) in that they (1) generally have volatile (i.e. H_2O plus CO_2) contents lower than 6 wt.% (Table 4.1); (2)

show coherent trace elements patterns of immobile elements normalized to PM (Fig. 4.5); (3) display good correlations of REE, Th, Ti, and Nb abundances with Zr content; (4) their Th-Nb-La inter-element ratios do not correlate with volatile (i.e. H_2O plus CO_2) content; and (5) show no correlation of element abundance with chloritization or carbonatization. However, sample KS-SW 32 has a high volatile (i.e. H_2O plus CO_2) content of 7.9 wt.%, resulting from its relatively strong chloritization and carbonatization. This sample has also too high MgO (22.9 wt.%) and low Na_2O (0.01 wt.%) and K_2O (0.03 wt.%) contents compared to less altered samples likely indicating mobility of Mg, Na, and K during greenschist-facies metamorphism. However, the Al_2O_3 (6.00 wt.%) and CaO (3.94 wt.%) contents of this sample are low and therefore seem to be a primary feature. Consequently, we consider the alkali content of sample KS-SW 32 to be disturbed. However, chloritization and carbonatization did not seem to have disturbed the REEs, HFSEs, and Hf-Nd isotope compositions of this sample. All other samples do not seem to have disturbed alkali contents and therefore are used for classification in the total alkalis vs. silica (TAS) diagram after Le Maitre (2002) in section 4.6.2 (Fig. 4.7a).

The Hf-Nd isotope compositions of sample KS-SW 31 plot off the modern terrestrial array (Vervoort et al. 2011) towards much higher $\varepsilon Hf_{(t)}$ at $\varepsilon Nd_{(t)}$ compared to our other samples and to the literature data for Nd isotopes of the Pongola and Usushwana suites (Hegner et al. 1984; Mukasa et al. 2013). There are two possible explanations for this. One is incomplete chemical separation on the resin, because the major and trace element contents of KS-SW 31 do not seem to be disturbed plus the sample has the lowest H_2O content and appears to be very fresh in thin section (Fig. 4.3a, b). Another explanation for the high $\varepsilon Hf_{(2980\ Ma)}$ at $\varepsilon Nd_{(2980\ Ma)}$ might be that this sample belongs to a different, much younger, volcanic event, possibly to the Karoo flood basalts, leading to overestimated radiogenic $\varepsilon Hf_{(t)}$ at $\varepsilon Nd_{(t)}$ values, because of incorrect age assignment. Other features in favor of this hypothesis are, for instance, the different petrographic texture (micro-gabbro) and the positive Eu anomaly of this rock compared to the other samples.

4.6.2 Classification, age contraints, and affiliation of Kubuta volcanic rocks

In the total alkalis vs. silica (TAS) diagram after Le Maitre (2002), our samples can be classified as sub-alkaline basalts and basaltic andesites (Fig. 4.7a). The basalts and basaltic andesites can further be classified as tholeiites using the AFM discrimination diagram. Including the literature data, a clear trend from low to high potassium contents

with increasing silica can be observed in the K_2O vs. SiO_2 diagram after Le Maitre (2002; Fig. 4.7b) for the Nsuze, Mozaan, and Hlagothi volcanic rocks. As discussed in the previous section, sample KS-SW 32 has low alkali contents due to alteration. Therefore its classification as tholeiitic basalt has to be treated conditionally.

Based on our isotope analysis, we obtained a Sm-Nd whole-rock regression line in an isochron diagram corresponding to an errorchron date of 2780 ± 580 Ma (MSWD = 65; Fig. 4.8a) and a Lu-Hf whole-rock regression line that corresponds to an errorchron date of 2973 ± 620 Ma (MSWD = 113; Fig. 4.8b) for five samples of the Kubuta sample suite. However, the uncertainties on the calculated ages are quite large which may result from the relatively small spread in $^{147}Sm/^{144}Nd$ and $^{176}Lu/^{177}Hf$ ratios in our samples. Alternatively, the large uncertainties on the regression lines may indicate that our samples are not cogenetic. Due to these relatively large uncertainties, our Sm-Nd and Lu-Hf whole-rock ages seem not very reliable. However, they give a first-order approximation on the geological unit to which our investigated meta-basalts could be assigned to. The most likely units that could correlate with our Kubuta samples in terms of age and composition are the mafic/ultramafic Nsuze and Mozaan Groups of the Pongola Supergroup, as well as the mafic/ultramafic Usushwana Igneous Complex (UIC), the mafic/ultramafic Hlagothi Complex, and the mafic volcanic rocks of the WMDS.

The age of the Nsuze Group is well constrained by zircon U-Pb dating of evolved volcanic rocks which range from 2977 ± 5 Ma to 2985 ± 1 Ma in age (Hegner et al. 1994; Nhleko 2003; Mukasa et al. 2013). In contrast, a Sm-Nd whole-rock errorchron age obtained from basaltic to rhyolitic samples yielded a slightly younger, but within uncertainty overlapping, age of 2934 ± 114 Ma (Hegner et al. 1984). The age of the overlying Mozaan Group ranges from 2860 ± 26 Ma (Walraven and Pape 1994) to 2869 ± 5 Ma (Gumsley et al. 2015), respectively. The mostly intrusive Usushwana Igneous Complex (UIC) yielded Rb-Sr whole-rock ages of 2871 ± 30 Ma (Hegner et al. 1984) and 2875 ± 40 Ma (Layer et al. 1988), post-dating the Nsuze volcanic rocks. However, recent U-Pb baddelyite dating from Gumsley et al. (2015) yielded slightly older ages ranging from 2978 ± 2 Ma to 2990 ± 2 Ma that indicate a synchronous evolution of the UIC and the Nsuze Group. Additionally, the ages for the Mozaan Group and UIC overlap within error with the ca. 2866 Ma mafic to ultramafic sills of the Hlagothi Complex (Gumsley et al. 2013) that intrude the basal units of the Nsuze Group. The WMDS was dated to 2662 ± 2 Ma (Gumsley et al. 2016), also overlapping with our Sm-Nd and Lu-Hf whole-rock errorchron dates.

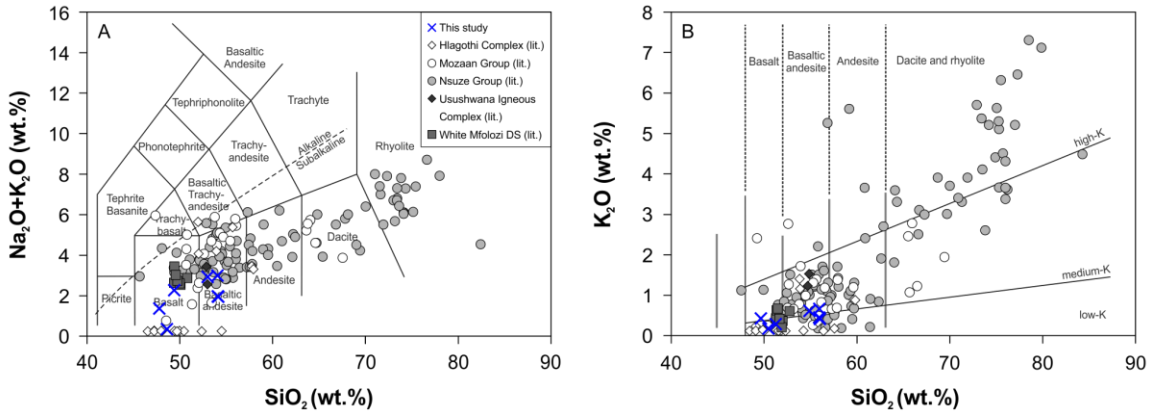

Figure 4.7: A) Total alkalis vs. silica (TAS) – diagram. B) K2O vs. SiO2. Both diagrams show that our Kubuta samples, together with samples from the UIC, Hlagothi Complex, and White Mfolizi Dyke Swarm are more mafic when compared to the Nsuze and Mozaan Groups (Armstrong et al. 1986; Nhleko 2003; Klausen et al. 2010; Gumsley et al. 2013, 2016; Mukasa et al. 2013; Dlamini et al. 2017).

When compared to geochemical data from the literature, the primitive mantle-normalized trace element patterns of our Kubuta samples are similar to the Nsuze and Mozaan Group volcanic rocks (Armstrong et al. 1986; Nhleko 2003; Mukasa et al. 2013; Dlamini et al. 2017) showing the same elemental anomalies, despite being slightly less enriched relative to primitive mantle (Fig. 4.5a). A better match in major and trace element compositions is observed when comparing our samples to the two most mafic rocks from the study of Nhleko (2003) and the volcanic rocks of the Hlagothi Complex (Gumsley et al. 2013; Fig. 4.5a, b). Nhleko (2003) originally grouped these two most mafic rocks as Mozaan Group volcanic rocks, but supposed in his thesis that they might rather belong to the Usushwana Igneous Complex based on their distinct composition. Following this interpretation, we plot these two samples as UIC in our diagrams. Unfortunately, we do not have more literature data from the UIC to test a possible conformity in element abundances of our Kubuta samples with the UIC, because only chondrite-normalized REEs are published for this unit (Hegner et al. 1984). However, Nd isotope data reported in the literature for both, the Nsuze Group (Hegner et al. 1984; Mukasa et al. 2013) and the UIC (Hegner et al. 1984), are in general agreement with our samples that have negative to chondritic $\varepsilon Nd_{(t)}$ values (Fig. 4.6a). When compared to the WMDS (Gumsley et al. 2016), the Kubuta volcanic rocks are much more enriched in light rare earth elements and depleted in heavy rare earth elements.

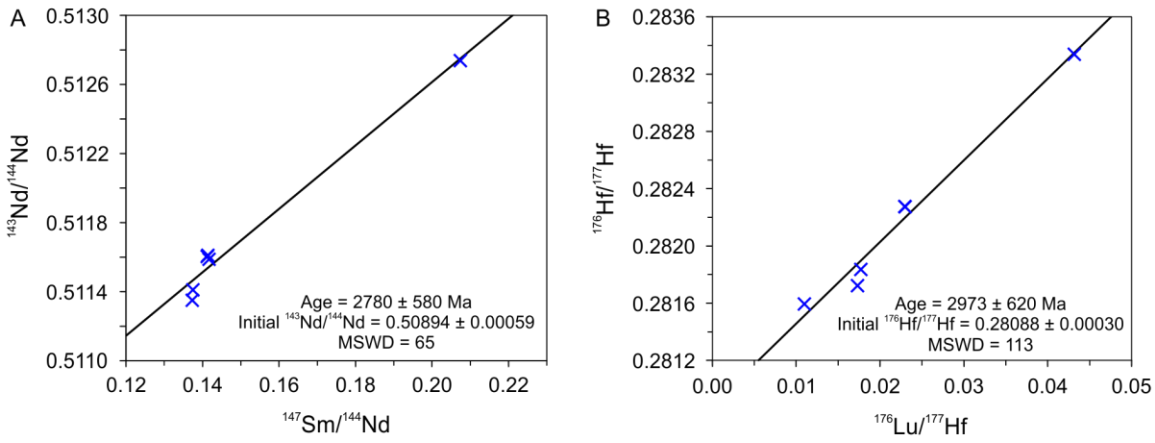

Figure 4.8: Whole-rock errorchrons for samples analyzed in this study. A) ^{147}Sm-^{143}Nd errorchron yielding an age of 2780 ± 580 Ma. B) ^{176}Lu-^{176}Hf errorchron yielding an age of 2973 ± 620 Ma. Both ages agree within error with the published age of the volcanic Nsuze and Mozaan Groups of the Pongola Supergroup (2934 to 2860 Ma; Hegner et al. 1984, 1994; Walraven and Pape 1994; Nhleko 2003; Mukasa et al. 2013; Gumsley et al. 2015) as well as the Usushwana Igneous Complex (2871 to 2990 Ma; Hegner et al. 1984; Layer et al. 1988; Gumsley et al. 2015) and the Hlagothi Complex (2866 Ma; Gumsley et al. 2013).

Hence, we do not think that our samples can be related to the WMDS. Consequently, based on the good match of major and trace element abundances, we assign our Kubuta samples to be part of the proposed large igneous province of (Gumsley et al. 2013), consisting of mafic and ultramafic rocks from the Mozaan Group, the Hlagothi Complex, and the UIC. However, the role of Nsuze lavas in this large igneous province needs further investigation.

4.6.3 Crustal contamination and mantle source composition of the volcanic rocks

Another way to test the relation of our Kubuta samples to the Nsuze Group or the supposed large igneous province consisting of Mozaan, Hlagothi, and Usushwana rocks (e.g., Gumsley et al. 2013) is to verify that they have similar compositions and to constrain the mantle sources for these units. The coherence in elemental anomalies of primitive mantle-normalized trace element patterns of our Kubuta samples compared to the Nsuze, Mozaan, Hlagothi, and Usushwana rocks (Fig. 4.5a, b) suggests that all these volcanic rocks could be genetically related. We note that in Th/Yb vs. Nb/Yb space (Fig. 4.9) the Kubuta samples, together with the samples from the literature, plot consistently above the modern MORB-OIB array towards higher Th/Yb. The low Nb/Th and LREE enrichment almost certainly result from contamination of the parental magmas of these rocks with continental crust.

In previous studies on the volcanic rocks of the Nsuze Group, different types of parental magmas for the evolved rocks were suggested. For example, Armstrong et al. (1986) proposed a basaltic parental magma for Nsuze volcanic rocks derived from a primitive mantle source comparable to a garnet-lherzolite, whereas Nhleko (2003) suggested that the basaltic parental magma was derived from a mixture of depleted mantle and enriched mantle melts. In contrast, Hegner et al. (1984) proposed that the Nsuze and Usushwana volcanic rocks were derived from an ultramafic komatiitic parental magma derived from a depleted mantle reservoir.

Tracing back the trend of crustal assimilation, indicated by the arrows in the upper left corner of the diagram (Fig. 4.9), towards the primitive end member on the modern MORB-OIB array, it becomes evident that more than one mantle sources were involved in the formation of the aforementioned sequences. Following this procedure, the parental melts of the Nsuze and Mozaan volcanic rocks could either be derived from primitive mantle melts (ca. 40% batch melting of a garnet-lherzolite) or ultramafic komatiitic melts, similar to Barberton komatiites. These results confirm the hypotheses of Armstrong et al. (1986) and Hegner et al. (1984) for the origin of Nsuze volcanic rocks.

In contrast, all other samples from the Hlagothi, Usushwana, and Kubuta units do not seem to be derived from primitive mantle or an ultramafic komatiitc parental magma. Instead, these more mafic to ultramafic rocks seem to be derived from a more depleted mantle source (Fig. 4.9). This feature indicates that despite the coherence of primitive mantle-normalized trace element patterns, the Kubuta samples together with the volcanic rocks from the Hlagothi and Usushwana units were sourced from a different mantle reservoir than the volcanic rocks from the Nsuze and Mozaan Groups. This observation contradicts the conclusions of Hegner et al. (1984) who proposed a komatiitic parental magma for Usushwana volcanic rocks, but confirms the possible existence of a common mantle reservoir for the Hlagothi, Usushwana, and Kubuta units, as proposed by Gumsley et al. (2013). However, in our modeling we use a modern depleted MORB source (Salters and Stracke 2004) which might not be representative of the depleted mantle in the Archean. However, taken as a rough approximation our results show that in the Archean mantle some reservoirs must have existed that were at least as depleted as modern MORB. Furthermore, different mantle reservoirs for Hlagothi, Usushwana, and Kubuta volcanic rocks on the one hand, and Nsuze and Mozaan Groups on the other hand, would argue for a more complex formation history of the large igneous province than previously proposed by Gumsley et al. (2013) based on age dating.

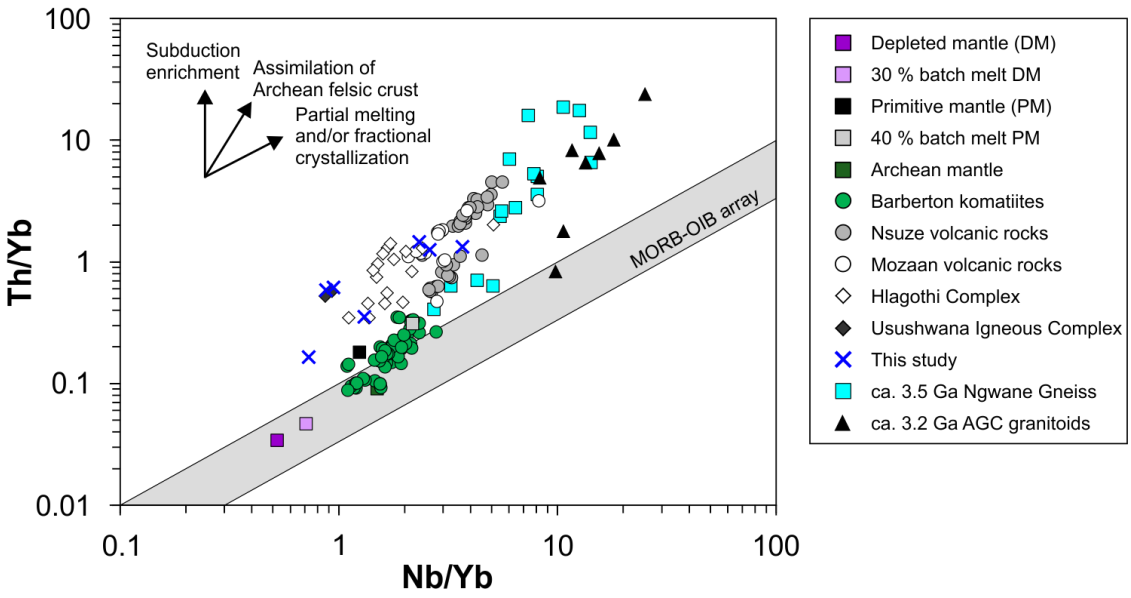

Figure 4.9: Th/Yb vs. Nb/Yb diagram after Pearce (2008) showing our samples and samples from the Nsuze (Nhleko 2003; Klausen et al. 2010; Mukasa et al. 2013), Mozaan (Dlamini et al. 2017), Hlagothi Complex (Gumsley et al. 2013), and Ushushwana Igneous Complex (e.g., Nhleko 2003) in comparison to possible mantle sources, i.e. depleted mantle (DM, Salters and Stracke 2004), primitive mantle (PM, Palme and O´Neill 2014), Archean mantle (Pearce 2008) represented by Barberton Komatiites (Parman et al. 2001, 2003; Chavagnac 2004; Robin-Popieul et al. 2012; Puchtel et al. 2013; Sossi et al. 2016; Schneider et al. in revision). The non-modal batch melts of DM (composition from Salters and Stracke (2004)) and PM (composition from Plame and O´Neill (2014)) were calculated using the equations after Shaw 1970 and the partition coefficients from Salters and Stracke (2004) and Stracke and Bourdon (2009) and are summarized in supplement 4.A. The Nsuze lavas seem to have evolved from a komatiitic parent magma, whereas the Mozaan, Hlagothi and our samples seem to have evolved from a more depleted mantle source. For comparison, ca. 3.5 Ga and 3.2 Ga AGC continental crust is also shown in the diagram (Kröner et al. 2014; Kröner et al. in press).

4.6.4 Crustal contamination mechanisms

Crustal contamination of Nsuze volcanic rocks has been suggested by several authors based on elemental composition and negative $\varepsilon Nd_{(t)}$ values (Hegner et al. 1984; Armstrong et al. 1986; Nhleko 2003; Klausen et al. 2010). As potential contaminants to the Nsuze volcanic rocks, granitoids from the Ancient Gneiss Complex (AGC) were favored (Hegner et al. 1984; Armstrong et al. 1986). The proposed assimilation processes vary from bulk assimilation of ca. 3.5 Ga old granitoid crust (Hegner et al. 1984) to assimilation-fractional crystallization (AFC) of more granitic AGC crust (Armstrong et al. 1986). In addition, Nhleko (2003) proposed magma mixing of basaltic melts and felsic melts derived from partial melting of the continental crust to explain the diverse compositions of Nsuze volcanic rocks.

Enrichment of incompatible elements combined with negative anomalies for Nb and Ta indicate the involvement of continental crust in the petrogenesis of the volcanic rocks from the Nsuze, Mozaan, Hlagothi, Usushwana, and Kubuta sample suites. Similar primitive mantle normalized trace element patterns and mostly negative $\varepsilon Nd_{(t)}$ values for the aforementioned volcanic rocks suggest a similar contamination history. In Th/Yb vs. Nb/Yb space (Pearce 2008) all samples plot well above the modern MORB-OIB array to higher Th/Yb and Nb/Yb indicating substantial contamination of the parental magmas resulting from Archean crustal input and/or partial melting and fractional crystallization (e.g., Smithies et al. 2018; Fig. 4.9). However, one type of crustal contaminant alone cannot account for the diversity in compositions of the Nsuze, Mozaan, Hlagothi, Usushwana, and Kubuta samples (e.g. Fig. 4.9).

Possible crustal contaminants that could have altered the composition of the aforementioned ca. 2.9 to 2.8 Ga volcanic rocks are granitoid gneisses from the AGC either belonging to the ca. 3.5 Ga (e.g., Hegner et al. 1984; Armstrong et al. 1986; Nhleko 2003) or the ca. 3.2 Ga crust-forming events (for a review on the ca. 3.5 and 3.2 Ga crust-forming events in the eastern Kaapvaal Craton, please refer to Kröner et al. (in press)). Contamination most likely occurred in the upper crustal levels (e.g., Hegner et al. 1984; Armstrong et al. 1986; Nhleko 2003), and the geochemical characteristics of our samples and of the literature data can best be explained by AFC processes. Arguments for AFC are fractionation of pyroxene and plagioclase as indicated by the fractionation trends in figure 4.4 and by the depletions in Ti and Eu illustrated in figure 4.5, as well as by the crustal contamination trend of $\varepsilon Nd_{(t)}$ vs. La/Sm in figure 4.6b.

In contrast, the increase in Zr concentration with increasing SiO_2 for Nsuze rhyolites, illustrated in figure 4.4f, is likely a result of the increased alkalinity of these rocks which hampers zircon fractionation (e.g. Watson and Harrison 1983), suggesting that these rocks are crustal melts (e.g. Nhleko 2003). Hence, magma mixing of mafic melts with these felsic partial melts could as well explain the evolved compositions of the volcanic rocks of the Nsuze and Mozaan Groups, as suggested previously by Nhleko (2003).

In the following, we will discuss the mechanisms of the two different contamination processes, i.e. magma mixing and assimilation-fractional crystallization.

4.6.4.1 The role of magma mixing

Partial melting of AGC crust and subsequent magma mixing with mafic underplated magma was suggested by Nhleko (2003) to have formed the Nsuze volcanic rocks. One argument for partial melting of AGC crust is based on one sample from the study of Hegner et al. (1984) which yields a strongly negative $\varepsilon Nd_{(t)}$ value of -7.8. Partial melting of crustal material would shift the resulting magma composition towards higher La/Yb and Zr concentrations and towards slightly lower Th/Yb and Nb/Yb than the AGC crustal rocks. This is observed for rhyolites of the Nsuze, and two andesites of the Mozaan and Hlagothi suites, respectively (Fig. 4.9). Hence, it is possible that at least some andesites and basaltic andesites of the Nsuze and Mozaan Groups might have been formed by magma mixing with subsequent fractional crystallization.

To explore the role of magma mixing, we calculated mixing paths using the Microsoft Excel calculation spreadsheet of Ersoy and Helvaci (2010). As mafic mixing end member, we chose basalt AG-F of the Hlagothi Complex (Gumsley et al. 2013), because it has the lowest Th/Nb, low La/Yb, and medium MgO (8.36 wt.%). As felsic mixing end member, we used rhyolite NZ-39 of the study of Nhleko (2003), because it has high SiO_2 (72.2 wt.%), very low MgO (0.05 wt.%), and the highest Zr concentration (601 ppm), and therefore likely represents a partial melt of the crust. The results of magma mixing are illustrated in figure 4.10. With this approach, most of the Nsuze and Mozaan volcanic rocks can be reproduced by 10 to 50 % mixing of a rhyolitic melt with a basaltic melt (Fig. 4.10a, b). However, some basalts, basaltic andesites, and andesites that plot to lower Th/Yb at similar Nb/Yb compared to the lavas that lie on the mixing line (Fig. 4.10a) cannot be reproduced by magma mixing. One reason for this is that there is no rhyolitic composition that could be used as mixing end member for these rocks. Likewise, the samples that plot to lower Nb/Th (Fig. 4.10a) and lower La/Yb (Fig. 4.10b) can also not be explained by magma mixing. Furthermore, magma mixing would have caused more heterogeneity in Nd isotope composition as a function of magma composition, i.e. the more felsic the magma, the lower the $\varepsilon Nd_{(t)}$ should be. However, this is not reflected by the relatively uniform negative $\varepsilon Nd_{(t)}$ values in most Nsuze, Usushwana, and three Kubuta volcanic rocks (Fig. 4.6). Consequently, another process different from simple magma mixing must have played a role in the formation of the Nsuze and Mozaan, but also the Hlagothi and Kubuta volcanic rocks.

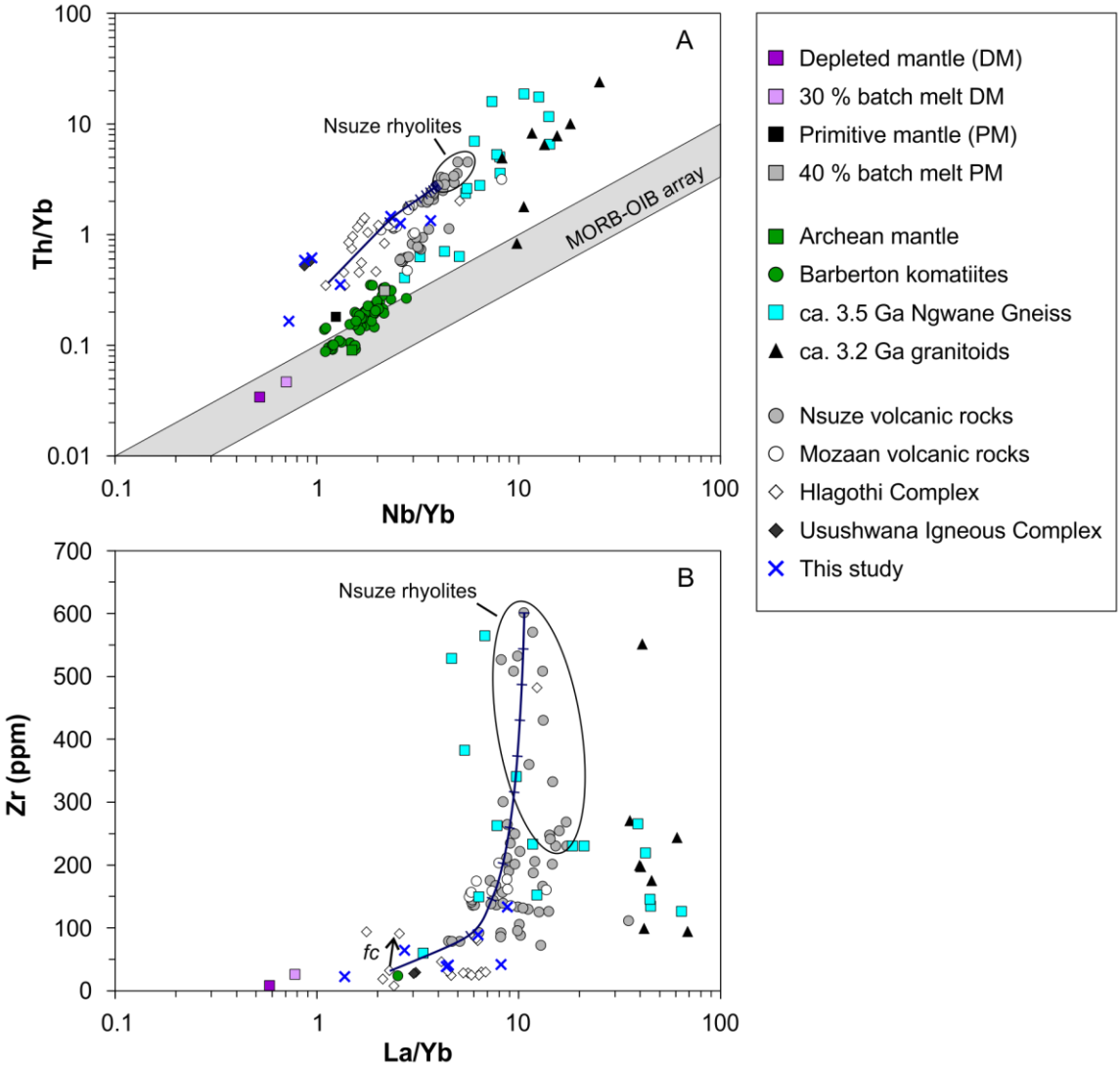

Figure 4.10: Magma mixing of basalt AG-F of the Hlagothi Complex (Gumsley et al. 2013) and rhyolite NZ-39 of the Nsuze Group (Nhleko 2003). A) Th/Yb vs. Nb/Yb. B) Zr concentration vs. La/Yb. Most samples of the Nsuze and Mozaan Groups can be reproduced by 10 to 50% rhyolite component mixed with basaltic melt. However, some basalts, basaltic andesites, and andesites that plot to lower Th/Yb at similar Nb/Yb compared to the lavas that lie on the mixing line cannot be reproduced. Likewise, the samples that plot to lower Nb/Th (A) and lower La/Yb (B) can also not be explained by magma mixing.

4.6.4.2 The role of assimilation-fractional crystallization

To constrain the possible crustal contaminants to the Nsuze, Mozaan, Hlagothi, Usushwana, and Kubuta volcanic rocks, we calculated AFC paths using the Microsoft Excel calculation spreadsheet of Ersoy and Helvaci (2010). For modeling the contamination history of Nsuze and Mozaan volcanic rocks, a komatiite from the study of Schneider et al. (in revision; chapter 3 of this dissertation) was used as analogue for the parental komatiitic magma, having 26.9 wt.% MgO (sample ZA 33). Our approach

follows the conclusion of Hegner et al. (1984) who proposed a komatiitic parental magma for Nsuze volcanic rocks. For all other volcanic suites including our Kubuta samples, a modeled 30 % batch melt of incompatible element-depleted mantle (after Salters and Stracke 2004; equations after Shaw 1970; partition coefficients for mantle melting are listed in Table S 4.1) was used, following our interpretation from the previous chapter. As possible contaminants, different crustal rocks from the AGC ranging in age from ca. 3.5 to 3.2 Ga were tested. Our AFC modeling shows that the volcanic rocks of the Nsuze, Mozaan, Hlagothi, Usushwana, and Kubuta suites most likely assimilated crustal rocks of both, the ca. 3.5 Ga and the ca. 3.2 Ga crust-forming events (Fig. 4.11).

The crustal compositions that yield AFC paths that best describe the evolved compositions of Nsuze and Mozaan volcanic rocks are two granitoid gneisses, of which one has a tonalitic composition and was sampled from the vicinity of our Kubuta samples (AGC 473, 3241 Ma; Kröner et al. in press). The other one (AGC 449, 3229 Ma; Kröner et al. in press) has a granodioritic to granitic composition and was sampled from the Piggs Peak inlier, the northernmost outcrop of AGC crust, at the fault that separates the AGC from the Barberton Greenstone Belt. Although this latter sample is not from the vicinity of exposed Nsuze or Mozaan volcanic rocks, we take its composition as an approximation of the composition of the crustal contaminant, because the two granitoid gneisses belong to the same crust forming event at ca. 3.2 Ga, which is considered to have been widespread in the AGC (e.g., Kröner et al. in press). Based on Hf-Nd whole-rock data, the ca. 3.2 Ga old AGC rocks are interpreted to have formed by melting of mafic lower crust and variable assimilation of older ca. 3.5 Ga felsic crust, resulting in variable enrichments of incompatible elements in these rocks (e.g., Kröner et al. in press).

The chosen potential crustal contaminants are distinct in their concentrations of incompatible elements. Tonalite AGC 449 has high Th/Yb, high Nb/Yb, a low Zr concentration, and high La/Yb, whereas granodiorite AGC 473 has lower Th/Yb at elevated Nb/Yb, a higher Zr concentration, and high La/Yb (Kröner et al. in press). These two granitoid gneisses sample the heterogeneity of ca. 3.2 Ga AGC crust and represent two distinct end members in our modeling (Fig. 4.11a). With this approach, two different AFC trends for Nsuze and Mozaan andesites and basaltic andesites in Th/Yb vs. Nb/Yb space can be reproduced. The upper AFC trend in figure 4.11a (red line) is described by a maximum of 18 % AFC of AGC 449, whereas the lower trend in figure 4.11a (black line) can be reproduced by maximum 12 % AFC for AGC 473. The rhyolites of the Nsuze Group likely represent partial melts of continental crust. In contrast, in Zr vs. La/Yb space

(Fig. 4.11c) the two distinct AFC paths for Nsuze and Mozaan andesites and basaltic andesites are not apparent anymore.

On the other hand, our modeling for the Hlagothi, Usushwana, and Kubuta units shows that parental magmas derived from a depleted mantle source likely underwent AFC processes involving a crustal contaminant that has a low concentration of incompatible over more compatible elements and a high Zr concentration. In our modeling, this crustal contaminant is represented by the 3534 Ma tonalitic gneiss sample AGC 200 from the Ngwane Gneiss Unit (Fig. 4.11b; Kröner et al. 2014). In Th/Yb vs. Nb/Yb space, our calculations show that the Hlagothi rocks and our Kubuta samples can be reproduced by maximum 10 % AFC and subsequent fractional crystallization of the parental magma shifting the composition along a parallel line to the MORB-OIB array to higher Th/Yb and Nb/Yb (Fig. 4.11b). In addition, in Zr vs. La/Yb space the Hlagothi and Kubuta rocks can be reproduced by maximum 12 % AFC and subsequent fractional crystallization as indicated by the arrow in figure 4.11d.

Figure 4.11: Modeling of assimilation-fractional crystallization (AFC) processes. Calculations were carried out using the spreadsheet of Ersoy and Helvaci (2010). A) AFC modeling for volcanic rocks in Th/Yb vs. Nb/Yb space after Pearce (2008) using a Barberton komatiite (ZA 33; Schneider et al. in revision) as parental magma composition. As crustal contaminants, two ca. 3.2 Ga old granitoids from the AGC (AGC 473 and AGC 449; Kröner et al. in press) were used. The Nsuze and Mozaan lavas seem to follow two distinct AFC paths that could be related to assimilation-fractional crystallization of different AGC rocks, in this case represented by the two ca. 3.2 Ga AGC granitoids. B) AFC modeling for volcanic rocks in Th/Yb vs. Nb/Yb space using a harzburgitic 30 % depleted mantle (DM; Salters and Stracke 2004) batch melt and a ca. 3.5 Ga old Ngwane Gneiss (AGC 200; Kröner et al. 2014) as end members. The AFC modeling can reproduce most of the samples from our study and from the Hlagothi and Usushwana units. Some samples can further be explained by fractional crystallization (fc) of the melts which is indicated by the arrow. However, three of our samples and the two samples from the UIC plot towards lower Th/Yb and Nb/Yb and cannot be reproduced by AFC modeling. These samples must be derived from an even more depleted mantle source than modern MORB or result from lower degrees of melting of the depleted mantle source. C) AFC modeling for volcanic rocks in Zr vs. La/Yb space using the same end members for modeling as in A). Here, the Nsuze and Mozaan lavas do not follow different AFC paths and could rather be explained by smaller amounts of AFC plus subsequent fractional crystallization. D) AFC modeling for volcanic rocks in Zr vs. La/Yb space using the same end members for modeling as in B). This AFC path yields the best-fit for all volcanic rocks, and not only the Hlaghoti and Usushwana units. See text for explanation. For all calculations a crystallizing assemblage consisting of 50% olivine, 30% clinopyroxene, and 20% plagioclase was used estimated from the fractionation trends in figure 4.4. The real crystallizing assemblage may differ from our assumed percentages.
The DM batch melt was calculated using the equations after Shaw 1970 and the partition coefficients from Salters and Stracke (2004) and Stracke and Bourdon (2009) that are summarized in supplement 4.A. Literature data for Nsuze, Mozaan, Hlagothi, and Usushwana volcanic rocks are from Armstrong et al. (1986), Nhleko (2003), Klausen et al. (2010), Gumsley et al. (2013), Mukasa et al. (2013), and Dlamini et al. (2017).

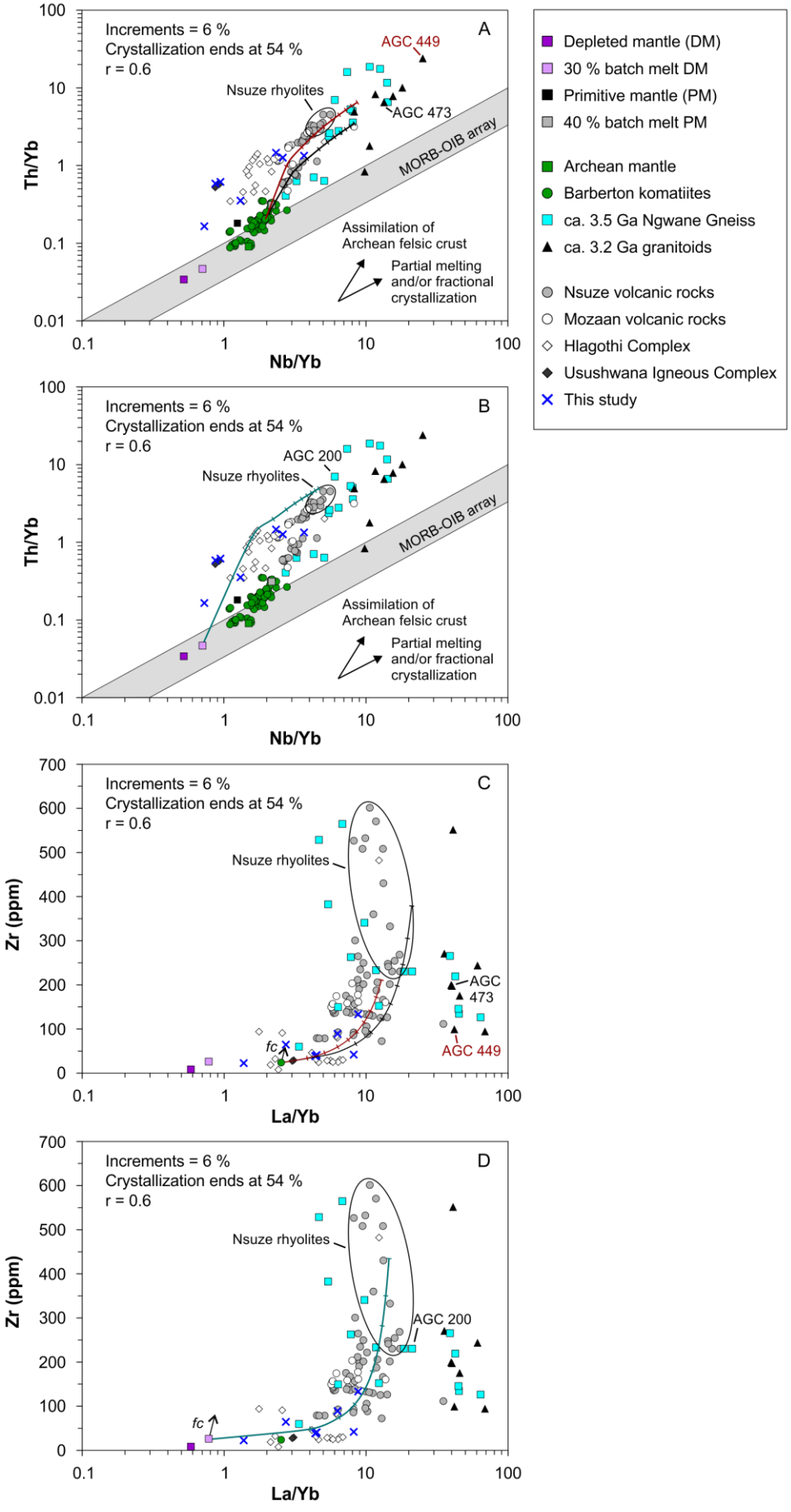
A
Increments = 6 %
Crystallization ends at 54 %
r = 0.6
AGC 449
Nsuze rhyolites
AGC 473
MORB-OIB array
Assimilation of
Archean felsic crust
Partial melting
and/or fractional
crystallization
Th/Yb
Nb/Yb
B
Increments = 6 %
Crystallization ends at 54 %
r = 0.6
AGC 200
Nsuze rhyolites
MORB-OIB array
Assimilation of
Archean felsic crust
Partial melting
and/or fractional
crystallization
Th/Yb
Nb/Yb
C
Increments = 6 %
Crystallization ends at 54 %
r = 0.6
Nsuze rhyolites
AGC
473
AGC 449
fc
Zr (ppm)
La/Yb
D
Increments = 6 %
Crystallization ends at 54 %
r = 0.6
Nsuze rhyolites
AGC 200
fc
Zr (ppm)
La/Yb
Depleted mantle (DM)
30 % batch melt DM
Primitive mantle (PM)
40 % batch melt PM
Archean mantle
Barberton komatiites
ca. 3.5 Ga Ngwane Gneiss
ca. 3.2 Ga granitoids
Nsuze volcanic rocks
Mozaan volcanic rocks
Hlagothi Complex
Usushwana Igneous Complex
This study

In summary, our calculations show that the variable compositions of the volcanic rocks from the Nsuze, Mozaan, Hlagothi, Usushwana, and Kubuta suites are the result of assimilation-fractional crystallization of either a komatiitic parental magma or a parental magma similar to depleted mantle melt. Furthermore, our modeling shows that the AGC crustal rocks from both, the ca. 3.5 Ga and the ca. 3.2 Ga crust-forming events are suitable contaminants to the aforementioned volcanic sequences. However, with our AFC modeling of elemental compositions we are not able to readily distinguish if one unit of continental crust (i.e. 3.5 or 3.2 Ga) was preferentially assimilated by one type of parental magma (i.e. komatiitic or incompatible element-depleted). Rather is seems likely that the parental magmas have assimilated AGC continental crust of both ages with subsequent fractional crystallization.

This observation, however, is not consistent with the resemblance in $\varepsilon Nd_{(t)}$ values of Nsuze, Usushwana, and Kubuta rocks that generally are about -2 to -3 (Fig 4.6). At ca. 3.0 Ga, the ca. 3.2 AGC crust developed only to $\varepsilon Nd_{(3.0)}$ values of about -3 to -4, whereas the ca. 3.5 Ga AGC crust had already developed to $\varepsilon Nd_{(3.0)}$ values of up to -8 (Fig. 4.6). Considering the low calculated amounts of AFC ranging from 10 to 18%, crustal assimilation of the younger generation TTGs seems to be unlikely. However, the geochemical characteristics of the actual ca. 3.5 Ga old assimilated crustal material could be similar to the ca. 3.2 Ga old crustal rocks used for modeling.

4.6.5 Petrogenetic model for Nsuze, Mozaan, Hlagothi, Usushwana, and Kubuta volcanic rocks

Petrogenetic models for Nsuze, Mozaan, Hlagothi, and Usushwana volcanic rocks have been proposed taking into account zircon and baddeleyite age dating, as well as common geochemical characteristics. These petrogenetic models invoke a plume origin for the aforementioned volcanic rocks with at least two pulses of magma generation (e.g., Hegner et al. 1984; Klausen et al. 2010; Gumsley et al. 2013, 2015). In this model, the first pulse of magma produced the parental magmas of the Nsuze lavas and the UIC, whereas a later mantle plume event produced the parental magmas of the Mozaan lavas and the Hlagothi Complex (Gumsley et al. 2013, 2015). Based on similar ages for the Usushwana and Nsuze suites and the more mafic composition of the Usushwana unit, Hegner et al. (1984) and Gumsley et al. (2015) interpreted the Usushwana dikes as being feeder dikes for the Nsuze volcanic rocks. Likewise, Gumsley et al. (2013) suggested that

the similar geochemical trace element patterns of the synchronous Hlagothi and Mozaan units together with the more mafic composition of Hlagothi rocks are indicative of the Hlagothi Complex being the feeding system for the Mozaan volcanism. Based on their observations, Gumsley et al. (2013, 2015) proposed that the sills of the Hlagothi Complex and the grabbros of the UIC together with the extrusive Mozaan lavas form part of a large igneous province in the southeastern part of the Kaapvaal Craton. This large igneous province is proposed to extent to the western Witwatersrand basin, based on synchronous volcanic sequences, dikes, sills and layered complexes that are found on the eastern Witwatersrand block (Gumsley et al. 2013, 2015). A relation of synchronous volcanic rocks of the Mozaan Group and Witwatersrand Supergroup has also been suggested by Mukasa et al. (2013).

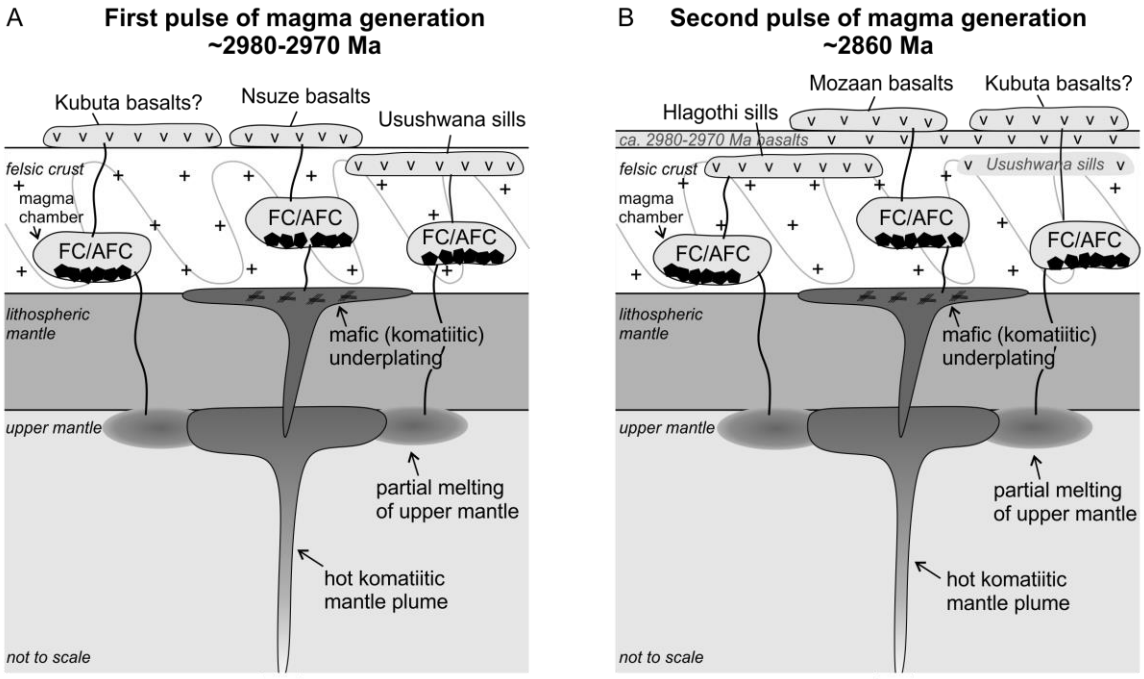

Figure 4.12: Schematic petrogenetic model for A) the first pulse of magma generation at around 2980 to 2979 Ma that formed the Nsuze, Usushwana (and Kubuta) volcanic rocks, and B) the second pulse of magma generation at ca. 2860 Ma that formed the Mozaan, Hlagothi (and Kubuta) volcanic rocks. Each magma pulse is expressed as an ascending komatiitic mantle plume that caused partial melting of depleted ambient mantle or depleted subcontinental lithospheric mantle. Both, the komatiitic and depleted mantle melts subsequently fill magma chambers in the felsic crust and underwent AFC processes involving ca. 3.5 Ga old AGC crust that reduced the density of the magmas prior to eruption. In this petrogenetic model we propose that the Nsuze and Mozaan volcanic rocks were sourced from a komatiitic mantle plume, whereas the Hlagothi, Usushwana, and Kubuta volcanic rocks were sourced from partial melting of the incompatible element depleted upper mantle. However, based on the poorly constrained age of our Kubuta samples, we cannot distinguish if these rocks were formed in the first or second pulse of magma generation.

In the present study, we investigated the geochemistry and possible relation of Nsuze, Mozaan, Hlagothi, Usushwana, and the newly sampled Kubuta volcanic rocks in more detail. At first glance, similar trace element and Nd isotope compositions (where available) suggest a common mantle source and a common crustal contamination process for the aforementioned volcanic sequences. Our AFC modeling of Nsuze, Mozaan, Hlagothi, Usushwana, and the newly sampled Kubuta volcanic rocks showed that the lavas from the Nsuze and Mozaan Groups likely were derived from a common parental melt similar to komatiite from a weakly depleted mantle source. In contrast, the volcanic rocks from the Hlagothi, Usushwana, and Kubuta suites were derived from a distinct much more incompatible element depleted mantle source.

Our findings challenge the hypothesis of Hegner et al. (1984) and Gumsley et al. (2013, 2015) that the Usushwana Igneous Complex and Hlagothi Complex would represent feeder systems for Nsuze and Mozaan lavas, respectively, because our results suggest that the UIC and the Hlagothi Complex were derived from a more incompatible element-depleted mantle source that the extrusive rocks of the Nsuze and Mozaan Groups. A synchronous formation of the Usushwana IC and Nsuze lavas as well as of the Hlagothi Complex and Mozaan lavas is supported by precise age determinations (Hegner et al. 1984; Gumsley et al. 2013, 2015). Hence, we propose a refined petrogenetic model for Nsuze, Mozaan, Hlagothi, Usushwana, and the newly sampled Kubuta volcanic rocks (Fig. 4.12) combining our findings and the conclusions of Hegner et al. (1984) and Gumsley et al. (2013, 2015): An ascending mantle plume sourced the komatiitic parental magma of Nsuze volcanic rocks. The heat of this komatiitic mantle plume caused partial melting of depleted ambient mantle or depleted subcontinental lithospheric mantle producing the parental melts of the UIC. Both, the komatiitic and depleted mantle melts subsequently fill magma chambers in the felsic AGC crust and underwent AFC processes that reduced the density of the magmas and the more evolved melts could ascend. After this first magmatic event, thermal subsidence led to the deposition of Mozaan Group sediments in an epicontinental sea (Gumsley et al. 2015). In a second event, magmatism was reactivated and plume-sourced komatiitic parental melts produced the parental magmas of the Mozaan lavas and ambient mantle or subcontinental lithospheric mantle partial melts produced the parental magmas of the Hlagothi Complex. Again, these parental melts filled magma chambers in the felsic AGC crust and underwent AFC prior to eruption. In this refined petrogenetic model, the Kubuta rocks represent differentiates from depleted mantle melts. However, based on the poorly constrained age of our Kubuta

samples, we cannot distinguish if these rocks were formed in the first or second pulse of magma generation.

4.7 Conclusions

The newly sampled greenstones from the vicinity of the Kubuta Ranch in southern Swaziland resemble the major and trace element compositions of the Hlagothi and Usushwana Igneous Complexes having similar trace element characteristics that indicate magmatic mineral fractionation and crustal assimilation. When compared to volcanic rocks of the Nsuze and Mozaan Groups of the Pongola Supergroup, the Kubuta, Hlagothi, and Usushwana suites are more mafic to ultramafic in composition. In addition, assimilation and partial melting of continental crust is indicated in Nsuze, Usushwana, and Kubuta volcanic rocks by generally negative $\varepsilon Nd_{(t)}$ values.

Assimilation-fractional crystallization modeling shows that the Nsuze and Mozaan volcanic rocks that were derived from a komatiitic parental magma were modified by AFC processes involving a crustal contaminant comparable in trace elemental composition to the samples of the ca. 3.2 Ga old AGC crust. In contrast, the Kubuta, Hlagothi, and Usushwana volcanic rocks originated from a more depleted source, comparable in composition to modern depleted MORB mantle, and subsequent AFC involving ca. 3.5 Ga old AGC crust. Based on the negative $\varepsilon Nd_{(t)}$ values of about -3 in Nsuze, Usushwana, and Kubuta lavas, assimilation of the relatively young ca. 3.2 Ga AGC crust is unlikely, because the Nd isotope compositions had too little time to develop to $\varepsilon Nd_{(3.0\ Ga)}$ values lower than -3. In contrast, the ca. 3.5 Ga AGC crust would have already developed to a mean $\varepsilon Nd_{(3.0\ Ga)}$ of about -6. Consequently, the parental magmas of the Nsuze, Mozaan, Hlagothi, Usushwana, and Kubuta lavas likely assimilated 3.5 Ga old AGC crust that was comparable in trace elemental composition to the ca. 3.2 Ga AGC crustal samples used for modeling. The compositional difference in some incompatible elements between crustal rocks from the ca. 3.5 Ga and 3.2 Ga crust-forming events might possibly be a result of sampling bias.

Based on our results and previous studies, we propose a refined petrogenetic model for the formation of Nsuze, Mozaan, Hlagothi, Usushwana, and the newly sampled Kubuta volcanic rocks. In this model, we follow the interpretation of Gumsley et al. (2013) that the aforementioned volcanic rocks formed a Mesoarchean large igneous province that probably extended into the eastern Witwatersrand block. However, we also

assign the Nsuze lavas to belong to this large igneous province. Furthermore, the Nsuze, Mozaan, Hlagothi, Usushwana, and Kubuta lavas were not derived from a single mantle plume, as proposed by Gumsley et al. (2013), but rather were derived from two distinct sources - a komatiitic plume (Nsuze and Mozaan) on the one hand and partial melting of depleted mantle (Hlagothi, Usushwana, and Kubuta) on the other hand.

To test our hypothesis of two different mantle sources and two different crustal units as possible contaminants, more geochemical work on the Mozaan, Hlagothi, and Usushwana volcanic rocks is needed in form of major and trace element as well as whole-rock Hf-Nd isotope analyses. Furthermore, precise age determinations of the Kubuta volcanic rocks are crucial to affiliate these rocks to either the first or second pulse of magma generation.

Nevertheless, our findings strengthen the geochemical fingerprint of the proposed large igneous province and provide information to better constrain the petrogenesis of these Mesoarchean flood basalts that record an important crustal growth process in the eastern Kaapvaal Craton at ca. 2.9 Ga.

4.8 Acknowledgements

JEH, KPS, CM, and AK thank the Deutsche Forschungsgemeinschaft for grants HO4794/1-1, HO4794/1-2, Mu1406/8, Mu1406/19-1, KR590/94-1, and KR590/94-2. Axel Hofmann is thanked for logistic support in the field and sample shipping. We thank Philipp Gleissner, Yogita Kadlag and Chunhui Li for support with the ICP-MS. Monika Feth is thanked for laboratory assistance. This is a contribution within the frame-work of the SPP1833 Project ‘Building a habitable Earth’ funded by the DFG.

4.9 Supplementary information

Supplement 4.A: Partition coefficients that were used for mantle melting.

$D^{melt\text{-}silicate}$	Olivine	Opx	Cpx	Garnet
Th	0.00005	0.002	0.00566	0.009
Nb	0.0005	0.004	0.01	0.015
Ta	0.0005	0.004	0.01	0.015
La	0.0005	0.004	0.015	0.0007
Ce	0.0005	0.004	0.038	0.017
Nd	0.00042	0.012	0.0884	0.064
Zr	0.0011	0.024	0.284	0.27
Hf	0.0011	0.024	0.14	0.4
Sm	0.0011	0.02	0.1509	0.23
Eu	0.0005	0.009	0.55	0.4
Ti	0.015	0.086	0.14	0.6
Gd	0.0011	0.065	0.06	1.2
Dy	0.0027	0.065	0.17	2
Y	0.015	0.065	0.74	3.1
Er	0.013	0.065	0.18	3
Yb	0.02	0.08	0.25	5.5
Lu	0.02	0.12	0.276	7

Partition coefficents for Th, Nb, Ta, La, Ce, Nd, Hf, Sm, Ti, Gd, Dy, Er, Yb, Lu are from Salters and Stracke (2004); Partition coefficents for Zr, Eu, Y are from Stracke and Bourdon (2009)

Chapter 5

Conclusions

This chapter summarizes the major findings of chapters 2 to 4, which represent the scientific achievements of this dissertation. Three main conclusions improve our understanding of crust formation processes in the eastern Kaapvaal Craton during the Hadean to Mesoarchean. Existing methods, including major and trace element, as well as Hf, ^{143}Nd, and ^{142}Nd analysis, were used to constrain Hadean to Archean crust formation processes.

I. The first high-precision ^{142}Nd/^{144}Nd analyses for representative and well characterized granitoids and amphibolites of the AGC, Swaziland, and the lower Onverwacht Group of the BGB, South Africa, show that two different mantle reservoirs must have been involved in crust-forming processes between 3.66 and 3.22 Ga. Negative μ^{142}Nd anomalies in mantle-derived rocks indicate the involvement of an early-enriched mantle reservoir in the formation of some AGC rocks that differentiated in the Hadean during the lifetime of ^{146}Sm, yielding a likely ^{142}Nd/^{144}Nd model age of ca. 4.3 Ga. The presence of negative μ^{142}Nd anomalies in mantle-derived rocks as late as 3.45 Ga confirms the presence of enriched ^{142}Nd reservoirs in the Paleoarchean mantle. During crust formation, these enriched ^{142}Nd signatures were transferred to crustal rocks and reworking of these crustal rocks may have further transferred the enriched signature to granitoids of the AGC that are as young as 3.22 Ga. Contemporaneous to AGC crust that was derived from enriched mantle domains, other mantle-derived rocks and complementary granitoids of the AGC and the BGB terrain were derived from mantle domains that do not show evidence for early differentiation events during the lifetime of ^{146}Sm. Such parallel behavior of enriched and modern-like mantle and crustal domains may have played a more pronounced role in the formation of Archean cratons around the world than previously thought.

II. The 3.55 to 3.48 Ga Sandspruit and Theespruit Formations of the lower Onverwacht Group of the BGB can be subdivided into three petrogenetic groups, based on their trace element and Hf-^{143}Nd isotope characteristics, namely a LREE-depleted, a

LREE-undepleted, and a LREE-enriched group. The depleted trace element characteristics, combined with positive $\varepsilon Hf_{(t)}$ and $\varepsilon Nd_{(t)}$ of the LREE-depleted group, are consistent with derivation of the rocks from an incompatible element-depleted mantle source, likely represented by depleted upper mantle. Assimilation-fractional crystallization modeling shows that the LREE-undepleted samples and the LREE-enriched samples can be explained by a combination of fractional crystallization and assimilation of older crustal material, likely represented by ca. 3.5 Ga crust of the AGC. The interaction of mafic magmas with felsic crust and the interlayered stratigraphy of mafic and felsic volcanic units of the Sandspruit and Theespruit Formations likely reflect a continental flood basalt setting for the formation of these rocks.

In contrast, the komatiites of the 3.48 to 3.45 Ga Komati Formation show trace element characteristics and overall positive $\varepsilon Hf_{(t)}$ and $\varepsilon Nd_{(t)}$ values that hint towards deep melting of a long-term incompatible element-depleted mantle source, possibly a mantle plume. This interpretation is in agreement with previous interpretations in the literature. The komatiitc and tholeiitic basalts formed by lower degrees of partial melting of upper mantle material, likely as a result of conductive heating by the komatiite mantle plume. This hypothesis is supported by the slight enrichement in ^{142}Nd observed in one basalt of the Komati Formation indicating that the mantle source of the basalts contained a contribution of a long-term isolated reservoir in contrast to the source of the komatiites. In agreement with the literature, the geodynamic setting of the volcanic rocks of the Komati Formation is most likely represented by an ocean plateau setting.

Collectively, the geodynamic setting for the formation of basalts and komatiites of the lower Onverwacht Group evolved from a continental-type setting to an oceanic plateau setting within ca. 100 Ma, possibly as a consequence of continental rifting.

III. The geochemistry of the sampled greenstones and amphibolites from Kubuta Ranch in south-central Swaziland resembles the major and trace element compositions of the Hlagothi and Usushwana Igneous Complexes, having similar trace element characteristics that indicate mineral fractionation and crustal assimilation. When compared to volcanic rocks of the Nsuze and Mozaan Groups of the Pongola Supergroup, the Kubuta, Hlagothi, and Usushwana suites are more mafic to ultramafic in composition.

This study revealed that the Nsuze and Mozaan volcanic rocks were derived from a komatiitic parental magma, whereas the Kubuta, Hlagothi, and Usushwana volcanic rocks originated from a more incompatible element-depleted source, comparable in composition to modern depleted MORB mantle. Assimilation-fractional crystallization (AFC) modeling shows that the parental magmas of the volcanic rocks of all units were modified by AFC processes involving ca. 3.5 Ga old AGC crust.

Based on our results and previous studies, I propose that the Nsuze, Mozaan, Hlagothi, Usushwana, and the Kubuta metavolcanic rocks formed a Mesoarchean large igneous province (LIP) that probably extended into the eastern Witwatersrand block. Furthermore, we propose that this Mesoarchean LIP formed from distinct mantle sources, namely a komatiitic plume (Nsuze and Mozaan) on the one hand and partial melting of depleted mantle (Hlagothi, Usushwana, and Kubuta) on the other hand.

These findings strengthen the geochemical fingerprints of the proposed LIP and provide information to better constrain the petrogenesis of these Mesoarchean flood basalts that record an important crustal growth process in the eastern Kaapvaal Craton at ca. 2.9 Ga.

In summary, the conclusions of this dissertation are that Hadean material indeed contributed to Archean crust formation in the eastern Kaapvaal Craton and that mantle-derived mafic and ultramafic rocks record a change in geological settings from a submerged continental platform to an ocean plateau setting, and back to a continental environment within a time period of ca. 600 Ma.

References

Allègre, C., 1982. Genesis of Archean komatiites in a wet ultramafic subducted plate. In: Arndt, N.T and Nisbet, E.G. (eds.) Komatiites. George Allen and Unwin, London, England, pp. 495-500.

Amelin, Y., Lee, D.C., Halliday, A.N., Pidgeon, R.T., 1999. Nature of the Earth's earliest crust from hafnium isotopes in single detrital zircons. *Nature* 399, 252-255.

Anhaeusser, C.R., 1976. The geology of the Sheba Hills area of the Barberton Mountain Land, South Africa, with particular reference to the Eureka syncline. *Trans. Geol. Soc. S. Afr.* 79, 253-280.

Anhaeusser, C.R., 1973. The evolution of the early Precambrian crust of southern Africa. *Philos. Trans. R. Soc. Lond.* A273, 359388.

Anhaeusser, C.R., 1984. Structural elements of Archaean granite-greenstone terraines as exemplified by the Barberton Mountain Land, southern Africa. In: Kröner, A. and Greiling, R. (eds.) Precambrian Tectonics Illustrated. E. Schweizerbart'sche Verlagsbuchhandlung, Stuttgart, pp. 57-78.

Anhaeusser, C.R., 2001. The anatomy of an extrusive-intrusive Archean mafic-ultramafic sequence: the Nelshoogte Schist Belt and Stolzburg Layered Ultramafic Complex, Barberton Greenstone Belt, South Africa. *South Afr. J. Geol.* 104, 167-204.

Anhaeusser, C.R., 2014. Archaean greenstone belts and associated granitic rocks – A review. *J Afr. Earth Sci.* 100, 684-732.

Anhaeusser, C.R., Mason, R., Viljoen, M.J., Viljoen, R.P. 1969. A reappraisal of some aspects of Precambrian shield geology. *Geol. Soc. Am. Bull.* 80, 2175-2200.

Anhaeusser, C.R. and Robb, L.J. 1980. Regional and detailed field and geochemical studies of Archean trondhjemitic gneisses, migmatites and greenstone xenoliths in the southern part of the Barberton Mountain Land, South Africa. *Precambrian Res.* 11, 373-397.

Armstrong, R.L., 1981. Radiogenic isotopes: the case for crustal recycling on a steady-state no-continental-growth Earth. *Philos. Trans. R. Soc. Lond.* A 301, 443-472.

Armstrong R.A., Compston W., De Wit M.J., Williams I.S. 1990. The stratigraphy of the 3.5-3.2 Ga Barberton greenstone belt revisited: a single zircon ion microprobe study. *Earth Planet. Sci. Lett.* 101(1), 90-106.

Armstrong, N.V., Hunter, D.R., Wilson, A.H., 1982. Stratigraphy and petrology of the Archean Nsuze Group, Northern Natal and Southeastern Transvaal, South Africa. *Precambrian Res.* 19, 75-107.

Armstrong, N.V., Wilson, A.H., Hunter, D.R., 1986. The Nsuze Group, Pongola Sequence. South Africa: geochemical evidence for Archean volcanism in a continental setting. *Precambrian Res.* 34, 175-203.

Arndt, N.T 1977. Ultrabasic magmas and high-degree melting of the mantle. *Contrib. Mineral. Petrol.* 64, 205-221.

Arndt, N.T., 1994. Archean komatiites. In: Condie, K.C. (ed.), Archean Crustal Evolution. Elsevier, Amsterdam, pp. 11-44.

Arndt, N.T. 1999. Why was flood volcanism on submerged continental platforms so common in the Precambrian? *Precambrian Res.* 97, 155-164

Arndt, N.T 2003. Komatiites, kimberlites, and boninites. *J. Geophysical Res.* 108, 2293.

Arndt, N., Ginibre, C., Chauval, C., Albarède, F., Cheadle, M., Herzberg, C., Jenner, G., Lahaye, Y., 1998. Were komatiites wet? *Geology* 26, 739-742.

Arndt, N.T. and Jenner, G.A. 1986. Crustally contaminated komatiites and basalts from Kambalda, Western Australia. *Chem. Geol.* 56, 229-255.

Arndt, N.T, Lesher, C.M., Barnes, S.J. 2008. Komatiite. Cambridge University Press, pp. 467.

Arndt, N.T., Teixeira, N.A., White, W.M., 1989. Bizarre geochemistry of komatiites from the Crixas greenstone belt, Brazil. *Contrib. Mineral. Petrol.* 101, 187-197.

Asavof, E.V., Sobolev, A.V., Gurenko, A.A., Arndt, N.T., Batanova, V.G., Portnyagin, M.V., Garbe-Schönberg, D., Krasheninnikov, S.P. 2018. Belingwe komatiites (2.7 Ga) originate from a plume with moderate water content, as inferred from inclusions in olivine. *Chem. Geol.* 478, 39-59.

Barnes, S.J. and Van Kranendonk, M.J. 2014. Archean andesites in the east Yilgarn craton, Australia: Products of plume-crust interaction? *Lithosphere* 6(2), 80-92.

Bédard, J.H., 2006. A catalytic delamination-driven model for coupled genesis of Archean crust and sub-continental lithospheric mantle. *Geochim. Cosmochim. Acta* 70, 1188-1214.

Bédard, J.H., 2018. Stagnant lids and mantle overturns: Implications for Archaean tectonics, magmagenesis, crustal growth, mantle evolution, and the start of plate tectonics. *Geosci. Frontiers* 9, 19-49.

Bédard J.H., Brouillette P., Madore L., Berlaz A., 2003. Archaean cratonization and deformation in the northern Superior Province, Canada: an evaluation of plate tectonic versus vertical tectonic models. *Precambrian Res.* 127, 61-87.

Bédard, J.H., Harris, L.B., Thurston, P.C., 2013. The hunting of the snArc. *Precambrian Res.* 229, 20-48.

Belousova, E.A., Kostitsyn, Y.A., Griffin, W.L., Begg, G.C., O'Reilly, S.Y., Pearson, N.J., 2010. The growth of the continental crust: constraints from zircon Hf-isotope data. *Lithos* 119, 457-466.

Bennett, V.C., Brandon, A.D., Nutman, A.P., 2007. Coupled ^{142}Nd-^{143}Nd isotopic evidence for Hadean mantle dynamics. *Science* 318, 1907-1910.

Beukes, N.J. and Cairncross, B., 1991. A lithostratigraphic-sedimentological reference profile of the late Archaean Mozaan Group. Pongola Supergroup: application to sequence stratigraphy and correlation to the Witwatersrand Supergroup. *S. Afr. J. Geol.* 94, 44-59.

Beukes, N.J. and Lowe, D.R., 1989. Environmental control on diverse stromatolite morphologies in the 3000 Myr Pongola Supergroup, South Africa. *Sedimentology* 36, 383-397.

Bickle, M.J., 1978. Heat loss from the earth: a constraint on Archaean tectonics from the relation between geothermal gradients and the rate of plate production. *Earth Planet. Sci. Lett.* 40, 301-315.

Bickle, M.J., 1986. Implications of melting for stabilization of the lithosphere and heat loss in the Archaean. *Earth Planet. Sci. Lett.* 80, 314-324.

Bickle, M.J. and Eriksson, K.A., 1982. Evolution and subsidence of Archean sedimentary basins. *Philos. Trans. R. Soc. Lond.* A305, 225-247.

Black, L.P., Williams, I.S., Compston, W., 1986. Four zircon ages from one rock: the history of a 3930 Ma old granulite from Mount Sones, Enderby Land, Antarctica. *Contrib. Mineral. Petrol.* 94, 427-437.

Blichert-Toft, J. and Arndt, N.T., 1999. Hf isotope compositions of komatiites. *Earth Planet. Sci. Lett.* 171, 439-451.

Blichert-Toft, J., Arndt, N.T. Gruau, G. 2004. Hf isotopic measurements on Barberton komatiites: effects of incomplete sample dissolution and importance for primary and secondary magmatic signatures. *Chem. Geol.* 207, 261-275.

Blichert-Toft, J., Arndt, N.T., Wilson, A. Coetzee, G., 2015. Hf and Nd isotope systematics of early Archean komatiites from surface sampling and ICDP drilling in the Barberton Greenstone Belt, South Africa. *Am. Mineralogist* 100, 2396-2411.

Boily, M., Leclair, A., Maurice, C., Bédard, J. H., David, J. 2009. Paleo- to Mesoarchean basement recycling and terrane definition in the Northeastern Superior Province, Québec, Canada. *Precambrian Res.* 168, 23-44.

Bolhar, R., Woodhead, J.D., Hergt, J.M. 2002. Comment on: "Growth and recycling of early Archaean continental crust: geochemical evidence from the Coonterunah and Warrawoona groups, Pilbara Craton, Australia" by Green, M.G. et al. (*Tectonophysics* 322, 69-88). *Tectonophysics* 344, 289-292.

Bolhar, R., Woodhead, J.D., Hergt, J.M. 2003. Continental setting inferred for emplacement of the 2.9-2.7 Ga Belingwe Greenstone Belt, Zimbabwe. *Geol. Soc. Am.* 31(4), 295-298.

Bouvier, A., Vervoort, J.D., Patchett, P.J. 2008. The Lu-Hf and Sm-Nd isotopic composition of CHUR: Constraints from unequilibrated chondrites and implications for the bulk composition of terrestrial planets. *Earth Planet. Sci. Lett.* 273, 48-57.

Bowring, S.A., Williams, I.S., Compston, W., 1989. 3.96 Ga gneisses from the Slave Province, NWT, Canada. *Geology* 17, 971-975.

Boyet M., Albarède F., Garcia M.O., Pik R., 2005. A search for 142Nd evidence of primordial mantle heterogeneities in plume basalts. *Geophys. Res. Lett.* 32, No 32, L04306.

Boyet, M. and Carlson, R.W., 2005. ^{142}Nd evidence for early (>4.53 Ga) global differentiation of the silicate Earth. *Science* 309, 576-581.

Boyet M. and Carlson R.W., 2006. A new geochemical model for the Earth's mantle inferred from ^{146}Sm-^{142}Nd systematics. *Earth Planet. Sci. Lett.* 250, 254-268.

Brown, M., 2015. Paleo- to Mesoarchean polymetamorphism in the Barberton Granite-Greenstone Belt, South Africa: Constraints from U-Pb monazite and Lu-Hf garnet geochronology on the tectonic processes that shaped the belt: discussion. *Geol. Soc. Am. Bull.* 127, 1550-1557.

Burke, K., Kidd, W.S.F., Kusky, T.M., 1985. The Pongola structure of southeastern Africa: the World's oldest preserved rift? *J. Geodyn.* 2, 35-49.

Byerly, G.R., Kröner, A., Lowe, D.R., Todt, W., Walsh, M.M., 1996. Prolonged magmatism and time constraints for sediment deposition in the early Archaean

Barberton greenstone belt: evidence from the Upper Onverwacht and Fig Tree groups. *Precambrian Res.* 78, 125-138.

Byerly, G.R., Kröner, A., Lowe, D.R., Walsh, M.M. 1993. Sequential magmatic evolution of the early Archean Onverwacht Group: evidence from the upper formations. *Eos* (Transactions, Amer. Geophysical Union) 74, pp. 660.

Byerly, G.R., Lowe, D.R., Heubeck, C., in press. Geologic evolution of the Barberton Greenstone Belt – A unique record of crustal development, surface processes, and early life 3.55–3.20 Ga. In: Van Kranendonk, M.J., Bennett, V.C., Hoffmann, J.E. (eds.) Earth's Oldest Rocks (2nd. Ed.), Elsevier, Amsterdam, 1050 p., ISBN: 9780444639011.

Campbell, I.H. and Davies, D.R. 2017. Raising the continental crust. *Earth Planet. Sci. Lett.* 460, 112-122.

Campbell, I.H., Griffiths, R.W., Hill, R.I. 1989. Melting in an Archaean mantle plume: heads it's basalts, tails it's komatiites. *Nature* 339, 697-699.

Carlson, R.W., Boyd, F.R., Shirey, S.B., Janney, P.E., Grove, T.L., Bowring, S.A., Schmitz, M.D., Dann, J.C., Bell, D.R., Gurney, J.J., Richardson, S.H., Tredoux, M., Menzies, A.H., Pearson, D.G., Hart, R.J., Wilson, A.H., Moser, D., 2000. Continental growth, preservation, and modification in southern Africa. *GSA Today* 10, 1-7.

Caro, G., 2011. Early silicate Earth differentiation. *Annu. Rev. Earth Planet. Sci.* 39, 31-58. http://dx.doi.org/10.1146/annurev-earth-040610-133400.

Caro, G., Bourdon, B., Wood, B.J., Corgne, A., 2005. Trace-element fractionation in Hadean mantle generated by melt segregation from a magma ocean. *Nature* 436, 249-249.

Caro G., Bourdon B., Birck J.L., Moorbath S., 2006. High-precision $^{142}Nd/^{144}Nd$ measurements in terrestrial rocks: constraints on the early differentiation of the Earth's mantle. *Geochim. Cosmochim. Acta* 70, 164-191.

Caro, G., Morino, P., Mojzsis, S.J., Cates, N.L., Bleeker, W., 2017. Sluggish Hadean geodynamics: Evidence from coupled $^{146,147}Sm$-$^{142,143}Nd$ systematics in Eoarchean supracrustal rocks of the Inukjuak domain (Québec). *Earth Planet. Sci. Lett.* 457, 23-37.

Cattell, A., Krogh, T.E., Arndt, N.T. 1984. Conflicting Sm-Nd whole rock and U-Pb zircon ages for Archean Lavas from Newton Township, Abitibi Belt, Ontario. *Earth Planet. Sci. Lett.* 70, 280-290.

Chauvel, C., Dupré, B., Todt, W., Arndt, N.T., Hofmann, A.W. 1983. Pb and Nd isotopic correlation in Archaean and Proterozoic greenstone belts. *Eos* 64, pp. 330.

Chavangac, V., 2004. A geochemical and Nd iosotopic study of Barberton komatiites (South Africa): implication for the Archean mantle. *Lithos* 75, 253-281.

Coffin, M.F. and Eldholm, O. 1993. Scratching the surface: estimating the dimensions of large igneous provinces. *Geology* 21, 515-518.

Collins, W.J., Van Kranendonk, M.J., and Teyssier, C., 1998. Partial convective overturn of Archaean crust in the east Pilbara Craton, Western Australia: driving mechanisms and tectonic implications. *J. Struct. Geol.* 20, 1405-1424.

Compston, W. and Kröner, A., 1988. Multiple zircon growth within early Archaean tonalitic gneiss from the Ancient Gneiss Complex, Swaziland. *Earth Planet. Sci. Lett.* 87, 13-28.

Condie, K.C., 1997. Contrasting sources for upper and lower continental crust: the greenstone connection. *J. Geology* 105, 729-736.

Condie, K.C., 2005. High field strength element ratios in Archean basalts: a window into evolving sources of mantle plumes? *Lithos* 79, 491-504.

Corgne, A., Liebske, C., Wood, B.J., Rubie, D.C., Frost, D.J., 2005. Silicate perovskite-melt partitioning of trace elements and geochemical signature of a deep perovskitic reservoir. *Geochim. Cosmochim. Acta* 69, No. 2, 485-496.

Cutts, K.A., Stevens, G., Hoffmann, J.E., Buick, I., Frei, D., Münker, C., 2013. Paleo- to Mesoarchean polymetamorphism in the Barberton Greenstone Belt: constraints from U-Pb monazite and Lu-Hf garnet geochronology on the tectonic processes that shaped the belt. *Geol. Soc. Am. Bull.* 126, 251-270.

Dale, C.W., Kruijer, T.S., Burton, K.W., 2016. Highly siderophile element and ^{182}W evidence for a partial late veneer in the source of 3.8 Ga rocks from Isua, Greenland. *Earth Planet. Sci. Lett.* 458, 394-404.

Davies, G.F., 1995. Punctuated tectonic evolution of the Earth. *Earth Planet. Sci. Lett.* 36, 363-380.

Debaille, V., O´Neill, C., Brandon, A.D., Haenecour, P., Yin, Q.-Z., Mattielli, N., Treiman, A.H., 2013. Stagnant-lid tectonics in early Earth revealed by ^{142}Nd variations in late Archean rocks. *Earth Planet. Sci. Lett.* 373, 83-92.

DePaolo, D.J. and Wasserburg, G.J., 1976. Nd isotopic variations and petrogenetic models. *Geophysical Res. Lett.* 3, 249-252.

DePaolo, D.J. and Wasserburg, G.J., 1979. Sm-Nd age of the Stillwater Complex and the mantle evolution curve for neodimium. *Geochim. Cosmochim. Acta* 43, 999-1008.

De Ronde, C.E.J. and De Wit, M.J., 1994. Tectonic history of the Barberton greenstone belt, South Africa: 490 million years of Archean crustal evolution. *Tectonics* 13, 983-1015.

De Ronde, C.E.J. and Kamo, S.L., 2000. An Archaean Arc-Arc collisional event: a short-lived (ca. 3 Myr) episode, Weltevreden area, Barberton greenstone belt, South Africa. *J. Afr. Earth Sci.* 30 (2), 219-248.

De Wit, M.J. and Ashwal, L.D. 1997. Convergence towards divergent models of greenstone belts. In: De Wit, M. and Ashwall, L.D. (eds.) Greenstone Belts. Oxford Monograph on Geology and Geophysics, vol. 35. Oxford University Press, pp. ix–xvii.

De Wit, M.J., Furnes, H., MacLennan, S., Doucouré, M., Schoene, B., Weckmann, U., Martinez, U., Bowring, S., 2018. Paleoarchean bedrock lithologies across the Makhonjwa Mountains of South Africa and Swaziland linked to geochemical, magnetic and tectonic data reveal early plate tectonic genes flanking subduction margins. *Geosci. Frontiers*, DOI: https://doi.org/10.1016/j.gsf.2017.10.005.

De Wit, M.J., Furnes, H., Robins, B., 2011. Geology and tectonostratigraphy of the Onverwacht Suite, Barberton greenstone belt, South Africa. *Precambrian Res.* 186, 1-27.

De Wit, M.J., Roering, C., Hart, R.J., Armstrong, R.A., de Ronde, C.E.J., Green, R.W.E., Tredoux, M., Peberdy, E., Hart, R.A., 1992. Formation of an Archaean continent. *Nature* 357, 553-562.

Dhuime, B., Hawkesworth, C.J., Cawood, P.A., Storey, C.D., 2012. A change in the geodynamics of continental growth 3 Billion years ago. *Science* 355, 1334-1336.

Diwu, C., Sun, Y., Wilde, S.A., Wang, H., Dong, Z., Zhang, H., Wang, Q., 2013. New evidence for ~4.45 Ga terrestrial crust from zircon xenocrysts in Ordovician ignimbrite in the North Qingling Orogenic Belt, China. *Gondwana Res.* 23(4), 1484-1490.

Dlamini, N., Hofmann, A., Belyanin, G., Xie, H., Kröner, A., Wilson, A., Slabunov, A., 2017. Supracrustal gneisses in southern Swaziland: a basalt-sandstone assemblage of upper Mozaan Group deformed in the Neoarchaean. *S. Afr. J. Geol.* 120.4, 477-500.

Drummond, B.J., 1988. A review of the crust/upper mantle structure in the Precambrian crustal evolution: *Precambrian Res.* 40, 101-116.

Dunn, J.C. 2000. The Komati Formation, Barberton greenstone belt, South Africa, Part I: new map and magmatic architecture. *S. Afr. J. Earth Sci.* 103, 47-68.

Dziggel, A., Armstrong, R.A., Stevens, G., Nasdala, L., 2005. Growth of zircon and titanite during metamorphism in the granitoid-gneiss terrane south of the Barberton greenstone belt, South Africa. *Mineral. Mag.* 69, 1019-1036.

Dziggel, A., Stevens, G., Poujol, M., Anhaeusser, C.R., Armstrong, R.A. 2002. Metamorphism of the granite-greenstone terrane south of the Barberton greenstone belt, South Africa: an insight into the tectono-thermal evolution of the 'lower' portions of the Onverwacht Group. *Precambrian Res.* 114, 221-247.

Echeverría, L.M., 1980. Tertiary or Mesozoic komatiites from Gorgona Island, Colombia: Field relations and geochemistry. *Contrib. Mineral. Petrol.* 73, 253-266.

Eglington, B.M. and Armstrong, R.A., 2004. The Kaapvaal Craton and adjacent orogens, southern Africa: a geochronological database and overview of the geological development of the craton. *S. Afr. J. Geol.* 107, 13-32.

Ersoy, Y. and Helvaci, C., 2010. FC-AFC-FCA and mixing modeller: A Microsoft® Excel© spreadsheet program for modelling geochemical differentiation of magma by crystal fractionation, crustal assimilation and mixing. *Computers Geosci.* 36, 383-390.

Fitton, J.G. and Godard, M. 2004. Origin and evolution of magmas on the Ontong Java Plateau. In: Fitton, J.G., Mahoney, J.J., Wallace, P.J., Saunders, A.D. (eds.) Origin and evolution of the Ontong Java Plateau. *Geol. Soc. Lond., Spec. Pub.* 229, 151-178.

Foley, S.F., Buhre, S., Jacob, D.E., 2003. Evolution of the Archaean crust by delamination and shallow subduction. *Nature* 421, 249-252.

François C., Philippot P., Rey P., Rubatto D., 2014. Burial and exhumation during Archean sagduction in the East Pilbara granite-greenstone terrane. *Earth Planet. Sci. Lett.* 396, 235-251.

Friend, C.R.L. and Nutman, A.P., 2005. Complex 3670-3500 Ma orogenic episodes superimposed on juvenile crust accreted between 3850-3690 Ma, Itsaq Gneiss Complex, southern West Greenland. *J. Geology* 113, 375-398.

Frimmel, H.E., Zeh, A., Lehrmann, B., Hallbauer, D., Frank, W., 2009. Geochemical and geochronological constraints on the nature of the immediate basement next to the Mesoarchaean auriferous Witwatersrand Basin, South Africa. *J. Petrol.* 5 (12), 2187-2220.

Froude, C.F., Ireland, T.R., Kinny, P.D., Williams, I.S., Compston, W., Williams, I.R., Myers, J.S., 1983. Ion-microprobe identification of 4100-4200 Myr old terrestrial zircons. *Nature* 304, 616-618.

Furnes, H., Robins, B., de Wit, M.J., 2012. Geochemistry and petrology of lavas in the upper Onverwacht suite, Barberton Mountain Land, South Africa. *Geol. Soc. S. Afr.* 115.2, 171-210.

Garbe-Schönberg, C.-D. 1993. Simultaneous determination of thirty-seven trace elements in twenty-eight international rock standards ICP-MS. *Geostand. Newsletter* 17, 81-93.

Gold, D.J.C., 2006. The Pongola Supergroup. In: Johnson, M.R., Anhaeusser, C.R., Thomas, R.J. (eds.) The Geology of South Africa. Geological Society of South Africa/Council of Geoscience, Johannesburg/Pretoria, pp. 135-154.

Goldschmidt, V.M., 1930. Geochemische Verteilungsgesetze und kosmische Häufigkeiten der Elemente. *Naturwissenschaften* 18, 999-1013.

Green, D.H. 1981. Petrogenesis of Archaean ultramafic magmas and implications for Archaean tectonics. In: Kröner, A. (ed.) Precambrian Plate Tectonics. Developments in Precambrian Geology, vol. 4. Elsevier, Amsterdam, pp. 469-489.

Griffin, W.L. and O'Reilly, S.Y., 2007a. Cratonic lithospheric mantle: is anything subducted? *Episodes* 1, 43-53.

Griffin, W.L. and O'Reilly, S.Y., 2007b. The earliest subcontinental lithospheric mantle. In: Van Kranendonk, M.J., Smithies, R.H., Bennett, V. (eds.) Earth's Oldest Rocks. Elsevier, Amsterdam, Developments in Precambrian Geology, 15, 1013-1036.

Groenewald, P.B., 2006. Hlagothi Complex. In: Johnson, M.R. (ed.), Catalogue of South African Lithostratigraphic Units 9. South African Committee for Stratigraphy, Pretoria, pp. 3-4.

Grove, T.L., de Wit, M.J., Dann, J. 1997. Komatiites from the Komati type section, Barberton, South Africa. In: De Wit, M.J. and Ashwal, L.D. (eds.) Greenstone Belts. Oxford: Oxford Science Publications, pp. 422-437.

Guitreau, M., Blichert-Toft, J., Martin, H., Moijzsis, S.J., Albarède, F., 2012. Hafnium isotope evidence from Archean granitic rocks for deep-mantle origin of continental crust. *Earth Planet. Sci. Lett.* 337-338, 211-223.

Gumsley, A., de Kock, M.O., Rajesh, H.M., Knoper, M.W., Söderlund, U., Ernst, R.E., 2013. The Hlagothi Complex: The identification of fragments from a Mesoarchaean large igneous province on the Kaapvaal Craton. *Lithos* 174, 333-348.

Gumsley, A., Olsson, J., Söderlund, U., de Kock, M., Hofmann, A., Klausen, M., 2015. Precise U-Pb baddeleyite dating of the Usushwana Complex, southern Africa – Implications for the Mesoarchaean magmatic and sedimentological evolution of the Pongola Supergroup, Kaapvaal Craton. *Precambrian Res.* 267, 174-185.

Gumsley, A., Rådman, J., Söderlund, U., Klausen, M.B., 2016. U-Pb baddeleyite geochronology and geochemistry of the White Mfolozi Dyke Swarm: unravelling the complexities of 2.70-2.66 Ga dyke swarms across the eastern Kaapvaal Craton, South Africa. GFF 138:1, 115-132, DOI: 10.1080/11035897.2015.1122665.

Gutzmer, J., Nhleko, N., Beukes, N.J., Pickard, A., Barley, M.E., 1999. SHRIMP age of a quartz porphyry sill in the Mozaan Group: geochronological implication for the Pongola and Witwatersrand Supergroups. *S. Afr. J. Geol.* 102, 139-146.

Hamilton, W.B., 2003. An alternative Earth. *GSA Today* 13, 4-12.

Hanski, E., Huhma, H., Rastas, P. Kamenetsky, V.S. 2001. The Palaeoproterozoic komatiite-picrite association of Finnish Lapland. *J. Pet.* 42, 855-876.

Harley, S.L. and Kelly, N.M., 2007. Ancient Antarctica: The Archaean of the East Antarctic Shield. In: Van Kranendonk, M.J., Smithies, R.H., Bennet, V.C. (eds.) Earth´s oldest rocks, Elsevier, Amsterdam, 149-186.

Harper, C.L. and Jacobsen, S.B., 1992. Evidence from coupled ^{147}Sm-^{143}Nd and ^{146}Sm-^{142}Nd systematics for very early (4.5-Gyr) differentiation of the Earth's mantle, *Nature* 360, 728-732.

Harrison, T.M., Blichert-Toft, J., Müller, W., Albarede, F., Holden, P., Mojzsis, S.J., 2005. Heterogeneous Hadean hafnium: evidence of continental crust at 4.4 to 4.5 Ga. *Science* 310, 1947-1950.

Hegner, E., Kröner, A., Hofmann, A.W., 1984. Age and isotope geochemistry of the Archaean Pongola and Usushwana suites in Swaziland, southern Africa: A case for crustal contamination of mantle-derived magma. *Earth Planet. Sci. Lett.* 70, 267-279.

Hegner, E., Kröner, A., Hunt, P., 1994. A precise U-Pb zircon age for the Archaean Pongola Supergroup volcanics in Swaziland. *J. Afr. Earth Sci.* 18, 339-341.

Heubeck, C.E. and Lowe, D.R., 1994. Depositional and tectonic setting of the Archean Moodies Group, Barberton Greenstone Belt, South Africa. *Precambrian Res.* 68, 257-290.

Herzberg, C., 1992. Depth and degree of melting of komatiite. *J. Geophys. Res.* 97, 4521-4540.

Herzberg, C., Asimow, P.D., Arndt, N., Niu, Y., Lesher, C.M., Fitton, J.G., Cheadle, M.J., Saunders, A.D., 2007. Temperatures in ambient mantle and plumes: constraints from basalts, picrites, and komatiites. *Geochem. Geophys. Geosyst.* 8, 1-34.

Herzberg, C., Condie, K., Korenaga, J. 2010. Thermal history of the Earth and its petrological expression. *Earth Planet. Sci. Lett.* 292, 79-88.

Heubeck, C., Engelhardt, J., Byerly, G.R., Zeh, A., Sell, B., Luber, T., Lowe, D.R., 2013. Timing of deposition and deformation of the Moodies Group (Barberton Greenstone Belt, South Africa): very high-resolution of Archaean surface processes. Precambrian Res. 231, 236-262.

Hickman, A.H., 1981. Crustal evolution of the Pilbara Block, Western Australia. *Geol. Soc. Australia Spec. Publ.* 7, 57-69.

Hickman, A.H. and Van Kranendonk, M.J., 2004. Diapiric processes in the formation of Archaean continental crust, East Pilbara Granite-Greenstone Terrane, Australia. In: Eriksson, P.G., Altermann, W., Nelson, D.R., Mueller, W.U., Catuneau, O. (eds.) The Precambrian Earth: Tempos and Events. Elsevier, Amsterdam, 54-75.

Hicks, N., Dunlevey, J.N., Liu, K.W., 2011. A new stromatolite occurrence in the Nsuze Group, Pongola Supergroup of northern KwaZulu-Natal, South Africa. *S. Afr. J. Geol.* 114, 195-200.

Hoffmann, J.E. and Kröner, A., in press. Early Archean crustal evolution in southern Africa - an updated record of the Ancient Gneiss Complex of Swaziland. In: Van Kranendonk, M.J., Bennett, V.C., Hoffmann, J.E. (eds.) Earth's Oldest Rocks (2nd. Ed.), Elsevier, Amsterdam, 1050 p., ISBN: 9780444639011.

Hoffmann, J.E., Kröner, A., Hegner, E., Viehmann, S., Xie, H., Iaccheri, L.M., Schneider, K.P., Hofmann, A., Wong, J., Geng, H., Yang, J., 2016. Source composition, fractional crystallization and magma mixing precesses in the 3.48-3.43 Ga Tsawela tonalite suite (Ancient Gneiss Complex, Swaziland) – Implications for Palaeoarchaean geodynamics. *Precambrian Res.* 276, 43-66.

Hoffmann, J.E., Musese, E., Kröner, A., Schneider, K.P., Wong, J., Hofmann, A., Hegner, E., Kasper, H.-U., Münker, C., in prep. Hafnium-Neodymium isotopes, trace element and zircon age constraints on the petrogenesis of the 3.45-3.46 Ga Dwalile greenstone remnant, Ancient Gneiss Complex, Swaziland.

Hoffmann, J.E., Münker, C., Næraa, T., Rosing, M.T., Herwartz, D., Garbe-Schönberg, D., Svahnberg, H., 2011. Mechanisms of Archean crust formation inferred from

high-precision HFSE systematic in TTGs. *Geochim. Cosmochim. Acta* 75, 4157-4178.

Hoffmann, J.E., Münker, C., Polat, A., König, S., Mezger, K., Rosing, M.T. 2010. Highly depleted Hadean mantle reservoirs in the sources of early Archean arc-like rocks, Isua supracrustal belt, southern West Greenland. *Geochim. Cosmochim. Acta* 74, 7236-7260.

Hoffmann, J.E. and Wilson, A.H. 2017. The origin of highly radiogenic Hf isotope compositions 3.33 Ga Commondale komatiite lavas (South Africa). *Chem. Geol.* 455, 6-21.

Hofmann, A. and Harris, C. 2008. Silica alteration zones in the Barberton greenstone belt: A window into subseafloor processes 3.5-3.3 Ga ago. *Chem. Geol.* 257, 221-239.

Hofmann, A., Kröner, A., Xie, H., Hegner, E., Belyanin, G., Kramers, J., Bolhar, R., Slabunov, A., Reinhardt, J., Horváth, P., 2015. The Nhlangano gneiss dome in south-west Swaziland – A record of crustal destabilization of the eastern Kaapvaal craton in the Neoarchaean. *Precambrian Res.* 258, 109-132.

Hunter, D.R., 1965. 1:50000 geological map of Swaziland, Sheets 24 and 25. Swaziland Geological Survey and Mines Department.

Hunter, D.R., 1974. Crustal development in the Kaapvaal craton. I. The Archaean. *Precambrian Res.* 1, 259-294.

Hunter, D.R., Barker, F., Millard, H.T., 1984. Geochemical investigation of Archaean bimodal and Dwalile metamorphic suites, Ancient Gneiss Complex, Swaziland. *Precambrian Res.* 24, 131-155.

Hunter, D.R. and Wilson, A.H., 1988. A continuous record of crustal evolution from 3.5 Ga to 2.6 Ga in Swaziland and northern Natal. *S. Afr. J. Geol.* 91, 57-74.

Iizuka, T., Komiya, T., Ueno, Y., Katayama, I., Uehara, Y., Maruyama, S., Hirata, T., Johnson, S.P., Dunkley, D.J., 2007. Geology and zircon geochronology of the Acasta Gneiss Complex, northwestern Canada: new constraints on its thermal history. *Precambrian Res.* 153, 179-208.

Jackson, M.P.A., 1984. Archaean structural styles in the Ancient Gneiss Complex of Swaziland, South Africa. In: Kröner, A. and Greiling, R. (eds.), Precambrian Tectonics Illustrated. Stuttgart, Schweizerbart'sche, Verlagsbuchhandlung, pp. 1-18.

Jacobsen, S.B. and Wasserburg, G.J., 1979. Mean age of mantle and crustal reservoirs. *J. Geophysical Res.* 84, 7411-7427.

Jahn, B.-M., Gruau, G., Glickson, A.Y. 1982. Komatiites of the Onverwacht Group, South Africa: REE chemistry, Sm-Nd age and mantle evolution. *Contrib. Mineral. Petrol.* 80, 25-40.

Jahn, B.M., Vidal, P., Tilton, G.R. 1979. Archean mantle heterogeneity: evidence from chemical and isotopic abundances in Archean igneous rocks. *Philos. Trans. R. Soc. Lond.* A 297, 353-364.

Jochum, K.P., Arndt, N.T., Hofmann, A.W., 1991. Nb-Th-La in komatiites and basalts: constraints on komatiite petrogenesis and mantle evolution. *Earth Planet. Sci. Lett.* 107, 272-289.

Jochum, K.P., Nohl, U., Herwig, K., Lammel, E., Stoll, B., Hofmann, A.W., 2005. GeoReM: A new geochemical database for reference materials and isotopic standards. *Geostand. Geoanalyt. Res.* 29, 333-338.

Johnson, T.E, Brown, M., Goodenough, K.M., Clark, C., Kinny, P.D., White, R.W., 2016. Subduction or sagduction? Ambiguity in constraining the origin of ultramafic-mafic bodies in the Archean crust of NW Scotland. *Precambrian Res.* 283, 89-105.

Kamo, S.L. and Davis, D.W., 1994. Reassessment of Archean crustal development in the Barberton Mountain Land, South Africa, based on U-Pb dating. *Tectonics* 13, 167-192.

Kemp, A.I.S., Wilde, S.A., Hawkesworth, C.J., Coath, C.D., Nemchin, A., Pidgeon, R.T., Vervoort, J.D., DuFrane, S.A., 2010. Hadean crustal evolution revisited: New constraints from Pb-Hf isotope systematics of the Jack Hills zircons. *Earth Planet. Sci. Lett.* 296, 45-56.

Kerr, A.C., Tarney, J., Marriner, G.F., Klaver, G.T., Saunders, A.D., Thirlwall, F. 1996. The geochemistry and petrogenesis of the late-Cretaceous picrites and basalts of Curacao, Netherlands Antilles: a remnant of an oceanic plateau. *Contrib. Mineral. Petrol.* 124: 29-43.

Kisters, A.F.M., Belcher, R.W., Poujol, M., Dziggel, A., 2010. Continental growth and convergence-related arc plutonism in the Mesoarchaean: evidence from the Barberton granitoid-greenstone terrain, South Africa. *Precambrian Res.* 178, 15-26.

Kisters, A.F.M., Stevens, G., Dziggel, A., Armstrong, R.A., 2003. Extensional detachment faulting and core-complex formation in the southern Barberton granite-greenstone terrane, South Africa: evidence for a 3.2 Ga orogenic collapse. *Precambrian Res. 127*, 355-378.

Klausen, M.B., Söderlund, U., Olsson, J.R., Ernst, R.E., Armoogam, M., Mkhize, S.W., Petzer, G., 2010. Petrological discrimination among Precambrian dyke swarms: Eastern Kaapvaal craton (South Africa). *Precambrian Res.* 183, 501-522.

Kohler, E.A. and Anhaeusser, C.R., 2002. Geology and geodynamic setting of Archaean silicic metavolcaniclastic rocks of the Bien Venue Formation, Fig Tree Group, northeast Barberton greenstone belt, South Africa. *Precambrian Res.* 116, 199-235.

Kröner, A., 2007. The Ancient Gneiss Complex of Swaziland and environs: Record of early Archean crustal evolution in southern Africa. In: Van Kranendonk, M.J., Smithies, R.H., Bennet, V.C. (eds.) Earth´s oldest rocks, Elsevier, Amsterdam, 465-480.

Kröner, A., Anhaeusser, C.R., Hoffmann, J.E., Wong, J., Geng, H., Hegner, E., Xie, H., Yang, J., Liu, D., 2016. Chronology of the oldest supracrustal sequences in the Palaeoarchaean Barberton Greenstone Belt, South Africa and Swaziland. *Precambrian Res.* 279, 123-143.

Kröner, A., Byerly, G.R., Lowe, D.R., 1991. Chronology of early Archean granite-greenstone evolution of the Barberton Mountain Land, South Africa, based on precise dating by single zircon evaporation. *Earth Planet. Sci. Lett.* 103(1-4), 41-54.

Kröner, A., Hegner, E., Wendt, J.I., Byerly, G.R., 1996. The oldest part of the Barberton granitoid-greenstone terrain, South Africa: evidence for crust formation between 3.5 and 3.7 Ga. *Precambrian Res.* 78(1-3), 105-124.

Kröner, A., Hoffmann, J.E., Wong, J., Geng, H.-Y., Schneider, K.P., Xie, H., Yang, J.H., Nhleko, N., in press. Early Archaean rocks of the eastern Kaapvaal Craton. In: Kröner, A. and Hofmann, A. (eds.), Archaean geology of the Kaapvaal Craton. Springer Geology, Springer-Verlag Berlin Heidelberg.

Kröner, A., Hoffmann, J.E., Xie, H., Münker, C, Hegner, E., Wan, Y., Hofmann, A., Liu, D., Yang, J., 2014. Generation of early Archaean grey gneisses through melting of older crust in the eastern Kapvaal craton, southern Africa. *Precambrian Res.* 255, 823-846.

Kröner, A., Hoffmann, J.E., Xie, H., Wu, F., Münker, C., Hegner, E., Wong, J., Wan, Y., Liu, D., 2013. Generation of early Archaean felsic greenstone volcanic rocks through crustal melting in the Kapvaal craton, southern Africa. *Earth Planet. Sci. Lett.* 381, 188-197.

Kröner, A. and Tegtmeyer, A., 1994. Gneiss-greenstone relationships in the Ancient Gneiss Complex of southwestern Swaziland, southern Africa, and implications for early crustal evolution. *Precambrian Res.* 67, 109-139.

Kröner, A., Wendt, J.I., Milisenda, C., Compston, W., Maphalala, R., 1993. Zircon geochronology and Nd isotope systematics of the Ancient Gneiss Complex, Swaziland, and implications for crustal evolution. In: Kröner, A. (ed.), The Ancient Gneiss Complex: Overview Papers and Guidebook for Excursion. *Geol. Surv. Mines Dep. Swaziland Bull.* No. 11, pp. 15-37.

Kröner, A., Anhaeusser, C.R., Hoffmann, J.E., Wong, J., Geng, H., Hegner, E., Xie, H., Yang, J., Liu, D., 2016. Chronology of the oldest supracrustal sequences in the Palaeoarchaean Barberton Greenstone Belt, South Africa and Swaziland. *Precambrian Res.* 279, 123-143.

Lahaye, Y., Arndt, N., Byerly, G., Chauvel, C., Fourcade, S., Gruau, G. 1995. The influence of alteration on trace-element and Nd isotopic compositions of komatiites. *Chem. Geol.* 126, 43-64.

Lana, C., Kisters, A.F.M., Stevens, G. 2010. Exhumation of Mesoarchean TTG gneisses from the middle crust: Insights from the Steynsdorp core complex, Barberton granitoid-greenstone terrain, South Africa. *Geol. Soc. Am. Bull.* 122, 183-197.

Laurent, O., Martin, H., Moyen, J.F., Doucelance, R., 2014. The diversity and evolution of late-Archean granitoids: evidence for the onset of modern-style plate tectonics between 3.0 and 2.5 Ga. *Lithos* 205, 208-235.

Layer, P.W., Kröner, A., McWilliams, M., Burghele, A., 1988. Paleomagnetism and age of the Archean Usushwana Complex, southern Africa. *J. Geophys. Res.* 93, 449-457.

Leclerc, F., Bédard, J.H., Harris, L.B., McNicoll, V., Goulet, N., Roy, P., and Houle, P. 2011. Tholeiitic to calc-alkaline cyclic volcanism in the Roy Group, Chibougamau area, Abitibi Greenstone Belt – Revised stratigraphy and implications for VHMS exploration. *Canad. J. Earth Sci.* 48, 661-694

Lécuyer, C., Gruau, G., Anhaeusser, C.R., Fourcade, S. 1994. The origin of fluids and the effects of metamorphism on the primary chemical compositions of Barberton komatiites: New evidence from geochemical (REE) and isotopic (Nd, O, H, $^{39}Ar/^{40}Ar$) data. *Geochim. Cosmochim. Acta* 58, 969-984.

Le Maitre RW, 2002. A classification and glossary of terms: recommendations of the international union of geological sciences subcommission on the systematics of igneous rocks. Cambridge University Press, Cambridge.

Liu, J., Touboul, M., Ishikawa, A., Walker, R.J., Pearson, D.G., 2016. Widespread tungsten isotope anomalies and W mobility in crustal and mantle rocks of the Eoarchean Saglek Block, northern Labrador, Canada: Implications for early Earth processes and W recycling. *Earth Planet. Sci. Lett.* 448, 13-23.

Lopez-Martinez, M., York, D., Hanes, J.A. 1992. A $^{40}Ar/^{39}Ar$ geochronological study of komatiites and komatiitic basalts from the lower Onverwacht volcanics: Barberton Mountain Land, South Africa. *Precambrian Res.* 57, 481-526.

Lowe D.R. and Byerly, G.R., 1999. Stratigraphy of the west-central part of the Barberton Greenstone Belt, South Africa. In: Lowe, D.R. and Byerly, G.R. (eds.), Geological Evolution of the Barberton Greenstone Belt. *Geol. Soc. Am. Spec. Paper* 329, 1-36.

Lowe, D.R. and Byerly, G.R., 2007. An overview of the geology of the Barberton greenstone belt and vicinity: implications for early crustal development. In: Van Kranendonk, M.J., Smithies, R.H., Bennett, V.C. (eds.) Earth's Oldest Rocks. Elsevier, Amsterdam, Developments in Precambrian Geology, 15, 481-526.

Lowe, D.R., Byerly, G.R., Ransom, B.L., Nocita, B.W., 1985. Stratigraphic and sedimentological evidence bearing on structural repetition in early Archean rocks of the Barberton greenstone belt, South Africa. *Precambrian Res.* 27, 165-186.

Ludden, J., Gelinas, L., Trudel, P., 1982. Archean metavolcanics from the Rouyn-Noranda district, Abitibi greenstone belt, Quebec: 2. Mobility of trace elements and petrogenetic constraints. *Can. J. Earth Sci.* 19, 2276-2287.

Lugmair, G.W. and Marti, K. 1977. Sm-Nd-Pu timepieces in the Angra Dos Reis meteorite. *Earth Planet. Sci. Lett.* 35, 273-284.

Martin, H., Moyen, J.-F., Guitreau, M., Blichert-Toft, J., Le Pennec, J.-L., 2014. Why Archaean TTG cannot be generated by MORB melting in subduction zones. *Lithos* 198-199, 1-13.

Martin, H., Smithies, R.H., Rapp, R., Moyen, J.F., Champion, D., 2005. An overview of adakite, tonalite–trondhjemite–granodiorite (TTG), and sanukitoid: relationships and some implications for crustal evolution. *Lithos* 79, 1-24.

Maurice, C., David, J., Bédard, J.H., Francis, D. 2009. Evidence for a widespread mafic cover sequence and its implications for continental growth in the Northeastern Superior Province. *Precambrian Res.* 168, 45-65.

Maya, J.M., Bhutani, R., Balakrishnan, R., Sandhya, S.R., 2016. Petrogenesis of 3.15 Ga old Banasandra komatiites from the Dharwar craton, India: Implications for early mantle heterogeneity. *Geosci. Frontiers* 8, 467-481.

McLennan, S.M. and Taylor, S.R., 1991. Sedimentary rocks and crustal evolution: Tectonic setting and secular trends. *J. Geol.* Vol. 99, No. 1, 1-21.

Meissner, F., Schmidt-Ott, W.-D., Ziegeler, L., 1987. Half-life and α-ray energy of ^{146}Sm. *Z. Phys.* A 327, 171-174.

Mojzsis, S.J., Harrison, T.M., Pidgeon, R.T., 2001. Oxygen-isotope evidence from ancient zircons for liquid water at the Earth's surface 4,300 Myr ago. *Nature* 409, 178-181.

Mole, D.R., Barnes, S.J., Yao, Z., White, A.J.R., Maas, R., Kirkland, C.L. 2018. The Archean Fortescue large igneous province: A result of komatiite contamination by a distinct Eo-Paleoarchean crust. *Precambrian Res.* 310, 365-390.

Moser, D.E., Flowers, R.M., Hart, R.J., 2001. Birth of the Kaapvaal tectosphere 3.08 billion years ago. *Science* 291, 465-468.

Moyen, J.-F., 2011. The composite Archaean grey gneisses: petrological significance, and evidence for a non-unique tectonic setting for Archaean crustal growth. *Lithos* 123, 21-36.

Moyen, J.F. and Martin, H., 2012. Forty years of TTG research. *Lithos* 148, 312-336.

Moyen, J.-F., Stevens, G., Kisters, A.F.M., 2006. Record of mid-Archaean subduction from metamorphism in the Barberton terrain, South Africa. *Nature* 443, 559–562.

Moyen, J.-F., Stevens, G., Kisters, A.F.M., Belcher, R.W., 2007. TTG Plutons of the Barberton Granitoid-Greenstone Terrain, South Africa. In: Van Kranendonk M.J., Smithies R.H., Bennett, V.C. (eds.) Earth´s oldest rocks. Elsevier B.V., 607-667.

Mukasa, S.B., Wilson, A.H., Young, K.R., 2013. Geochronological constrains on the magmatic and tectonic development of the Pongola Supergroup (Central Region), South Africa. *Precambrian Res.* 224, 268-286.

Münker C., Weyer S., Scherer E., Mezger K., 2001. Separation of high field strength elements (Nb, Ta, Zr, Hf) and Lu from rock samples for MC-ICPMS measurements. *Geochem. Geophys. Geosys.* 2, 10.1029/2001GC000183.

Murphy, R.C.L., 2015. Stabilising a craton: The origin and emplacement of the 3.1 Ga Mpuluzi Batholith. Unpublished PhD thesis, Macquarie University, Sydney, Australia, pp. 224 and appendices, http://hdl.handle.net/1959.14/1069283.

Nebel, O. Arculus, R.J., Ivanic, T.J., Nebel-Jacobsen, Y.J. 2013. Lu-Hf isotopic memory of plume-lithosphere interaction in the source of layered mafic intrusions, Windimurra Igneous Complex, Yilgarn Craton, Australia. *Earth Planet. Sci. Lett.* 380, 151-161.

Nédélec A., Chevrel M.O., Moyen J.F., Ganne J., Fabre, S., 2012. TTGs in the making: Natural evidence from the Inyoni shear zone (Barberton, South Africa). *Lithos* 153, 25-38.

Nelson, D.R., Robinson, B.W., Myres, J.S., 2000. Complex geological histories extending for ≥4.0 Ga deciphered from xenocryst zircon microstructures. *Earth Planet. Sci. Lett.* 181, 89-102.

Nesbitt, R.W., Sun, S.S., Purvis, A.C. 1979. Komatiites: geochemistry and genesis. *Canad. Mineralogist* 17, 165-186.

Nhleko, N., 2003. The Pongola Supergroup in Swaziland. Unpublished PhD thesis, Rand Afrikaans University, Johannesburg, pp. 132.

Nisbet, E.G. 1982. The tectonic setting and petrogenesis of komatiites. In: Arndt, N.T. and Nisbet, E.G. (eds.) Komatiites. London: George Allen and Unwin, pp. 501-520.

Nisbet, E.G., Cheadle, M.J., Arndt, N.J., Bickle, M.J., 1993. Constraining the potential temperature of the Archean mantle: A review of the evidence from komatiites. *Lithos* 30, 291-307.

Nutman, A.P., Friend, C.R.L., Bennett, V.C., 2002. Evidence for 3650-3600 Ma assembly of the northern end of the Itsaq Gneiss complex, Greenland: implications for early Archean tectonics. *Tectonics* 21 (1), 10.1029/2000TC001203.

Nutman, A.P., McGregor, V.R., Friend, C.R.L., Bennett, V.C., Kinny, P.D., 1996. The Itsaq Gneiss Complex of southern West Greenland; the world's most extensive record of early crustal evolution (3900-3600 Ma). *Precambrian Res.* 78, 1-397.

O´Hara, M.J. 1977. Geochemical evolution during fractional crystallisation of a periodically refilled magma chamber. *Nature* 266, 503-507.

Ohtani, E. 1984. Generation of komatiite magma and gravitational differentiation in the deep upper mantle. *Earth Planet. Sci. Lett.* 67, 261-272.

Ohtani, E., Kawabe, I., Moriyama, J., Nagata, Y. 1989. Partitioning of elements between majorite garnet and melt and implications for petrogenesis of komatiite. *Contrib. Mineral. Petrol.* 103, 263-269.

Olsson. J.R., Söderlund, U., Hamilton, M.A., Klausen, M.B., Helffrich, G.R., 2011. A late Archaean radiating dyke swarm as possible clue to the origin of the Bushveld Complex. *Nature Geosci.* 4, 865-869.

Olsson, J.R., Söderlund, U. Klausen, M.B., Ernst, R.E., 2010. U-Pb baddeleyite ages linking major Archean dyke swarms to volcanic-rift forming events in the Kaapvaal

craton (South Africa), and a precise age for the Bushveld Complex. *Precambrian Res.* 183, 490-500.

O'Neil, J., Boyet, M., Carlson, R.W., Paquette, J.-L., 2013. Half a billion years of reworking of Hadean mafic crust to produce the Nuuvuagittuq Eoarchean felsic crust. *Earth Planet, Sci. Lett.* 379, 13-25.

O'Neil, J. and Carlson, R.W., 2017. Building Archean cratons from Hadean mafic crust. *Science* 355, 1199-1202.

O'Neil, J., Carlson, R.W., Francis, D., Stevenson, R.K., 2008. Neodymium-142 evidence for hadean mafic crust. *Science* 321, 1828-1831.

O'Neil, J., Carlson, R.W., Paquette, J.-L., Francis, D., 2012. Formation age and metamorphic history of the Nuvvuagittuq greenstone belt. *Precambrian Res.* 220-221, 23-44.

O´Neil, J., Maurice, C., Stevenson, R.K., Larocque, J., Cloquet, C., David, J., Francis, D., 2007. The geology of the ca. 3.8 Ga Nuvvuagittuq (Porpoise Cove) Greenstone Belt, northeastern Superior Province, Canada. In: Van Kranendonk, M.J., Smithies, R.H., Bennet, V.C. (eds.) Earth´s oldest rocks, Elsevier, Amsterdam, pp. 219-250.

O'Neil, J., Rizo, H., Boyet, M., Carlson, R.W., Rosing, M.T., 2016. Geochemistry and Nd isotopic characteristics of Earth´s Hadean mantle and primitive crust. *Earth Planet. Sci. Lett.* 442, 194-205.

Ossa Ossa, F., Hofmann, A., Vidal, O., Kramers, J.D., Belyanin, G., Cavalazzi, B., 2016. Unusual manganese enrichment in the Mesoarchean Mozaan Group, Pongola Supergroup, South Africa. *Precambrian. Res.* 281, 414-433.

Palme, H. and O´Neill, H.S.C., 2014. Cosmochemical estimates of mantle composition. In: Holland, H.D. and Turekian, K.K. (eds.) Treatise on Geochemistry, Volume 3: The Mantle and Core. 2nd edn., Elsevier Ltd, Amsterdam, pp 1-39.

Parman, S., Dann, J., Grove, T.L., de Wit, M.J. 1997. Emplacement conditions of komatiite magmas from the 3.49 Ga Komati Formation, Barberton Greenstone Belt, South Africa. *Earth Planet. Sci. Lett.* 150, 303-323.

Parman, S.W., Grove, T.L., Dann, J.C., 2001. The production of Barberton komatiites in an Archean subduction zone. *Geophys. Res. Lett.* vol. 28, no. 13, 2513-2516.

Parman S.W., Shimizu, N., Grove, T.L., Dann, J.C., 2003. Constraints on the pre-metamorphic trace element composition of Barberton komatiites from ion probe analyses of preserved clinopyroxene. *Contrib. Mineral. Petrol.* 144, 383-396.

Patchett, P.J., Kauvo, O., Hedge, C.E., Tatsumoto, M., 1981. Evolution of continental crust and mantle heterogeneity: evidence from Hf isotopes. *Contrib. Mineral. Petrol.* 78, 279-297.

Paquette, J.L., Barbosa, J.S.F., Rohais, S., Cruz, S.C.P., Goncalves, P., Peucat, J.J., Leal, A.B.M., Santos-Pinto, M., Martin, H., 2015. The geological roots of South America: 4.2 Ga and 3.7 Ga zircon crystals discovered in N.E. Brazil and N.W. Argentina. *Precambrian Res.* 271, 49-55.

Pearce, J.A., 2008. Geochemical fingerprinting of oceanic basalts with applications to ophiolite classification and the search for Archean oceanic crust. *Lithos* 100, 14-48.

Philpotts, A.R. and Ague, J.J., 2009. Principles of igneous and metamorphic petrology, Cambridge University Press, 2nd edition, pp. 684.

Pin, C. and Zalduegui, J.F.S., 1997. Sequential separation of light rare-earth elements, thorium and uranum by miniaturized extraction chromatography: Application to isotopic analyses of silicate rocks. *Analyt. Chim. Acta* 339, 79-89.

Polat, A., Herzberg, C., Münker, C., Rodgers, R., Kusky, T., Li, J., Fryer, B., Delaney, J. 2006. Geochemical and petrological evidence for a supra-subduction zone origin of Neoarchean (ca. 2.5 Ga) peridotites, central orogenic belt, North China craton. *Geol. Soc. Am. Bull.* 118, 771-784.

Polat, A., Hofmann, A.W., Rosing, M.T., 2002. Boninite-like volcanic rocks in the 3.7 - 3.8 Ga Isua Greenstone Belt, West Greenland: geochemical evidence for intra-oceanic subduction zone processes in the early Earth. *Chem. Geol.* 184, 231-254.

Polat, A., Li, J., Fryer, B., Kusky, T., Gagnon, J., Zhang, S. 2005. Geochemical characteristics of the Neoarchean (2800–2700 Ma) Taishan greenstone belt, North China Craton: evidence for plume-craton interaction. *Chem. Geol.* 230, 60-87.

Poujol, M., 2007. An overview of the pre-Mesoarchean rocks of the Kaapvaal Craton, South Africa. In: Van Kranendonk, M.J., Smithies, R.H., Bennet, V.C. (eds.) Earth´s oldest rocks, Elsevier, Amsterdam, 453-464.

Poujol, M., Robb, L.J., Anhaeusser, C.R., Gericke, B., 2003. A review of the geochronological constraints on the evolution of the Kaapvaal Craton, South Africa. *Precambrian Res.* 127, 181-213.

Puchtel, I.S., Blichert-Toft, J., Touboul, M., Horan, M.F., Walker, R.J., 2016b. The coupled ^{182}W-^{142}Nd record of early terrestrial mantle differentiation. *Geochem. Geophys. Geosyst.* 17, DOI:10.1002/2016GC006324.

Puchtel, I.S., Blichert-Toft, J., Touboul, M., Walker, R.J., Byerly, G.R., Nisbet, E.G., Anhaeusser, C.R., 2013. Insights into early Earth from Barberton komatiites: evidence from lithophile isotope and trace element systematics. *Geochim. Cosmochim. Acta* 108, 63-90.

Puchtel, I.S., Touboul, M., Blichert-Toft, J., Walker, R.J., Brandon, A.D., Nicklas, R.W., Kulikov, V.S., Samsonov, A.V., 2016a. Lithophile and siderophile element systematics of Earth's mantle at the Archean-Proterozoic boundary: Evidence from 2.4 Ga komatiites. *Geochim. Cosmochim. Acta* 180, 227-255.

Reinhard J., Elburg M.A., Andersen T., 2015. Zircon U-Pb age data and Hf isotopic signature of Kaapvaal basement granitoids from the Archaean White Mfolozi Inlier, Northern Kwazulu-Natal. *S. Afr. J. Geol.* 118, 473-488.

Rizo, H., Boyet, M., Blichert-Toft, J., O'Neil, J., Rosing, M.T., Paquette, J.-L., 2012. The elusive Hadean enriched reservoir revealed by ^{142}Nd deficits in Isua Archean rocks. *Nature* 491, 96-100.

Rizo, H., Boyet, M., Blichert-Toft, J., Rosing, M.T., 2011. Combined Nd and Hf isotope evidence for deep-seated source of Isua lavas. *Earth Planet. Sci. Lett.* 312, 267-279.

Rizo, H., Boyet, M., Blichert-Toft, J., Rosing, M.T., 2013. Early mantle dynamics inferred from ^{142}Nd variations in Archean rocks from southwest Greenland. *Earth Planet. Sci. Lett.* 377, 324-335.

Rizo, H., Walker, R.J., Carlson, R.W., Touboul, M., Horan, M.F., Puchtel, I.S., Boyet, M., Rosing, M.T., 2016. Early Earth differentiation investigated through ^{142}Nd, ^{182}W, and highly siderophile element abundances in samples from Isua, Greenland. *Geochim. Cosmochim. Acta* 175, 319-336.

Robb L.J., Brandl G., Anhaeusser C.R., Poujol M., 2006. Archaean granitoid intrusions. In: Johnson, M.R., Anhaeusser, C.R., Thomas, R.J. (eds.) The geology of South Africa. Geological Society of South Africa and Council for Geoscience, Johannesburg and Pretoria: 57-94.

Robin-Popieul, C.C.M., Arndt, N.T., Chauvel, C., Byerly, G.R., Sobolev, A.V., Wilson, A., 2012. A new model for Barberton komatiites: deep critical melting with high melt retention. *J. Pet.* 53, 2191-2229.

Roerdink, D.L. 2013. Geology and stable isotope geochemistry of Paleoarchean sulfur. Formation, preservation and geobiology of ancient pyrite and barite. Unpublished Ph.D thesis, Utrecht University.

Roerdink, D.L., Mason, P.R.D., Whitehouse, M.J., Brouwer, F.M., 2016. Reworking of atmospheric sulfur in a Paleoarchean hydrothermal system at Londozi, Barberton Greenstone Belt, Swaziland. *Precambrian Res.* 280, 195-204.

Roth, A.S.G., Bourdon, B., Mojzsis, S.J., Touboul, M., Sprung, P., Guitreau, M., Blichert-Toft J., 2013. Inherited ^{142}Nd anomalies in Eoarchean protoliths. *Earth Planet. Sci. Lett.* 361, 50-57.

Roth, A.S.G., Bourdon, B., Mojzsis, S.J., Rudge, J.F., Guitreau, M., Blichert-Toft, J., 2014a. Combined ^{147,146}Sm-^{143,142}Nd constraints on the longevity and residence time of early terrestrial crust. *Geochem. Geophys. Geosyst.* 15, 2329-2345.

Roth, A.S.G., Scherer, E.E., Maden, C., Mezger, K., Bourdon, B., 2014b. Revisiting the ^{142}Nd deficits in the 1.48 Ga Khariar alkaline rocks, India. *Chem. Geol.* 386, 238-248.

Salters, V.J.M. and Stracke, A., 2004. Composition of the depleted mantle. *Geochem. Geophys. Geosyst.* 5, Q05B07, DOI:10.1029/2003GC000597.

Scherer, E.E., Cameron, K.L., Blichert-Toft, J. 2000. Lu-Hf garnet geochronology: Closure temperature relative to the Sm-Nd system and the effects of trace mineral inclusions. *Geochim. Cosmochim. Acta* 64, 3413-3432.

Scherer, E.E., Münker, C., Metzger, K. 2001. Calibrating the Lu-Hf clock. *Science* 293, 683-686.

Schneider, K.P., Hoffmann, J.E., Boyet, M., Münker, C., Kröner, A., 2018. Coexistence of enriched and modern-like ^{142}Nd signatures in Archean igneous rocks of the eastern Kaapvaal Craton, southern Africa. *Earth Planet. Sci. Lett.* 487, 54-66.

Schneider, K.P., Hoffmann, J.E., Münker, C., Patyniak, M., Sprung, P., Roerdink, D., Garbe-Schönberg, D., Kröner, A., in revision. Petrogenetic evolution of metabasalts and metakomatiites of the lower Onverwacht Group, Barbertin Greenstone Belt (South Africa). *Chem. Geol.*

Schoene, B. and Bowring, S.A., 2010. Rates and mechanisms of Mesoarchean magmatic arc construction, eastern Kaapvaal craton, Swaziland. *GSA Bulletin* 122, 408-429.

Schoene, B., De Wit, M.J., Bowring, S.A., 2008. Mesoarchean assembly and stabilization of the eastern Kaapvaal Craton: a structural-thermochronological perspective. *Tectonics* 27, TC5010.

Schoene, B., Dudäs, F.O.L., Bowring, S.A., de Wit, M.J., 2009. Sm-Nd isotopic mapping of lithospheric growth and stabilization in the eastern Kaapvaal craton. *Terra Nova* 21, 219-228.

Shaw D.M., 1970. Trace element fractionation during anatexis. *Geochim. Cosmochim. Acta* 34, 237-243.

Shirey, S.B., Harris, J.W., Richardson, S.H., Fouch, M.J., James, D.E., Cartigny, P., Deines, P., Viljoen, F., 2002. Diamond genesis, seismic structure, and evolution of the Kaapvaal-Zimbabwe Craton. *Science* 297, 1683-1686.

Shirey, S.B. and Richardson, S.H., 2011. Start of the Wilson Cycle at 3 Ga shown by diamonds from subcontinental mantle. *Science* 333, 434-436.

Sizova, E., Gerya, T., Brown, M., Stüwe, K., in press. What drives metamorphism in early Archean greenstone belts? Insights from numerical modeling. *Tectonophysics*.

Sleep, N.H. and Windley, B.F., 1982. Archean plate tectonics: constraints and inferences. *J. Geol.* 90, 363-379.

Smithies, R.H., 2000. The Archaean tonalite-trondhjemite-granodiorite (TTG) series is not an analogue of Cenozoic adakite. *Earth Planet. Sci. Lett.* 182, 115-125.

Smithies, R.H., Champion, D.C., Van Kranendonk, M.J. 2007. The oldest well-preserved volcanic rocks on Earth: geochemical clues to the early evolution of the Pilbara Supergroup and implications for the growth of a Paleoarchean continent. In: Van Kranendonk, M.J., Smithies, R.H., Bennet, V. (eds.) Earth's Oldest Rocks. Developments in Precambrian Geology. Elsevier, Amsterdam, 15, 339-367.

Smithies, R.H., Champion, D.C., Van Kranendonk, M.J., Howard, H.M., Hickman, A.H., 2005a. Modern-style subduction processes in the Mesoarchaean: geochemical evidence from the 3.12 Ga Whundo intraoceanic arc. *Earth Planet. Sci. Lett.* 231, 221-237.

Smithies, R.H., Ivanic, T.J., Lowrey, J.R., Morris, P.A., Barns, S.J., Wyche, S., Lu, Y.-J., 2018. Two distinct origins for Archean greenstone belts. *Earth Planet. Sci. Lett.* 487, 1069-116.

Smithies, R.H., Van Kranendonk, M.J., Champion, D.C., 2005b. It started with a plume – early Archaean basaltic proto-continental crust. *Earth Planet. Sci. Lett.* 238, 284-297.

Smithies, R.H., Van Kranendonk, M.J., Champion, D.C., 2007. The Mesoarchaean emergence of modern style subduction. In: Maruyama, S. and Santosh, M. (eds.) Island Arcs: Past and Present. *Gondwana Res.* 11, 50-68.

Sobolev, A.V., Asafov, E.V., Gurenko, A.A., Arndt, N.T., Batanova, V.G., Portnyagin, M.V., Garbe-Schönberg, D., Krasheninnikov, S.P. 2016. Komatiites reveal a hydrous Archaean deep-mantle reservoir. *Nature* 531, 628-632.

Söderlund, U., Patchett, J.P., Vervoort, J.D., Isachsen, C.E. 2004. The ^{176}Lu decay constant determined by Lu-Hf and U-Pb isotope systematics of Precambrian mafic intrusions. *Earth Planet. Sci. Lett.* 219, 311-324.

Song, B., Nutman, A.P., Liu, D., Wu, J., 1996. 3800 to 2500 Ma crustal evolution in the Anshan area of Lianoning Province, NW China. *Precambrian Res.* 78, 79-94.

Sossi, P.A., Eggins, S.M., Nesbitt, R.W., Nebel, O., Hergt, J.M., Campbell, I.H., O´Neill, H.S.C., Van Kranendonk, M., Davies, D.R., 2016. Petrogenesis and geochemistry of Archean komatiites. *J. Pet.* 57, 147-184.

Sprung, P., Schuth, S., Münker, C., Hoke, L. 2007. Intraplate volcanism in New Zealand: the role of fossil plume material and variable lithospheric properties. *Contrib. Mineral. Petrol.* 153, 669-687.

Stone, W.E., Deloule, E., Larson, M.S., Lesher, C.M. 1997. Evidence for hydrous high-MgO melts in the Precambrian. *Geology* 25, 143-146.

Storey, M., Mahoney, J.J., Kroenke, L.W., Saunders, A.D., 1991. Are oceanic plateaus sites of komatiite formation? *Geology* 19, 376-379.

Stracke, A. and Bourdon, B., 2009. The importance of melt extraction for tracing mantle heterogeneity. *Geochim. Cosmochim. Acta* 73, 218-238.

Suhr, N., Hoffmann, J.E., Kröner, A., Schröder, S., 2015. Archaean granulite-facies paragneisses from central Swaziland: inferences on Palaeoarchaean crustal reworking and a complex metamorphic history. *J. Geol. Soc. Lond.* 172, 139-152.

Sun, S.S. and Nesbitt, R.W. 1978. Petrogenesis of Archean ultrabasic and basic volcanics: evidence from rare earth elements. *Contrib. Mineral. Petrol.* 65, 301-325.

Szilas, K., Tusch, J., Hoffmann, J.E., Garde, A.A., Münker, C. 2017. Hafnium isotope constraints on the origin of Mesoarchaean andesites in southern West Greenland, North Atlantic Craton. *Geol. Soc. London, Spec. Publ.* 449, https://doi.org/10.1144/SP449.2.

Tanaka, T., Togashi, S., Kamioka, H. Amakawa, H., Kagami, H., Hamamoto, T., Yuhara, M., Orihashi, Y., Yoneda, S., Shimizu, H., Kunimaru, T., Takahashi, K., Yanagi, T., Nakano, T., Fujimaki, H., Shinjo, R., Asahara, Y., Tanimizu, M., Dragusanu, C. 2000. JNdi-1: a neodymium isotopic reference in consistency with LaJolla neodymium. *Chem. Geol.* 168, 279-281.

Tang, M., Wang, X.-L., Shu, X.-J., Wang, D., Yang, T., Gopon, P., 2014. Hafnium isotopic heterogeneity in zircons from granitic rocks: geochemical evalution and modeling of "zircon effect" in crustal anatexis. *Earth Planet. Sci. Lett.* 389, 188-199.

Tang, Y.-J., Zhang, H.-F., Ying, J.-F., Su, B.-X., 2013. Widespread refertilization of cratonic and circum-cratonic lithospheric mantle. *Earth-Sci. Rev.* 118, 45-68.

Tankard, A.J., Jackson, M.P.A., Eriksson, K.A., Hobday, O.K., Hunter, D.R., Minter, W.E.L., 1982. Crustal Evolution of Southern Africa. Springer-Verlag, New York, pp. 523.

Taylor, S.R. and McLennan, S.M., 1985. The Continental Crust: Its Composition and Evolution. Blackwell Scientific Publications, Oxford pp. 312.

Taylor, J., Stevens, G., Buick, I.S., Lana, C., 2012. Successive mid-crustal, high-grade metamorphic events prove insight into Mid-Archean mountain-building along the SE margin of the proto-Kaapvaal craton. *Geol. Soc. Am. Bull.* 124, 1191-1211.

Tazoe H., Obata H., Gamo T., 2007. Determination of cerium isotope ratios in geochemical samples using oxidative extraction technique with chelating resin. *J. Anal. At. Spectrom.* 22, 616-622.

Touboul, M., Liu, J., O´Neil, J., Puchtel, I.S., Walker, R.J., 2014. New insights into the Hadean mantle revealed by ^{182}W and highly siderophile element abundances of supracrustal rocks from the Nuvvuagittuq Greenstone Belt, Quebec, Canada. *Chem. Geol.* 383, 63-75.

Touboul, M., Puchtel, I.S., Walker, R.J., 2012. ^{182}W evidence for long-term preservation of early mantle differentiation products. *Science* 335, 1065-1069.

Trela, J., Gazel, E., Sobolev, A.V., Moore, L., Bizimis, M., Jicha, B., Batanova, V.G. 2017. The hottest lavas of the Phanerozoic and the survival of deep Archean reservoirs. *Nature Geosci.* 10, 451-456.

Van Kranendonk, M.J., 2010. Two types of Archean continental crust: plume and plate tectonics on early Earth. *Amer. J. Sci.* 310, 1187-1209.

Van Kranendonk, M.J., 2011a. Onset of plate tectonics. *Science* 333, 413-414.

Van Kranendonk, M.J., 2011b. Cool greenstone drips, hot rising domes, and the role of partial convective overturn in Barberton greenstone belt evolution. *J. Afr. Earth Sci.* 60, 346-352.

Van Kranendonk, M.J., Collins, W.J., Hickman, A.H., Pawley, M.J., 2004. Critical tests of vertical vs horizontal tectonic models for the Archaean East Pilbara Granite-Greenstone Terrane, Pilbara Craton, Western Australia. *Precambrian Res.* 131, 173-211.

Van Kranendonk, M.J., Hickman, A., Smithies, R.H., 2007a. Paleoarchean development of a continental nucleus: the East Pilbara Terrane of the Pilbara Craton, Western

Australia. In: Van Kranendonk, M.J., Smithies, R.H., Bennet, V. (eds.), Earth's Oldest Rocks. Elsevier, Amsterdam, Developments in Precambrian Geology 15, 307-337.

Van Kranendonk, M.J., Hickman, A.H., Smithies, R.H., Nelson, D.R., 2002. Geology and tectonic evolution of the Archean North Pilbara terrain, Pilbara Craton, Western Australia. *Econ. Geol.* 97, 695-732.

Van Kranendonk, M.J., Kröner, A., Hegner, E., Connelly, J., 2009. Age, lithology and structural evolution of the c. 3.53 Ga Theespruit Formation in the Tjakastad area, southwestern Barberton Greenstone Belt, South Africa, with implications for Archean tectonics. *Chem. Geol.* 261, 115-139.

Van Kranendonk, M.J., Kröner, A., Hoffman, J.E., Nagel, T., Anhaeusser, C.R., 2014. Just another drip: re-analysis of a proposed Mesoarchean suture from the Barberton Mountain Land. *Precambrian Res.* 254, 19-35.

Van Kranendonk, M.J., Smithies, R.H., Griffin, W.L., Huston, D.L., Hickman, A.H., Champion, D.C., Anhaeusser, C.R., Pirajno, F., 2015. Making it thick: a volcanic plateau origin of Palaeoarchean continental lithosphere of the Pilbara and Kaapvaal cratons. In: Roberts, N.M.W., Van Kranendonk, M.J., Parman, S., Shirey, S., Clift, P.D. (eds.) Continent formation through time. *Geol. Soc. London, Spec. Publ.* 389, 83-111.

Van Kranendonk, M.J., Smithies, R.H., Hickman, A.H., Champion, D.C. 2007b. Secular tectonic evolution of Archaean continental crust: interplay between horizontal and vertical processes in the formation of the Pilbara Craton, Australia. *Terra Nova* 19, 1-38.

Van Kranendonk, M.J., Smithies, R.H., Hickman, A.H.,Wingate, M.T.D., Bodorkos, S., 2010. Evidence for Mesoarchean (~3.2 Ga) rifting of the Pilbara Craton: the missing link in an early Precambrian Wilson cycle. *Precambrian Res.* 177, 145-161.

Van Schijndel, V., Stevens, G., Zeh, A., Frei, D., Lana, C., 2017. Zircon geochronology and Hf isotopes of the Dwalile Supracrustal Suite, Ancient Gneiss Complex, Swaziland: Insights into the diversity of Palaeoarchaean source rocks, depositional and metamorphic ages. *Precambrian Res.* 295, 48-66.

Vervoort, J.D., Plank, T., Prytulak, J., 2011. The Hf-Nd isotopic composition of marine sediments. *Geochim. Cosmochim. Acta* 75, 5903-5926.

Vennemann, T.W. and Smith, H.S, 1999. Geochemistry of mafic and ultramafic rocks in the Kromberg Formation in its type section, Barberton Greenstone Belt, South

Africa. In: Lowe, D.R. and Byerly, G.R (eds.), Geologic evolution of the Barberton Greenstone Belt, South Africa. *Geol. Soc. America Spec. Paper* 329, pp. 133-150.

Viljoen M.J. and Viljoen R.P. 1969a. An introduction to the geology of the Barberton granite greenstone terrain. *Geol. Soc. S. Afr., Spec. Publ.* 2 (1), 9-28.

Viljoen, M.J. and Viljoen, R.P., 1969b. The geology and geochemistry of the lower ultramafic unit of the Onverwacht Group and a proposed new class of igneous rocks. *Geol. Soc. South Africa, Spec. Publ.* 2, pp. 55-86.

Viljoen, R.P. and Viljoen, M.J., 1969. The geological and geochemical significance of the upper formations of the Onverwacht Group. *Spec. Publ. Geol. Soc. South Africa* 2, 113-151.

Vinnik, L.P., Green, R.W.E., Nicolaysen, L.O., 1996. Seismic constraints of the mantle of the Kaapvaal craton. *Physics Earth Planet. Interiors* 95, 139-151.

Vockenhuber, C., Oberli, F., Bichler, M., Ahmad, I., Quitté, G., Meier, M., Halliday, A.N., Lee, D.-C., Kutschera, W., Steier, P., Gehrke, R.J., Helmer, R.G., 2004. New half-life measurement of ^{182}Hf: improved chronometer for the early Solar system. *Phys. Rev. Lett.* 93, 172501.

Von Brunn, V. and Hobday, D.K., 1976. Early Precambrian tidal sedimentation in the Pongola Supergroup of South Africa. J. *Sedimentary Petrol.* 46, 670-679.

Walraven, F. and Pape, J., 1994. Pb-Pb whole-rock ages for the Pongola Supergroup and the Usushwana Complex, South Africa. *J. Afr. Earth Sci.* 18, 297-308.

Wan, Y.-S., Liu, D.-Y., Dong, C.-Y., Xie, H.-Q., Kröner, A., Ma, M.-Z., Liu, S.-J., Xie, S.-W., Ren, P., 2015. Formation and evolution of the North China Craton. In: Zhai, M. (ed.) Precambrian geology of China. Springer Geology, Berlin-Heidelberg, pp. 59-135.

Watson, E.B. and Harrison, T.M., 1983. Zircon saturation revisited: temperature and composition effects in a variety of crustal magma types. *Earth Planet. Sci. Lett.* 64, 295-304.

Weis, D., Kieffer, B., Maerschalk, C., Barling, J., de Jong, J., Williams, G.A., Hanano, D., Pretorius, W., Mattielli, N., Scoates, J.S., Goolaerts, A., Friedman, R.M., Mahoney, J.B. (2006) High-precision isotopic characterization of USGS reference materials by TIMS and MC-ICP-MS. *Geochem. Geophys. Geosyst.* 7, Q08006, doi:10.1029/2006GC001283.

Weyer S., Münker C., Rehkämper M., Mezger K., 2002. Determination of ultra-low Nb, Ta, Zr and Hf concentrations and the chondritic Zr/Hf and Nb/Ta ratios by isotope dilution analyses with multiple collector ICP-MS. *Chem. Geol.* 187, 295-313.

White, W.M. and Patchett, J., 1984. Hf-Nd-Sr isotopes and incompatible element abundances in island arcs: implications for magma origins and crust-mantle evolution. *Earth Planet. Sci. Lett.* 67, 167-185.

Wilde, S.A., Valley, J.W., Peck, W.H., Graham, C.M., 2001. Evidence from detrital zircons for the existence of continental crust and oceans on the Earth 4.4 Gyr ago. *Nature* 409, 175-178.

Willbold, M., Elliott, T., Moorbath, S., 2011. The tungsten isotopic composition of the Earth's mantle before the terminal bombardment. *Nature* 477, 195-198.

Willbold, M., Mojzsis, S.J., Chen, H.-W., Elliott, T., 2015. Tungsten isotope composition of the Acasta Gneiss Complex. *Earth Planet. Sci. Lett.* 419, 168-177.

Wilson, A.H. and Carlson, R.W 1989. A Sm-Nd and Pb isotope study of Archaean greenstone belts in the southern Kaapvaal Craton, South Africa. *Earth Planet. Sci. Lett.* 96, 89-105.

Wilson, A.H. and Grant, C.E., 2006. Physical volcanology and compositions of the basaltic lavas in the Archaean Nsuze Group, White Mfolozi inlier, South Africa. In: Reimold, W.U. and Gibson, R.L. (eds.), Processes on the Early Earth. *Geol. Soc. America Spec. Paper* 405, pp. 255-289.

Wilson, A.H. and Zeh, A., 2018. U-Pb and Hf isotopes of detrital zircons from the Pongola Supergroup: Constraints on deposition ages, provenance and Archean evolution of the Kaapvaal craton. *Precambrian Res.* 305, 177-196.

Xie, Q., Kerrich, R., Fan, J., 1993. HFSE/REE fractionations recorded in three komatiite – basalt sequences, Archean Abitibi greenstone belt: implications for multiple plume sources and depths. *Geochim. Cosmochim. Acta* 57, 4111-4118.

Zhang, J. and Herzberg, C. 1994. Melting experiments on anhydrous peridotite KLB-1 from 5.0 to 22.5 GPa. *J. Geophysical Res.* 99, 17729-17742.

Zeh, A., Gerdes, A., Millonig, L., 2011. Hafnium isotope record of the Ancient Gneiss Complex, Swaziland, southern Africa; evidence for Archaean crust-mantle formation and crust reworking between 3.66 and 2.73 Ga. *J. Geol. Soc. Lond.* 168, 1-11.

Curriculum Vitae

Mein Lebenslauf wird aus Gründen des Datenschutzes in der elektronischen Fassung meiner Arbeit nicht veröffentlicht.